DISSERTATION

SINGLE PIXEL COMPUTATIONAL IMAGING

Submitted by

Patrick Allen Stockton

Department of Electrical and Computer Engineering

In partial fulfillment of the requirements

For the Degree of Doctor of Philosophy

Colorado State University

Fort Collins, Colorado

Spring 2023

Doctoral Committee:

Advisor: Randy A. Bartels

Ali Pezeshki
Jennifer Muller
Jesse Wilson

Copyright by Patrick A. Stockton 2023

All Rights Reserved

ABSTRACT

SINGLE PIXEL COMPUTATIONAL IMAGING

Microscopy has a long rich history of peering into life's smallest mysteries. Ever since the first microscope, the ability to see objects that would otherwise be impossible to see with the naked eye have allowed new discoveries and modern technology has benefited tremendously. There have been many improvements on microscopes over the centuries with each improvement unlocking more knowledge as we go. Some of these advancements are the modern objective lens correcting for numerous optical aberrations, phase contrast imaging allowing nearly transparent samples to have high contrast, the confocal pinhole allowing an easy method to get optical sectioning, and super resolution microscopy surpassing the diffraction limit by several orders of magnitude. One of the most amazing things about all these discoveries is that they all rely on the same fundamental concepts.

This work focuses on expanding the capabilities of single pixel imaging. Single pixel imaging is a class of imaging that encodes spatial information on a temporal signal using a single element detector; having knowledge of the encoding allows the time signal to be reconstructed to generate a spatial image. A canonical example of single pixel imaging is laser scanning microscopy (LSM). More complicated encoding systems have been developed but the basic idea for reconstruction remains the same. There are several advantages conferred to single pixel imaging such as image formation is resistant to scattering, very fast temporal response, flexibility in detector selection at a given wavelength, and exotic imaging information.

My research primarily utilizes two techniques, SPatIal Frequency modulated Imaging (SPIFI) and Coherent Holographic Image Reconstruction by Phase Transfer (CHIRPT), both are explained in detail. My research aims to expand the capability of SPIFI by providing a method for homogenizing the anisotropic resolution observed in the higher orders, additionally, I present a method of solving the inverse problem that allows the measurement matrix to

more accurately represent to true image formation process thereby increasing the performance of the reconstruction. I present research for CHIRPT which takes advantage of the encoded coherent phase information of two interfering beams to measure the quantitative phase of an object. I also present a new technique utilizing CHIRPT's holographic phase information to extend optical diffraction tomography to incoherent emitters which has long been an illusive task.

ACKNOWLEDGEMENTS

Throughout the writing of this dissertation I have received a great deal of support and assistance.

I would like to acknowledge my colleagues Jeff Field, Keith Wernsing, Dave Smith, Robby Stokoe, and Gabe Murray their wonderful collaboration, insights, and encouragement over the years.

In addition, I would like to thank my parents for their wise counsel and sympathetic ear. You are always there for me. Finally, I could not have completed this dissertation without the support of my friends, Cameron Coleal and Clayton Bargsten, who provided stimulating discussions as well as happy distractions to rest my mind outside of my research.

DEDICATION

I would like to dedicate this dissertation to my loving parents, Everett and Sharon Stockton.

TABLE OF CONTENTS

LIST OF FIGURES

Chapter 1

Introduction to Imaging

1.1 Introduction

This chapter lays the groundwork upon which my subsequent research is built. It provides a comprehensive introduction to essential imaging theory concepts, with an emphasis on intuitive explanations to facilitate comprehension. Light interference is the primary methodology used to describe core concepts, with the goal of painting a cohesive portrait of the necessary optical background for my research. I also discuss absorption and scattering using analogies to further aid understanding of these fundamental concepts. Furthermore, refraction and diffraction are described from a wave-based perspective, in order to provide a more detailed account of these phenomena. Finally, I finish this chapter off with an in-depth comparison of coherent versus incoherent imaging.

1.2 Core Imaging Concepts

In imaging theory, there are several key concepts that repeatedly show up and the understanding of these concepts help explain the vast majority of imaging systems. The core concepts will be briefly described below and referenced throughout this manuscript. The primary objective of an imaging system is to relay object information to a detection plane so that a spatial map or image can be formed of the contrast mechanism of interest. The number of contrast mechanisms that can be probed are vast and many can be categorized as absorbing or scattering the input illumination. Both categories may result in a change in the input illumination intensity, wavelength, phase shift, or any combination of the three. The specific contrast mechanism of interest depends on the sample and the information needed to answer questions about the sample. In the following sections, I will describe these general categories and give some specific examples to help solidify the concepts.

The image formation process can be quite varied from one system to the next, however, all imaging systems are going to act as a low pass filter of the object's spatial frequency information. This low pass filtering leads to blurring of the imaged object information, often referred to as the diffraction limit. There are many clever techniques that have been developed to circumvent the diffraction limit but even these super-resolution imaging systems still suffer from low pass filtering. There are many great books that should be referenced if more detail is required such as Mertz' *Introduction to Optical Microscopy* [95], Barrett's *Foundations of Image Science* [6] and Wang' *Biomedical Optics Principles and Imaging* [144], to name a few.

1.2.1 Absorption

Absorption is a light-matter interaction where excitation light excites or deposits energy into an atom or molecule causing an increase in the energy of an electron. Then, depending on the decay pathway of the electron, the absorption will be classified as radiative or non-radiative. A radiative decay pathway will release light at a new optical wavelength such as fluorescence or phosphorescence. A non-radiative decay pathway will convert the optical energy into vibrational energy in the atom/molecule or transfer energy into the surrounding environment as heat. Figure 1.1 shows a simple Jablonski energy diagram of several absorption pathways where both radiative and non-radiative pathways may occur.

1.2.2 Scattering

Now that we have taken a brief look at absorption, let us turn our attention to scattering. Scattering, like most topics, is very broad in scope but can be categorized into several main classes, coherent vs incoherent scattering, and elastic vs inelastic scattering. Here coherent scattering means that there is a defined phase relationship between the input light and the output light, and incoherent scattering means that there is a random phase relationship between the incoming and outgoing light. Elastic scattering means that there is no change of energy of the incoming and outgoing light, i.e. both photons have the same wavelength, and inelastic scattering means the incoming and outgoing photons will have different energies such as in

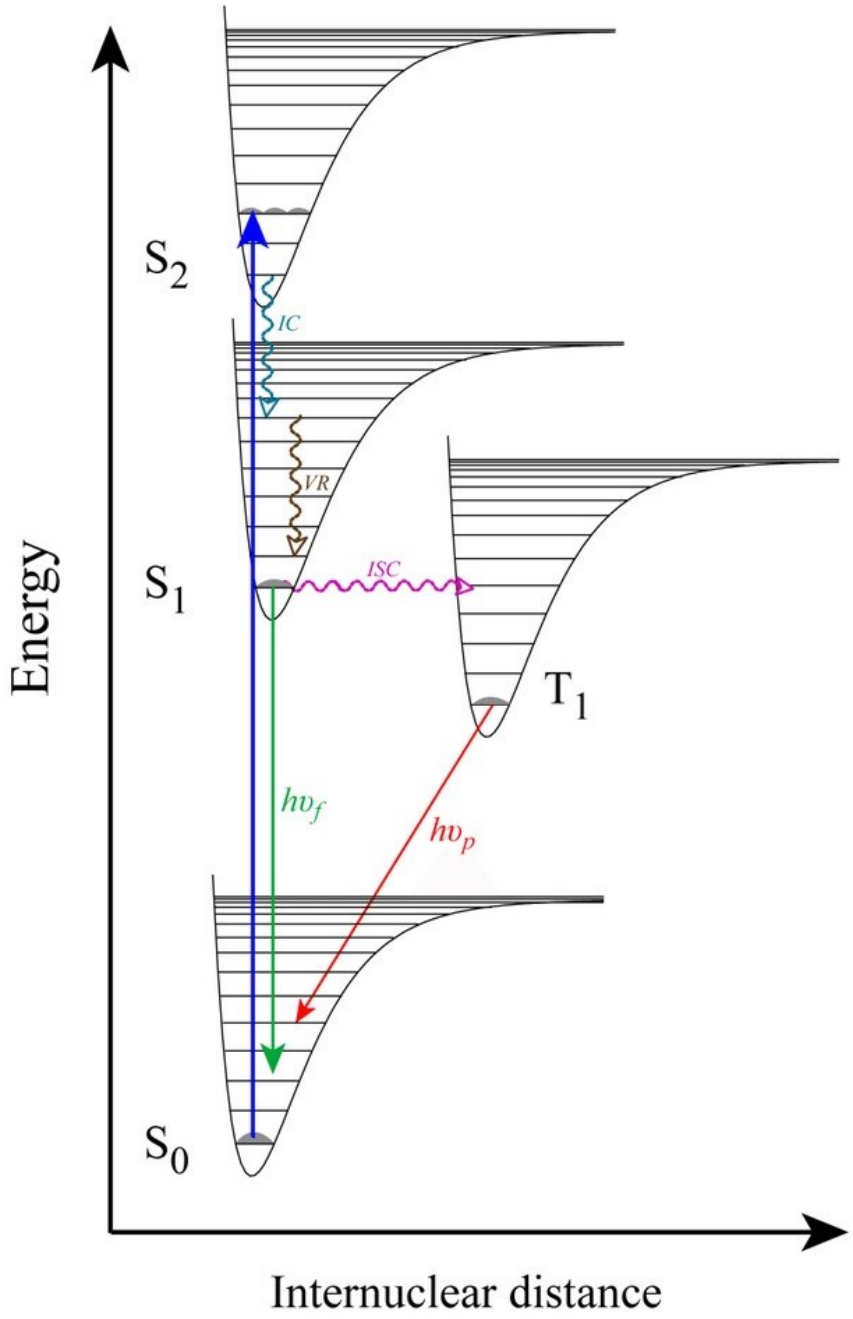

Figure 1.1: This figure shows the Jablonski energy diagram. The Jablonski diagram shows real atomic energy levels of an atomic system, S_0, S_1, S_2, and T_1 with the y-axis representing energy and the x-axis representing internuclear distance. The black U-shaped lines illustrate energy levels and the ladder of black lines represent vibrational energy levels. The Blue arrows pointing up show absorption, the squiggly lines represent non-radiative pathways internal conversion (IC), vibrational relaxation (VR), or intersystem crossing (ICS), the arrows pointing down show radiative pathways. This figure was borrowed from [79].

Raman scattering. Scattering can be defined as a change in the propagation direction, phase, or wavelength of incoming light by means of interacting with matter.

Simple linear elastic scattering derives its physical origin from the electric field of the incoming light causing electrons to oscillate in atoms or molecules. In the case of absorption, the electron will get promoted to a higher energy state of the energy manifold of the atomic system. In the case of scattering, an electron will be driven to oscillate at the same frequency as the incident light. The oscillating electron acts as a primary source, re-emitting radiation or scattering the illumination light, causing a change in the phase and direction of the input illumination. This description of absorption and scattering is only scratching the surface of a very large topic, there are many books devoted to these topics (see resources [71, 83, 9, 21])

1.2.3 Diffraction and Refraction

Diffraction and refraction are key optical phenomena that play a significant role in the field of optics, and a thorough understanding of these concepts is necessary to make sense of many other related concepts. These phenomena can be best understood by considering the wave nature of light. In essence, both diffraction and refraction involve the bending of light around or off an object [71]. In the following section, I will provide a detailed account of both phenomena.

Diffraction

Diffraction is a complex phenomenon with several formulations of definition available [71]. For the purposes of this discussion, the definition of diffraction as the bending of waves around the corners of an obstacle or aperture into the geometric shadow of that obstacle or aperture will be utilized. One of the earliest optical diffraction models was proposed by Christiaan Huygens, a prominent Dutch mathematician and physicist of the 17th century. Huygens hypothesized that a wavefront of light could be comprised of numerous spherical wavelets, where a single wavelet could be represented as $E = E_0/r' \exp\{i(kr' - \omega t)\}$, with E denoting the electric field, E_0 representing the amplitude, r' representing the position (x,y), $k = 2\pi/\lambda$ indicating the wavenumber, and ω signifying the optical frequency. These wavelets would then

propagate over a small distance, creating additional secondary/virtual sources, known as Huygens wavelets [112], as shown in Fig. 1.2 (depicted as yellow dots). Huygens proposed that the secondary spherical wavelets would interfere with one another to create the propagating wavefront, $E_1 = C_0 \int\int \exp\{i(kr' - \omega t)\} \mathrm{d}r'$, where C_0 is an overall constant (refer to the left side of Fig. 1.2(a) for E_1). Subsequently, Huygens envisioned the wavefront being partially obstructed or clipped by an obstacle, leading some of the spherical wavelets to no longer interfere with the rest of the wavefront, thereby causing the spherical wavelets to disperse around the corner of the object, resulting in diffraction. This can be represented mathematically as $E_A = C_0 \int\int \exp\{i(kr' - \omega t)\} \mathrm{d}A$, where $\mathrm{d}A$ refers to a differential area over the aperture [112]. While this formulation of diffraction has proven to be highly effective in practice, it should be noted that it is only a model and does not reflect the manner in which the physical world functions. A more accurate but less intuitive model of light propagation is described by Maxwell's equations, in which the 'wave equation' can be formulated and solved, enabling diffraction to be calculated directly. However, this approach entails a higher level of mathematical complexity [95].

A classic example of diffraction is Young's double slit experiment, shown in Fig. 1.2(b). Young's double-slit experiment allows coherent light to pass through two slits. Then some distance, L, from the slits is a screen or camera on which the light that passes through the slits is observed. If light behaved as a particle or as a ray then one might expect to only see two thin lines on the screen. However, this is not what is observed! What is actually observed is an interference pattern that depends on the wavelength of light, the slit separation, and the distance from the aperture to the screen. From these parameters, the interference pattern can be predicted from simple geometry and an assumption of spherical waves emanating from each slit. The resulting illumination pattern will be that of two single slit sinc patterns interfering with one another, illustrated in Fig. 1.2(b). The mathematical details are not shown here because there are many great references that explain the calculations in extensive detail, [112, 95].

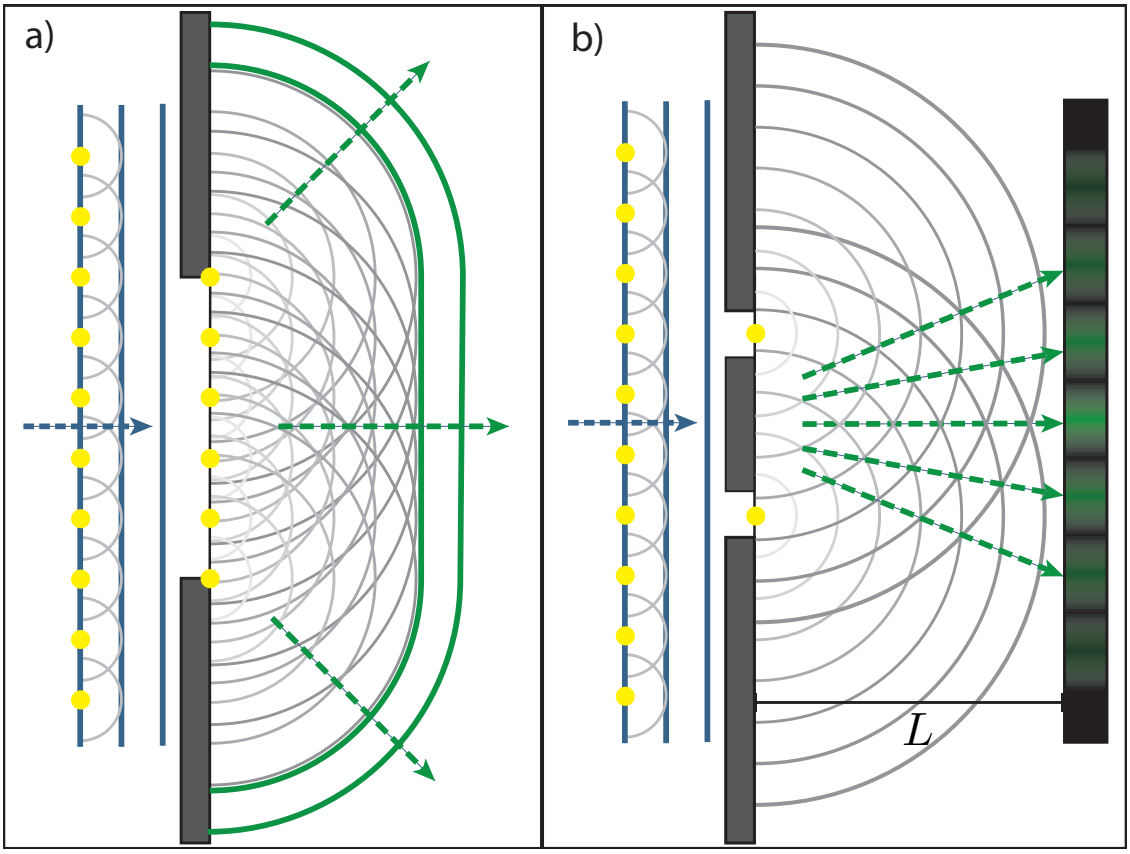

Figure 1.2: Depictions of Huygens wavelets in diffraction. Panel (a) shows Huygens wavelets on the left propagating to the right. A spherical wave is produced at the yellow dots. The wavelets propagate forward creating a wavefront, blue solid lines. The dashed arrows represent the direction of energy propagation. The aperture clips part of the wavefront, leaving only the center of the beam. The spherical waves again propagate out from the yellow dots, this time the wavefront is a curved, solid green line, due to the interference of the remaining wavelets. Panel (b) depicts a similar scenario as (a) however this time there are two slits that only allow two spherical waves to emanate, one for each slit. These spherical waves gain interfere with each other causing the double-slit interference pattern.

Diffraction is observed regularly in optics. It plays an important role in determining a beam's spatial profile when passed through a pinhole or through a microscope's back aperture [95]. Diffraction also occurs when light falls on an opaque sample causing light to 'scatter'. Diffraction is particularly important in Chapter 8.2.5, as Fluorescent Diffraction Tomography is capable of imaging highly scattering objects.

Refraction

Refraction is a fundamental concept in optics that occurs when light changes direction as it passes through an interface between two mediums with different refractive indices. This phenomenon is commonly experienced in everyday life, such as the apparent bending of a pencil when submerged in water. Refraction plays a critical role in imaging biological samples like cells or tissues, which are often referred to as phase objects due to their minimal absorption compared to their scattering, which is caused by refraction. In this chapter, I will present an intuitive derivation of the effect of refraction on light propagation and explain why it is of particular importance in Sections 4.2 and 5.7 when discussing the measurement of quantitative phase.

To start, let's first define the refractive index of a material. There are rigorous derivations of the refractive index, however, let it suffice for now to give a simple definition. The refractive index, n, of a material is the ratio of the speed of light in a vacuum, c, compared to the speed of light in a homogeneous (uniform) material, v, giving $n = c/v$. Now, let's consider a plane wave propagating in air, $n_{air} = n_1 = 1$ toward a homogeneous flat surface such as glass, $n_{glass} = n_2 = 1.5$. When the plane wave crosses the boundary at some angle θ_1, (see the left of Fig. 1.3), the light will slow as it enters the glass. Due to the fact that the light is propagating more slowly the wavefronts of the light will build up on each other, this will cause the wavelength of the light to decrease with respect to the light propagating in the first medium, air. The phase of the electric field must be continuous across the interface, i.e. where there is a peak in the first medium, there will also be a peak in the second medium at the interface. With this reasoning, we see why the wavefront must bend at the interface. In order for the light to propagate slower in the second medium and the electric field to be continuous, the light must bend in towards the surface normal of the interface when $n_1 < n_2$ and away from the surface normal when $n_1 > n_2$, Fig. 1.3. As the difference between the two refractive indices increases the light will bend even more, Fig. 1.3 (right). This brings up an interesting point, since scattering in biological samples is primarily a function of refractive index difference, if the refractive index difference between

surfaces is minimized the scattering will also be minimized. This technique is often referred to as optical clearing and can be very useful when studying large biological samples.

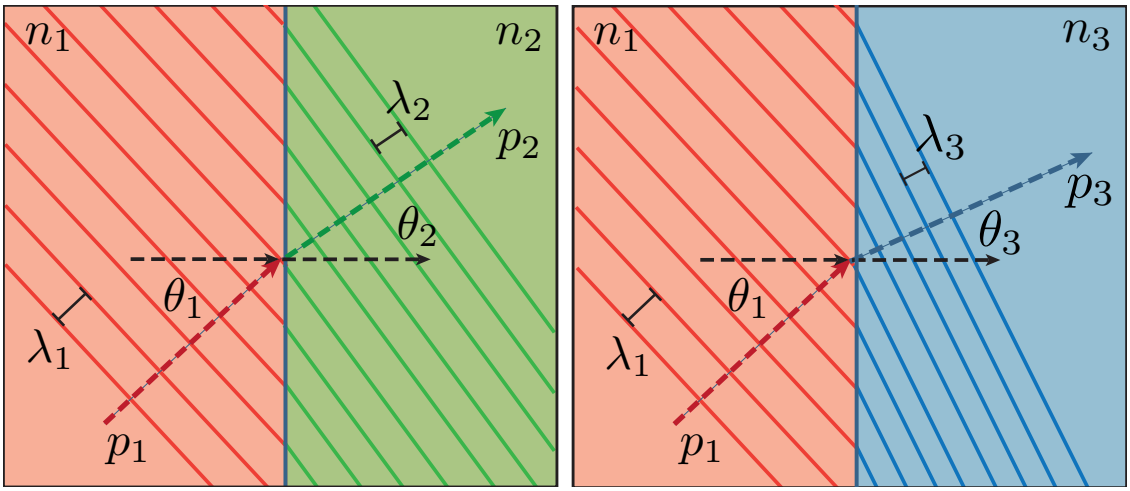

Figure 1.3: This figure shows a depiction of how Snell's Law works. The red medium (left side) has a refractive index n_1 that is less than the right side medium n_2 and n_3. When a wavefront (red solid line) impinges on the interface between the two media, the wavefront spacing will decrease causing the wavelength to decrease ($\lambda_1 > \lambda_2$). In order to satisfy the continuity boundary condition the wavefront must bend. The left image shows a small refractive index difference between n_1 and n_2. The right image shows a large refractive index difference causing the wavefront to bend more.

The description of refraction above does provide sufficient information to gain an intuitive understanding of why light bends due to refraction, additionally a formula of how much the light bends could be derived, however, I want to present an argument based on the conservation of momentum because of its elegance. Note, optical momentum is a bit tricky to define, it seems that there are at least two different formulations of optical momentum which both agree with experiments depending on which experiment is performed [4, 13]. I will use the form of optical momentum that seems to be related to kinetic momentum and ignore angular momentum. Since there is no loss of photon energy across the interface, we can infer that there is no momentum change either, $p_1 = p_2$. We can then use the definition for photon momentum, $p = \hbar\mathbf{k}$, here $\hbar$ is the reduced Planck's constant and $\mathbf{k} = n\mathbf{k}_0$ is the wavenumber (the wavenumber is described later in Section 1.3). We can then use the fact that the wavenumber can be decomposed into spatial frequency components (x, y, z), without loss of generality we can set

$y = 0$ giving $(x, 0, z) = (x, z)$ plane, $\mathbf{k} = (k_x, k_z) = nk_0(\sin\theta, \cos\theta)$. Plugging in our decomposition into the conservation of momentum expression and looking at the x-component we get

$$k_{x1} = k_{x2}$$

$$n_1 k_0 \sin\theta_1 = n_2 k_0 \sin\theta_2.$$

Interestingly this equation can be interpreted as the wavenumber being conserved across an interface. This yields the well-known 'law of refraction' also known as 'Snell's Law'

$$\frac{\sin(\theta_1)}{\sin(\theta_2)} = \frac{n_2}{n_1}. \tag{1.1}$$

Using the conservation of momentum, the direction of propagation, k_x changes at the interface due to the change in refractive index. In the next section, we will look at one of the most useful mathematical tools in optics, the Fourier transform, and we will see that it can decompose our signal into a powerful concept known as spatial frequencies.

1.2.4 Fourier Transform

The Fourier transform is one of the most powerful tools in mathematics. It will be very useful in assisting in the analysis of optical theory and for understanding the concept of spatial frequencies, which is described in greater detail in Section 1.3. The goal of this section is to give an intuitive understanding of the Fourier transform and show its relevance in optics.

The idea of the Fourier transform is that any signal can be decomposed into a set of sinusoids, each with an amplitude, frequency, and phase. When the Fourier transform is applied to a signal, the signal is said to be in the frequency domain (inverse domain or conjugate domain). It is important to note that the frequency is not confined to just temporal signals, units [$\sec^{-1}$] but rather it can have any inverse units such as inverse space, i.e. spatial frequencies, units

$[m^{-1}]$. Calculating the Fourier transform is fairly straightforward, defined as

$$\hat{f}(k) = \int_{-\infty}^{\infty} f(x) \mathrm{e}^{-i2\pi xk} \mathrm{d}x \tag{1.2}$$

where $\hat{f}(k)$ is the Fourier transform of the real domain function, $f(x)$, k is the frequency or inverse domain variable which can be n-dimensional, x is the real domain variable such as time or space, also n-dimensional, and $\mathrm{e}^{i2\pi xk}$ is called the Fourier kernel. One way to interpret Eqn. 1.2 is by first considering only one frequency say k_0 and plugging that frequency into the Fourier kernel. Then by investigating the Fourier kernel, $\mathrm{e}^{-i2\pi xk_0}$, we can interpret the result as finding the center of mass of that frequency, k_0, on the complex plane, $\mathrm{a} + i\mathrm{b}$, where a and b are some real values. This center of mass can be converted into amplitude and phase of the sinusoid at the frequency k_0. The amplitude can be calculated by finding the magnitude of the complex number, $r = \sqrt{a^2 + b^2}$ and the phase/angle can be calculated using $\phi = \mathrm{atan2}(a, b)$. The $\mathrm{atan2}(\cdot, \cdot)$ function is a computer science function that returns the true angle regardless of the quadrant the vector resides [161]. Let's suppose the amplitude at k_0 was zero, this would mean that there is no sinusoid at frequency k_0 contained in the signal of interest. However, if the amplitude is non-zero then the signal contains that 'amount' of the sinusoid, and the angle represents the starting phase. This can then be done for all frequencies resulting in the Fourier transform.

Once the Fourier transform has been performed, and the signal is in the frequency domain, it is very easy to apply mathematical operations such as low pass, high pass, or band pass filtering or to perform a convolution of multiple signals. The frequency domain signal can be readily converted back into the real domain signal by performing an inverse Fourier transform,

$$f(x) = \int_{-\infty}^{\infty} \hat{f}(k) \mathrm{e}^{i2\pi xk} \mathrm{d}k. \tag{1.3}$$

The inverse Fourier transform can be interpreted as summing up all the decomposed sinusoids with the proper weighting (amplitude and phase) to reconstruct the original real domain signal,

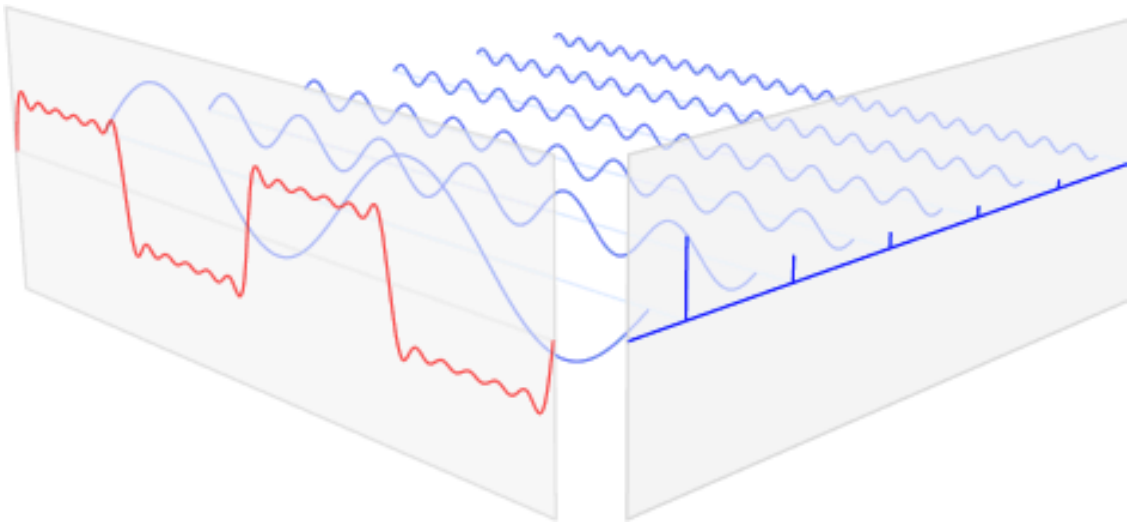

Figure 1.4: This figure shows how a time signal (red line) can be decomposed into a set of sinusoids (light blue lines) as well as the resulting amplitude spectrum from the Fourier transform (dark blue line). Figure obtained from https://www.ritchievink.com/blog /2017/04/23/understanding-the-fourier-transform-by-example.

$f(x)$. Said differently, the inverse Fourier transform is a phasor sum of complex numbers which reconstruct the real domain signal. In this case, the $e^{i2\pi xk}$ is known as the inverse kernel which is weighted by complex coefficients, $\hat{f}(k)$.

Equations 1.2 and 1.3 compute the Fourier transform pair for continuous signals, however, in practice, most mathematics is going to be performed by a modern digital computer. This means that a continuous signal from a detector such as a photodiode will have to be digitized so that it can be operated by a computer. The digitization process turns a continuous signal into a discrete signal, therefore, it is necessary to modify the above formulas to deal with discrete signals. I will just give the discrete Fourier transform equations, however, a full derivation can be found here [1]. The forward discrete Fourier transform (DFT) is

$$\hat{f}_k = \sum_{n=0}^{N-1} f_n \, e^{-i2\pi kn/N} \tag{1.4}$$

The frequency variable, k, is evaluated on the domain $k \in [0, N-1]$. The DFT operates on a finite number of samples, N, and the sampling frequency, k_s, the signal is sampled on will determine the maximum resolvable frequency.

One interesting effect that arises from digitizing a signal is aliasing. Aliasing occurs when part of the high frequencies 'wrap around' into low-frequency components; this is not a problem that exists for continuous signals. The reason for this is beyond the scope of this introduction, however, it is useful to understand when it will occur and how to avoid it. Aliasing will occur when the continuous signal contains frequencies that are greater than half the sampling frequency, $k_s/2$. Therefore, for a signal to be properly represented the digitized signal must be band-limited so that any frequency greater than $k_s/2$ is removed from the signal before the signal is digitized. This criterion is known as the Nyquist sampling theorem.

The inverse discrete Fourier transform (IDFT) is computed using the following equation,

$$f_n = \frac{1}{N} \sum_{k=0}^{N-1} \hat{f}_k \, \mathrm{e}^{i2\pi kn/N}. \tag{1.5}$$

The IDFT will return the original discrete function assuming Nyquist sampling was satisfied.

Figure 1.4 depicts the decomposition of a time signal (red) into sinusoids (light blue), each with an amplitude (dark blue line) and relative phase. The loss or scrambling of phase information results in significant distortion of the reconstructed signal in the real domain. If faced with the choice of losing either amplitude or phase information in the Fourier transform, it is advisable to always select the former. The significance of phase information as compared to amplitude information is illustrated in Figure 1.5. The left panel of the figure shows a real domain image of a lion, while the middle panel shows the two-dimensional Fourier transform information, including both magnitude and phase. The right column of the figure displays the reconstructions of the lion using only the magnitude of the Fourier transform with the phase set to zero (top right) and using only the phase with the magnitude set to one (bottom right). From this illustration, it is evident that phase information is more important than amplitude information, as the phase-only reconstruction is recognizable as a lion, while the amplitude-only reconstruction is not.

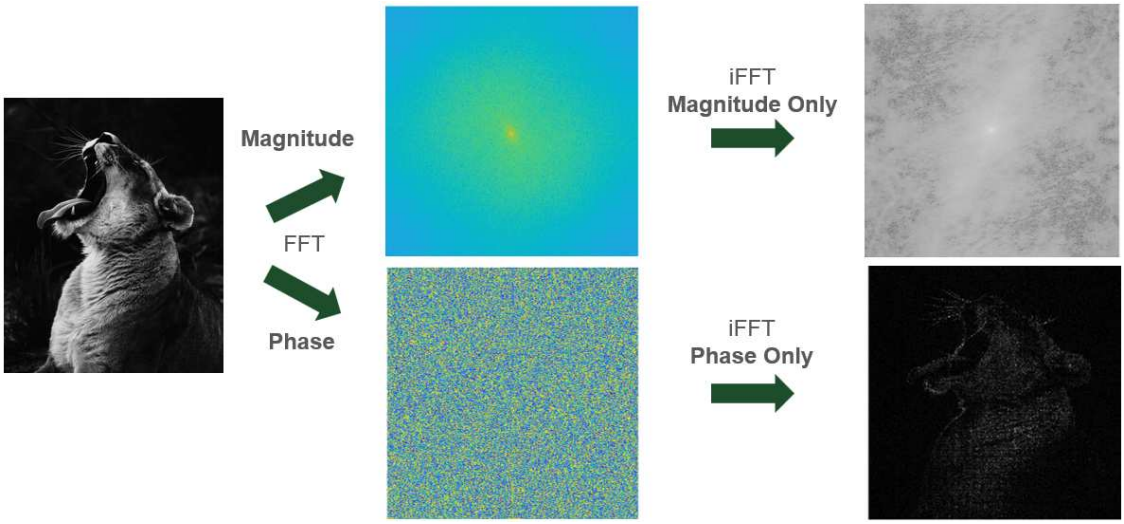

Figure 1.5: This figure shows that magnitude and phase of the Fourier transform (center column) of the lion (left). The right column shows the reconstruction of the lion when (top) only the magnitude is unchanged and the phase is set to all zeros and (bottom) when the phase is unchanged and the magnitude is set to all ones.

1.3 Spatial Frequencies

After discussing the Fourier transform, it is now pertinent to delve into the closely related topic of spatial frequencies, which is considered one of the most important concepts in imaging theory. Spatial frequencies offer a simple yet powerful means of describing an imaging system's response, filtering operations, tomographic reconstruction, image aberrations, and more. In fact, spatial frequencies are used extensively in the following chapters: 5.7, 7.6, 8.2.5, and 9.6.2. Its significance cannot be overstated, and it can be defined rather simply.

The idea of spatial frequencies, or angular spectrum representation of a field, posits that any field can be broken down into a set of plane waves propagating at various angles with respect to the optic axis. A plane wave is essentially a field that is uniform and extends infinitely in the transverse directions. If a particular direction is assigned to the z-axis, then the plane wave can be represented as $E_0 e^{i(k_x x + k_y y)} e^{\pm i|k_z|z}$, where E_0 is the amplitude, k_x, k_y, and k_z are spatial frequencies, and x, y, and z are spatial coordinates. The term $e^{\pm i|k_z|z}$ is referred to as the propagator in reciprocal space. It is noteworthy that the '-' sign indicates propagation in the half-space $z < 0$, while the '+' sign signifies propagation in the half-space $z > 0$ [104].

The wavevector $\mathbf{k} = (k_x, k_y, k_z)$ has a length given by $|\mathbf{k}| = k = 2\pi/\lambda$. Figure 1.6(a) shows the wavevector in reciprocal space. We see that it can be decomposed into its spatial frequency components. From geometry, we write down the well-known spatial frequency relationship,

$$k_z = \sqrt{k^2 - k_x^2 - k_y^2}. \tag{1.6}$$

From the above equation, we see that the k_z will vary as the transverse spatial frequencies, k_x and k_y, vary.

Spatial frequencies are defined as plane waves propagating at an angle with respect to the optic axis. However, this definition lacks intuition in visualizing what a spatial frequency looks like in real space. In order to gain a better understanding, let us consider a tilted plane wave, $(k_x, k_y = 0)$, with a spatial frequency, $\mathbf{k} = k(\sin\theta, 0, \cos\theta)$, where $\theta \neq 0$, propagating to some plane, p_0. We place a camera at plane p_0 and ask, "what will the camera see?" The camera responds to the intensity, $I(\mathbf{x}) = |E_\theta(\mathbf{x})|^2$, so the phase information in the field will be lost and the camera will simply see a uniformly illuminated screen, similar to what we would expect if the plane wave was propagating on the optic axis.

To visualize what a spatial frequency looks like, we need to introduce an additional component. Let us introduce a second wave that propagates on the optic axis, E_{DC}. This time, when we ask what the camera sees with both waves at plane p_0, the answer will yield the desired result. The camera will see the interference between $E_\theta(\mathbf{x})$ and $E_{DC}(\mathbf{x})$, resulting in an intensity of $I(\mathbf{x}) = |E_\theta(\mathbf{x}) + E_{DC}(\mathbf{x})|^2 = 2I_0\left[1 + 1/2\cos\left(\omega t + \Delta\mathbf{k}\cdot\mathbf{x} + \phi\right)\right]$. The cosine is the interference between the two fields, and the frequency of the cosine term is what a spatial frequency looks like in real space, as shown in Fig. 1.5(b).

The depicted diagram underscores a critical aspect of the interference of spatial frequencies, which facilitates the focusing of collimated laser beams to a minute point focus via a lens, or the formation of an image of a sample using an imaging system. Notably, the image creation process is fundamentally predicated on the interference of titled plane waves. Moreover, it is

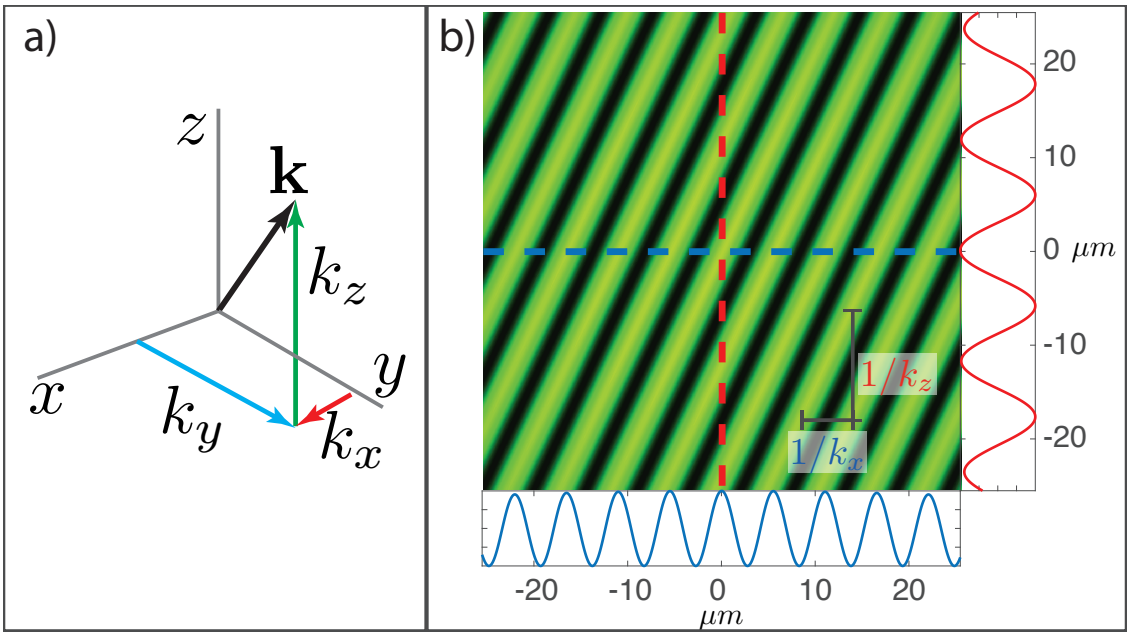

Figure 1.6: Panel a) shows the spatial frequency decomposition of the wavevector. Panel b) illustrates what a spatial frequency looks like in 2D space. The shortest distance from peak to peak is the optical wavelength, however, since the wavefront is propagating at some angle with respect to the x-axis, the wavefront can be decomposed into constituent components. The blue lines show the line out of the x-spatial frequency and the red lines show the z-spatial frequency. If the x-spatial frequency changes the z-spatial frequency must also change according to the dispersion relationship, $k_z = \sqrt{k^2 - k_x^2 - k_z^2}$

important to note that the maximum spatial frequency, which is determined by the numerical aperture of the imaging system, will serve as the limiting factor for the image resolution.

1.3.1 Numerical Aperture

One of the most important optical parameters for microscopy is the numerical aperture. The numerical aperture defines the highest spatial frequency that will be collected by an imaging system, defined as

$$\text{NA} = n \sin(\theta_{max}) \tag{1.7}$$

where NA is the numerical aperture, n is the refractive index of the immersion media, (i.e. $n_{air} = 1$, $n_{water} = 1.3$, $n_{oil} = 1.5$), and θ_{max} is the largest collected angle of light. The largest collection angle can be easily determined geometrically by using the diameter of the lens, D, and focal

length, f, of the objective with this equation, $\theta_{max} = \tan^{-1}(D/2f)$. This equation is especially useful if a non-standard objective is used in the microscope such that the numerical aperture is not printed on the side of the lens housing.

1.4 Mathematical Description of Coherence

The concept of coherence can be defined as the correlation across time and space of an electromagnetic wave. Simply put, coherence refers to how much temporal or spatial separation can exist between two waves before they no longer meaningfully interfere with each other. It is important to note that all electromagnetic waves can interfere with one another, regardless of whether they are classified as coherent or incoherent. Therefore, the statement "Coherent waves interfere with one another, while incoherent waves do not" is false. The relevant question is not whether waves interfere with one another, but over what range the interference occurs.

In this section, we will develop the mathematical formalism that is used to describe the degree of coherence of a light source. This derivation follows the approach presented in [6]. The next section will use this formalism to describe the effects that coherence has on imaging systems.

It is common to describe light as an ideal source such as a continuous wave (CW) laser, $E(t) = E_0(\mathbf{r})\exp(-2\pi i \nu_0 t)$, which is perfectly monochromatic, ν_0, with uniform amplitude. This type of light will be coherent across all time and space. However, natural light will have variations in amplitude and have a spectral bandwidth, $E(\mathbf{r},t) = \tilde{E}_0(\mathbf{r},t)\exp(-2\pi i \bar{\nu} t)$, where $\tilde{E}_0(\mathbf{r},t)$ is a complex amplitude that varies in time and space, and $\bar{\nu}$ is the center wavelength. By taking the normalized autocorrelation of the electric field the complex degree of coherence can be determined, defined as

$$\gamma(\mathbf{r},\mathbf{r}',\tau) = \frac{\langle \tilde{E}_0(\mathbf{r},t+\tau)\tilde{E}_0^*(\mathbf{r}',t)\rangle}{\sqrt{\langle|\tilde{E}_0(\mathbf{r},t)|^2\rangle\langle|\tilde{E}_0(\mathbf{r}',t)|^2\rangle}} = \frac{\Gamma(\mathbf{r},\mathbf{r}',\tau)}{\sqrt{\langle|\tilde{E}_0(\mathbf{r},t)|^2\rangle\langle|\tilde{E}_0(\mathbf{r}',t)|^2\rangle}}. \tag{1.8}$$

Where $\Gamma(\mathbf{r},\mathbf{r},\tau) = \langle \tilde{E}_0(\mathbf{r},t+\tau)\tilde{E}_0^*(\mathbf{r}',t)\rangle$ is the mutual coherence function. The complex degree of coherence characterizes the ability of two space-time points to interfere with each other.

Specifically, the degree of coherence, denoted by $\gamma(\mathbf{r}, \mathbf{r}', \tau)$, quantifies the extent to which points $(\mathbf{r}, t)$ and $(\mathbf{r}', t')$ can interfere at a third point $(\mathbf{r}'', \tau)$, where $\tau = t - t'$. This quantity can be readily measured using an interferometer, additionally, the degree of coherence is a valuable tool for analyzing the coherence properties of natural light. While the degree of coherence is a complex function, it is often simplified to two coherence measures: coherence time and coherence length. The coherence length is the full width at half max of $\gamma(\mathbf{r}, \mathbf{r}', \tau)$ versus τ, and is denoted by τ_c. The coherence length, or the distance over which the light source is temporally coherent, can then be calculated by multiplying the coherence time by the speed of light, $c\tau_c$.

For monochromatic light, the coherence length is infinite; however, for chaotic sources like incandescent bulbs or fluorescent light, the coherence length is sharply peaked, with a coherence time on the order of $1/\Delta\nu$, where $\Delta\nu$ is the bandwidth of the source. To establish or improve temporal coherence, broadband light can be filtered with a narrowband filter, resulting in a quasimonochromatic light source. This occurs when the coherence time is greater than the maximum time delay achievable by the optical system, denoted by τ_{max}.

The second measurement commonly done is $\gamma(\mathbf{r}, \mathbf{r}', \tau)$ vs. $\mathbf{r}'$. Again using the full width at half max measurement of the peak width will give the correlation length, L_c. For perfectly spatially coherent light, the correlation length will be infinite. In the case of spatially incoherent light the correlation length can be approximated as

$$\gamma(\mathbf{r}, \mathbf{r}', \tau) = A_c \delta(\mathbf{r} - \mathbf{r}'), \tag{1.9}$$

where A_c is the coherence area approximately equal to L_c^2. For temporally stationary light, $\tau = 0$, the degree of coherence function can be simplified to

$$\gamma(\mathbf{r}, \mathbf{r}', 0) = \gamma(\mathbf{r}, \mathbf{r}'). \tag{1.10}$$

This equation is sometimes referred to as mutual intensity. Furthermore when $\mathbf{r} = \mathbf{r}'$ we get the mean irradiance which is often referred to as intensity,

$$\bar{I}(\mathbf{r}) = \Gamma(\mathbf{r},\mathbf{r}) = \langle|\tilde{E}_0(\mathbf{r},t)|^2\rangle. \tag{1.11}$$

Below we will also show that the mean irradiance is measured by a photodetector such as a camera.

1.5 Coherent versus Incoherent Imaging

Imaging systems can be analyzed using linear shift-invariant (LSI) theory, which establishes a relationship between the recorded image and the specimen being observed [95, 56]. Any LSI system can be described through the convolution of an impulse response function with the input signal. In an optical microscope, the impulse response function is referred to as the spread function, which broadens every point in the object by an amount determined by the numerical aperture of the system. In other words, all imaging systems act as low-pass spatial frequency filters, with the spatial frequencies present in the object that are captured in the image dictating the spatial frequency transfer function. The spatial resolution of an imaging process is often characterized by a parameter that measures the width of the spread function, denoted by δr, which is inversely proportional to a measure of the spatial frequency support's width, $\Delta k \sim 1/\delta r$. Moreover, the coherence of the light affects the imaging performance. In this section, we will discuss how coherence modifies the behavior of an imaging system.

1.5.1 Light Detection

Let us first look at how a detector/camera will respond to an incident electric field so that we can better understand the measurement that is produced by a detector. A photodetector responds to the time-averaged Poynting vector which is referred to as the irradiance. Following the derivation in [111], the Poynting vector, defined as $\mathbf{S} = \mathbf{E} \times \mathbf{B}/\mu_0$, is the flow of energy in free space or in an isotropic medium, where

$$\mathbf{E}(\mathbf{r},t) = \frac{1}{2}\left[\mathbf{E}_0 e^{i(\mathbf{k}\cdot\mathbf{r}-\omega t)} + \mathbf{E}_0^* e^{-i(\mathbf{k}\cdot\mathbf{r}-\omega t)}\right] \tag{1.12}$$

is the electric field vector and

$$\mathbf{B}(\mathbf{r},t)=\frac{1}{2}\left[\frac{\mathbf{k}\times\mathbf{E}_0}{\omega}e^{i(\mathbf{k}\cdot\mathbf{r}-\omega t)}+\frac{\mathbf{k}\times\mathbf{E}_0^*}{\omega}e^{-i(\mathbf{k}\cdot\mathbf{r}-\omega t)}\right] \tag{1.13}$$

is the magnetic field vector, $\times$ is the cross product between the two vectors, and $\mathbf{E}_0$ is the amplitude of the electric field vector. The Poynting vector can be rewritten using Eqn. 4.1 and 4.2 giving,

$$\mathbf{S}=\frac{\hat{\mathbf{u}}}{4\mu_0}\left[\frac{k}{\omega}(\mathbf{E}_0\cdot\mathbf{E}_0)e^{2i(\mathbf{k}\cdot\mathbf{r}-\omega t)}+\frac{k}{\omega}(\mathbf{E}_0\cdot\mathbf{E}_0^*)e^{-2\frac{k\omega}{c}\hat{\mathbf{u}}\cdot\mathbf{r}}+c.c.\right] \tag{1.14}$$

where $\hat{\mathbf{u}}$ is a unit vector in the direction of the energy flow and $c.c.$ stands for the complex conjugate of the terms that came before it.

The Poynting vector can be used to describe the response of an optical detector. Notice in Eqn. 1.14 that the first term oscillates at the optical frequency, ω, which is on the order of 10^{15}Hz. This frequency is way too fast for current optical detectors which have an optical response of 10^6-10^9Hz. For this reason, it is often the case that the time-averaged optical response is what is measured,

$$\langle\mathbf{S}\rangle_t=\hat{\mathbf{u}}\frac{n\epsilon_0 c}{2}(\mathbf{E}_0\cdot\mathbf{E}_0^*)e^{-2\frac{k\omega}{c}\hat{\mathbf{u}}\cdot\mathbf{r}} \tag{1.15}$$

where $\langle\cdot\rangle_t$ is the time average. Notice that the first term in Eqn. 1.14 has vanished, the reason for this is that it oscillates symmetrically both positively and negatively, therefore, canceling out with the time average. Interestingly, the time-averaged Poynting vector, often called irradiance, includes the direction of energy flow, $\hat{\mathbf{u}}$. However, it has become common practice to refer to the intensity rather than the irradiance, where the difference between the irradiance and intensity is that the direction is dropped, giving intensity as

$$I=\frac{n\epsilon_0 c}{2}\mathbf{E}_0\cdot\mathbf{E}_0^*. \tag{1.16}$$

It is common to take things one step further dropping the scaling constants and the vector nature of the electric field leaving the well-known equation for intensity

$$I = \langle |E|^2 \rangle = E_0 E_0^*. \tag{1.17}$$

Now we see what is meant when it is said "the optical detector responds to the intensity of the field (the modulus squared) and not the field itself" [96, 115, 95, 111]. This fact of time averaging is an important factor that drives the differences in imaging behavior of coherent and incoherent imaging.

1.5.2 Coherent Imaging

For spatially coherent imaging, and assuming a monochromatic, spatially uniform, unity amplitude illumination field, the image field is given by

$$E_i(\mathbf{r}) = c(\mathbf{r}) \circledast h_{coh}(\mathbf{r}), \tag{1.18}$$

where $c(\mathbf{r})$ is the complex object field transmission function that relates the incident field to the exit surface wave emerging from the back face of the object, $h(\mathbf{r})$ is the coherent spread function, and $\circledast$ is the convolution operator, $f(r) \circledast g(r) = \int_{-\infty}^{\infty} f(r')g(r-r')\mathrm{d}r' = \langle f(r')g(r-r')\rangle_{r'}$, [95]. The coherent spread function is approximated to be shift-invariant by assuming the object covers a small region over the pupil plane, $t_{pupil}(\rho)$. The pupil serves to act as a spatial filter in the frequency domain, ρ, therefore,

$$h_{coh}(\mathbf{r}) = \frac{m}{\lambda^2 f^2} \mathscr{F}\{t_{pupil}(\rho)\}_\rho = \frac{m}{\lambda^2 f^2} T_{pupil}\Big(\frac{\mathbf{r}}{\lambda f}\Big). \tag{1.19}$$

Here we see that the PSF is a scaled Fourier transform of the pupil function, and m is the system magnification.

The convolution is much easier to calculate in the frequency domain; according to the convolution theorem the spatial frequency domain representation of the imaged field is the

product of the coherent transfer function and the field transmission function (object), $\hat{E}_i(\mathbf{k}) = H(\mathbf{k}) \cdot C_{coh}(\mathbf{k})$. Here $C_c(\mathbf{k}) = \left\langle c_{coh}(\mathbf{r}) \exp(-\mathrm{i}\mathbf{k}\cdot\mathbf{r}) \right\rangle_{\mathbf{r}}$ where we utilize Dirac integral notation, $\langle f(\mathbf{r})\rangle_{\mathbf{r}} = \int f(\mathbf{r}) \mathrm{d}^n\mathbf{r}$, where n is the dimension of the spatial coordinate vector $\mathbf{r}$, $C_{coh}(\mathbf{k})$ is the object spatial frequency spectrum given by the Fourier transform of the object. The coherent spread and transfer functions are related by a Fourier transform $H(\mathbf{k}) = \left\langle h(\mathbf{r}) \exp(-\mathrm{i}\mathbf{k}\cdot\mathbf{r}) \right\rangle_{\mathbf{r}}$ [95].

We see from the perfectly monochromatic and spatially coherent case that the imaged field is linear in the field, however, to extend coherent imaging to incoherent imaging it is first necessary to assume a quasimonochromatic source so that we can introduce our statistical description of light developed in Section 1.4. We will utilize linear superposition to describe the total imaged field. To do this we will need to use the frequency domain description of the object using the Fourier transform. The object field can be written as

$$E_{obj}(\mathbf{r}, t) = \langle \hat{E}_{obj}(\mathbf{r}, \nu) \exp(-2\pi i \nu t) \rangle_{\nu}. \tag{1.20}$$

Plugging the object field into Eqn. 1.18 gives

$$E_{im}(\mathbf{r}, t) = \left\langle \exp(-2\pi i \nu t) \hat{E}_{obj}(\mathbf{r}', \nu) h_{coh}(\mathbf{r} - \mathbf{r}'; \nu) \right\rangle_{\nu, \mathbf{r}'} \tag{1.21}$$

where h_{coh} now depends explicitly on the optical frequency, ν, because the PSF can vary with frequency. The frequency dependant PSF can be written as

$$h_{coh}(\mathbf{r} - \mathbf{r}'; \nu) = \frac{m}{\lambda^2 f^2} \exp\left[i2\pi\nu \frac{w(\mathbf{r}, \mathbf{r}')}{c} \right] \left| T_{pupil}\left[\frac{m}{\lambda f}(\mathbf{r} - \mathbf{r}') \right] \right|, \tag{1.22}$$

where $\exp\left[i2\pi\nu w(\mathbf{r}, \mathbf{r}')/c \right]$ accounts for the phase of the pupil. In order to simplify this expression let's set $\tau_p = w(\mathbf{r}, \mathbf{r}')/c$ to be the time delay for light emanating from point $\mathbf{r}'$ to point $\mathbf{r}$. Inserting these expressions into the Eqn. 1.21 yields

$$E_{im}(\mathbf{r}, t) = \frac{m}{\bar{\lambda}^2 f^2} \left\langle \exp(-2\pi i \nu t) \hat{E}_{obj}(\mathbf{r}', \nu) \exp\left[i2\pi\nu\tau_p \right] \left| T_{pupil}\left[\frac{m}{\bar{\lambda} f}(\mathbf{r} - \mathbf{r}') \right] \right| \right\rangle_{\nu, \mathbf{r}'}. \tag{1.23}$$

Using the definition of the object Fourier transform with a shift from the pupil phase, we can rewrite this equation as

$$E_{im}(\mathbf{r},t) = \frac{m}{\bar{\lambda}^2 f^2}\left\langle E_{obj}(\mathbf{r}',t-\tau_p)\exp\left[i2\pi\bar{\nu}\tau_p\right]\middle| T_{pupil}\left[\frac{m}{\bar{\lambda}f}(\mathbf{r}-\mathbf{r}')\right]\right|\Big\rangle_{\mathbf{r}'}. \tag{1.24}$$

Finally, we recognize that we have the coherent PSF at the mean frequency, dropping the unimportant scaling constant in the front gives

$$\begin{aligned} E_{im}(\mathbf{r},t) &= \left\langle E_{obj}(\mathbf{r}',t-\tau_p)h_{coh}(\mathbf{r}-\mathbf{r}';\bar{\nu})\right\rangle_{\mathbf{r}'} \\ &= E_{obj}(\mathbf{r}',t-\tau_p)\circledast h_{coh}(\mathbf{r};\bar{\nu}). \end{aligned} \tag{1.25}$$

At first glance, it may appear that we have not made much progress, however, with further inspection, we see that the object field is now related to the image field by a retarded time of $t-\tau_p$ which is the propagation time through the imaging system which allows for arbitrary wavelength-dependent optical aberrations.

Now that we have developed what field is at the image plane, it follows naturally to ask 'what do we measure at the image plane?' To answer this question we can refer back to Eqn. 1.17 which showed that a photo-detector responds to the magnitude squared of the electric field. We can plug in the imaged electric field, Eqn. 1.25, into Eqn. 1.17 which gives

$$\begin{aligned} I_{im}(\mathbf{r}) &= \left\langle E_{im}(\mathbf{r})E_{im}^*(\mathbf{r})\right\rangle_t \\ &= \left\langle \left\langle E_{obj}(\mathbf{r}',t-\tau_p)h_{coh}(\mathbf{r}-\mathbf{r}';\bar{\nu})\right\rangle_{\mathbf{r}'}\left\langle E_{obj}^*(\mathbf{r}'',t-\tau_p)h_{coh}^*(\mathbf{r}-\mathbf{r}'';\bar{\nu})\right\rangle_{\mathbf{r}''}\right\rangle_t \end{aligned} \tag{1.26}$$

If we rearrange the order of integration we get

$$I_{im}(\mathbf{r}) = \left\langle \left\langle E_{obj}(\mathbf{r}',t-\tau_p)E_{obj}^*(\mathbf{r}'',t-\tau_p)\right\rangle_t h_{coh}(\mathbf{r}-\mathbf{r}';\bar{\nu})h_{coh}^*(\mathbf{r}-\mathbf{r}'';\bar{\nu})\right\rangle_{\mathbf{r}',\mathbf{r}''} \tag{1.27}$$

We then use the definition of mutual coherence defined in, Eqn. 1.8,

$$I_{im}(\mathbf{r}) = \left\langle \Gamma_{obj}(\mathbf{r}', \mathbf{r}''; \Delta\tau(\mathbf{r}, \mathbf{r}'\mathbf{r}'') h_{coh}(\mathbf{r} - \mathbf{r}'; \bar{\nu}) h^*_{coh}(\mathbf{r} - \mathbf{r}''; \bar{\nu}) \right\rangle_{\mathbf{r}', \mathbf{r}''} \tag{1.28}$$

The image irradiance is

$$I_{im}(\mathbf{r}) = \left\langle \gamma_{obj}(\mathbf{r}', \mathbf{r}'') \sqrt{\bar{I}_{obj}(\mathbf{r}') \bar{I}_{obj}(\mathbf{r}'')} h_{coh}(\mathbf{r} - \mathbf{r}'; \bar{\nu}) h^*_{coh}(\mathbf{r} - \mathbf{r}''; \bar{\nu}) \right\rangle_{\mathbf{r}', \mathbf{r}''} \tag{1.29}$$

where $\bar{I}(\mathbf{r}') = \langle |\tilde{E}_{obj}(\mathbf{r}')|^2 \rangle$ is the mean intensity emanating from the object, the degree of coherence of the light emanating from the object is described by $\gamma_{obj}(\mathbf{r}', \mathbf{r}'')$, in the case of fully coherent light $\gamma_{obj}(\mathbf{r}', \mathbf{r}'') = 1$.

1.5.3 Incoherent Imaging

In the case of spatially incoherent, quasimonochromatic (narrow band) illumination, we can use the spatial incoherent approximation, Eqn. 1.9, which was

$$\gamma(\mathbf{r}, \mathbf{r}') = A_c \delta(\mathbf{r}' - \mathbf{r}''). \tag{1.30}$$

We can plug this into Eqn. 1.29 giving

$$I_{im}(\mathbf{r}) = \left\langle A_c \delta(\mathbf{r}' - \mathbf{r}'') \sqrt{\bar{I}_{obj}(\mathbf{r}') \bar{I}_{obj}(\mathbf{r}'')} h_{coh}(\mathbf{r} - \mathbf{r}'; \bar{\nu}) h^*_{coh}(\mathbf{r} - \mathbf{r}''; \bar{\nu}) \right\rangle_{\mathbf{r}', \mathbf{r}''}. \tag{1.31}$$

The delta function allows us to use the sifting property when the integration on $\mathbf{r}''$ is performed giving a much-simplified expression

$$\begin{aligned} I_{im}(\mathbf{r}) &= \left\langle A_c \sqrt{\bar{I}_{obj}(\mathbf{r}') \bar{I}_{obj}(\mathbf{r}')} h_{coh}(\mathbf{r} - \mathbf{r}'; \bar{\nu}) h^*_{coh}(\mathbf{r} - \mathbf{r}'; \bar{\nu}) \right\rangle_{\mathbf{r}'} \\ &= A_c \left\langle \bar{I}_{obj}(\mathbf{r}') \left| h_{coh}(\mathbf{r} - \mathbf{r}'; \bar{\nu}) \right|^2 \right\rangle_{\mathbf{r}'}. \end{aligned} \tag{1.32}$$

Eqn. 1.32 gives us an equation for spatially incoherent imaged intensity on a photodetector. We have assumed that the object is planar and in focus however, this is a very useful formula

that says the imaged intensity is equal to the emitted object intensity convolved with the magnitude squared of the coherent spread function (CSF). We can define the incoherent spread function or more commonly referred to as the point spread function (PSF) to be

$$h_{incoh}(\mathbf{r}-\mathbf{r}') = A_c\left|h_{coh}(\mathbf{r}-\mathbf{r}';\bar{\nu})\right|^2, \tag{1.33}$$

therefore we can rewrite Eqn. 1.32 as

$$I_{im}(\mathbf{r}) = \bar{I}_{obj}(\mathbf{r}) \circledast h_{incoh}(\mathbf{r}). \tag{1.34}$$

This gives the well-known convolution formula. It is common to say that spatially coherent (quasimonochromatic) imaging is linear in the electric field and spatially incoherent (quasimonochromatic) imaging is linear in intensity, from the above derivation, we can see where this expression comes from.

1.5.4 Comparison of Coherent vs. Incoherent Imaging

In the spatial frequency domain, the imaging process is described by $\hat{I}_{im}(\mathbf{k}) = H(\mathbf{k}) \cdot \hat{I}_{obj}(\mathbf{k})$. The spatial frequency spectrum of the spatial distribution of the object intensity is given by the Fourier transform $\hat{I}_{obj}(\mathbf{k}) = \left\langle I_{obj}(\mathbf{r}) \exp(-\mathrm{i}\mathbf{k}\cdot\mathbf{r})\right\rangle_{\mathbf{r}}$. It follows from the definition of the PSF that $\mathrm{OTF}(\mathbf{k}) = H(\mathbf{k}) \star H(\mathbf{k})$, where $\star$ is the correlation operator, known as the optical transfer function [95].

Taking the Fourier transform of the PSF will yield the optical transfer function (OTF). It is common to refer to the modulation transfer function (MTF) interchangeably with the OTF, the reason for this is that the MTF is simply the magnitude of the complex-valued OTF.

At this point, it would appear that incoherent imaging is far superior to coherent imaging since the bandpass of the incoherent system is twice that of the coherent. However, this conclusion is not so clear. The reason for this is that CTF pertains to the field while the MTF pertains to the intensity. Therefore, these quantities can not be directly compared. In order to compare

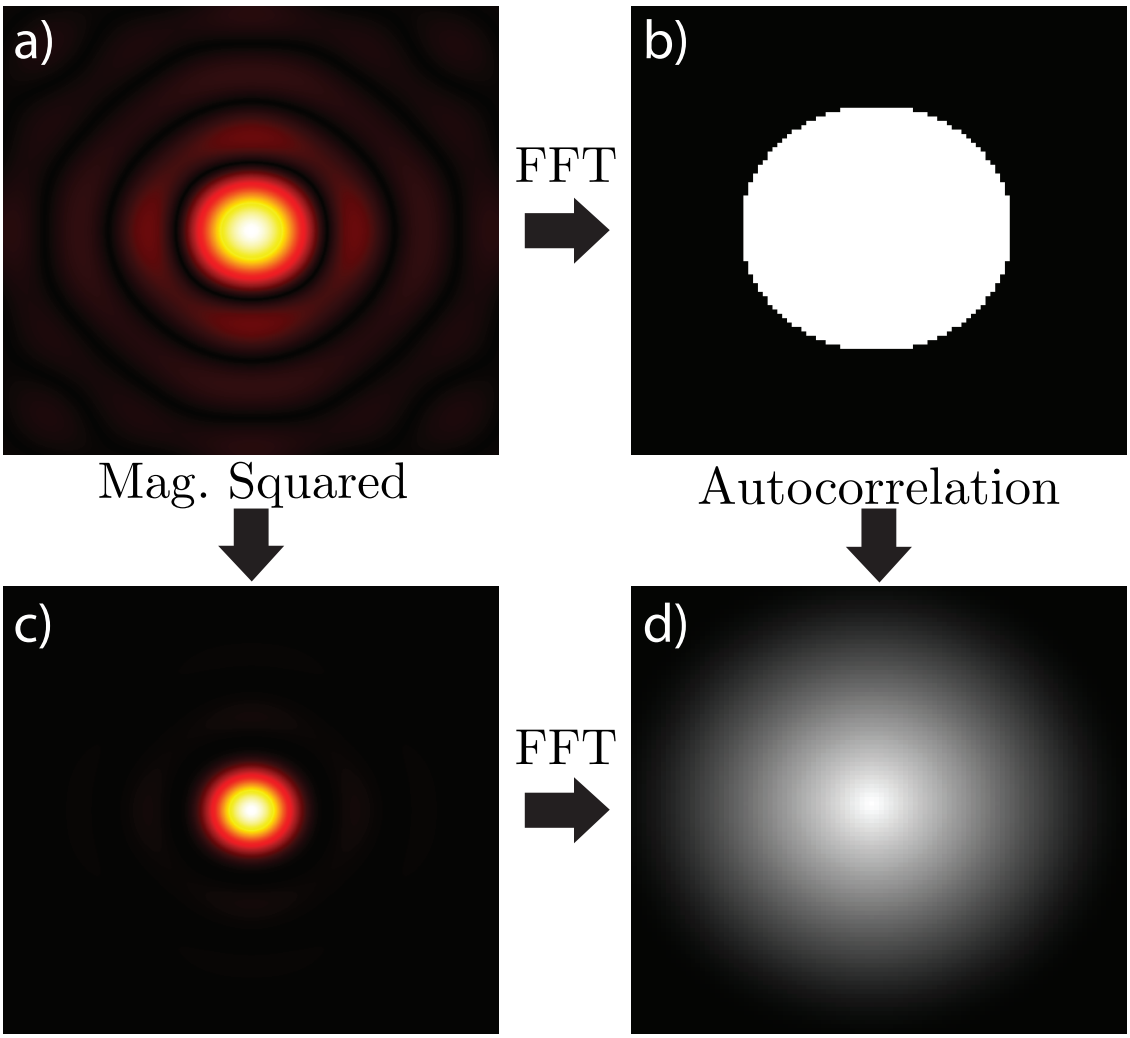

Figure 1.7: This figure shows the relationship between the CSF (a), the CTF (b), the PSF (c), and the MTF (d).

the two systems it is necessary that they both be compared on the same footing, i.e. intensity. Goodman has a discussion that I will use as a guide for the following discussion, [56].

Let's take a moment to explore the distinction between coherent and incoherent illumination, as it provides insight into the impact on image formation of these two types of light. Coherent illumination refers to light rays that are highly correlated in amplitude and phase, such that knowledge of the properties of one ray extends to its neighboring rays. Conversely, in the case of incoherent light, the amplitude and phase of a single ray does not provide any information about the surrounding light, which varies randomly over time and is therefore completely uncorrelated. This distinction has significant implications for imaging. If we imagine each point

in the object to be imaged as having its own unique spread function with corresponding amplitude and phase, it's easy to envision how these points may interfere with one another when they overlap. The stability of these interference patterns is determined by the coherence of the illumination. With coherent illumination, the interference pattern will be stable over time, whereas in the case of incoherent illumination, the interference patterns will fluctuate rapidly and average out over time. While this description is heuristic, it provides a useful framework for intuitively grasping the distinction between the two types of illumination.

In order to compare coherent and incoherent imaging quantitatively, it is necessary to discuss on which grounds the comparison will be made. Since imaging systems readily image the intensity and not the field, let us make the choice to compare the two modalities based on intensity since that is what will be detected by the photodetector. I will briefly summarize the key results from the above sections, the coherent imaged electric field is

$$E_{im}(\mathbf{r}) = h(\mathbf{r}) \circledast E_{obj}(\mathbf{r}) \tag{1.35}$$

where the detected intensity for coherent imaging is

$$I_{coh}(\mathbf{r}) = |E_{im}(\mathbf{r})|^2 = |h(\mathbf{r}) \circledast E_{obj}(\mathbf{r})|^2. \tag{1.36}$$

Here we see that coherent imaging is linear in the field while it is nonlinear in intensity. In the case of incoherent imaging, the intensity is

$$I_{incoh}(\mathbf{r}) = |h(\mathbf{r})|^2 \circledast |E_{obj}(\mathbf{r})|^2. \tag{1.37}$$

We can see a major difference between incoherent imaged intensity compared to coherent imaged intensity. Equation 1.37 shows that incoherent imaging is linear in intensity.

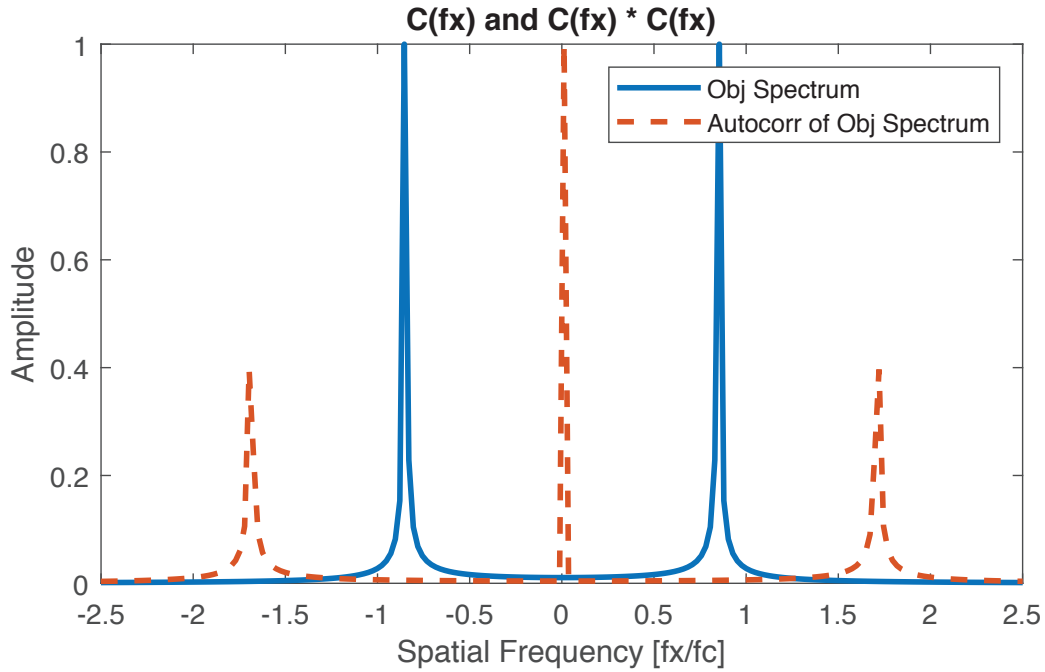

Figure 1.8: This figure shows the difference between mathematical operations in coherent and incoherent imaging. Object A, $E_{obj}(\mathbf{r}) = \cos(2\pi f_o x)$, amplitude spectrum (blue) verse the autocorrelation of the object spectrum (red dotted line).

The difference in imaging performance becomes more clear when evaluated in the frequency domain. Taking the Fourier transform of Eqn. 1.36 and Eqn. 1.37 yields,

$$\hat{I}_{coh}(\mathbf{k}) = H(\mathbf{k})\hat{E}_{obj}(\mathbf{k}) \star H^*(\mathbf{k})\hat{E}^*_{obj}(\mathbf{k}) \tag{1.38}$$

and

$$\hat{I}_{incoh}(\mathbf{k}) = [H(\mathbf{k}) \star H^*(\mathbf{k})][\hat{E}_{obj}(\mathbf{k}) \star \hat{E}^*_{obj}(\mathbf{k})]. \tag{1.39}$$

Here we see that the coherent and incoherent spectral bandpass have the same cutoff frequency, however, the order of operations is quite different which will have a profound impact on imaging characteristics. Figure 1.8 shows the spectral content passed through the bandpass of both coherent illumination (blue) and incoherent illumination (red dotted line) for a sinusoidal object. For a coherent system, the field spectrum will be filtered by the imaging system, while the autocorrelation of the object spectrum will be filtered by the incoherent imaging system.

Note, then it is said that the spread function of an imaging system is convolved with the object. We do not mean that there is an actual convolution of space reversals followed by a shifting of the spread function across the object (unless it is point scanning), but rather we are referring to a mathematical description of the outcome of the imaging system. However, if one wants to try to locate where the physical operation is performed it is easiest to see this occurring in the frequency domain where the object spectrum is multiplied by the transfer function. Again, this statement can not be taken too literally either, as it ignores the detection process which is a nonlinear operation in the field that gives rise to the autocorrelation function. It should be reiterated that no physical autocorrelation is performed in the same manner that no convolution is performed, we must remember that this is a mathematical description of the result of the detection of the field by nonlinear means and the result is a model that is best described as an autocorrelation. It is also the case that we are able to detect spatial frequencies above the bandpass of the physical optics by means of nonlinear detection. It is probably best to show a couple of examples to illustrate the differences between coherent and incoherent illumination imaging systems.

From the above equations, it is not clear which imaging modality will perform better than the other. Before we go further let us define what we mean by better. An imaging system is better if it has a higher cutoff frequency in the detected quantity (i.e. intensity) and has higher contrast. So let us consider three examples of test objects to help shed some light on this issue.

$$\text{A}: \; E_{obj}(\mathbf{r}) = \cos\left(2\pi f_o x\right)$$

$$\text{B}: \; E_{obj}(\mathbf{r}) = \left|\cos\left(2\pi f_o x\right)\right|$$

$$\text{C}: \; E_{obj}(\mathbf{r}) = \exp\left\{\mathrm{i}\pi 0.5\cos\left(2\pi f_o x\right)\right\}$$

where f_o is $f_c/2 < f_o < f_c$, f_c is the cutoff frequency of the CSF. Starting with function A which is a cosine with a frequency of f_o ranging from $[-1,1]$. When this object is imaged it will transmit through the low pass filter of the CSF so both coherent and incoherent modalities will form an image of the object. However, since the intensity will be detected (as the magnitude squared of

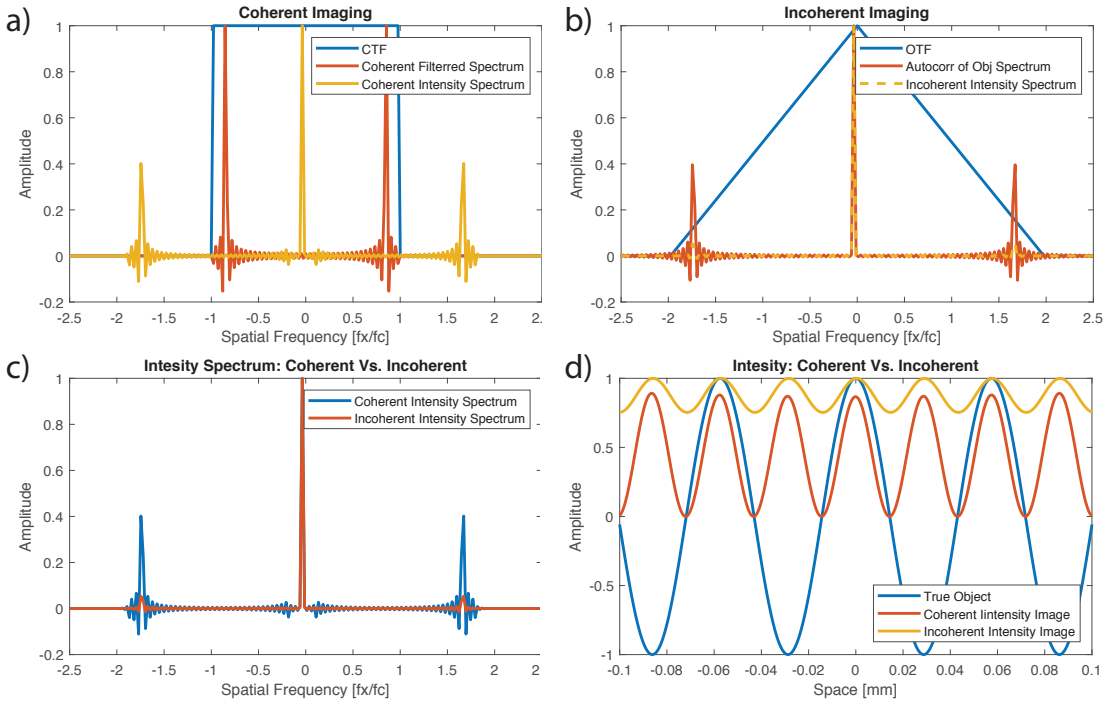

Figure 1.9: This figure shows several mathematical operations performed in the image formation of both coherent and incoherent illumination imaging. Panel (a) shows the CTF (blue) of a coherent imaging system, the filtered field spectrum of object A passed through the imaging system (red), and the autocorrelation of the filtered spectrum detected at the image plane of object A (yellow). Panel (b) shows the OTF of an incoherent imaging system (blue), the autocorrelation of object A's spectrum (red), and the filtered autocorrelation of object A's spectrum detected at the image plane. Panel (c) compares the detected spectral content of the coherent (blue) and incoherent (red) imaging systems of object A. Panel (d) shows the true object (blue), the intensity image formed by the coherent system (red), and the intensity image formed by the incoherent system (yellow).

the electric field) the effective imaged cutoff spatial frequency will be $2f_o$. Figure 1.9 compares the coherent illumination to the incoherent illumination with a series of images for the mathematical operations involved in detecting the intensity. We see in the final image that coherent illumination can be said to be better than incoherent since the depth of modulation is significantly better for coherent. Notice that the imaged spatial frequency is twice that of the true object, the reason for this is that the object has negative values which are not possible when detecting intensity.

Object B is a bit more straightforward as the periodic structure is $2f_o$. Therefore, when this object is imaged with coherent illumination the fundamental spatial frequency of the object will not pass through the amplitude transfer function and the resulting image is of DC illumination,

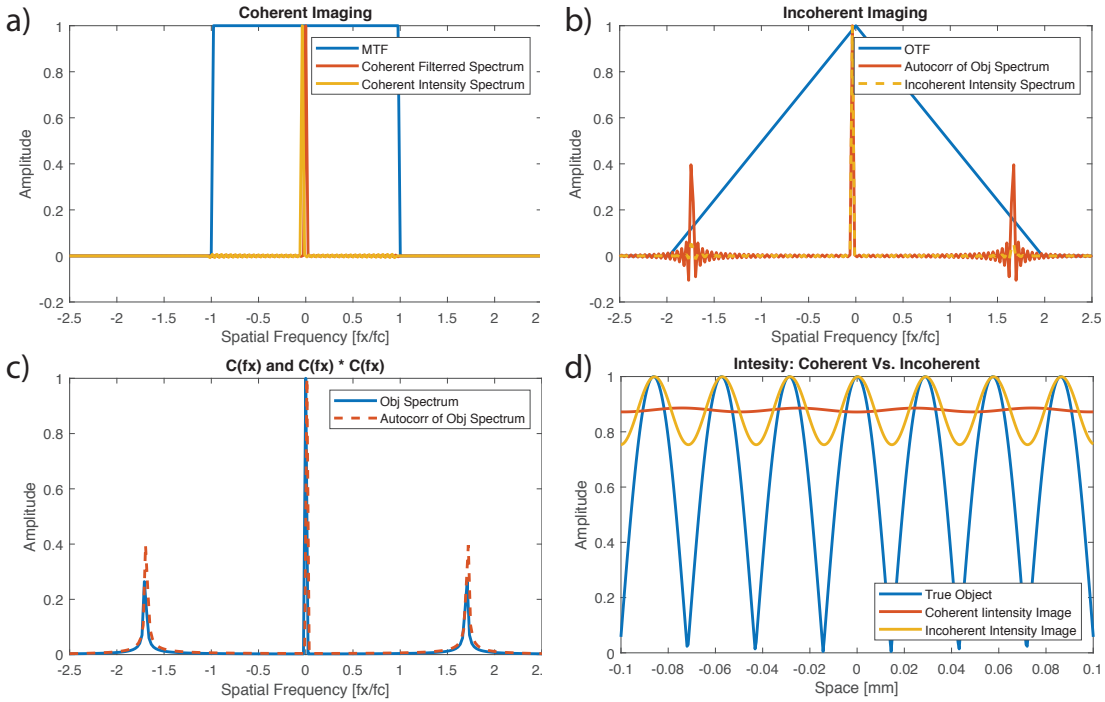

Figure 1.10: This figure shows several mathematical operations performed in the image formation of both coherent and incoherent illumination imaging. Panel (a) shows the CTF (blue) of a coherent imaging system, the filtered field spectrum of object B passed through the imaging system (red), and the autocorrelation of the filtered spectrum detected at the image plane of object B (yellow). Panel (b) shows the OTF of an incoherent imaging system (blue), the autocorrelation of object B's spectrum (red), and the filtered autocorrelation of object B's spectrum detected at the image plane. Panel (c) compares the detected spectral content of the coherent (blue) and incoherent (red) imaging systems of object B. Panel (d) shows the true object (blue), the intensity image formed by the coherent system (red), and the intensity image formed by the incoherent system (yellow).

as seen in Figure 1.10. However, in the case of incoherent illumination, the fundamental frequency will be imaged, albeit with a low modulation depth. We see that in this case, incoherent illumination is better than coherent. Figure 1.10 shows that the spatial frequency does not pass through the CTF of the coherent imaging system (panel a) and therefore leads to an image that has no object features (panel d, red), however, the incoherent imaging system will pass the first order spatial frequency (panel b) but the OTF will attenuate the high spatial frequency leading to a low contrast image (panel d, yellow).

Object C is a complex phase object with a fundamental period of f_o which acts like a phase grating. In the case of coherent imaging, the resulting images will be a modulated intensity pattern at the fundamental spatial frequency of the object. In the case of incoherent imaging,

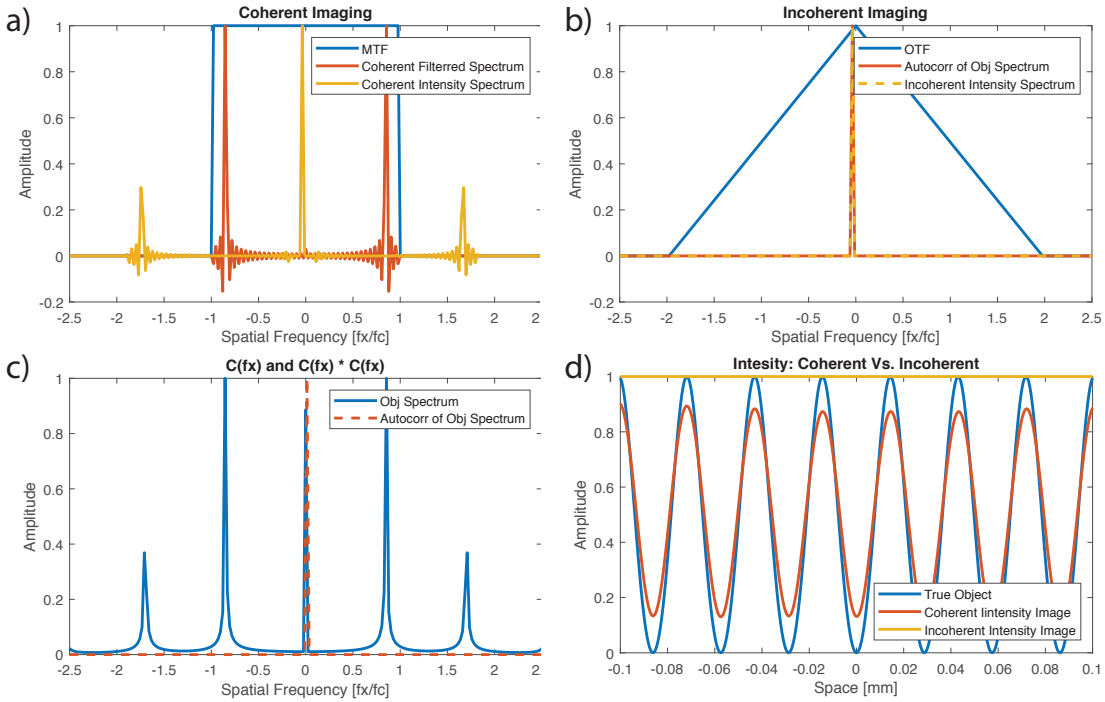

Figure 1.11: This figure shows several mathematical operations performed in the image formation of both coherent and incoherent illumination imaging. Panel (a) shows the CTF (blue) of a coherent imaging system, the filtered field spectrum of object C passed through the imaging system (red), and the autocorrelation of the filtered spectrum detected at the image plane of object C (yellow). Panel (b) shows the OTF of an incoherent imaging system (blue), the autocorrelation of object C's spectrum (red), and the filtered autocorrelation of object C's spectrum detected at the image plane. Panel (c) compares the detected spectral content of the coherent (blue) and incoherent (red) imaging systems of object C. Panel (d) shows the true object (blue), the intensity image formed by the coherent system (red), and the intensity image formed by the incoherent system (yellow).

the resulting image will be DC illumination with no modulation. Clearly, in this case, coherent imaging can be said to be better than incoherent imaging. Figure 1.11 shows that the coherent imaging system will image the complex object resulting in a high contrast image at the object spatial frequency (panel d, red). On the other hand, the incoherent imaging system will not be able to image the complex object because the phase information is completely lost resulting in an image of uniform intensity (panel d, yellow).

Here we have seen several examples of objects where coherent and incoherent imaging can be said to be better than the other. The fact is that neither type of illumination is better than the other, but rather it depends on what sample is being imaged and what the objective of the imaging system is. However, if a general statement about performance is going to be made, it is

generally accepted that incoherent imaging is going to be easier to work with and the results that it produces will be straightforward to interpret since incoherent imaging is linear in intensity. Then if incoherent illumination is not sufficient for the purposes of the imaging system then coherent illumination should be used. See Appendix A for code that generated Figures 1.9, 1.10, and 1.11.

So far I have described the mathematical representation of an imaging system, next I will give some intuition into what the diffraction limit means and how spatial frequencies play a key role. One way to define the diffraction limit would be the tightest point focus that is achievable with a given wavelength and NA, $\delta r = \lambda/2NA$. What this means is that given a range of spatial frequencies, ranging from $[-NA/\lambda, NA/\lambda]$, with a perfect parabolic wavefront, will interfere so that there is the tightest possible point focus at the focal plane of the lens. The wider the range of spatial frequencies the tighter and more localized the point focus will be. Additionally, if there is an optical aberration, such as a cubic phase across the wavefront, then at the focus there will be some interference which will cause the point focus to spread out, no longer being diffraction limited. Figure 1.12 shows a beam focus from a superposition of plane waves. The top row on the left side shows a diffraction-limited focus from 41 plane waves interfering together where the angles of the plane waves are uniformly spaced from [-20,20] degrees, giving an effective NA of 0.34. We see that the focus of a lens is nothing more than an interfering tilted plane wave. In the middle and right-hand side there is a spot focus from the same set of plane waves but a cubic phase has been added with additional random noise. We see the cubic phase (phase aberration) causes the focal spot to become distorted, no longer yielding a diffraction-limited spot size since the interfering plane wave no longer has a flat phase. The bottom row of Fig. 1.12 shows the same thing as the top except the are 81 plane waves informally spaced from [-40,40] degrees. This range gives an effective NA of 0.64. We see that the spot size is much smaller than that of the top row. Again, a cubic phase was added to the plane wave to cause distortion on the focal spot. The code used to generate Fig. 1.12 can be found in Appendix B.

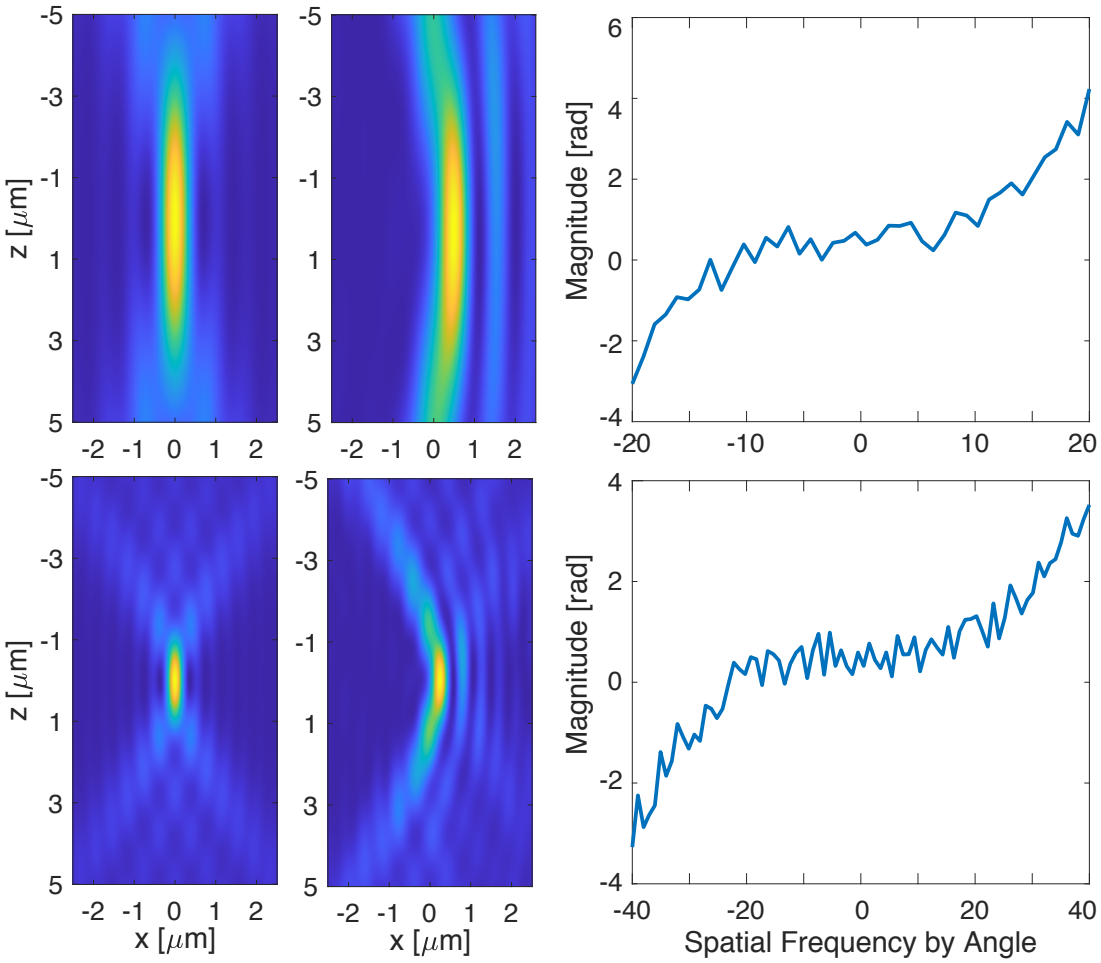

Figure 1.12: This figure shows plane wave interference which produces a focal spot. The top left figure shows 41 plane waves with uniform spacing from [-20,20] degrees. The top middle figure is the same set of plane waves with cubic and random phases. The added phase is shown on the top right. The bottom row is the same as the top except 81 plane waves were used ranging from [-40,40] degrees.

Chapter 2

Introduction to Single Pixel Imaging

2.1 Single Pixel Imaging

In this section, I describe some of the differences between camera-based imaging systems compared to single-pixel imaging systems and describe the advantages of single-pixel imaging. As discussed in the previous section, most imaging systems can be described by LSI theory. For example, a small point object imaged by point scanning a beam focus and detecting the signal light with a single pixel detector will have the same point spread function (PSF) as it would under widefield coherent illumination, image relayed to a camera. The primary difference here is that point scanning encodes the object information in time while camera-based imaging captures the spatial information in parallel simultaneously across space. It may seem at first glance that camera-based detection is superior since it collects all the image data simultaneously, however, this is not the full story.

Camera-based imaging plays an important role in image acquisition but there are liabilities that can be overcome with single-pixel imaging. Some of the advantages of single-pixel imaging are scattering robustness in highly scattering samples [39, 75, 139]. The reason for this is that the single-pixel detector only requires the signal light to fall on the detector (no need for an imaging condition) so even if the signal light experiences multiple scattering through the sample to the detector, an image can still be formed robustly. The question, of primary importance, is how much the illumination beam distorted on transmission through the scattering sample to the focal plane and how much signal light was collected. Single-pixel imaging is only susceptible to scattering of the illumination beam. This can be a huge advantage, especially in the case of multi-photon excitation imaging since longer wavelengths of light are used for the illumination which experience far less scattering compared to shorter wavelengths [33]. The second question is concerned with the SNR of the measurement. However, as long as a repre-

sentative proportion of light from the field of view falls on the detector a reconstruction of the object can be formed. This is due to the fact that in low signal regimes, photon counting can be used which mitigates many noise sources such as thermal and electronic noise providing better SNR. Additionally, the constraints on the collection optics can be relaxed from an imaging condition which allows easy placement of multiple detection arms.

Another advantage is the temporal bandwidth is very high for a single pixel detector so a large amount of information can be encoded in time, allowing very rapid imaging to be carried out [59] or a large amount of spatial information to be encoded [46]. The final advantage I will mention here is improved SNR under weak signals. This is often referred to as the multiplex advantage, the idea is that if your signal is weak and barely above the noise floor then multiplexing your signal together can allow the detected signal to rise above the noise floor, improving the fidelity of the measurement [64]. This advantage can turn into a liability if there is a strong source in the same field of view as a weak source. The reason for this is that the shot noise (white noise) from the strong source will be multiplex across the entire field of view raising the noise floor which may result in burying weak sources in the noise [64].

There are many approaches to single-pixel imaging, such approaches include point scanning (Confocal,STED), line imaging (OCT,SPIFI), 2D imaging (Ghost imaging, Single-pixel cameras), 3D imaging (Confocal, Tomography) to name a few. There are basically two configurations for single-pixel imaging, the first is to structure the illumination light before the sample and detect the signal light with a single-pixel detector after the sample. The second configuration is to use unstructured illumination light and structure the signal light after the sample, then detect the signal light with a single pixel detector. In this chapter, I will focus on the first configuration because it is the most common and has advantages over the second configuration such as less photo-damage and scattering robustness on collection [139]. Single-pixel imaging techniques can be written in a standard form to be solved as an inverse problem. The general idea is that the illumination intensity, $I_{ill}(\mathbf{r}, t)$ has a spatial structure and varies in time. The illumination intensity excites the contrast distribution, $c(\mathbf{r})$. The contrast distribu-

tion can be any light-matter interaction, such as absorption, linear and nonlinear fluorescent emission, second harmonic generation (SHG), phase contrast, etc. The illumination light is projected onto the contrast distribution, the signal light can be modeled as a spatial multiplication, $I_{sig}(\mathbf{r},t) = I_{ill}(\mathbf{r},t)c(\mathbf{r})$. The signal light is then collected by a single pixel detector (typically a photodiode or PMT) which acts as a spatial integration, generating a continuous-time signal. Therefore, a mathematical model of the detected signal can be written as

$$S(t) = \langle I_{sig}(\mathbf{r},t)\rangle_{\mathbf{r}} = \langle I_{ill}(\mathbf{r},t)c(\mathbf{r})\rangle_{\mathbf{r}}. \tag{2.1}$$

where $\langle\cdot\rangle_{\mathbf{r}}$ is a spatial integral over the dimensions of $\mathbf{r} = (x,y,z)$. Note that $I_{ill}(\mathbf{r},t)$ also has dimensions of (x,y,z). This equation can be interpreted as a projection of the contrast distribution onto an illumination intensity distribution. Figure 2.1 shows several examples of various types of illumination patterns that can be used for single-pixel imaging. Note, I have implicitly assumed that the signal light collected on the detector is a representative portion of light collected by the collection optics from the total signal generated by the sample. This assumption means that it is not necessary to collect all of the signal light, it is only necessary to collect part of the signal, as long as the part that is collected is an accurate proportion of the total signal light.

Since the signal will be digitized and processed on a computer, a discrete model needs to be formulated so that the image reconstruction can be performed on a computer. There are numerous ways to formulate to discrete model, I will model all continuous objects (sample, illumination patterns, and temporal signals) as discrete. In this way, the forward model can be easily represented using linear algebra. A continuous to discrete mapping can be generated using this general function, $f_m = \int_a^b f(\mathbf{x})h_m(\mathbf{x})\mathrm{d}\mathbf{x}$, where f_m is the m^{th} component of the discrete vector and $h_m(x)$ is a kernel such as a box car called the point response function, [6]. For example, the continuous to discrete mapping to take place in a camera where ($f(\mathbf{x})$ is a continuous image, the camera will discretely sample the image intensity with each pixel of the camera sensor array. Therefore each pixel can be modeled as $h_m(x) = 1$ on the interval of $a-b$ at the m^{th}

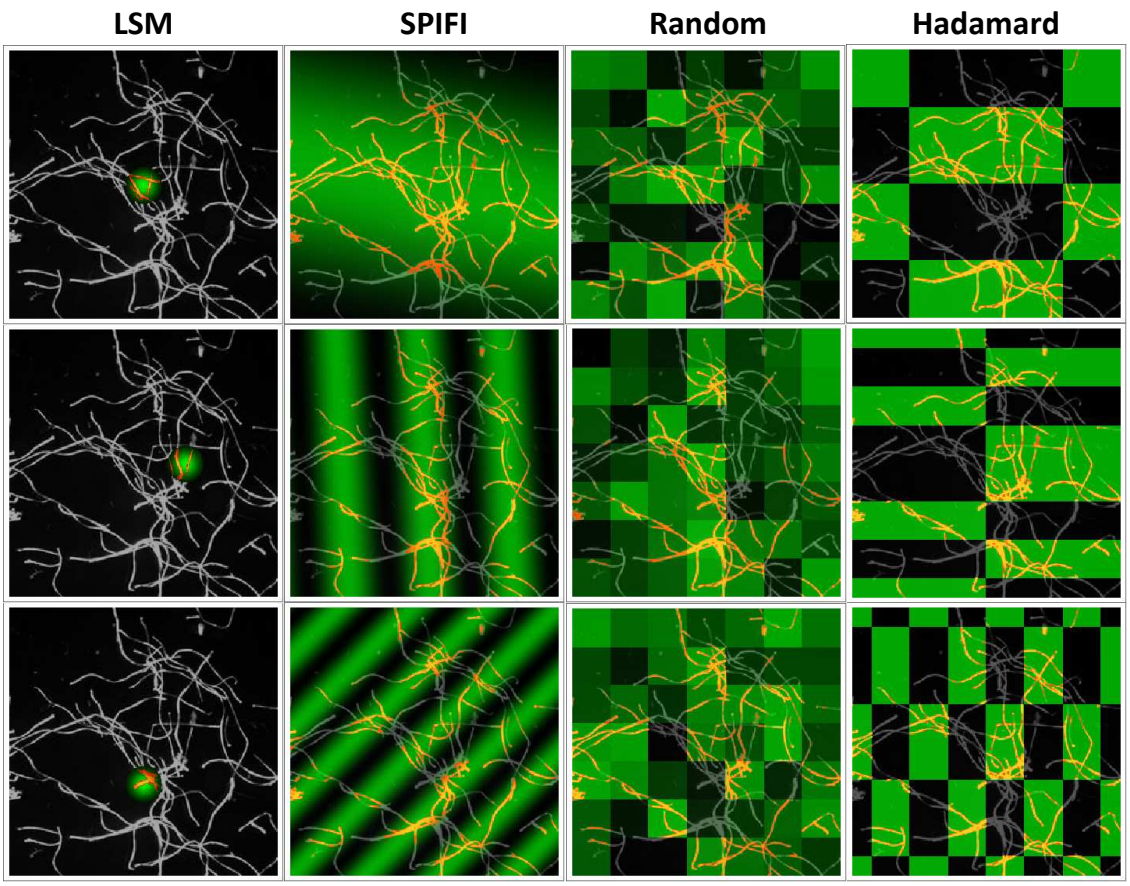

Figure 2.1: This figure shows four different illumination strategies for single-pixel imaging. The first column shows point scanning, the second shows spatial frequency illumination, the third shows random speckle patterns, and the fourth shows 2D Hadamard matrices. The black and gray represents the object or contrast function, $\mathbf{c}(\mathbf{r})$, the green represents the illumination intensity, $I_{ill}(\mathbf{r})$, and the orange represents the fluorescent signal, $S(t)$.

pixel location and zero otherwise. Running the contrast distribution and illumination intensity through a continuous-to-discrete mapping function yields a discretely sampled signal that can be modeled using linear algebra, giving the well-known forward problem

$$\mathbf{S} = \mathbf{A}\,\mathbf{c} + \epsilon \tag{2.2}$$

where $\mathbf{S} = [s_1, s_2, \ldots, s_{N_t}]^T$ is the signal vector sampled by the single pixel detector with size $[N_t \times 1]$, N_t is the number of sampled time points, $\mathbf{A}$ is the measurement matrix or sensing matrix of size $[N_t \times N_x]$, where N_x is the number of discrete spatial points, $\mathbf{c}$ is the discretely sampled

object vector of size $[N_x \times 1]$, and ϵ is the additive noise of size $[N_t \times 1]$. The measurement matrix **A** is a matrix that contains the vectorized illumination patterns. Once the signal has been measured, the question then becomes given the measured data, **S**, and the measurement matrix, **A**, how can one recover an estimate of the true object, **c**. This is known as an inverse problem. There are many ways to solve the inverse problem in the following sections we will explore several methods to solve an inverse problem

2.2 General theory of single pixel intensity imaging

In this analysis, we restrict our discussion to thin objects. Extension of this theory for single-pixel imaging to three-dimensional objects is straightforward but requires that the spatial coherence of the illumination and collected light be specified. For planar single-pixel intensity imaging of thin objects, the spatial coherence of the illumination and emitted light does not alter the results, so a more straightforward interpretation is possible. Moreover, our discussion of single-pixel phase imaging with DOPE is similarly focused on thin objects, although we note that DOPE requires illumination with spatially coherent light to obtain the phase.

Single-pixel imaging exploits a time-sequence of spatially modulated illumination light, $I_{\text{ill}}(\boldsymbol{\rho}, t)$, that is directed toward an object under study. Images are formed by first collecting light from the object, $I_{\text{obj}}(\boldsymbol{\rho}, t)$, and directing that collected light onto a single pixel (single element or bucket) detector. Here $\boldsymbol{\rho}$ is the two-dimensional transverse spatial vector, and we assume that the object lies entirely in that plane. Assuming that the single pixel detector is large enough in spatial extent to capture all of the light in the detection plane, the intensity distribution incident on the detector, $I_d(\boldsymbol{\rho}_d, t)$, is spatially integrated, i.e., the photocurrent generated at each spatial point where the collected light impinges on the detector surface is summed at the output of the photodetector.

A wide range of modulated illumination light patterns have been explored for single-pixel intensity imaging. In each case, the illumination light produces light emerging from the object that is recorded as a discrete sequence of coefficients proportional to the total photocurrent

generated by the single pixel detector in response to each spatially structured illumination pattern. Confocal microscopy is a limiting case of structured light single-pixel imaging where the effective illumination light is a single point focus [94]. The illumination light can be focused to a line [51] for one-dimensional, i.e. line imaging. One-dimensional modulation patterns can be used for two-dimensional imaging by extruding a line modulation pattern to two dimensions, allowing the object intensity to be recovered with lateral tomography [125] or a linear array of photodetectors [62]. Moreover, two-dimensional modulation patterns can be employed [121, 150], provided a large enough set of modulation patterns span the two-dimensional object space.

2.2.1 Intensity-contrast single-pixel imaging theory

Assuming that the collection optics faithfully deliver the light emerging from the object onto the single pixel detector, the temporal variation of the signal from the detector is given by

$$S_t = \langle I_d(\boldsymbol{\rho}_d, t)\rangle_{\boldsymbol{\rho}_d} = \langle I_{\text{obj}}(\boldsymbol{\rho}, t)\rangle_{\boldsymbol{\rho}}, \tag{2.3}$$

where we have adopted Dirac's integral notation, $\langle b(\boldsymbol{\rho})\rangle_{\boldsymbol{\rho}} \equiv \int b(\boldsymbol{\rho})\, d^2\boldsymbol{\rho}$. The object intensity will depend on whether we are recoding spatially coherent or incoherent light emerging from the object. Note that we are not treating partially coherent light, as that description requires a more complete theory that makes use of the cross-spectral density.

For the case of spatially incoherent light collection, the object intensity reads $I_{\text{obj}}(\boldsymbol{\rho}, t) = I_{\text{ill}}(\boldsymbol{\rho}, t)c(\boldsymbol{\rho})$, where $c(\boldsymbol{\rho})$ is the relevant object spatial distribution, such as the intensity transmission of the object under study or the variation in concentration of a fluorescent emitter.

In the case of spatially coherent illumination, we consider a modulated unity-amplitude illumination field that passes through a modulator that produces the illumination field, $E_{\text{ill}}(\boldsymbol{\rho}, t) = f_{\text{mod}}(\boldsymbol{\rho}, t)$, where $f_{\text{mod}}(\boldsymbol{\rho}, t)$ is the field modulation function imparted by an SLM. This modulated illumination field passes through (or is reflected off of) a thin object that dis-

plays a complex field response, $g(\boldsymbol{\rho})$. The intensity of the light exiting the object is

$$I_{\text{obj}}(\boldsymbol{\rho}, t) = \left|E_{\text{ill}}(\boldsymbol{\rho}, t)\ g(\boldsymbol{\rho})\right|^2 = \left|f_{\text{mod}}(\boldsymbol{\rho}, t)\right|^2 c(\boldsymbol{\rho}). \tag{2.4}$$

The intensity transmission of the object is denoted by $c(\boldsymbol{\rho}) = \left|g(\boldsymbol{\rho})\right|^2$, and the intensity modulation is $\left|f_{\text{mod}}(\boldsymbol{\rho}, t)\right|^2$, leading to a modulated illumination intensity of $I_{\text{ill}}(\boldsymbol{\rho}, t) = \left|f_{\text{mod}}(\boldsymbol{\rho}, t)\right|^2$.

While in general the spatio-temporal modulation can be applied to the electric field with a suitable spatial light modulator, we will restrict our discussion to a modulation function of the form $f_{\text{mod}}(\boldsymbol{\rho}, t) = 1 + M(\boldsymbol{\rho}, t)$, where we assume that $\left|M(\boldsymbol{\rho}, t)\right| \leq 1$. This imparts a spatially and temporally varying modulation on the incident field that produces the illumination field $E_{\text{ill}}(\boldsymbol{\rho}, t) = 1 + M(\boldsymbol{\rho}, t)$. Under these assumptions, the modulated illumination intensity reads

$$I_{\text{ill}}(\boldsymbol{\rho}, t) = \left|1 + M(\boldsymbol{\rho}, t)\right|^2 \equiv 1 + M_{\text{I}}(\boldsymbol{\rho}, t), \tag{2.5}$$

where $M_{\text{I}} = 2M(\boldsymbol{\rho}, t) + M^2(\boldsymbol{\rho}, t)$ defines the intensity modulation.

The temporal signal arising from the modulation of the illumination light, S_t, can be decomposed into a sum of the average signal, S_0, and a signal that fluctuates relative to the mean, $\Delta S(t)$, such that: $S_t \equiv S_0 + \Delta S(t)$. In that case, we write the average signal as $S_0 = \langle c(\boldsymbol{\rho})\rangle_{\boldsymbol{\rho}}$, while the fluctuating signal is

$$\Delta S(t) = \langle M_{\text{I}}(\boldsymbol{\rho}, t) c(\boldsymbol{\rho})\rangle_{\boldsymbol{\rho}}. \tag{2.6}$$

Here, we have assumed that the modulation function has a zero mean, i.e., $\langle M(\boldsymbol{\rho}, t)\rangle_t = 0$ and $\langle M_{\text{I}}(\boldsymbol{\rho}, t)\rangle_t = 0$.

When the modulation masks, $M_{\text{I}}(\boldsymbol{\rho}, t)$, are drawn from an orthonormal basis, the object is reconstructed by synthesizing the object from the projections weighting the superposition of the basis functions

$$\hat{c}(\boldsymbol{\rho}) = \langle \Delta S(t) M_{\text{I}}(\boldsymbol{\rho}, t)\rangle_t. \tag{2.7}$$

Note that the unity bias in the modulation function is critical for this object reconstruction because a set of non-negative modulation functions cannot be orthonormal, which motivates adopting this approach.

2.2.2 Modulation of the illumination or collected light intensity is equivalent

For the case of a thin object, the image synthesis is independent of when the illumination light is modulated, either before or after interacting with the object. When the input illumination light is modulated we denote this by $f_{\text{ill}}(\boldsymbol{\rho}, t)$, or when the light exiting the object is modulated we denote this by $f_{\text{ex}}(\boldsymbol{\rho}, t)$. In the most general scenario, both the illumination and collected light can be modulated, leading to a double modulation such that $f_{\text{mod}}(\boldsymbol{\rho}, t) = f_{\text{ill}}(\boldsymbol{\rho}, t) f_{\text{ex}}(\boldsymbol{\rho}, t)$, producing a temporal signal given by

$$S_t = \langle \left| f_{\text{ill}}(\boldsymbol{\rho}, t) f_{\text{ex}}(\boldsymbol{\rho}, t) \right|^2 c(\boldsymbol{\rho}) \rangle. \tag{2.8}$$

Clearly, either modulation term in the expression above can be set to unity to reduce our expression to a pre- or post-modulation condition. The commutation of the pre and post-object illumination is only possible in the limit of a thin object, where we assume that the illumination light is not significantly modified during propagation in the object.

2.3 Closed Form Inverse Problems

Perhaps the simplest closed-form inverse problem is often referred to as the 'naive' reconstruction. It has the form

$$\mathbf{A}^{-1}\mathbf{S} = \hat{\mathbf{c}} \tag{2.9}$$

where $\mathbf{A}^{-1}$ is the inverse of the $\mathbf{A}$ matrix. Eqn. 2.9 is equally valid for both standard imaging with an arrayed detector and single-pixel imaging. The only difference between the two classes of imaging is that the measured data, S, needs to be vectorized for standard imaging while single-

pixel imaging reads out a vector of data. This solution is considered naive because it assumes that $\mathbf{A}^{-1}$ exists and is well-posed. In general, this technique does not work well even in the absence of noise. The reason for this is that the condition number of the measurement matrix is typically very large which will have the effect of amplifying noise in the reconstruction resulting in a very poor estimate of the object of interest. The condition number is the ratio between the largest and smallest singular values of a matrix,

$$\kappa(\mathbf{A}) = \frac{\sigma_{max}(\mathbf{A})}{\sigma_{min}(\mathbf{A})}. \tag{2.10}$$

The condition number can be thought of as describing the sensitivity of an input to its output. That is if the condition number is small then a small change in the input will yield a small change to the output and the mapping is said to be stable. If the condition number is large, a small change in the input will yield a large change in the output. This means that if the measurement matrix has a large condition number then when a solution is sought with the inverse of the matrix the noise present in the measurement will cause large changes to the estimated object, which results in a very poor reconstruction of the object [6, 99].

It is possible to improve the stability of the 'naive' reconstruction algorithm by improving the condition number of the measurement matrix. One such method, sometimes called the low-rank approximation or truncated SVD method, works by calculating the singular value decomposition of the measurement matrix, $\mathbf{A} = \mathbf{U}\Sigma\mathbf{V}^*$, then truncating the singular values of Σ to give $\tilde{\Sigma}$ where $\tilde{\Sigma}$ is the same matrix as Σ except it contains only the first r largest values and all other values are set to zero. This has the effect of filtering out all the singular vectors with small singular values. Then a low rank approximation is formed by $\tilde{\mathbf{A}} = \mathbf{U}\tilde{\Sigma}\mathbf{V}^*$. Finally, the pseudo-inverse of $\tilde{\mathbf{A}}$ is calculated to yield an L_2 norm solution

$$\hat{\mathbf{c}} = \left(\tilde{\mathbf{A}}^*\tilde{\mathbf{A}}\right)^{-1}\tilde{\mathbf{A}}^*\mathbf{S}, \tag{2.11}$$

where $*$ is the complex conjugate. The reconstruction often represents the true object of interest much more accurately, however, it typically comes at the cost of filtering out high spatial frequency information resulting in a blurred object estimation.

2.4 Iterative Inverse Problems

Alternatively, the inverse problem can be solved iteratively. There are several advantages to solving the inverse problem with iterative methods. First, it is often the case that the inverse of the measurement matrix does not need to be calculated, we will see this below. Second, the full inverse problem may be so large that it is impractical/impossible to store in memory. Finally, prior knowledge or assumption on the object can be enforced without having to find a closed-form representation which may not exist. The iterative inverse problem will solve a minimization problem where the best fit or estimate of the object is returned given by the choice of error metric subject to regularization. This can be mathematically written as

$$\hat{\mathbf{c}} = \min_{\hat{\mathbf{c}}}. \frac{1}{2}\|\mathbf{A}\,\hat{\mathbf{c}} - \mathbf{S}\|_n + \gamma R\{\hat{\mathbf{c}}\} \tag{2.12}$$

where $\|\cdot\|_n = \sqrt[n]{\sum |x|^n}$ is the L_n norm for an integer value n, $\hat{\mathbf{c}}$ is the estimated object vector of size [N_x x 1] where n is the number of columns and m is the number of rows, γ is the regularization weighting coefficient, and $R\{\cdot\}$ is some regularization or constraint placed on the object estimate. The measurement matrix must accurately represent the signal formation of the imaging system which is a discretized representation of the effective illumination intensity.

There are many types of regularization constraints that can be applied in eqn. 2.12. Some of the most common are L_1 norm (total variation), L_2 norm (Tikhonov), non-negativity constraint, and total energy constraints to name a few of the most common. The regularization can be applied in combination with the various constraints. The first term is on the right-hand side of eqn. 2.12 is a norm error between the estimated signal, $\mathbf{A}\,\hat{\mathbf{c}}$ and the measured signal $\mathbf{S}$. Depending on the norm used to calculate the error, the norm will cause the solution to take

on different characteristics. For example, if the L_1 norm is used this is typically good for discontinuous objects and robust to outliers in the data. If the L_2 norm is used as the measure for error then typically smooth solutions will be found and will be more sensitive to outliers in the data. Non-negativity and total energy constraints correspond to the real properties of the object being imaged.

One of the major advantages of using regularization in eqn. 2.12 is that the first term on the right-hand side is typically ill-posed resulting in an infinite number of equally good solutions to the minimization problem. That is, there is an infinite set of estimated objects $\hat{c}$ that satisfy the minimization problem. Therefore, regularization is used to help constrain the set of possible solutions. This is typically done by placing constraints that represent the underlying physics such as non-negativity or energy constraints. Regularization can also be thought of as improving the ill-posedness of the problem by artificially improving the rank of the problem. Alternatively, regularization can be thought of as providing a place for the noise on the measurement to be represented. Whichever form of regularization is used, the goal is to push the solution toward a desirable solution and minimize the effects of noise in the measurement.

Eqn. 2.12 is related to a technique known as convex relaxation, [20, 143], where the inverse problem is solved subject to a norm ball,

$$\hat{\mathbf{c}} = \min_{\hat{\mathbf{c}}}. ||\mathbf{c}||_1 \text{ subject to } ||\mathbf{A}\hat{\mathbf{c}} - \mathbf{S}||_2 < \epsilon. \tag{2.13}$$

The radius of the norm ball is set by the estimated or expected noise level, ϵ. The norm ball will penalize any solution that falls outside the radius set by the noise level. This ensures that the solution to the minimization problem does not "blow up" due to the noise present in the data. This is especially relevant when the inverse problem is ill-posed and the solution is prone to the amplification of noise [20].

Chapter 3

Introduction to SPIFI and CHIRPT Imaging

3.1 Introduction to CHIRPT and SPIFI

Coherent Holographic Image Reconstruction by Phase Transfer (CHIRPT) and SPatIal Frequency modulated Imaging (SPIFI) imaging are single-pixel imaging techniques that utilize light sheet illumination to form an image. Both techniques have their respective advantages and disadvantages which I will discuss at the end of this chapter, however, both modalities share the same core idea for image formation which I will discuss here.

CHIRPT and SPIFI first got their inspiration from desiring to multiplex multiple spatial points together instead of raster scanning a point around which is commonly done in confocal microscopy. The motivation is that by multiplexing the spatial data there would be a subsequent decrease in acquisition time. The idea was then if each spatial location has a unique temporal modulation frequency then the spatial information can be easily recovered with a Fourier transform of the time signal. This then leads naturally to the modulator disk with a pattern $m(x,t) = 1/2[1+\cos(\Delta\kappa x t)]$ where each spatial location has a unique modulation frequency set by the chirp rate, $\Delta\kappa$, of the modulator. The modulator pattern can be image relayed to the object and the signal light will be collected by a single pixel detector producing a time signal. Figure 3.1 shows an example of a modulation mask with a chirp rate of $\Delta\kappa = 1$.

An interesting fact about this imaging modality is that looking at the illumination in time leads to the interpretation of each spatial location encoded by a unique temporal modulation frequency and summed together by the single pixel detector. However, if instead of looking at the illumination in time, the illumination is viewed as a snapshot in time when we see that the illumination is actually a product of plane waves interfering with each other producing a sinusoidal illumination pattern. This sinusoidal illumination pattern is exactly what is meant by a single spatial frequency. Therefore, CHRIPT and SPIFI can be interpreted as projecting a

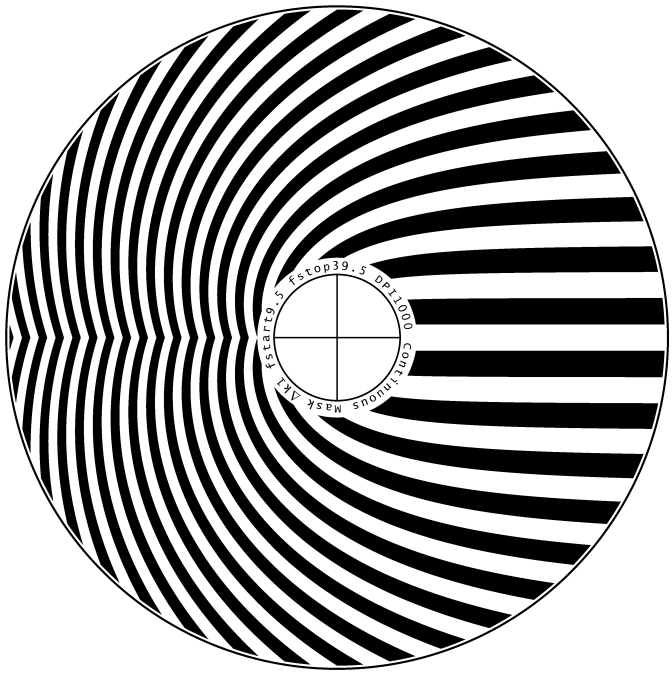

Figure 3.1: This figure shows an example of a SPIFI/CHIRPT modulation mask, $m(x,t) = 1/2[1 + \cos(\Delta\kappa x t)]$ where each spatial location has a unique modulation frequency set by the chirp rate, $\Delta\kappa = 1/mm$, for this modulator

set of spatial frequencies onto a sample and the highest spatial frequency is set by the NA of the objective. What is detected then are the Fourier coefficients, giving the interpretation that the object is being detected in the spatial frequency domain. This will be shown in the sections below.

3.1.1 Mathematical Description of CHIRPT

In CHIRPT [14, 44, 45, 47, 48, 136] and SPIFI [51, 125, 66, 46, 152, 137, 153] imaging, the modulator disc is illuminated with a line focus, fig. 3.2(a). This can be written as $E_1(x,t) = E_0(x)m(x,t)$, where $E_1(x,t)$ is the illumination beam directly after the modulation disc, $E_0(x) = E_0 u_0(x)e^{i\omega_0 t}$, where E_0 is the amplitude of the electric field, $u_0(x)$ is the spatial profile, and ω_0 is the optical frequency. We can plug in our definitions into the above equation and rewrite cosine

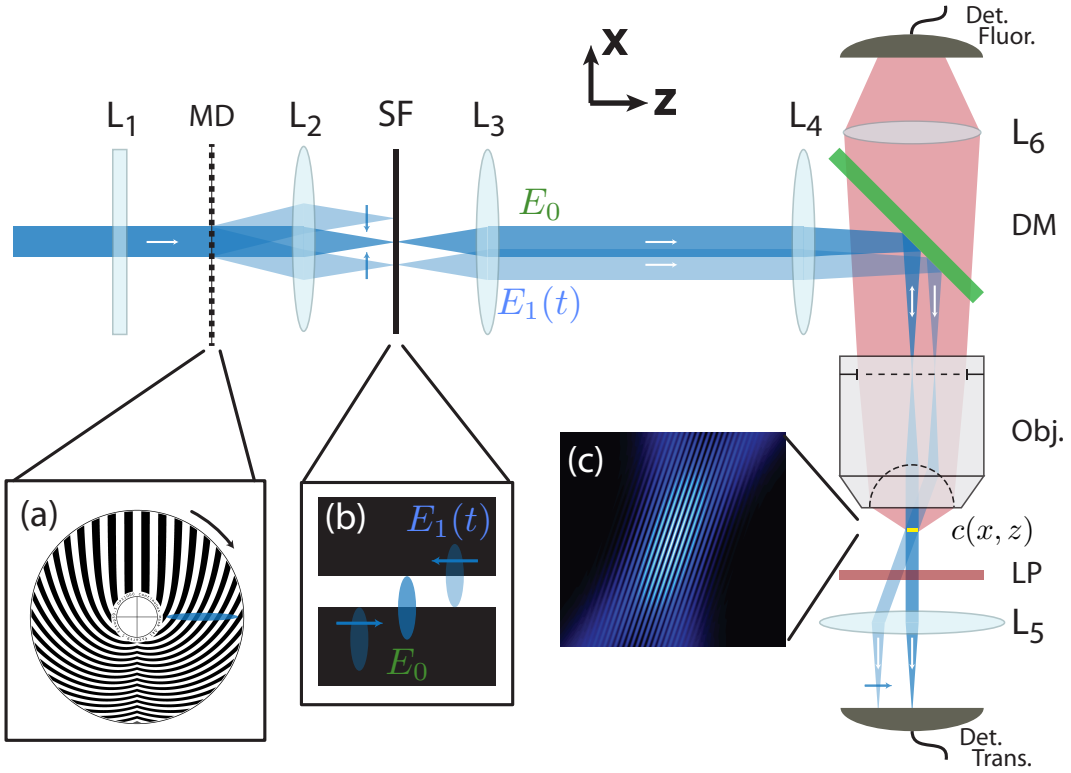

Figure 3.2: Schematic diagram of a CHIRPT microscope. Panel (a) shows the modulation disc, panel (b) shows the spatial filter which selects the two illumination beams, and (c) shows the illumination intensity profile at a snapshot in time.

using Euler's identity gives,

$$\begin{aligned} E_1(x) &= E_0 u_0(x) \mathrm{e}^{\mathrm{i}\omega_0 t} \frac{1}{2}[1+\cos(\Delta\kappa x t)] \\ &= \frac{1}{2} E_0 u_0(x) \mathrm{e}^{\mathrm{i}\omega_0 t}[1+\frac{1}{2}(\mathrm{e}^{\mathrm{i}\Delta\kappa x t}+\mathrm{e}^{-\mathrm{i}\Delta\kappa x t})] \\ &= \frac{1}{2} E_0 u_0(x) + \frac{1}{4} E_0 u_0(x) \mathrm{e}^{\mathrm{i}(\Delta\kappa x t)} + \frac{1}{4} E_0 u_0(x) \mathrm{e}^{-\mathrm{i}(\Delta\kappa x t)} \end{aligned} \tag{3.1}$$

, where we have suppressed the optical frequency for compactness. From eqn. 3.1 we see that the modulator disc produces three beams, a zero order time stationary beam, and positive and negative first diffraction orders which vary in time. This result is expected as it is simple diffraction of a time-varying sinusoidal grating. CHIRPT imaging uses two beams for its illumination, so the next step after the modulator mask is to filter out one of the first-order diffraction beams, in practice, this is done by using a spatial filter as seen in fig. 3.2(b). Mathematically we can just

drop one of the diffraction orders. The filtered illumination beam will then be relayed to the object plane. At this point is it advantageous to rewrite some of the variables so that they will be more physically meaningful. First, time, t, is going to vary from $[-T/2, T/2]$ where T is the period for one disc revolution. Next, we can define the angular spatial frequency as $\Delta\kappa\, t = k_1(t)$, the incident illumination beam on the modulation mask does not transmit through the center of the mask as seen in fig. 3.2(a) therefore we can capture this offset by letting $x = x_c + \Delta x$, where x_c denote the location of the centroid of the illumination beam and Δx is the width of the illumination beam on the mask. Now, let $\varphi_c = k_1(t)x_c$ be the modulation carrier frequency. Now the electric field reads as $E_1(x,t) = \frac{1}{2}E_0 u_0(x) + \frac{1}{4}E_0 u_0(x)\mathrm{e}^{\mathrm{i}(k_1\Delta x + \varphi_c)}$.

The illumination beam will be focused to a line in the object region where the illumination is a spatially coherent field with an intensity that varies in space and time. Now the illumination intensity for CHIRPT is formed by the interference of two spatially coherent fields as described in section 1.3, giving

$$E_{\mathrm{ill}}(\mathbf{r}_\perp, t) = E_0 \left[u_0(\mathbf{r}_\perp)\,\mathrm{e}^{\mathrm{i}\mathbf{k}_0\cdot\mathbf{r}_\perp} + \mu(t)\, u_1(\mathbf{r}_\perp)\,\mathrm{e}^{\mathrm{i}\mathbf{k}_1(t)\cdot\mathbf{r}_\perp}\mathrm{e}^{\mathrm{i}\varphi_c} \right] \tag{3.2}$$

with k-vectors $\mathbf{k}_0$ and $\mathbf{k}_1(t)$ indicating the direction of propagation of each beam, the transverse plane denoted by the coordinates $\mathbf{r}_\perp = x\,\hat{e}_x + y\,\hat{e}_y$, where $\hat{e}_j$ is a unit vector in the j^{th} direction (x, y, z), $u_j(\mathbf{r}_\perp)$ is the 2D spatial beam profile, $\mu(t)$ is the fringe visibility or modulation contrast (defined below), and φ_c is the carrier frequency. The angle of the incident beams with respect to the optical axis of the imaging system, θ_j, is defined through the projection onto the optical axis, $\hat{e}_z$, which is normal to the plane of the thin object. Specifically, the angle of propagation for each beam is $\mathbf{k}_j \cdot \hat{e}_z = k\cos\theta_j$, where $k = 2\pi/\lambda$ is the vacuum wavenumber of the illumination light with wavelength λ. The reference beam is denoted as $j = 0$ and is generally chosen to propagate co-linearly with the optic axis. The angle of the second beam is scanned with time so that the spatial frequency difference, $\Delta\mathbf{k}(t) = \mathbf{k}_1(t) - \mathbf{k}_0$, between the beams varies with the crossing angle of the beams with time, $\cos[\Delta\theta(t)] = [\mathbf{k}_0 \cdot \mathbf{k}_1(t)]/k^2$.

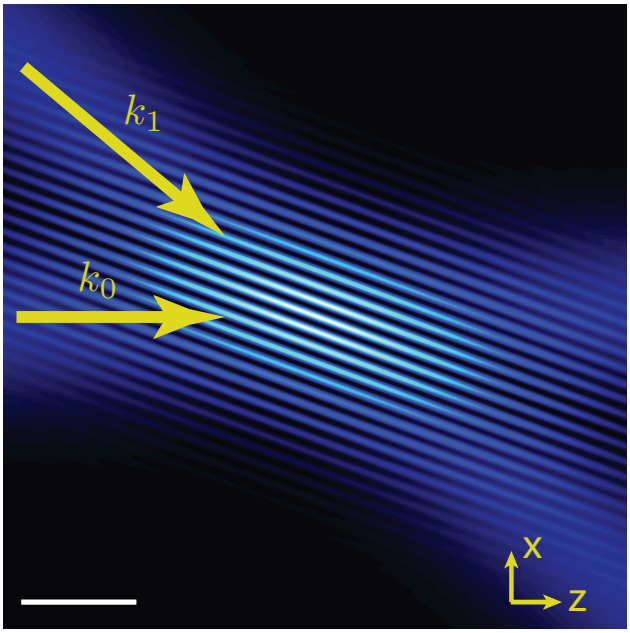

Figure 3.3: This figure illustrates CHIRPT intensity profile of two beams interfering at some crossing angle. The yellow arrows illustrate the k-vectors from both illumination beams. This beam interference simulation was generated using a wavelength of $\lambda = 600$nm and a crossing angle of 30 degrees, code in appendix C, scale bar = 1 micron

In general, the wavevectors can be expressed by their transverse and axial components as $\mathbf{k}_j(t) = \left(\mathbf{k}_{j,\perp}(t), k_{j,z}(t)\right)$, where the transverse wavevector can be further decomposed to $\mathbf{k}_{j,\perp}(t) = k_{j,x}(t)\,\hat{e}_x + k_{j,y}(t)\,\hat{e}_y$. The spatial frequency difference can thus be expressed in the transverse and axial dimensions as $\Delta\mathbf{k}(t) = (\Delta\mathbf{k}_\perp(t), \Delta k_z(t))$, where $\Delta\mathbf{k}_\perp(t) = \mathbf{k}_{1,\perp}(t) - \mathbf{k}_{0,\perp}$ and $\Delta k_z(t) = k_{1,z}(t) - k_{0,z}$. Figure 3.3 illustrates two beam interference as seen in the object region of the CHIRPT microscope.

Throughout this text it will be assumed that the $j = 0$ reference beam propagates along the optic axis such that $\theta_0 = 0$ and $\mathbf{k}_0 = (0, k) = k\,\hat{e}_z$. In the transverse plane, the spatial frequency difference is simply the spatial frequency of the scanning beam, $\Delta\mathbf{k}_\perp(t) = \mathbf{k}_{1,\perp}(t)$. In the axial dimension, the spatial frequency difference becomes: $\Delta k_z(t) = k_{1,z}(t) - k = k\,[\cos\theta_1(t) - 1]$. This can be expressed in terms of the familiar Ewald shell, which arises as a result of the dispersion relation:

$$\Delta k_z(t) = k\left(\sqrt{1 - \frac{\left|\mathbf{k}_{1,\perp}(t)\right|^2}{k^2}} - 1\right), \tag{3.3}$$

where $\left|\mathbf{k}_{j,\perp}(t)\right| = k\sin\theta_j(t)$, the derivation can be found here [45, 47].

Let's look at the interference of light sheet beams that are focused to a diffraction-limited line along the y-direction, and extend over a large transverse region along the x-direction. Under these conditions, only the transverse spatial frequency of beam $j = 1$ varies along the x-direction. The beam interference produces a sinusoidal modulation pattern that can be written in the form

$$I_{\text{ill}}(\mathbf{r}_\perp, t) = |E_{\text{ill}}(\mathbf{r}_\perp, t)|^2 = I_{\max}\left(\frac{u_0^2(\mathbf{r}_\perp)}{4} + \frac{\mu^2(t)\,u_1^2(\mathbf{r}_\perp)}{4} + \frac{\mu(t)\,u_0(\mathbf{r}_\perp)\,u_1(\mathbf{r}_\perp)}{2}\cos\Phi(x,t)\right) \tag{3.4}$$

The maximum intensity of the line focus is $I_{\max} = 4|E_0|^2$.

The beams impart a sinusoidal modulation along the x-direction, with $\Phi(x,t) = \Delta\mathbf{k}_\perp\cdot\mathbf{r}_\perp + \varphi_c$ describing the phase of the spatial frequency projection illumination patterns, where φ_c is the phase shift that sweeps rapidly compared to the spatial frequency sweep, and thus acts like a carrier modulation frequency and allows the separation of interference terms [45, 44].

The modulation depth of the spatial frequency along the x-direction is denoted by $\mu(t)$. The modulation depth is the relative amplitude of the fields in CHIRPT and determines the spatial frequency support along the spatial frequency projection direction, and thus the OTF [47].

For the usual situation in which a standard microscope objective is used to focus the CHIRPT illumination light to a line focus in the object where the illumination along the y-spatial frequency direction in the pupil plane of the objective is overfilled, the spatial frequency support will depend on the instantaneous spatial frequency, $\mathbf{k}_1(t)$, of the scanning beam and the unscanned beam, passes through the center of the objective pupil along the k_x direction, we find that the fringe visibility is given by the chord length of the pupil function along k_y centered at $\mathbf{k}_1(t) \rightarrow \Delta\mathbf{k}_\perp(t) = \mathbf{k}_{\perp,1}(t) = \mathbf{k}_{1,x}(t)\,\hat{e}_x$

$$\mu(t) = \sqrt{1 + \left[\frac{\mathbf{k}_{1,x}(t)}{k}\right]^2}\,\text{rect}\left[\frac{\mathbf{k}_{1,x}(t)}{2k_c}\right] \tag{3.5}$$

where $k_c = 2\pi f_c \approx \mathrm{NA}/n\lambda_\ell$ is the coherent imaging cutoff spatial frequency for the illumination objective with numerical aperture NA, an immersion medium with refractive index n, and an excitation wavelength λ_ℓ. Following the definition of the fringe visibility, $u_0(y) = \mathrm{sinc}(2\ f_c\ y)$ and $u_1(y,t) = \mathrm{sinc}[2\ \mu(t)\ f_c\ y]$, where we have used $\mathrm{sinc}(x) = \sin(\pi x)/\pi x$.

The time signal is given by the projection of the illumination intensity onto the sample,

$$S_t = A\langle I_{\mathrm{ill}}(\mathbf{r},t)\, c(\mathbf{r})\rangle_{\mathbf{r}}, \tag{3.6}$$

where $A = \frac{\eta}{\hbar\omega_f}\left(\frac{\Omega_c}{4\pi}\right)$ is the collection efficient, η is the detector quantum efficiency, ω_f is the angular frequency of the fluorescent light, and Ω_c is the collection solid angle. The spatial integral, $\langle\cdot\rangle_x = \int \cdot\, \mathrm{d}x$, is performed by the single pixel detector. This model is valid for linear detection for both coherent and incoherent contrast mechanisms. It should be noted that the illumination intensity can be generalized to be the effective illumination, see chapter 10.7 for details, which allows the signal model to extend to nonlinear excitation, however, the forward model can still be considered linear in the detection.

When (3.4) is plugged into (3.6), we get

$$\begin{aligned} S_t &= S_0 + \Delta S \\ &= A\left\langle I_{\max}\left(\frac{u_0^2(\mathbf{r}_\perp)}{4} + \frac{\mu^2(t)\, u_1^2(\mathbf{r}_\perp)}{4} + \frac{\mu(t)\, u_0(\mathbf{r}_\perp)\, u_1(\mathbf{r}_\perp)}{2}\cos\Phi(x,t)\right) c(\mathbf{r})\right\rangle_{\mathbf{r}} \end{aligned} \tag{3.7}$$

the first two terms evaluate to a constant value in time defined as $S_0 = AI_{\max}\left(\frac{u_0^2(\mathbf{r}_\perp)}{4} + \frac{\mu^2(t)\, u_1^2(\mathbf{r}_\perp)}{4}\right)$, the temporally fluctuating portion of the signal is

$$\Delta S(t) = \frac{1}{2}\mu(t) A\langle u_0(y)\ u_1(y,t)\cos\Phi(x,t)\, c(\mathbf{r}_\perp)\rangle_{\mathbf{r}_\perp}. \tag{3.8}$$

The expression above gives a cosine transform of the object, $c(\mathbf{r}_\perp)$. Notice that the modulation depth $\mu(t)$ gives the relative amplitude of each spatial frequency cosine projection at the instantaneous spatial frequency, $\mathbf{k}_{1,x}(t) = \mathbf{k}_{\perp,1}(t)\cdot\hat{e}_x$, of the illumination pattern – serv-

ing the role of the modulation transfer function (MTF) of the CHIRPT imaging system, where MTF = |OTF| = $\mu(t)$. The object is reconstructed by assembling the object from the measured spatial frequency projections [49, 47, 48], which is obtained from the single sideband (SSB) term from (3.12) where the object information has been shifted down to baseband (DC),

$$\tilde{S}(t) = \mu(t)\,\mathrm{e}^{-\mathrm{i}\varphi_t}\langle u_0(y)\; u_1(y)\mathrm{e}^{i\Phi(x,t)}c(\mathbf{r}_\perp)\rangle_{\mathbf{r}_\perp}. \tag{3.9}$$

Here the signal has been demodulated by $\mathrm{e}^{-\mathrm{i}\varphi_t}$ so that the object can be recovered with a Fourier transform (FFT) of the demodulated time signal. This will produce a line image of the object. A 2D image of the object can be constructed by line scanning perpendicular to the modulation direction and stacking the images. The data processing for CHIRPT is illustrated in figure 3.4.

CHIRPT has the remarkable ability to numerically refocus the object, known as digital holography. Since the recovered object information is complex due to the isolated single sideband. The signal in the spatial frequency domain needs a spatial propagator applied to the signal. Taking an inverse Fourier transform of the propagated signal will result in the focal plane of the image being shifted to the new axial location, [45, 44]. This can be written mathematically as

$$\begin{aligned}\tilde{S}(z,t) &= \tilde{S}(t)\mathrm{e}^{iz\Delta k_z(t)} \\ &= \tilde{S}(x,t)\mathrm{e}^{izk\left(\sqrt{1-\frac{|\mathbf{k}_{1,\perp}(t)|^2}{k^2}}-1\right)}\end{aligned} \tag{3.10}$$

CHIRPT allows incoherent emission such as fluorescence to be treated as if it came from a coherent source. This is due to the encoded phase information from the illumination source.

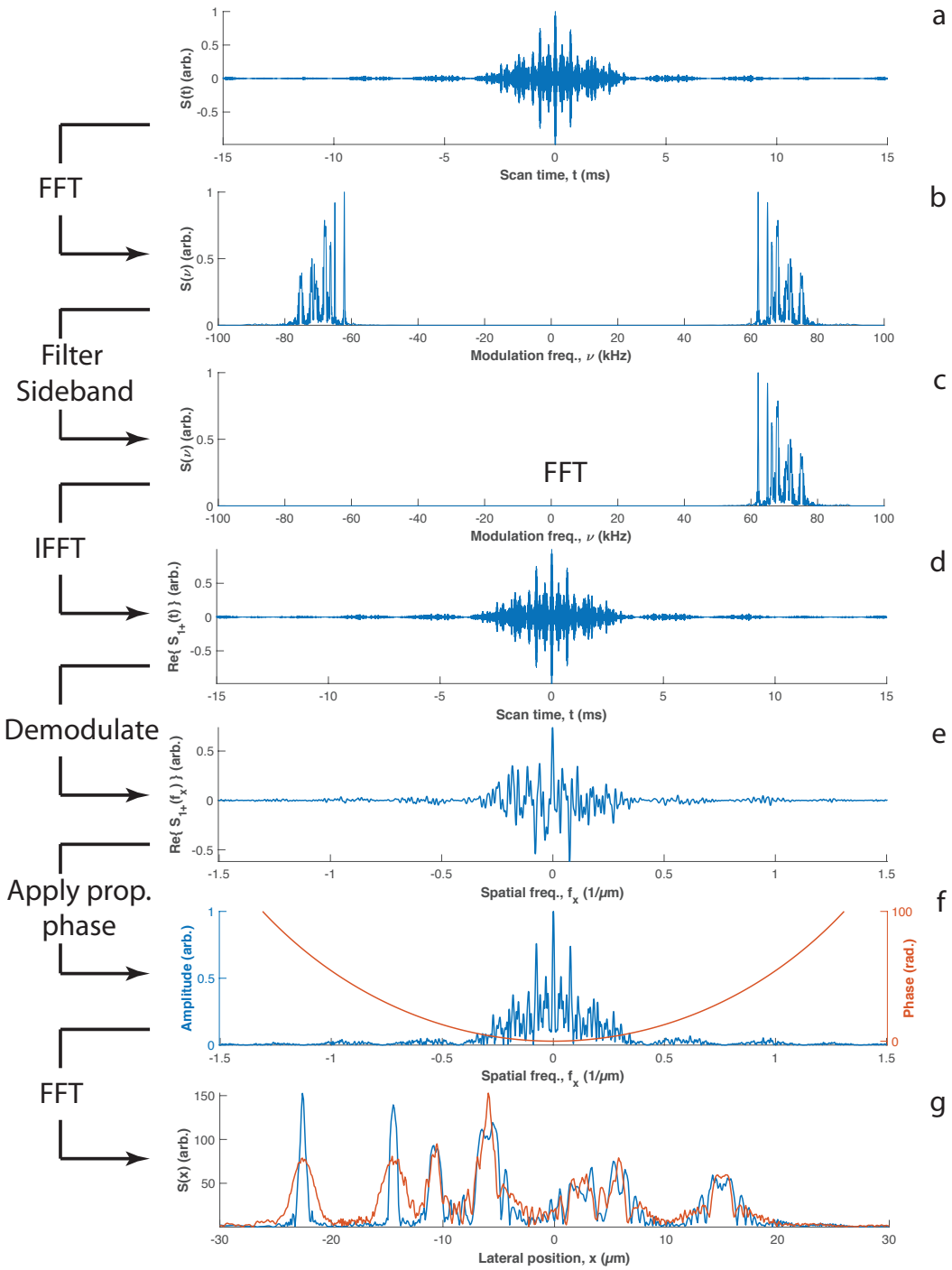

Figure 3.4: This figure illustrates the CHIRPT data processing procedure. Panel a) shows a CHIRPT time trace. Panel b) shows the Fourier transform of the CHIRPT time trace. Panel c) shows the positive sideband filtering operation done in the frequency domain. Panel d) shows the real portion of the complex time trace recovered by taking the inverse Fourier transform of the filtered frequency domain information. Panel e) shows the demodulated complex time trace where the object information has been shifted to the baseband (DC). Panel f) shows the propagation phase applied to the filtered demodulated complex time signal. Panel g) shows the numerically refocused object image in orange and the original object image in blue.

3.1.2 Mathematical Description of SPIFI

SPIFI uses a three-beam interference, fig. 3.5, with a set of interfering spatially coherent fields that produces the illumination intensity. By following the same procedure as outlined in the above section, the SPIFI illumination intensity is found to be

$$I_{ill} = \frac{I_{max}}{8}\left[2u_0^2 + \mu^2(t)\ u_1^2 + 4\mu(t)\ u_0\ u_1 \cos\Phi + \mu^2(t) u_1^2 \cos 2\Phi\right]. \tag{3.11}$$

For SPIFI illumination there is an extra interference term from the $j = -1$ and $j = 1$ beams which causes a second cosine modulation term that is at twice the modulation frequency of the $j = 0$ and $j = 1$ interference. Additionally, the second-order modulation contains twice the spacial resolution since the spatial frequency projection has twice the crossing angle. Figure 3.5 shows three-beam interference used in SPIFI microscopy.

The time-varying signal collected according to (3.6) for linear excitation will again yield a cosine transform for each fluctuating signal. In the same manner as CHIRPT each image order can be isolated as

$$\tilde{S}_t^{(q)} = \mu^{|q|}(t)\, \mathrm{e}^{\mathrm{i}\, q\varphi_t}\, \langle u_a(y)\, u_b(y)\, \mathrm{e}^{-\mathrm{i}\, q\Phi(x,t)}\ c(\mathbf{r}_\perp)\rangle_{\mathbf{r}_\perp}. \tag{3.12}$$

Here $u_j(y)$ is the spatial amplitude of the two interfering beams, $j \in \{a, b\}$, that produce the relevant signal order $q \in \{1, 2\}$. Again, a Fourier transform can be applied to the demodulated signal to recover an image of the object.

CHIRPT and SPIFI are normally arranged so that a linear sweep in spatial frequency is imparted so that $\Delta\mathbf{k}(t) = k_1(t)\hat{e}_x$ with $k_1(t) = \gamma\ t$, where $\gamma \equiv 2\pi\kappa$. In this case, the phase shift is $\varphi_t = \gamma x_c t \equiv \omega_c t$. For CHIRPT illumination, sidebands appear at only $q = \pm 1$ for an effective cutoff spatial frequency of f_c, and in the case of SPIFI, sidebands appear at both $q = \pm 1$ and $q = \pm 2$. The second-order image has a cutoff spatial frequency of $2f_c$, just as widefield incoherent imaging, however, the shape of the OTF has a larger amplitude at the higher spatial frequencies which results in images with better contrast. Additionally, nonlinear excitation can be

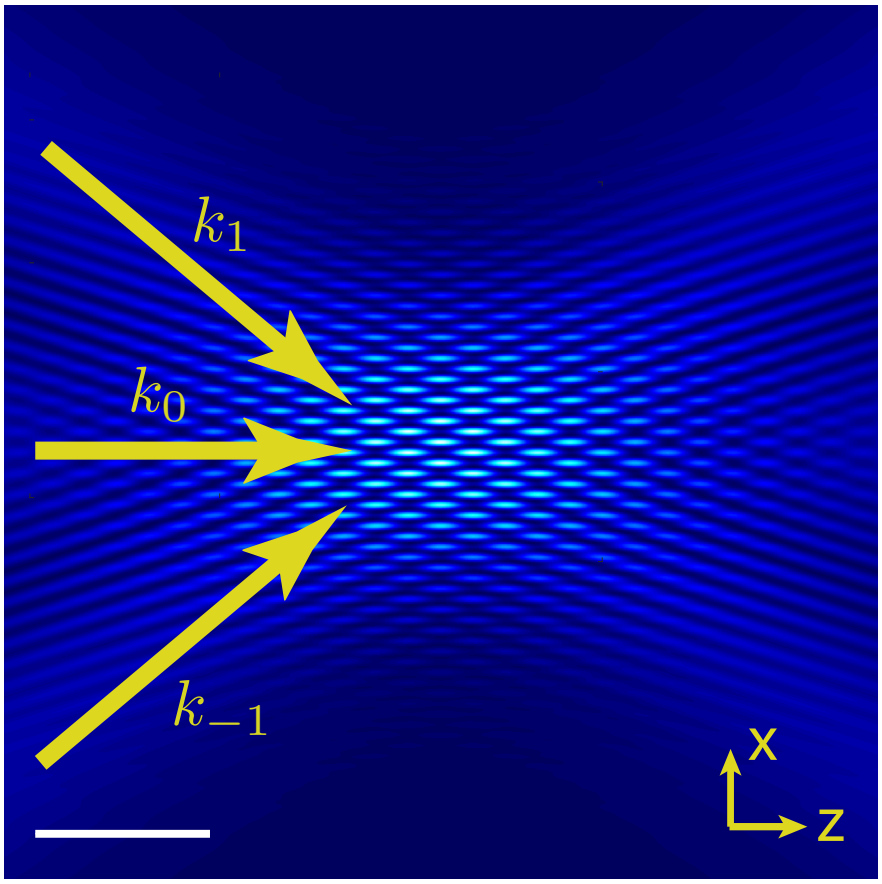

Figure 3.5: Example of 3 beam interference used in SPIFI systems taken at a snapshot in time. The yellow arrows illustrate the k-vectors from the illumination beams. This beam interference simulation was generated using a wavelength of λ = 600nm and a crossing angle of ±30 degrees, code in appendix C. Scale bar = 1 micron

used, typically done with SPIFI, which results in 3^{rd} and 4^{th} order image bands which contain spatial frequency cutoffs at $3f_c$ and $4f_c$, respectively.

3.2 Pros & Cons

In general, single-pixel imaging has several advantages compared to its camera-based counterparts, such as flexibility with high-quality detectors in many wavelength regimes, large temporal bandwidth, scattering robustness, and relaxed imaging constraints for the collected signal light. There are also several liabilities to consider as well, such as multiplexed shot noise and sometimes slow computational reconstructions. The cost and benefits are general to all single-pixel imaging techniques, but what about CHIRPT and SPIFI specifically?

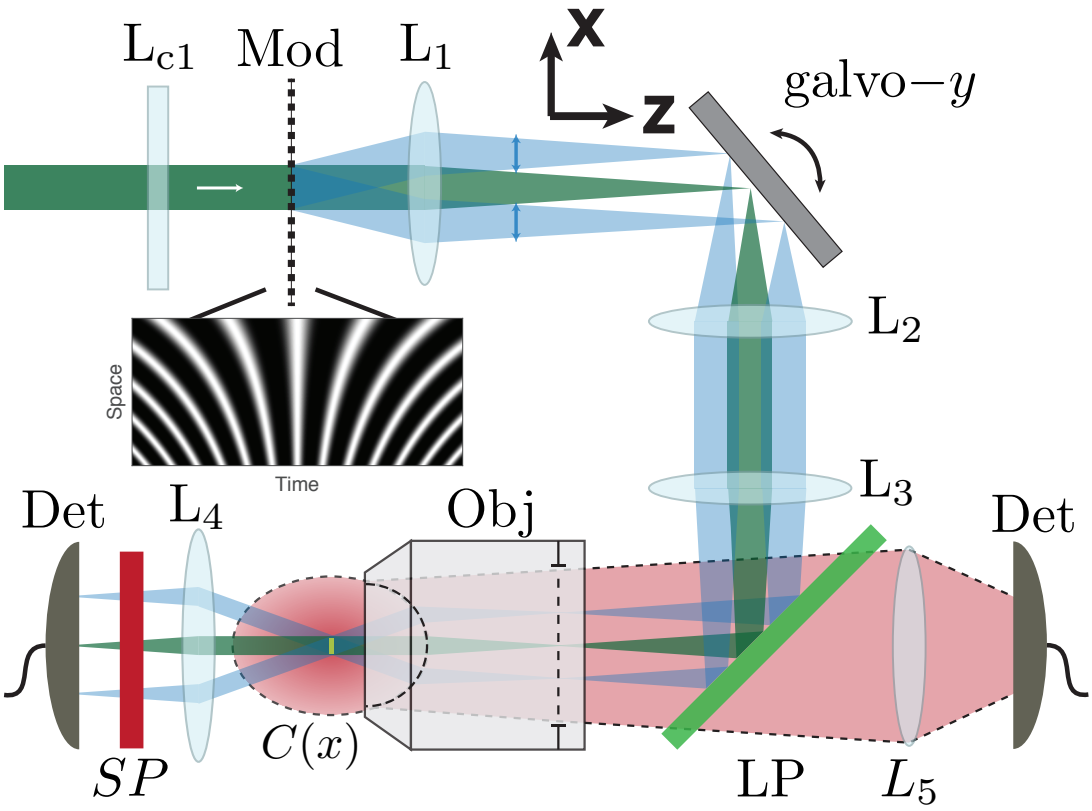

Figure 3.6: Schematic diagram of a SPIFI microscope.

CHIRPT's primary advantage is that it encodes the coherent propagation phase from the illuminations beam on incoherent contrast mechanisms, such as fluorescent emission, which allows holographic refocusing [45]. This holographic information can be used for diffraction tomography as discussed in chapter 8.2.5. This turns out to be a major advantage since it is the first technique to allow for 3D tomographic reconstructions with a large field of view of fluorophores without sacrificing spatial resolution. Another advantage of CHIRPT illumination is that it permits single-pixel quantitative phase imaging as discussed in chapter 5.7. One of the costs of CHIRPT is reduced illumination transmission efficiency due to the spatial beam blocking that is required to generate the two-beam illumination.

SPIFI illumination has its own set of advantages. First, the transmission efficiency is higher than CHIRPT since it does not require the blocking of diffracted beams. The increased efficiency helps with SPIFI's primary advantage which is multi-photon excitation to drive super-resolution imaging as discussed in chapters 7.6 and 9.6.2.

Chapter 4

Introduction to Quantitative Phase Imaging

4.1 Phase Contrast Imaging

Phase contrast imaging was first realized by Fritz Zernike in 1942 [160, 159]. Zernike realized that image formation could be understood as interference from many tilted plane waves (spatial frequencies), therefore, the amplitude and phase would play a critical role in the contrast of image formation. It was this insight that allowed Zernike to come up with the idea of modifying the phase of the unscattered portion of the illumination light (a ballistic component of the illumination). When a phase shift is applied to the ballistic component then the contrast of a nearly transparent object can be increased substantially. Zernike noted that a phase object could be changed to appear as an absorbing object depending on how much phase was applied to the ballistic light relative to the scattered light. One of the major drawbacks of Zernike's technique is that the mapping of the field phase to intensity is highly nonlinear. For example, if positive phase contrast is implemented (the ballistic component is delayed by a quarter wavelength compared to the scattered light) then a thick, high refractive index object will appear darker than the background, however, if the phase delay is too large the object will become bright, giving the impression that is has a lower refractive index compared to the background. This type of behavior has led researchers to search for other phase contrast methods so that quantitative values can be assigned to the acquired image.

4.2 Quantitative Phase Imaging

Quantitative phase imaging (QPI) deals with measuring the complex field produced by a sample of interest. The sample is typically weakly scattering and weakly absorbing. The complex field information is really the phase difference produced by interfering with the imaged field with a reference field. The phase difference can be used to calculate the refractive index

and optical path length. This information can be used to determine the thickness of a sample, and/or the dry mass of a cell to monitor cell growth [96]. There have been a number of quantitative phase techniques that have been developed in the last two decades each with its own strengths and weaknesses, however, they all ultimately aim to solve the same problem. The problem is how one recovers the object's absorption and phase function, $E_0(\mathbf{r})e^{i\phi(\mathbf{r})}$, despite the fact that phase information is lost at detection.

Let us first look at how a detector/camera will respond to an incident electric field so that we can better understand the problem of measuring the complex electric field. A photodetector responds to the time-averaged Poynting vector which is referred to as the irradiance. Following the derivation in [111], the Poynting vector, defined as $\mathbf{S} = \mathbf{E} \times \mathbf{B}/\mu_0$, is the flow of energy in free space or in an isotropic medium, where

$$\mathbf{E}(\mathbf{r}, t) = \frac{1}{2}\left[\mathbf{E}_0 e^{i(\mathbf{k}\cdot\mathbf{r}-\omega t)} + \mathbf{E}_0^* e^{-i(\mathbf{k}\cdot\mathbf{r}-\omega t)}\right] \tag{4.1}$$

is the electric field vector and

$$\mathbf{B}(\mathbf{r}, t) = \frac{1}{2}\left[\frac{\mathbf{k}\times\mathbf{E}_0}{\omega} e^{i(\mathbf{k}\cdot\mathbf{r}-\omega t)} + \frac{\mathbf{k}\times\mathbf{E}_0^*}{\omega} e^{-i(\mathbf{k}\cdot\mathbf{r}-\omega t)}\right] \tag{4.2}$$

is the magnetic field vector, $\times$ is the cross product between the two vectors, and $\mathbf{E}_0$ is the amplitude of the electric field vector. The Poynting vector can be rewritten using eqn. 4.1 and 4.2 giving,

$$\mathbf{S} = \frac{\hat{\mathbf{u}}}{4\mu_0}\left[\frac{k}{\omega}(\mathbf{E}_0\cdot\mathbf{E}_0)e^{2i(\mathbf{k}\cdot\mathbf{r}-\omega t)} + \frac{k}{\omega}(\mathbf{E}_0\cdot\mathbf{E}_0^*)e^{-2\frac{k\omega}{c}\hat{\mathbf{u}}\cdot\mathbf{r}} + c.c.\right] \tag{4.3}$$

where $\hat{\mathbf{u}}$ is a unit vector in the direction of the energy flow and $c.c.$ stands for the complex conjugate of the terms that came before it.

The Poynting vector can be used to describe the response of an optical detector. Notice in eqn. 4.3 that the first term oscillates at the optical frequency, ω, which is on the order of 10^{15}Hz. This frequency is way too fast for current optical detectors which have an optical response of

$10^6 - 10^9$Hz. For this reason, it is often the case that the time-averaged optical response is what is measured,

$$\langle \mathbf{S} \rangle_t = \hat{\mathbf{u}} \frac{n\epsilon_0 c}{2} (\mathbf{E}_0 \cdot \mathbf{E}_0^*) \mathrm{e}^{-2\frac{k\omega}{c}\hat{\mathbf{u}}\cdot\mathbf{r}} \tag{4.4}$$

where $\langle \cdot \rangle_t$ is the time average. Notice that the first term in eqn. 4.3 has vanished, the reason for this is that it oscillates symmetrically both positively and negatively, therefore, canceling out with the time average. Interestingly, the time-averaged Poynting vector, often called irradiance, includes the direction of energy flow, $\hat{\mathbf{u}}$. However, it has become common practice to refer to the intensity rather than the irradiance, where the difference between the two is that the direction is dropped, giving

$$I = \frac{n\epsilon_0 c}{2} \mathbf{E}_0 \cdot \mathbf{E}_0^*. \tag{4.5}$$

It is common to take things one step further dropping the scaling constants and the vector nature of the electric field leaving the well-known equation for intensity

$$I = \langle |E|^2 \rangle = E_0 E_0^*. \tag{4.6}$$

Now we see what is meant when it is said 'the optical detector responds to the intensity of the field (the modulus squared) and not the field itself' [96, 115, 95, 111].

Returning to our objective of describing the challenge of detecting the complex field. We will define the imaged field,

$$E_i(\mathbf{r}, t) = E_0(\mathbf{r}, t) h(\mathbf{r}) \tag{4.7}$$

where E_i is the imaged field, E_0 is the amplitude of the imaged field, and $h(\mathbf{r}) = \exp\big(i\varphi(\mathbf{r})\big)$ is the phase object of interest. This model for $h(\mathbf{r})$ is only valid when the absorption in the sample is negligible and the object acts as a phase object. The measured intensity, with unimportant

scaling constants being dropped, would be

$$\begin{aligned} I(\mathbf{r},t) &= \langle |E_i(\mathbf{r},t)|^2 \rangle_t \\ &= \langle E_i^* E_i \rangle_t \\ &= \langle E_0(\mathbf{r},t)\exp\big(-i\varphi(\mathbf{r})\big)E_0(\mathbf{r},t)\exp\big(i\varphi(\mathbf{r})\big)\rangle_t \\ &= E_0^2(\mathbf{r},t). \end{aligned} \tag{4.8}$$

Here we clearly see that the phase information is lost. In order to recover the phase, it is common to use the idea developed in holography for recovering the phase by the interference of the imaged field with a reference field, $E_r(\mathbf{r})$, the resulting measured intensity is

$$\begin{aligned} I(\mathbf{r},t) &= \langle |E_i(\mathbf{r},t) + E_r(\mathbf{r})|^2 \rangle_t \\ &= \langle (E_i(\mathbf{r},t) + E_r(\mathbf{r}))^* (E_i(\mathbf{r},t) + E_r(\mathbf{r})) \rangle_t \\ &= \langle |E_i(\mathbf{r},t)|^2 \rangle_t + \langle |E_r(\mathbf{r})|^2 \rangle_t + \langle E_i(\mathbf{r},t)^* E_r(\mathbf{r}) \rangle_t + \langle E_i(\mathbf{r},t) E_r(\mathbf{r})^* \rangle_t \\ &= I_i(\mathbf{r},t) + I_r(\mathbf{r}) + \langle E_i(\mathbf{r},t)^* E_r(\mathbf{r}) \rangle_t + \langle E_i(\mathbf{r},t) E_r(\mathbf{r})^* \rangle_t \end{aligned} \tag{4.9}$$

where $I_i(\mathbf{r},t)$ is the imaged intensity, $I_r(\mathbf{r})$ is the reference intensity. The third and fourth terms on the right-hand side contain the complex field that we are interested in recovering [115, 95]. The goal of QPI is to recover the third term in eqn 4.9, $I_{ir} = \langle E_i(\mathbf{r},t)^* E_r(\mathbf{r}) \rangle_t$. There are two common classes of methods for extracting this information from the measured interference. The first class is referred to as *phase stepping methods* and the second class is *off-axis methods*. Below we will consider how each of these classes of QPI solves the complex recovery problem.

4.2.1 Phase Stepping Methods

Phase-shifting methods for quantitative phase imaging rely on exploiting the relative phase difference between the imaged field and the reference field. This is done by controlling the time delay of either of the two fields, however, it is most common to delay the reference arm. We can write the reference field as, $E_r(\mathbf{r})\mathrm{e}^{-\mathrm{i}\phi}$ where ϕ is a time shift or phase delay. Typically, phase

shifting methods use a reference beam that propagates along the optic axis, i.e. $\mathbf{k}_r = 0$, this allows eqn. 4.9 to be rewritten as

$$I(\mathbf{r},t) = I_i(\mathbf{r},t) + I_r(\mathbf{r}) + \langle E_i(\mathbf{r},t)^* E_r(\mathbf{r})\rangle_t e^{-i\phi} + \langle E_i(\mathbf{r},t) E_r(\mathbf{r})^*\rangle_t e^{i\phi}. \tag{4.10}$$

Phase shifting methods typically measure 3 to 5 phase steps in order to recover $I_{ir}(\mathbf{r})$ [26, 95]. There are many methods used for producing the desired phase delay, ϕ, such as a moving mirror, tilting a glass slide, rotating a half wave plate, or a spatial light modulator (SLM) among many other techniques, [26, 155]. In general, it does not matter how the phase delay is produced but each technique will have trade-offs such as temporal stability, repeatability, eases of implementation, and cost, however, these are simple technical issues that do not change the fundamentals of recovering the phase of an object, [26].

While there have been many phase-stepping techniques and algorithms for recovering the complex field, I will present the M-step method which involves M equal steps over one period of the center optical wavelength, $\phi_m = 2\pi m/M$, where m is stepped from 0 to $M-1$. The algorithm used to recover the complex field is,

$$I_{ir}(\mathbf{r}) = \frac{1}{M}\sum_{m=0}^{M-1} e^{i\phi_m} I^{\phi_m}(\mathbf{r}) \tag{4.11}$$

where $I^{\phi_m}(\mathbf{r})$ is the measured interference intensity at phase delay, ϕ_m. For example, let $K = 4$,

$$\begin{aligned} I_{ir}(\mathbf{r}) &= \frac{1}{4}\left(e^{i0} I^{(0)}(\mathbf{r}) + e^{i\pi/2} I^{(\pi/2)}(\mathbf{r}) + e^{i\pi} I^{(\pi)}(\mathbf{r}) + e^{i3\pi/2} I^{(3\pi/2)}(\mathbf{r})\right) \\ &= \frac{1}{4}\left(I^{(0)}(\mathbf{r}) + iI^{(\pi/2)}(\mathbf{r}) - I^{(\pi)}(\mathbf{r}) - iI^{(3\pi/2)}(\mathbf{r})\right) \\ &= \frac{1}{4}\left(I^{(0)}(\mathbf{r}) - I^{(\pi)}(\mathbf{r}) + i\left[I^{(\pi/2)}(\mathbf{r}) - I^{(3\pi/2)}(\mathbf{r})\right]\right). \end{aligned} \tag{4.12}$$

The primary advantage of phase shifting techniques are noise robustness and retention of spatial resolution. The noise robustness is due to the fact that multiple images are acquired and some averaging can be employed to reduce the noise in the reconstruction. The spatial resolu-

tion is generally retained due to the fact that no filtering operations are required to isolate the information of interest, assuming proper sampling of the interference images typically 5-6 pixels per interference fringe. The primary cost is speed. Phase-stepping methods will necessarily run 3x to 4x slower and possibly much more than that depending on the number of phase steps needed for the particular method compared to off-axis methods, discussed below.

4.2.2 Off-axis Methods/Digital Holography

Off-axis methods for quantitative phase imaging derive their core inspiration from traditional holography [53, 55]. The idea of holography is that a field of interest can be interfered with a reference field to encode the amplitude and phase on a photographic film. The holographic image is recovered by illuminating the film with a duplicate of the reference field. That is, when the duplicated reference field scatters off the hologram, the transmitted field would match the original total field on the holographic plate allowing the amplitude and phase of the object to be recovered. In modern holography, the holographic plate has been replaced with a CCD camera chip and the amplitude and phase are recovered by numerical propagation but the core idea remains the same.

QPI off-axis methods could also be called digital holography. Off-axis methods refer to interfering with the field of interest with a reference beam that is at some angle α with respect to the optic axis, this is typically achieved in practice with a Mach-Zehnder interferometer, however, there are many geometries that can be used, [115]. Returning to eqn. 4.9, we are interested in recovering the third term which we are calling, $I_{ir}(\mathbf{r})$. In phase-stepping, we utilized a controllable phase delay to recover the complex field that was aligned with the optic axis, with off-axis QPI we will use a tilted plane wave for the reference that is at an angle to the optic axis. We can write our reference field as, $E_r(\mathbf{r}) = E_r e^{-i\mathbf{k}_r\cdot\mathbf{r}}$. Plugging this into eqn. 4.9 gives,

$$I(\mathbf{r}) = I_i(\mathbf{r}) + I_r(\mathbf{r}) + \langle E_i(\mathbf{r},t)^* E_r(\mathbf{r})\rangle_t e^{-i\mathbf{k}_r\cdot\mathbf{r}} + \langle E_i(\mathbf{r},t) E_r(\mathbf{r})^*\rangle_t e^{i\mathbf{k}_r\cdot\mathbf{r}} \tag{4.13}$$

where $|\mathbf{k}_r| = k_0 \sin(\alpha)$, k_0 is the center wavenumber of the reference beam. The first term is the imaged intensity and if it were isolated it would look like a standard camera image of the object of interest, the second term is a uniform intensity across the image plane, and the third and fourth terms together give a sinusoidal modulation at the spatial frequency, $\mathbf{k}_r$.

The question becomes how can the phase information be separated from all the other information contained in the detected intensity. The key lies with $\mathbf{k}_r$ which is the relative spatial frequency of the fringes created from the interference of the imaged field and the reference field. If the imaged field propagates along the optic axis of the imaging system then $\mathbf{k}_r$ is simply the spatial frequency of the reference field. The signal processing to recover the complex object information consists of taking a 2D Fourier transform to the imaged intensity,

$$\hat{I}(\mathbf{k}_\perp) = \hat{I}_i(\mathbf{k}_\perp) + \hat{I}_r \delta^2(\mathbf{k}_\perp) + E_r \hat{E}_i^*(\mathbf{k}_\perp + \mathbf{k}_{\perp r}) + E_r^* \hat{E}_i(\mathbf{k}_\perp - \mathbf{k}_{\perp r}) \tag{4.14}$$

where $\mathbf{k}_\perp = (k_x, k_y)$ is the transverse spatial frequency. Notice the second term is a 2D delta at zero spatial frequency amounting to a large spike in the Fourier domain as a result of the uniform plane wave used as the reference field. The third and fourth terms are shifted by, $\mathbf{k}_{\perp r}$, causing the complex object information to move left and right, respectively, in the Fourier domain. A bandpass filter to can be applied to isolate one of the complex side bands, typically the positive side band, $\hat{I}_{ir}(\mathbf{k}_\perp) = E_r^* \hat{E}_i(\mathbf{k}_\perp - \mathbf{k}_{\perp r})$. Finally, the isolated complex side band is shifted down to baseband (DC), $\hat{I}_{ir}^{\text{shifted}}(\mathbf{k}_\perp) = E_r^* \hat{E}_i(\mathbf{k}_\perp - \mathbf{k}_{\perp r} + \mathbf{k}_{\perp r}) = E_r^* \hat{E}_i(\mathbf{k}_\perp)$. The complex object is recovered using an inverse 2D Fourier transform applied to $\hat{I}_{ir}^{\text{shifted}}(\mathbf{k}_\perp)$ [72]. Typically, the phase unwrapping of the recovered object is the most challenging step of the entire processing due to the fact that there are phase vortexes where the amplitude drops to zero.

The choice of $\mathbf{k}_r$ is crucial to the success of off-axis methods as it allows the complex sideband to shift so that it can be easily separated from the rest of the information contained in the acquired intensity measurement. If $\mathbf{k}_r = 0$ then all the complex information will overlap in the frequency domain causing the separation of the complex object information to be more challenging to recover. Note, it is possible to solve the phase retrieval problem when $\mathbf{k}_r = 0$ with

single shot exposure, however, these solutions are iterative and come with new sets of obstacles. Now, if $\mathbf{k}_r \neq 0$, this will cause the positive and negative sideband to shear in the spatial frequency domain, if the shear is large enough the complex sideband can be cleanly separated from each other. In practice, a good choice is $\mathbf{k}_r \geq 2\mathbf{k}_c$, where $\mathbf{k}_c$ is the cutoff spatial frequency of the OTF imaging system. We can also relate the reference field angle, α, to the numerical aperture and magnification of the collection system, giving $\alpha \geq \sin^{-1}(\mathrm{NA}/n)/|M|$ is the numerical aperture of the objective lens, n is the refractive index of the immersion medium, and $|M|$ is the magnification of the image relay system. This inequality simply states that the reference field angle, α must be larger than or equal to the largest angle captured by the imaging system falling on the camera.

The primary advantage of off-axis methods is the speed at which the data can be acquired. Off-axis methods only need one image in order to recover the phase information, therefore, they are only limited by the frame rate of the camera or the integration time needed to acquire the desired SNR, whichever is greater. Depending on the particular optical design, (common-path methods) these methods can be very stable both temporally and spatially. One primary drawback is the increased sampling requirement placed on the camera to resolve the interference pattern and the object structure. This can be seen in fig. 4.1 where the reference spatial frequency shifts the sideband information out. If the detection bandwidth (size of the pixels) is too small (pixels too large) then aliasing of the sideband information may occur. Therefore, it is necessary to take into account both the increased optical bandwidth and the detection bandwidth. Of course, there are many types of QPI techniques that recover complex object field information, the above descriptions are meant to give an idea of how complex field information can be recovered. It is not meant to be exhaustive or suggest these are the only two methods for recovering the complex field.

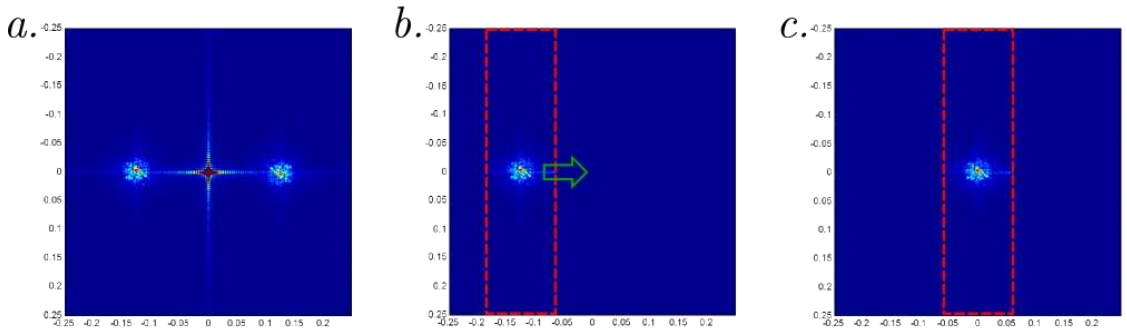

Figure 4.1: Off-axis holography data processing. Panel a) shows the 2D Fourier transform of an off-axis image. Panel b) filters the negative image sideband. Panel c) shows the shifted negative sideband of the holographic image. Figured borrowed from https://www.wavefrontshaping.net/post/id/12.

Chapter 5

Single pixel quantitative phase imaging with spatial frequency projections

5.1 Summary

This chapter is a reproduction of the Methods publication [136]. We introduce a new single-pixel imaging technique that automatically co-registers quantitative phase and incoherent image modalities through the simultaneous acquisition of identical object spatial frequency information. The technique consists of using a time-varying groove density diffraction grating to produce a reference and scan beam. The interference between the beams produce time-varying spatial frequencies in the sample. The collected light on a single pixel detector produces a time trace that allows easy recovery of coherent and incoherent contrast mechanisms. We derive theory for the quantitative phase and show excellent agreement with experimental data and the numeric model. Additionally, we derive a general theory of single-pixel quantitative phase theory that can be applied broadly to general methods that use a sequence of modulated light patterns for single-pixel phase imaging.

5.2 Introduction

Optical imaging is a powerful technique for probing the physical organization, chemical composition, and temporal dynamics of a wide range of objects, from biological specimens to precision metrology of nanomaching. Numerous scientific endeavors rely on collecting high-fidelity images of the system under study – covering microscopic and macroscopic scales. Regardless of the spatial scale involved in an optical imaging process, the light collected from an object is re-imaged to a detector and recorded. When possible, it is advantageous to record light with a segmented optical detector that serves as a camera detector chip, such as a charge-coupled

device (CCD). To produce a high-quality image, the light emitted by the specimen must be minimally perturbed to prevent distortions of the image incident on the detector. This limits the scope of optical microscopy with cameras to objects that are weakly scattering.

In many cases, specimens imaged in a microscope display weak absorption and small refractive index changes, rendering them nearly transparent when illuminated by visible light. Weak absorption becomes particularly problematic for thin tissue slices or cell cultures due to the small interaction volume. Fluorescent and phase contrast modalities are the most common methods to image transparent biological specimens [84, 98, 100] with high contrast. Fluorescence allows for visualization of cellular dynamics with high specificity, while phase imaging probes endogenous contrast mechanisms [98, 146].

Fluorescence microscopy is a mature technology whose use in recent years has been propelled by high-sensitivity detectors that allow single-molecule detection. While some natively expressed biochemicals display strong autofluorescence, the introduction of exogenous or transgenic fluorescent labels has greatly expanded the impact of fluorescent microscopy by enabling particular biochemicals to be targeted and observed in biological specimens [133]. Yet fluorescent imaging is limited because not all molecules fluoresce, and the broad optical absorption and emission spectra can make it difficult to distinguish particular target molecules. In addition, fluorescent molecules are subject to photo-bleaching that can permanently degrade the ability to image a specimen for long periods of time, thus limiting the ability to perform long-term studies.

An alternative approach to fluorescence microscopy, which requires no external fluorescent probes and yields complementary information, is phase contrast microscopy. Phase contrast microscopy records spatial phase distortions of a light wave passing through a specimen due to spatial variations in optical path length (OPL). The phase accumulated by the illumination beam upon propagation through a specimen is proportional to the local index of refraction variations of the sample integrated along the direction of propagation. The vast potential of

extracting information from biological specimens without adding exogenous contrast agents has motivated significant development in methods for quantitative phase imaging [115, 12].

Early phase imaging methods, such as Zernike phase contrast microscopy, provided only a qualitative map of phase information because optical phase information is mapped nonlinearly in intensity [159, 98]. However, the realization that the accumulated phase shift through a cell is directly proportional to protein concentration [3] has motivated the development of quantitative phase microscopy (QPM) techniques to quantitatively map the OPL difference introduced by an object [98, 84]. There is strong motivation to quantitatively extract the spatial distribution of the refractive index of biological specimens because the spatial distribution of the content of cells – protein expression, cell membrane and vesicle distribution – changes during normal cell behavior and cell cycles, as well as when a cell is diseased or invaded by a pathogen [28, 96, 120, 85, 54]. Thus, a quantitative map of refractive index variations in a cell can be used to infer complex biomolecular interactions taking place within a cell.

Although optical detectors cannot directly record the rapid oscillations of the electric field, and thus fail to record the optical phase, interference between two coherent fields can convert phase differences into optical intensity variations – enabling the extraction of the phase with the processing of a measured intensity map. In-line and off-axis holography [53, 86] and phase shifting interferometry [26, 155] have been used for quantitative phase microscopy [27, 154]. Similarly, Hilbert phase microscopy is a hybrid of off-axis and phase-shifting holographies that allows for high spatial resolution measurements with rapid (single-shot) measurements [72].

A common problem in these interferometric methods is that the two coherent fields – the beam that passes through the specimen and the reference beam – traverse differing optical pathways. Consequently, it is difficult to extract a stable phase of the object due to changing OPL differences from systematic aberrations, e.g., mechanical vibrations and atmospheric turbulence, causing the total accumulated phase difference between the two beams to vary with time. In response, common-path QPM methods have been developed that counter this problem by negating the need for two sets of imaging optics. Shearing interferometry [15], trans-

port of intensity equation [140, 7, 107, 5, 113], Fourier ptychography [106], diffraction phase microscopy (DPM) [116, 108], spatial light interference microscopy (SLIM) [145], and use of a partitioned detection aperture [109] are all methods for common-path QPM.

Other common-path QPM methods create interference patterns after image collection. This can be done with, for example, a spatial light modulator (SLM) [117, 145], although this method requires multiple measurements to synthesize a phase image, slowing down the net acquisition rate significantly. Similarly, diffraction after image collection can be used to extract a reference beam that enables off-axis interferometry to obtain a phase image [116]. However, this method is a variation of self-referenced off-axis holography, and thus there is a tradeoff between the spatial frequency bandwidth attainable with single-shot acquisition. Yet another variation, spiral phase microscopy [10], uses a 2D Hilbert transform applied to an image collected with a spiral phase plate applied in the collected object field Fourier plane, providing excellent phase stability [97].

Despite the sustained development of QPM methods, camera-based QPM suffers several drawbacks that limit its applicability under certain experimental conditions. For example, speckle, common when imaging with monochromatic light, partially scrambles the image on the camera. To circumvent this issue, broad bandwidth light can be used in place of monochromatic light to significantly reduce the speckle background [145, 11, 80].

Single-pixel imaging offers a unique solution to partially circumvent loss in image fidelity due to a mismatch between the Si-detector bandgap and longer wavelengths. Whereas segmented detectors in the short-wave infrared (SWIR), mid-infrared (MWIR), and THz regimes can be quite expensive, offer poor performance, or simply not exist. Single-pixel detectors on the other hand, such as photomultiplier tubes (PMT) and avalanche photodiodes (APD), are available with good quantum efficiencies at these longer wavelengths. Single-pixel imaging has been demonstrated at THz [22], SWIR [125], and MWIR [123] spectral bands.

A wide range of single-pixel techniques have emerged over the years to address limitations in both fluorescence microscopy and QPM. Common imaging methods that utilize single-pixel

detection include laser-scanning confocal microscopy [94], multiphoton laser-scanning microscopy [31, 61], stimulated emission depletion microscopy [60], optical coherence tomography [42], time correlated fluorescent lifetime imaging [8], pump-probe microscopy [50, 37], ghost imaging [128], single-pixel camera methods [121], and spatial frequency projection microscopy for both linear [41, 51, 63, 34] and multiphoton imaging [66, 67, 46]. Single-pixel imaging methods can be easily integrated into other optical systems, such as for monitoring laser micromachining [14]. Each of these imaging modalities has shown superior performance to conventional optical microscopes in the presence of optical scattering, imaging with high fidelity in a scattering object by encoding information from the local region around the focal plane, which has been shown even for linear optical contrast signals [63, 38].

The wide electronic bandwidth of single-pixel optical detectors also opens the capability of multiplexing additional information into the temporal signal. Temporal multiplexing has been used for simultaneously acquiring multiphoton images from multiple depths in a specimen [66, 43]. Depth information can also be encoded into a linear fluorescent excitation process by transferring the phase difference of a propagating optical modulation field to mark spatial depth positions with a distinguishable temporal modulation pattern [45, 44]. Frequency multiplexing has been used for both spatial and fluorescent lifetime imaging of phosphorescent emitters [67]. The nonlinear response of a contrast agent, such as a fluorescent probe or a coherent nonlinear scattering process, can be exploited for super-resolution imaging [46]. In addition, optical spectral information can be integrated with further illumination light modulations for applications such as background-free absorption imaging [36, 35] and spectrally-resolved single pixel diffuse optical imaging [142].

While single-pixel fluorescence microscopy methods are routine, single-pixel QPM methods are relatively new. In principle, a single-pixel QPM method that permits imaging at high frame rates with automatically co-registered fluorescence intensity measurements would be desirable for a wide range of biological measurements. The information provided by QPM is complimentary to fluorescence microscopy and does not require external fluorescent probes –

making it attractive for a variety of microscopy applications, particularly in biological studies. Consequently, there has been significant effort in the past decade to develop single-pixel QPM techniques that are compatible with fluorescence microscopy. While several methods for single pixel QPM have been reported, they have relied on non-common path interference for extracting quantitative phase, and thus inherit the phase noise problems of non-common path QPM systems [73, 77, 25].

In this chapter, I introduce a new imaging technique dubbed direct optical phase extraction (DOPE) to simultaneously record spatial frequency information from the spatial distribution of three contrast modalities of an object – quantitative phase, absorption, and fluorescence. In this method, we eliminate the need for a reference arm. By using a modulated illumination beam, all of the light propagating through and collected from the object is nearly collinear – mitigating optical phase noise. The modulation makes use of a sequential phase shift applied to the modulated field that is exploited to isolate a complex term and thus obtain a complex object response, from which the coherent field response of the object is obtained. The same modulation pattern is used to recover a fluorescence image from the object. The phase, absorption, and fluorescent intensity images are built from a time sequence of spatial frequency measurements due to the modulated illumination beam, where the exact same spatial frequency information is sampled at each time point on two detectors, one for the coherent image and one for the fluorescence image. This ensures that the co-registered modalities automatically align in both position and magnification. Additionally, we derive a general theoretical framework for single-pixel imaging of both intensity- and phase-contrast imaging and utilize this framework to motivate the results of our DOPE QPM experiments. Finally, we compare DOPE QPM and absorptive imaging in both the forward- and backward-scattered directions and provide a physical optics description of the image formation process.

5.2.1 Single pixel imaging with spatial frequency projections

In the bulk of this chapter, I will restrict our discussion to modulation functions that impart a linear sweep in a single transverse spatial frequency with time. The use of a sequence of single spatial frequencies for the modulation function is a natural choice because plane waves are eigenfunctions of the Helmholtz equation that governs scalar electromagnetic wave propagation in a medium with spatially homogeneous electrical properties, and thus allows for very large field of view imaging [45, 44]. In the case of a complex modulation function with a linear sweep of a single transverse spatial frequency, the modulation function reads

$$M_{\mathrm{c}}(\boldsymbol{\rho}, t) = m_t \, \mathrm{e}^{-\mathrm{i}\varphi_t} = \exp\left(-\mathrm{i}\,\mathbf{k}_{\mathrm{t}} \cdot \boldsymbol{\rho}\right) \exp\left(-\mathrm{i}\,\varphi_t\right). \tag{5.1}$$

Here, $\mathbf{k}_{\mathrm{t}}$ is the time-varying sweep in transverse spatial frequency, and φ_t is a phase shift that sweeps with modulation transverse spatial frequency. This is the modulation function for CHIRPT microscopy [45, 44].

While modulation of the spatial frequencies can be imparted across the entire two-dimensional transverse plane, $\boldsymbol{\rho}$, our experimental implementation uses a beam brought to a line focus on a spinning modulator disk that imparts a linear sweep in spatial frequency in the x-dimension. Assuming that the modulation occurs along the x-dimension, the time-varying spatial frequency becomes $\mathbf{k}_t = 2\pi f_x(t)\hat{e}_x$, where $\hat{e}_x$ is a unit vector along one dimension. The modulator disk is designed to sweep through transverse spatial frequencies linearly in time, $f_x(t) = \kappa\, t$, such that $k_t = 2\pi\kappa\, t$, where κ depends on the spatial frequency of features on the disk and the rotation rate [45]. In addition, a phase shift imparted by the disk shifts the intensity fringes in the object region as the disk rotates, and thereby acts as a carrier frequency imparted to the spatio-temporal modulation so that we may write $\varphi_t = k_t x_c \equiv \omega_c t$, where x_c is the centroid of the line focus on the modulation mask [45]. Our complex modulation term now reads

$$M_c(x, t) = \mathrm{e}^{-\mathrm{i}\omega_c t} e^{-\mathrm{i}2\pi\kappa\, t\, x}. \tag{5.2}$$

For the one-dimensional modulation case, the single-sideband complex modulation using M_c leads to signal fluctuation relative to the mean given by $\Delta S(t) = S_1 + S_1^*$, where

$$S_1 = e^{-i\omega_c t}\langle e^{-ik_t x} c(x)\rangle_x = e^{-i\omega_c t} C(k_t) \tag{5.3}$$

is a complex single sideband (SSB) term that is centered at the carrier modulation frequency ω_c, called the first-order signal. The demodulated first-order SSB reads

$$\tilde{S}_1 = e^{i\omega_c t} S_1 = C(k_t), \tag{5.4}$$

which is the spatial frequency projection of the object at the illumination spatial frequency k_t – the value of the spatial Fourier transform of the object *intensity* response $C(k_x) = \langle c(x) e^{-ik_x x}\rangle_x$ at the instantaneous modulation transverse spatial frequency, $k_x = k_t$.

Physically, we see that the combination of illumination with a single transverse spatial frequency containing spatial-temporal modulation and the use of a single-pixel detector causes the temporal signal of the photodiode to output a spatial frequency coefficient of the object at the illumination spatial frequency k_t. An inverse Fourier transform of the demodulated SSB signal directly yields the intensity image of the object, $\tilde{s}_1(x) = \langle e^{ik_t x}\tilde{S}_1\rangle_{k_t} = c(x)$, which is our desired image.

In the case of a purely real modulation function, the linear sweep in spatial frequency reads

$$M_{\mathrm{re}}(\boldsymbol{\rho}, t) = \frac{1}{2} m_t \exp\left(-i\varphi_t\right) + \frac{1}{2} m_t^* \exp\left(i\varphi_t\right). \tag{5.5}$$

In this case, the signal fluctuation becomes $\Delta S(t) = S_1 + S_1^* + S_2 + S_2^*$, which, in addition to the first-order signal S_1, also produces a second order signal $S_2 = e^{-i2\omega_c t}\langle e^{-i2k_t x} c(x)\rangle_x$. The second-order signal is an SSB term centered at $2\omega_c$, leading to a demodulated second-order signal

$$\tilde{S}_2 = e^{i2\omega_c t} S_2 = C(2k_t). \tag{5.6}$$

Such a real-valued modulation function is used in SPIFI [51, 63, 66, 46], which is closely related to CHIRPT microscopy. Application of an inverse Fourier transform to the demodulated signals extracted from the real modulation function used in SPIFI produces two intensity images: one from the first order signal, $\tilde{s}_1(x) = c(x)$, and another from the second order signal, $\tilde{s}_2(x) = c(x)$. The image recovered from the second-order signal has twice the spatial resolution of the first-order signal. This is because the interference structure for the second order signal is formed with the pair of waves incident on the object that interferes at $\pm k_t$, creating an intensity modulation structure at $2k_t$ with twice the spatial frequency support of the first order, which is limited to the spatial frequency cutoff of a coherent imaging system [46].

5.2.2 Phase information is lost in single pixel intensity imaging

The single-pixel imaging theory above shows that, in general, the projection coefficients recorded by single-pixel detectors are given by $\Delta S(t) = \langle c(\boldsymbol{\rho}) M_{\mathrm{I}}(\boldsymbol{\rho}, t)\rangle_{\boldsymbol{\rho}}$. Since both the object, $c(\boldsymbol{\rho}) = \left|g(\boldsymbol{\rho})\right|^2$, and the intensity modulation function, $M_{\mathrm{I}}(\boldsymbol{\rho}, t)$, are real and positive functions, and because the object is an intensity transmission function, all phase information is lost in the imaging process. This phenomenon also occurs in conventional imaging.

Consider the specific case of single-pixel illumination of the object with a varying single spatial frequency of the illumination beam. Then, the recovered object will be the autocorrelation of the complex object spatial frequency distribution

$$\begin{aligned} C(k_t) &= \langle m_t\, g(x)\, g^*(x)\rangle_{\boldsymbol{\rho}} \\ &= e^{-i\varphi_t}\langle G(\mathbf{k}_\perp)\; G^*(\mathbf{k}_{\mathrm{t}} - \mathbf{k}_\perp)\rangle_{\mathbf{k}_\perp}, \end{aligned} \tag{5.7}$$

where $G(\mathbf{k}_\perp)$ is the spatial frequency distribution of the complex object. We conclude that conventional single-pixel intensity imaging is not able to image a complex object electric field response, and thus obtains no phase information.

5.3 DOPE microscopy – single-pixel QPM with spatial frequency projections

Fluorescent and quantitative phase imaging provide complementary information about a specimen under investigation. Several methods have been developed that allow for the sequential acquisition of QPM and fluorescent images on the same microscope system [108, 2]. The individual fluorescent and QPM images are taken from separate optical paths on the same microscope.

Here a new single-pixel QPM method is demonstrated called direct optical phase extraction (DOPE) microscopy. DOPE uses spatial frequency projections in a transmission geometry to measure the quantitative phase of a specimen along one transverse dimension. Like CHIRPT, DOPE utilizes complex SSB modulation as defined in Eq. (5.2). Since the DOPE modulation and the CHIRPT modulation patterns are identical, DOPE and CHIRPT can be combined in a single microscope to provide images of fluorescence intensity and quantitative phase that are automatically co-registered.

5.3.1 Physical principle of DOPE QPM

With complex modulation, we can view the DOPE illumination scheme as decomposing the line-focused electric field that illuminates a weakly scattering and thin object, $E_{\text{ill}}(x,t) = 1 + M_c$ where M_c defined in Eq. (5.2), into two spatially coherent light beams, such that $E_{\text{ill}} = E_0 + E_1$. The first term, $E_0 = 1$, is a reference field that is time stationary and co-propagates with the optic axis. This field arises from the bias term in the modulation function. The second field scans with time and reads $E_1 = e^{-i\omega_c t}e^{-ik_t x}$. Both fields are incident on the specimen, with the reference field at normal incidence with respect to the optic axis, and the scanning field at an angle with respect to the optic axis that varies with time (Fig. 5.1).

Both incident beams are brought to a line focus in the vertical (y) dimension in the object plane and are well approximated by plane waves in the lateral (x) dimension [45, 44]. In this microscope, the scanning beam linearly sweeps through all lateral spatial frequencies sup-

ported by the microscope objective (Fig. 5.1), providing diffraction-limited spatial resolution. The transmitted light is collected by a low NA objective lens in a 2-F configuration with the object and detector, and the detector is placed at the back focal plane of the 2-F optical system. This optical design allows for the recording of spatial frequency information from multiple modalities.

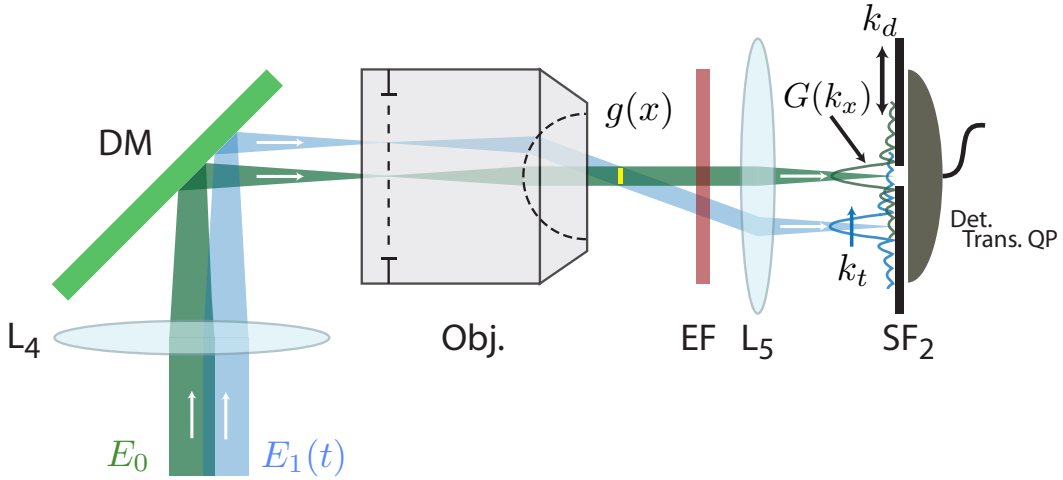

Figure 5.1: Schematic representation of a DOPE transmission microscope. Two illumination beams, E_0 and $E_1(t)$, are brought to a line focus in the specimen, which has a complex contrast function, $g(x)$. The electric fields are spatially filtered by an aperture in the back focal plane of the collection lens, SF_2, and collected by a large area single-element detector. $L_{4,5}$ - spherical lenses, DM - dichroic mirror, Obj. - objective lens, EF - emission filter, SF_2 - spatial filter, $g(x)$ - complex object, $G(k_x)$ - Fourier transform of the complex object, k_d - detector spatial location, k_t - scan beam input spatial frequency. Figure from [136].

The scanning beam spatially translates the object's spatial frequency content in the detection plane as the incident scan angle is varied; this arises as a consequence of the Fourier shift theorem. The spatial frequency content of the object over a narrow spatial frequency band is isolated by placing a narrow slit in front of the detector to restrict the region of spatial integration across the detection plane (Fig. 5.1). For a sufficiently narrow slit, the light transmission is functionally approximated by a Dirac-δ function, so that the transmitted field from the scanning beam produces a temporal signal that reads out the object's complex spatial frequency

information. The reference beam enables recovery of the complex object spatial frequency information after numerical processing of the recorded temporal trace. A Fourier transform of the recovered complex spatial frequency amplitude produces the complex object transmission function, amplitude and phase.

DOPE is able to simultaneously record object spatial frequency information of specimen phase and amplitude absorption, and can be combined with CHIRPT to image fluorescent emission using two single-pixel detectors – producing automatically co-registered images. The specimen must be adequately thin so that the field transmitted through the object is simply the product of the incident field and the complex field transmission function, $g(x)$, thus the imaging theory can be described as a one-dimensional process along the x coordinate [40].

5.3.2 Theoretical analysis of DOPE QPM

The reference beam will carry the object spatial frequency information, written as $E_0\ g(x) = g(x)$, using the assumption that E_0 is a line focus with unity amplitude spatially. The scanning beam has a time-varying incident transverse spatial frequency, $f_x(t) = n \sin[\theta_t]/\lambda$, that spans the full transverse spatial frequency support of the illumination objective, i.e., $\lambda\, f_x(t)/n \in [-\mathrm{NA}, \mathrm{NA}]$. Here n is the refractive index of the surrounding medium, λ is the wavelength of the illumination beam, and the numerical aperture is defined as $\mathrm{NA} = n \sin\alpha$, where α is the largest angle supported by the lens. The scanning beam also contains a phase shift that imparts a modulation carrier frequency to the beam, ω_c, like the complex CHIRPT modulation function in Eq. (5.2). This carrier frequency is critical for uniquely isolating the complex specimen field transmission from the recorded signal. The carrier frequency serves as a temporal analog of off-axis holography [86, 88, 45, 44]. Including the carrier frequency, the scanning field transmitted through the object is $E_1(x,t)\ g(x) = g(x)\ \mathrm{e}^{-\mathrm{i}\ k_t\, x}\mathrm{e}^{-\mathrm{i}\ \omega_c\ t}$.

Propagating the electric field incident on the front focal plane (FFP) to the back focal plane (BFP) will yield a spatial Fourier transform of the electric field in the FFP [56]. Consequently, the total object field in the BFP is a sum of the scaled Fourier transform of the reference and

scanning fields transmitted through the specimen

$$\mathscr{E}_{\text{obj}}(k_x) = G(k_x) + G(k_x - k_t)\,\mathrm{e}^{-\mathrm{i}\omega_c t}. \tag{5.8}$$

We have suppressed unimportant scaling factors in the expression above for simplicity.

The single-pixel detector spatially integrates the total intensity incident on the detector surface. We define the intensity transmission of a spatial filter placed in front of the detector as $T(x)$. Noting that the BFP spatial coordinate is linearly related to the spatial frequency via $x_{\text{BFP}} = \lambda F k_x / 2\pi n$, where F is the focal length of the collection lens, we can integrate over the spatial frequency coordinate to compute the photocurrent generated by the detector, which is given by $S_t = \langle T(k_x) \left|\mathscr{E}_{\text{obj}}(k_x)\right|^2 \rangle_{k_x}$. The demodulated SSB signal isolated near ω_c, as defined in Eq. (5.4), then reads

$$\tilde{S}_1 = \langle T(k_x)\, G^*(k_x) G(k_x - k_t) \rangle_{k_x}. \tag{5.9}$$

The transmission aperture, $T(k_x)$, determines whether object phase information can be recovered from the measured time trace. To make this point clear, let's consider two limiting cases.

First, consider the case of an infinite collection aperture, i.e., $T_1(x) = 1$. In this case, the time signal of the positive frequency sideband is an autocorrelation of the specimen complex transmittance function $\tilde{S}_1 = \langle G^*(k_x) G(k_x - k_t) \rangle_{k_x}$. It follows that a Fourier transform of $\tilde{S}_1$ is simply the magnitude squared of the complex field transmittance. Thus, in the case of no restricting aperture in the BFP, the recovered object is simply $\tilde{s}_1(x) = \left|g(x)\right|^2 = c(x)$. The intensity transmitted is identical to the SPIFI and CHIRPT signals [51, 45, 46, 44], and no specimen phase information can be recovered.

Next, consider the case in which the detection aperture in the BFP restricts the light collected by the detector to a small range of spatial frequencies near zero. Such an aperture can be approximated in the limiting case by a Dirac-δ function, i.e., $T_\delta(x) \approx \delta(k_x)$. The demodulated

SSB signal now represents the complex object's spatial frequency as a function of scan time

$$\tilde{S}_1 = \langle \delta(k_x)\, G^*(k_x) G(k_x - k_t) \rangle_{k_x} = G^*(0) G(-k_t). \tag{5.10}$$

A Fourier transform of the isolated signal then gives the complex object field response, $\tilde{s}_1(x) = G^*(0)\, g(x)$. A delta function transmission is achieved in practice with a small slit oriented along the y-direction of the imaging system and aligned to the optic axis.

5.3.3 Automatic co-registration with CHIRPT and DOPE

An advantage to the DOPE microscope is that fluorescent emission from the specimen can be imaged simultaneously with phase contrast and absorption. The illumination beams used for DOPE interfere to form fringes with the illumination intensity given by $I_{\text{ill}}(x,t) = 1 + M_{\text{I}}(x,t)$, with $M_{\text{I}}(x,t) = \cos[k_t\, x + \omega_c\, t]$. Fluorescent molecules in the illumination region with a concentration denoted by $c_{\text{f}}(x)$ emit fluorescent light with a spatial distribution of $I_{\text{obj}}(x,t) = c_{\text{f}}(x) I_{\text{ill}}(x,t)$. The emitted fluorescence is collected in the epi-direction with a second single-element detector (Fig. 5.2), producing a second-time trace, $S_t^{(\text{fl})} = \langle c_{\text{f}}(x) \rangle_x + \langle c_{\text{f}}(x) \cos[k_t\, x + \omega_c\, t] \rangle_x$. The first-order demodulated SSB temporal signal from the fluorescent detector provides a measure of the fluorescence intensity, $\tilde{S}_1^{(\text{fl})} = C_{\text{f}}(k_t)$, as noted in §5.2.1 [44]. This fluorescent time signal maps exactly the same transverse spatial frequency with scan time as the DOPE signal. Consequently, the fluorescent time signal encodes a 1D Fourier transform of the fluorophore distribution, $\tilde{s}_1^{(\text{fl})}(x) = c_{\text{f}}(x)$, and a 1D image can be recovered in a similar manner to the DOPE image.

5.3.4 Experimental validation of DOPE QPM

In order to validate the concept of DOPE, a spinning disk was used to generate two input beams with an intensity transmission modulator [45, 44]. The mask was illuminated with a continuous-wave 532-nm laser focused to a line. The zero- and first-order diffraction beams, which serve as the reference and scan beams respectively, were isolated with a spatial filter in

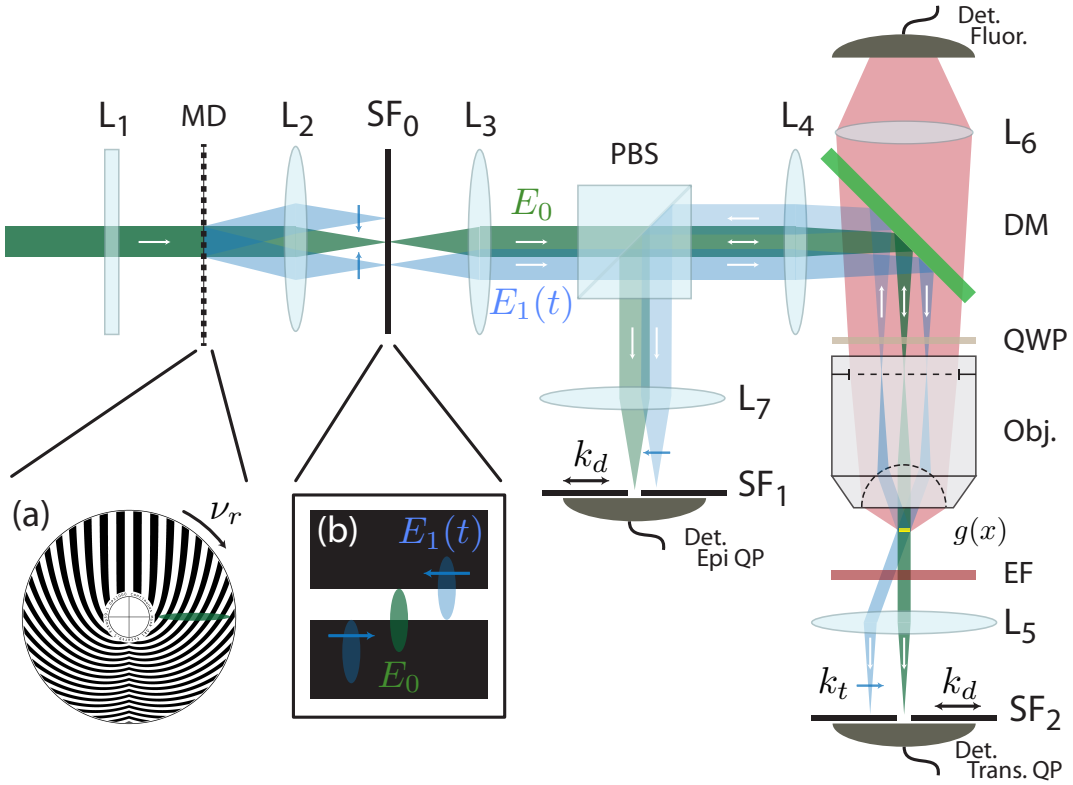

Figure 5.2: Schematic representation of a DOPE microscope. Two illumination beams the reference and scan beams, E_0 and $E_1(t)$, respectively. The schematic shows three imaging modalities, forward and epi single-pixel quantitative phase and fluorescent single-pixel imaging. (a) shows the modulator disc which creates the reference and scan beams. (b) shows the spatial filter which blocks the negative diffraction order. L_1 - cylindrical lens, $L_{2\text{-}7}$ - spherical lens, MD - modulator disc, $SF_{0\text{-}2}$ - spatial filter, PBS - polarizing beam splitter, DM - dichroic mirror, QWP - quarter-wave plate, Obj. - objective lens, EF - emission filter, E_0 - reference beam, $E_1(t)$ - scan beam, k_d - detection spatial frequency location, k_t - scan beam input spatial frequency, ν_r - modulator rotation frequency, $g(x)$ - complex object, Det. - single-pixel detector. Figure from [136].

the pupil plane of the objective lens, Fig. 5.2(b) [45]. The two line focus beams were re-imaged to the specimen plane using a 250 mm focal length lens and a 0.9 NA objective (Mitutoyo M Plan Apo HR 100×) configured as a 4-F imaging system. Light transmitted through the object was collected with a 0.25 NA aspheric lens placed one focal length away from the specimen. The Fourier plane, i.e., the BFP of the aspheric collection lens, was image relayed by a 4-F imaging system, then spatially filtered by a variable width slit. The filtered light was measured with a large area silicon photodiode detector (Thorlabs DET100A). Two-dimensional images were collected by translating the specimen in the vertical dimension (y), perpendicular to the line focus.

The positive SSB of the recorded signal was Fourier transformed and scaled by κ [51]. Quantitative phase and absorption images were obtained by taking the imaginary argument and magnitude of the recovered complex specimen transmission, respectively. Fluorescence images were recovered from the Fourier transform of the temporal signal collected with a PMT (Hamamatsu H7422-40P) in the epi-direction, where a dichroic filter beamsplitter (Semrock FF562-Di03) and an interference filter (Semrock FF01-593/40) isolated the fluorescent light [45, 44].

To demonstrate co-registration of the DOPE and CHIRPT images, we imaged 15 μm diameter, shell-stained fluorescent beads (LifeTechnologies, FocalCheck Slide 1, Well A1), which contains a thin layer of fluorescent molecules near the surface. The phase delay imparted to a transmitted beam by a single bead exhibits a spherical cross-section, with the largest delay appearing at the center of the bead. Fig. 5.3(a) shows a composite image of two shell-stained beads. The quantitative phase recovered from the DOPE measurement is shown in grayscale, while the fluorescence intensity recovered from CHIRPT is shown in red. Fig. 5.3(b) shows a line out of the absorbed intensity measured with DOPE compared with the fluorescence intensity measured with CHIRPT near the equator of one bead. The excellent agreement in both the shape of these profiles and their alignment is expected because the absorption is proportional to $c_{\mathrm{f}}(x) \approx 1-|g(x)|^2$. Moreover, since the absorption image collected with DOPE is co-registered with the fluorescence image collected with CHIRPT, it follows that the phase image extracted from the DOPE measurement will be co-registered as well.

To validate that the DOPE phase image is quantitative, the phase extracted at the equator of the bead was compared to a model of the theoretically expected phase delay. We computed the expected phase delay from the OPL variation across the bead, which is the chord length of the bead scaled by the index difference between the bead and the immersion media. The theoretical phase delay at the equator of a bead has the form $\phi(x) = 2\pi/\lambda\,\{n_1\ell(x) + n_0\,[2\,r - \ell(x)]\}$, where $\phi(x)$ is the phase difference, n_1 is the refractive index of the bead, n_0 is the refractive index of the immersion media, r is the radius of the bead, and the local chord length of the bead is given by $\ell(x) = 2\sqrt{r^2 - x^2}$. Fig. 5.3(c) shows the phase measured with the DOPE microscope

(green), compared with the modeled phase (blue). We fit the analytic model to the measured data with the differential index of refraction, $\Delta n = n_1 - n_0$, as the only free parameter. The best fit produced a value of $\Delta n = 0.03$.

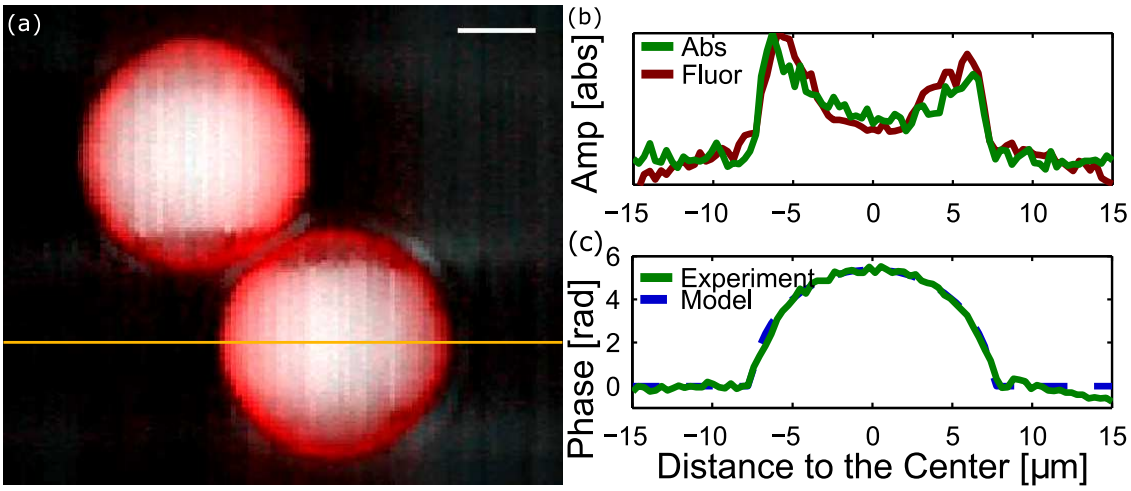

Figure 5.3: Co-registered quantitative phase, absorption, and fluorescence emission of 15 μm shell stained fluorescent beads. (a) Composite image of the phase and fluorescence image with gray and red color scales, respectively. (b) Co-localized line outs of the absorbed intensity and fluorescent intensity from the yellow line indicated in panel (a). These data show excellent alignment between modalities. (c) Comparison of the theoretical phase (dashed blue) and the measured phase (green). The phase was measured at the equator of the lower bead indicated by the yellow line in panel (a). Scale Bar: 5 μm. Figure from [136].

We tested the ability to collect simultaneously co-registered images of quantitative phase and fluorescent intensity in a biological sample by imaging fixed HeLa cells where tubulin was labeled with Alexa 555. Figure 5.4(a) and Fig. 5.4(b) are QPM (DOPE) and fluorescent (CHIRPT) images of a HeLa cell, respectively. Figure 5.4(c) is an overlay of the QPM and fluorescence channels, demonstrating that there was no need to align the images in post-processing.

5.4 General theory of single pixel quantitative phase imaging

DOPE imaging demonstrates that quantitative phase and amplitude images of a thin, complex object can be obtained simultaneously and can be automatically co-registered with a CHIRPT fluorescence image by illuminating the object with two beams an on-axis reference beam and a

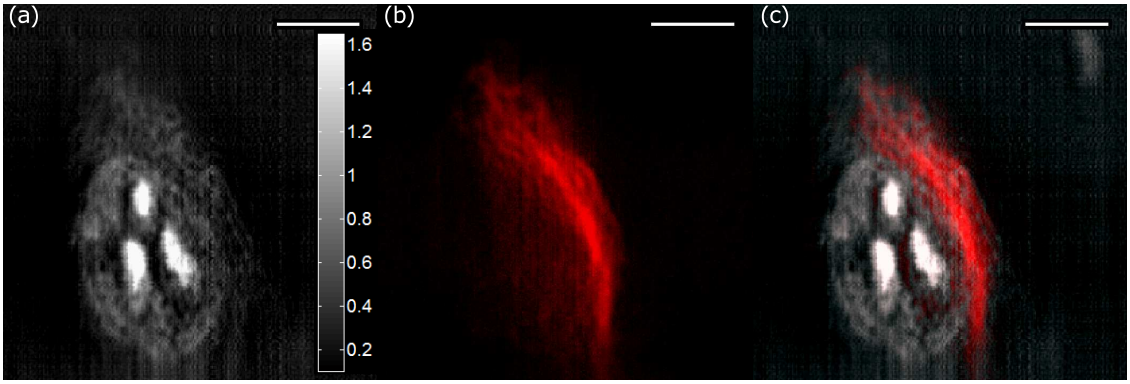

Figure 5.4: Simultaneous quantitative phase and fluorescence images of a HeLa cell. (a) The DOPE phase image. (b) The fluorescent image resulting from tubulin tagged with Alexa 555. (c) A composite of the phase and fluorescence images. Scale bar: 10 μm, Color bar: [rad]. Figure from [136].

scanned beam with increasing transverse spatial frequency. In this section, a generalized theory of phase-sensitive single-pixel imaging is presented. In order to obtain QP images with single-pixel modulated imaging, several assumptions are made.

Firstly, it is assumed that the illumination is a spatially coherent optical beam that passes through a thin object, with a complex response to the optical field (either in transmission or reflection) given by $g(\boldsymbol{\rho})$. Secondly, we assume the modulated object field emerging from the specimen takes the form $E_{\text{obj}}(\boldsymbol{\rho}, t) = g(\boldsymbol{\rho}) f_{\text{mod}}(\boldsymbol{\rho})$, where we can either modulate the field incident upon the object or after it exits the object, $f_{\text{mod}}(\boldsymbol{\rho}) = f_{\text{ill}}(\boldsymbol{\rho}, t) f_{\text{ex}}(\boldsymbol{\rho}, t)$. Finally, we assume that the signal is recorded from a photodiode placed behind a pinhole in the back focal plane of a 2-F optical collection configuration, as shown in Fig. 5.1.

At the BFP, the field is the spatial Fourier transform of the modulated object field, $\mathscr{E}(\mathbf{k}) = \langle e^{-i\,\mathbf{k}\cdot\boldsymbol{\rho}} E_{\text{obj}}(\boldsymbol{\rho})\rangle_{\boldsymbol{\rho}}$. Thus, the signal detected by a single pixel detector with a pinhole centered at $\mathbf{k}_d$ is given by

$$S_t^{(\mathbf{k}_d)} = |\mathscr{E}(\mathbf{k}_d)|^2 = \left|\langle e^{-i\,\mathbf{k}_d\cdot\boldsymbol{\rho}} g(\boldsymbol{\rho}) f_{\text{mod}}(\boldsymbol{\rho})\rangle_{\boldsymbol{\rho}}\right|^2. \tag{5.11}$$

Making use of the general form of the field modulation function of $f_{\text{mod}}(\boldsymbol{\rho}, t) = 1 + M(\boldsymbol{\rho}, t)$, this expression simplifies to read

$$\begin{aligned} S_t^{(\mathbf{k}_d)} &= \left| G_0^{(\mathbf{k}_d)} + G_M^{(\mathbf{k}_d)} \right|^2 \\ &= \left| G_0^{(\mathbf{k}_d)} \right|^2 + \left| {}^2 G_M^{(\mathbf{k}_d)} \right|^2 \\ &\quad + G_0^{(\mathbf{k}_d)*} G_M^{(\mathbf{k}_d)} + G_0^{(\mathbf{k}_d)} G_M^{(\mathbf{k}_d)*}, \end{aligned} \tag{5.12}$$

where $\mathscr{E}(\mathbf{k}_d)$ is the value of the object spatial frequency distribution at $\mathbf{k}_d$, and we define projections of the object onto the modulation patterns as

$$G_0^{(\mathbf{k}_d)} \equiv \langle \mathrm{e}^{-\mathrm{i}\mathbf{k}_d \cdot \boldsymbol{\rho}} g(\boldsymbol{\rho}) \rangle_{\boldsymbol{\rho}} \tag{5.13}$$

$$G_M^{(\mathbf{k}_d)} \equiv \langle \mathrm{e}^{-\mathrm{i}\mathbf{k}_d \cdot \boldsymbol{\rho}} g(\boldsymbol{\rho}) M(\boldsymbol{\rho}, t) \rangle_{\boldsymbol{\rho}}. \tag{5.14}$$

Isolation of a single sideband term allows for recovery of the set of projections of the complex object projections onto the modulation functions, $M(\boldsymbol{\rho}, t)$.

For a weak phase object, where absorption and phase changes are small, the majority of the energy in the diffracted field (i.e., the Fourier transform of the field) is contained at $\mathbf{k}_d = 0$. Thus, the most efficient configuration for QPM is to place the detector on the axis, leading to a simplified expression $S_t = |\mathscr{E}(\mathbf{0})|^2 = \left| \langle f_{\text{mod}}(\boldsymbol{\rho}, t) g(\boldsymbol{\rho}) \rangle_{\boldsymbol{\rho}} \right|^2$. This expression for single pixel QPM, written in terms of the object field, i.e.,

$$S_t = \left| \int E_{\text{obj}}(\boldsymbol{\rho}, t) g(\boldsymbol{\rho}) \, d^2\boldsymbol{\rho} \right|^2 \tag{5.15}$$

is quite different than that obtained for single pixel *intensity* imaging, where

$$S_t = \int \left| E_{\text{obj}}(\boldsymbol{\rho}, t) g(\boldsymbol{\rho}) \right|^2 d^2\boldsymbol{\rho}. \tag{5.16}$$

For our usual case of $f_{\mathrm{mod}}(\boldsymbol{\rho},t) = 1 + M(\boldsymbol{\rho},t)$, the total QPM signal expands to read $S_t = |G_0|^2 + |G_M|^2 + G_0^* G_M + G_0 G_M^*$, where for this case on-axis detection case, $G_0 = \langle g(\boldsymbol{\rho})\rangle_{\boldsymbol{\rho}}$ and $G_M = \langle g(\boldsymbol{\rho}) M(\boldsymbol{\rho},t)\rangle_{\boldsymbol{\rho}}$. Assuming that $M(x,t)$ are members of an orthonormal basis, the object can be synthesized from the measured temporal signal trace according to $\hat{g}(x) = \langle M^*(x,t) S_t\rangle_t$. The complex spatial frequencies detected can, additionally, be expanded by using multiple slits and detectors by placing the detection at $\pm k_d \neq 0$.

5.4.1 Single pixel QPM with spatial frequency projections

To validate the general single-pixel QPM analysis presented above, we use the theory to derive the expressions for DOPE microscopy. In DOPE, we are interested in the complex modulation function, $M(x,t) = M_{\mathrm{c}}(x,t) = m_t e^{-i\omega_c t}$, which means that the projection term reads $G_{\mathrm{M0}} = e^{-ik_t x_c} G(k_t)$. This leads to the temporal signal that we found earlier, namely

$$S_t = |G_0|^2 + |G(k_t)|^2 + e^{-ik_t x_c} G_0^* G(k_t) + e^{ik_t x_c} G_0 G(k_t). \tag{5.17}$$

An inverse Fourier transform of the signal produces

$$\begin{aligned} s_t &= |G_0|^2 \delta(x) + g(x) \star g^*(x) \\ &\quad + G_0^*\, g(x - x_c) + G_0\, g^*(-x + x_c). \end{aligned} \tag{5.18}$$

Selection of the the demodulated SSB term, $\tilde{S}_1 = G_0^* G(k_t)$, gives us the desired complex object, $\tilde{s}_1 = G_0^* g(x)$ centered at $x = 0$. This strategy for DOPE is motivated by the ability of a lens to perform a spatial Fourier transform of a complex optical field. Reconstruction through object synthesis, $\hat{g}(x) = \langle e^{ik_t(x+x_c)} S_t\rangle_{k_t}$, gives the same result.

The complex object is weighted by a complex number, G_0. Writing the complex object as a phasor, $g(x) = g_m(x) e^{i\phi(x)}$, lets us write the complex reference number in phasor form as $G_0 = A e^{i\phi_0} = G_r + iG_i$. Here, $G_r = \langle g_m(x)\cos\big(\phi(x)\big)\rangle_x$ and $G_i = \langle g_m(x)\sin\big(\phi(x)\big)\rangle_x$ so that the magnitude is given by $A^2 = |G_r|^2 + |G_i|^2$ and the phase is defined by $\tan\phi_0 = G_i/G_r$. In the weak

phase approximation, $A \approx g_m(x)$ and $\phi_0 \approx \langle g_m(x)\phi(x)\rangle_x / \langle g_m(x)\rangle_x$ is an amplitude-weighted average object phase. This provides an interpretation of the final result recovered from the single-pixel imaging process of $\tilde{s}_1 = A g_m(x) e^{i[\phi(x)-\phi_0]}$.

5.5 Physical optics picture of single-pixel phase imaging

So far, we have presented a fairly general description of single-pixel QPM, describing the imaging as a sequential acquisition of spatial frequency information. However, this description fails to give an intuitive physical picture of how the illuminating electric fields interact with the sample, and how those interactions relate to scattering theory. Here we present a physical scattering picture of DOPE microscopy.

As described above, DOPE uses two illumination beams. One beam is a reference, which is stationary with time, while the other beam sweeps out all angles supported by the NA of the illumination objective lens as a function of time. We begin by examining the scattering of the reference beam from a small cylindrical rod with a diameter on the order of the illumination wavelength. Given the relative size of the object with respect to the wavelength, the scattered electric field distribution is readily computed with the Mie scattering theory. The magnitude of the reference electric field scattered from a 1.5 μm diameter rod of infinite vertical extent is shown in Fig. 5.5(a) (green line). Consider collecting the scattered field in the forward (transmission) and back-scattered (epi) directions. Due to the spatial filtering process of DOPE, only light scattered to the optic axis will be detected, indicated by the thin yellow line in Fig. 5.5(a). The yellow line is positioned with respect to the detector slit location, k_d; here we assume $k_d = 0$. In general, the yellow line will rotate if k_d is non-zero and no longer lies on the optic axis. The squares in Fig. 5.5(a) represent the collected complex scattering coefficients from the reference beam that are isolated by the vertically-oriented slit used in DOPE QPM. The purple and orange colored circles illustrate the direction of scattering, forward and back-scattering, respectively.

Next, consider the scanning illumination field, which illuminates the specimen with a time-dependent angle θ_t, where $\sin\theta_t = \lambda \kappa\, t/n$. Since the object, we consider here is cylindrical,

the Mie scattering distribution for the scanning beam will be identical in shape to that of the reference beam, but will be rotated by the incident angle θ_t with respect to the optic axis. This field is represented by the blue line in Fig. 5.5(a). The maximum angle the scanning beam can traverse is defined by the NA of the illumination objective, green shaded region of Fig. 5.5. The collected complex scattering coefficients for the scanning beam at time t are represented by the circles, Fig. 5.5(a). Note, that the resolution is independent of the NA of the detection optics and is instead limited by the NA of the illumination objective.

Overall, the transmissive DOPE detector measures two scattering coefficients of the scattered electric field, one for each illumination beam, while the epi detector measures two different electric field amplitudes from the scattered field. The collected scattered light will interfere, permitting the complex coefficients to be recovered. To further clarify what is being measured by each detector, the collected coefficients can be mapped into the spatial frequency space. Figure 5.5(b) shows the mapping of the complex scattering coefficients into k-space of the object spatial frequency information, where the colored points represent the spatial frequency collected at a time t corresponding to the illumination angle in Fig. 5.5(a). As a function of time, all the spatial frequencies supported by the illumination objective are mapped out along an arc defined by the cross-section of the Ewald sphere determined by the illumination and scattered k-vectors.

According to the physical arguments outlined above, DOPE measures the complex scattering function in either the transmission or reflection modes. In most cases, forward scatter is stronger because back-scattering is only strong for spatial structures that are small compared to the optical wavelength. As a consequence, the transmission geometry will produce more reliable reconstructions with better SNR, since the majority of the scattered light is forward scattered with a very small fraction being back-scattered.

To test the ability of DOPE to form quantitative phase-contrast images in the forward- and back-scattered directions, we imaged a Fresnel lens in the transmissive and epi-directions simultaneously. We also collected intensity-contrast images (i.e., CHIRPT images) in both the

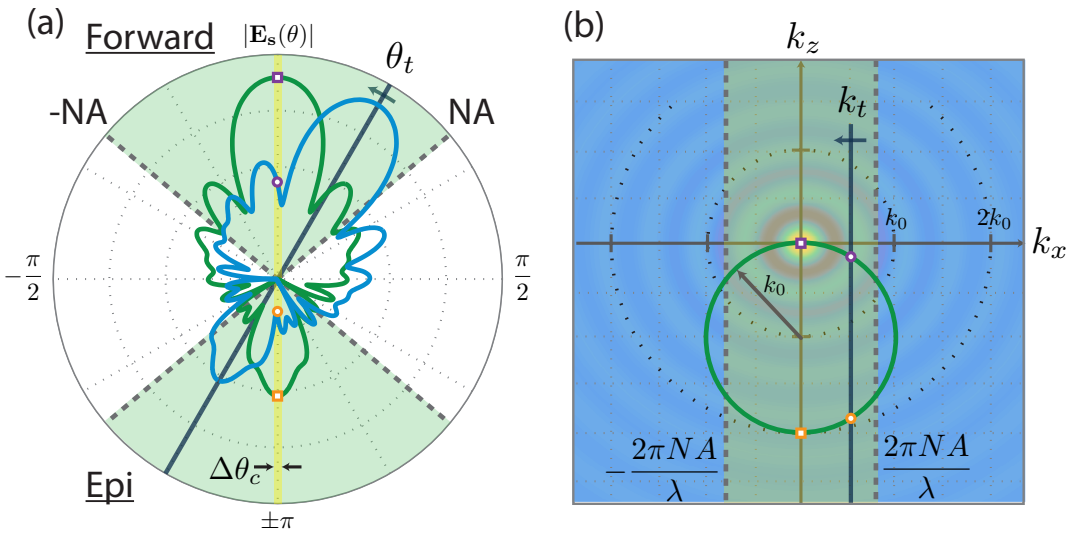

Figure 5.5: Figure (a) shows the Mie scattering magnitude distribution for a 1.5μm diameter scattering particle plotted on a log scale. The green line represents the scattering distribution of the reference beam and the blue line represents the scattering distribution of the scan beam. The light green shaded area represents all the scan angles that are swept out in a scan supported by the NA of the illumination objective. The purple points are forward scattering coefficients and the orange points are back-scattering coefficients collected at some time t on the optic axis, where the squares and circles are reference and scanning beam scattering coefficients, respectively. The yellow region represents the collection cone defined by the width of the spatial filter. Figure (b) shows the k-space which is collected during the time scan. The green circle represents a conic section of the Ewald sphere with a radius defined by the illumination wavelength. The colored points represent the spatial frequencies captured at some time t corresponding to the scattering picture on the left. Figure from [136].

transmissive and epi-directed directions by removing the vertical spatial slit. Figure 5.6 compares DOPE and intensity images collected in both directions, where it is clear that DOPE provides a reliable measurement of the OPL variation in the Fresnel lens. Conversely, the intensity modality shows contrast in the phase image only where the amplitude of the intensity image drops to near zero. According to the analyses presented above, CHIRPT is an intensity-contrast modality, and thus should not provide any phase information, we, therefore, hypothesize that the rings visible in the intensity phase images are due to diffraction of the illumination beams from each successive Fresnel zone plate ring.

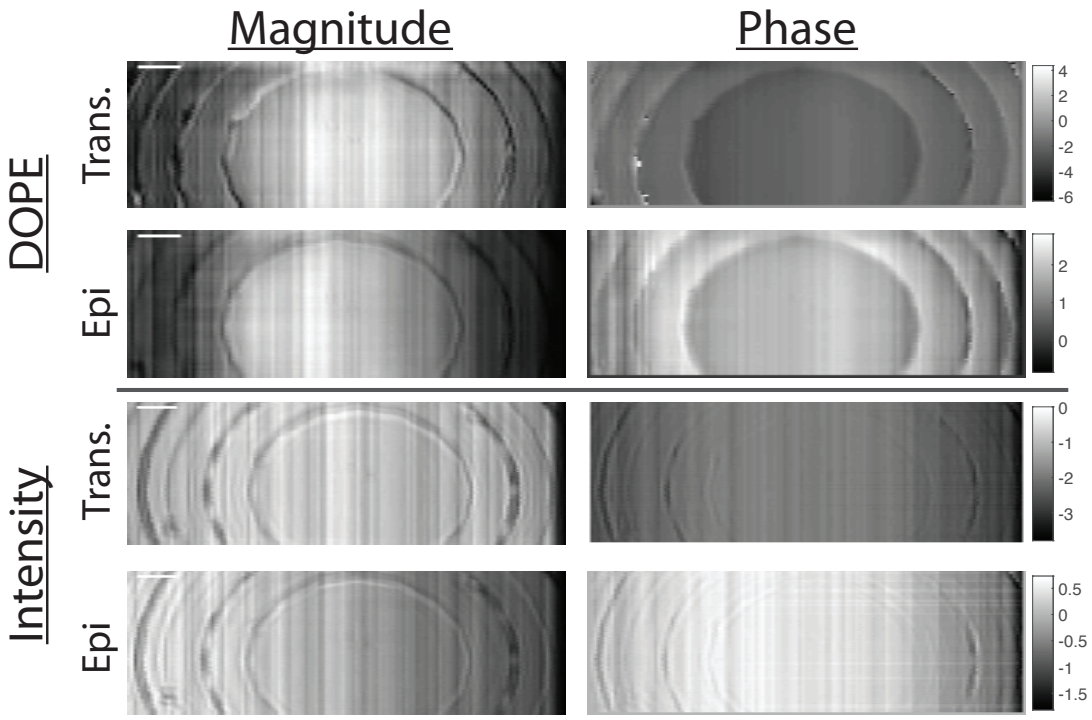

Figure 5.6: Micro Fresnel lens. Top DOPE images in both transmission and epi scattering directions with the spatial filter on the optic axis with a width of 15 μm. The bottom images are intensity images without a spatial filter. Scale Bar: 10 μm. Figure from [136].

5.6 Discussion

Forming images with multiple optical modalities provide complementary information that enhances our understanding of a specimen under study. Any microscope can be adapted to collect a set of images from multiple optical modalities; however, careful spatial alignment of the images is necessary to compare identical spatial features of simultaneously recorded coherent and incoherent optical images. Here, we have introduced the capture of multiple optical modality images through the simultaneous recording of identical spatial frequency content of quantitative phase, optical field absorption, and fluorescent emission spatial distributions, allowing for the automatic overlay of all three modalities.

The technique described in this chapter opens the path for greatly expanding the capabilities of QPM and fluorescent imaging. Our new microscope uses single-pixel detectors to record light from a specimen illuminated by a pair of interfering light beams. The illumination pattern

carries a spatial frequency dictated by the difference in the incident k-vectors of the interfering beams. The transmitted light fields are used to record the spatial frequency value of the complex specimen transmittance at the frequency difference of the two illumination beams. Due to the spatial filtering process, DOPE images are independent of the NA of the collection optics. Simultaneously, the same spatial frequency is recorded from the concentration distribution of fluorescing molecules excited by the intensity pattern from the interfering illumination beams. The image formation process is general and can be extended to other coherent and incoherent optical interactions, such as two-photon absorption, Raman scattering, coherent nonlinear scattering, photothermal, and photoacoustic imaging modalities. Moreover, by exploiting the large bandwidth of the single-pixel detector, additional information can be integrated into the time signal. This offers the expansion of DOPE to recent single pixel-imaging advances for multimodal hyperspectral imaging [36], super-resolution imaging [46], and new methods for spectrally-resolved QPM.

One of the biggest advantages DOPE has compared to camera-based QPM is its versatility in the wavelengths that can be used to image objects of interest. Traditional 2D array detectors are largely limited to Silicon-based detectors due to their availability, low noise, and low cost. However, when other wavelength ranges are desirable for probing the object of interest, such as SWIR, MWIR, and THz wavelengths, single-pixel detection is likely the only choice available. In recent years, improved SWIR 2D array cameras have become available. In the case of single-pixel imaging, however, there is a large selection of detectors for these wavelengths, which are widely available and comparatively inexpensive.

DOPE relies on a modulator disk that is easily scaled to high speeds. The cost of a modulator disc is on the order of hundreds of dollars, depending on the quality of the print and the desired resolution of the printed features. Using a modulator disk for DOPE imaging, the ultimate limit in acquisition speed will be determined by how fast the modulator disc can spin, the beam scanning speed across the sample (perpendicular to the line focus), or by incident laser power –

whichever of these parameters is lowest will be the limiting factor. There are, however, strategies to overcome each of these challenges that will permit high-speed DOPE imaging.

If the rotation speed of the modulator disk is the limiting factor, the printed patterns can be multiplexed so that multiple patterns can be imaged in a single disc rotation. When the speed of scanning the line focus is the limiting factor, resonant galvanometers or polygonal mirrors can be used to rapidly acquire 2D images. Finally, when the laser power is limited, requiring longer scan times to enhance SNR, PMTs and photon counting can be used to compensate for the low photon flux.

Considering all of these factors that can limit acquisition speed in DOPE imaging, we argue that high frame rates, up to 600 lines per second, can be achieved in our current configuration. To date, we have operated at 30-180 seconds to obtain a 2D image using stop-and-hold stage scanning to translate the specimen orthogonal to the line focus. This scheme is very slow compared to scanning the line focus with, e.g., galvanometric mirrors, and we expect the acquisition rate to scale to >50 Hz per 2D image with an appropriate modulator disc.

One drawback to DOPE QPM is that a large number of data points are required to temporally resolve the measured data, which, as we show in Eq. (5.3), contains a carrier frequency ω_c. In the experimental configuration reported here, typical carrier frequencies are on the order of 10-100 kHz. In theory, a sampling rate of $2\omega_c$ must be used to fully resolve the time signal. In practice, however, we have found better performance by setting the sampling rate to $\sim 6\omega_c$-$8\omega_c$. This becomes problematic when high speeds are to be achieved where the carrier frequency can easily reach the MHz regime. On the other hand, such high sampling rates can be advantageous, as $1/f$ noise (pink noise) is significantly lower at these temporal frequencies [147]. We note that it is possible to downmix the carrier frequency with a reference electronic signal so that high sampling rates can be avoided, which will improve the efficiency of the acquisition. Note also that this carrier frequency negates the need to acquire multiple images to extract a complex SSB.

Another drawback to DOPE QPM is that shot noise is multiplexed across all imaging bins, causing the noise floor to vary depending on the light intensity impinging on the detector. Additionally, the dynamic range of the detector is consequently divided between all image bins. However, this problem is not unique to DOPE and is a general problem for all single-pixel imaging techniques.

Finally, we note that the theory for DOPE imaging presented here relies on the assumption of a Dirac-δ spatial filter in the detection plane. This is, of course, not realized in practice. Rather, a slit ranging from 5-20 μm allows sufficient light transmission while serving as a good approximation of a Dirac-δ spatial filter. The details of how the measured time trace transitions from an intensity measurement when the spatial filter is unity to a phase measurement when the spatial filter is an ideal Dirac-δ distribution is outside the scope of this work but will be addressed in future works.

5.7 Conclusion

In this work, we have introduced a new imaging technique that simultaneously captures quantitative phase and fluorescence using single-pixel detection. We have described the theory for DOPE and demonstrated its utility on several samples. We have also described a general theory for single-pixel QPM for any arbitrary set of modulation patterns, provided that the set of patterns spans the space of the object information, and a phase shift can be imparted to isolate the relevant complex terms. This work opens new capabilities in the SWIR and MIR for quantitative phase imaging. This new direction may prove particularly valuable for biomedical imaging since the absorption cross-section of vibrational overtone spectral features in the SWIR region are generally much larger than in the NIR and visible [148]. Since biologically relevant markers such as collagen, water, and lipids appear at distinct wavelength regions, these spectral features could be used for optical medical diagnostic instrumentation. The increased absorption cross section in the SWIR spectral region, combined with the longer wavelength, indicates that the phase shift introduced by these critical biological materials will be larger than in the NIR and

the visible. Moreover, an extension of DOPE imaging to acquire hyperspectral single-pixel images [36] will enable the use of the complex spectral response of a tissue, which is anticipated to improve the differentiation of the concentration of QP chromophores.

Chapter 6

Introduction to Tomography

6.1 Introduction: Three-Dimensional Imaging

Considerable information can be obtained from 2-dimensional (2D) images, which is the standard type of imaging with which nearly everyone is familiar. 2D imaging can be thought of as a projection of 3-dimensional (3D) space onto a 2D surface, that is, one dimension (depth) has been integrated along to form the 2D image. While depth information can be inferred when the size of an object is known a priori or there are clues in a scene that suggests depth. In fact, there are many ways to recover depth information such as engineered PSFs, [141, 110], stereo vision [92], and lidar [69], to name a few. While these techniques give depth information, they fail to recover the true 3D structure of the object. When the true 3D object is to be recovered it is necessary to acquire 2D images from either many directions or many depths and computationally reconstruct an estimate of the true 3D object. In this chapter, I will focus on tomographic reconstructions where images are captured from many different angles to reconstruct the 3D object. While there is a myriad of techniques that are capable of 3D reconstruction, such as confocal, transport of intensity (TIE) methods, and localization methods, I will not devote any space to these techniques as they are not of direct importance to the research that I present in the following chapters. I only mention them here so that the reader is aware of other research pertaining to the topic of 3D imaging.

6.2 Tomography

Tomography classically refers to reconstructing a 3D object from 2D images taken at various angles. However, modern tomography has been broadened to refer to the reconstruction of a higher dimensional space from images taken at lower dimensions using angular diversity to obtain enough information to recover the higher dimensional object. The low-dimensional image

is formed by integrating along one or more dimensions, this operation is known as a projection. The first implementation of tomography was implemented with X-rays illumination where the light that is used experiences minimal diffraction and can be approximated as traveling in a straight line through the specimen to be imaged. In this type of imaging the 2D images are acquired in transmission and are sometimes referred to as a radiogram or a shadowgram because the 2D images are measuring the absorption or density through the specimen. The set of angularly resolved radiograms is called a sinogram which refers to the sinusoidal shape that objects traverse. The sinogram is the starting point for reconstruction algorithms. The goal is to reconstruct the higher-dimensional object from the set of low-dimensional images. There have been many different algorithms developed for reconstructing tomographic data, however, there are two main classes of algorithms: filtered back-projection (FBP) and iterative reconstruction (IR) algorithms, this is not to say that this is an exhaustive classification there are many other algorithms that exist for solving tomographic imaging problems however I will not touch on them. However, the IR methods typically have FBP steps for combining the radiogram data so I will focus on FBP algorithms in the following sections. The FBP algorithm assumes that no diffraction of the illumination light occurs, however, if longer wavelengths are used, such as visible light, then diffraction can no longer be ignored and must be accounted for in the reconstruction. Methods that account for diffraction are known as filtered back-propagation algorithms which refer to using the complex field information to back-propagate the measured field information to properly account for diffraction.

In the following sections, I will give a brief overview of X-ray computed tomography and equivalent methods as well as optical diffraction tomography. I will describe the core ideas for both techniques and the assumptions that are used in the reconstruction. Next, I will lay out how the reconstruction algorithms work. There are many great resources on the subject so I will refer the reader to these texts if further details are required.

6.2.1 X-ray Computed Tomography

X-ray computed tomography (CT) utilizes x-ray illumination, the x-rays penetrate straight through the specimen with minimal diffraction. In addition, the penetration depth is extremely good so that large specimens can be imaged. As the light propagates through the sample the light will be attenuated/absorbed so that the measured transmission signal can be thought of as a line integral of the sample density or a projection of the sample density onto the imaging surface, this is often referred to as a Radon transform [119, 78]. With x-ray tomography, we can consider the object as being sectioned into slices along the y-axis and each slice can be considered independent of the neighboring slices. This assumption allows us to consider the xz-plane at an arbitrary y location y_0 giving $\mathbf{x} = (x, y = y_0, z) \longrightarrow (x, z)$. When the full 3D object is to be reconstructed a stack of xz 2D images can be assembled to recover the full 3D object. Mathematically the projection can be written as,

$$S(x,\phi) = \left\langle I_{\text{ill}}(\mathbf{R}_\phi \mathbf{x}) c(\mathbf{x}) \right\rangle_z, \tag{6.1}$$

where $S(x,\phi)$ is the measured signal or projection at rotation angle ϕ. The full angular set of projections results in a stack of images which is known as a sinogram. I_{ill} is the illumination beam (typically assumed to be a uniform plane wave), $\mathbf{R}_\phi$ is a rotation matrix which operates on the spatial coordinates $\mathbf{x} = (x, z) \longrightarrow \mathbf{R}_\phi \mathbf{x} = (x\cos\phi - z\sin\phi, x\sin\phi + z\cos\phi)$, and $c(\mathbf{x})$ is the object to be imaged. Here, Dirac integral notation is used, $\langle\cdot\rangle_z = \int \cdot\, dz$, which represents a line integral along the z-coordinate. Fig. 6.1(a) illustrates the projection of the sample onto a detector at a rotation angle, ϕ_0. The set of all projections is commonly referred to as a sinogram, fig. 6.1(b). Eqn. 6.1 is commonly referred to as a Radon transform named after Johann Radon who developed the transform in 1917 which is the mathematical operation that generates the sinogram. Notice that most formulations of the Radon transform, eqn. 6.1, do not contain the illumination beam profile, I_{ill}, however, I use it here for several reasons, first, it serves as a convenient way to apply the object rotation; in principle, it does not matter if the object is rotated

and the illumination is stationary or the illumination is rotated and the object is stationary, so I have elected to rotate the illumination. Second, this formulation allows the beam to have structure along the x-direction, although it is typically assumed to be uniform with unity, as I have done here. Finally, this formulation allows for easy comparison to diffraction tomography shown in the next section.

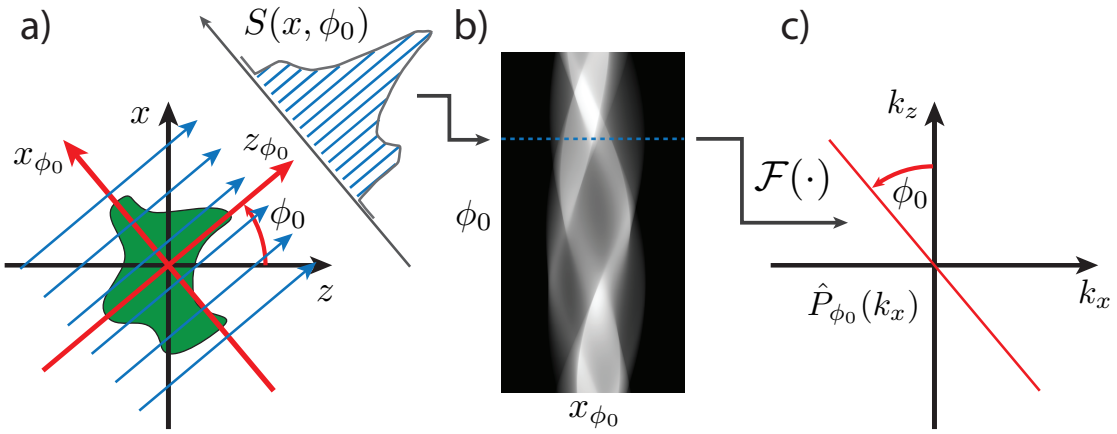

Figure 6.1: (a) shows the absorption profile of an object (green) when x-rays (blue) pass through the material at some angle, ϕ_0. (b) shows the sinogram for the green object in panel (a) where $\phi_0 = [0, 180]$ degrees. (c) illustrates the Fourier slice theorem where the projection $S(x,\phi_0)$ is Fourier transformed and mapped into frequency space corresponding to the measurement angle.

The object, $c(\mathbf{x})$, can be reconstructed from the sinogram with the use of a critical tool known as the Fourier slice theorem [18, 103, 19]. The Fourier slice theorem states that the Fourier transform of a projection $\hat{P}(k_x)$ at an angle, ϕ_0, yields the same spatial frequency information as a straight line at an angle, ϕ_0, through the origin of the Fourier space of the 2D Fourier transform of the object, see fig. 6.1(c). The Fourier slice theorem can be written as,

$$\hat{P}_{\phi_0}(k_x) = \mathscr{F}\{S(\mathbf{x},\phi_0)\} = \left\langle S(\mathbf{x},\phi_0) e^{-ik_x\cdot\mathbf{R}_{\phi_0}\mathbf{x}} \right\rangle_{\mathbf{x}} = C(k_{x\phi},0), \tag{6.2}$$

where $\mathscr{F}$ is the Fourier transform operator, $e^{-ik_x\cdot\mathbf{R}_{\phi_0}\mathbf{x}}$ is the Fourier kernel, and $C(k_{x\phi},0)$ is the Fourier transform of the object $c(\mathbf{x})$ that lies on the line through the origin rotated by an angle ϕ_0. Alternatively, $C(k_{x\phi},0)$ can be interpreted as recovering the spatial frequency information

of the object, $c(\mathbf{x})$, in a rotated Fourier space where only the k_x axis is recovered. The Fourier slice theorem informs a method to reconstruct the original 2D object from the 1D line integral. That is, given that the Fourier information can be recovered from the projections, the object frequency information in the Fourier domain can be recovered by summing all measured angles in the Fourier domain, applying proper weights/filters to the summed frequency information, and finally computing the 2D inverse Fourier transform to reconstruct the object. This set of steps is commonly referred to as filtered back-projection (FBP).

From fig. 6.1 (c) we see that we recover a thin slice of frequency information. It is possible to maintain a Cartesian coordinate system, however, it would be necessary to perform interpolation on some grid to assign the measured frequency information to the correct grid location. This can be a slow and inaccurate process. A better strategy is to convert the Cartesian coordinate system to a polar coordinate system. When this is done the frequency information can readily be mapped to the correct location in frequency space. This comes at the small price of having to apply the Jacobian to the transformation. We will calculate the Jacobian, but first, let's define the coordinate transformation

$$k_x = k_{x\phi}\cos\phi$$

$$k_z = k_{x\phi}\sin\phi.$$

The Jacobian is defined as

$$\det J = \det\left|\frac{\partial(k_x,k_y)}{\partial(k_{x\phi},\phi)}\right| = \det\begin{vmatrix}\frac{\partial k_x}{\partial k_{x\phi}} & \frac{\partial k_x}{\partial \phi}\\ \frac{\partial k_y}{\partial k_{x\phi}} & \frac{\partial k_y}{\partial \phi}\end{vmatrix} = \det\begin{vmatrix}\cos\phi & -k_{x\phi}\sin\phi\\ \sin\phi & k_{x\phi}\cos\phi\end{vmatrix} = k_{x\phi}\cos^2\phi + k_{x\phi}\sin^2\phi = |k_{x\phi}|. \tag{6.3}$$

We see that the magnitude of the coordinate transform is simply a ramp, when applied to the Fourier transform of the projection it behaves as a weighting/filtering of the frequency information, which is where the filter comes from in filtered back-projection. Next, we can define

the object in terms of its Fourier transform

$$c(x,z) = \left\langle \hat{c}(k_x,k_z)\mathrm{e}^{i(k_x x + k_z z)} \right\rangle_{k_x,k_z} \tag{6.4}$$

Plugging in eqn. 6.2 and eqn. 6.3 into eqn. 6.4 and integrating from $\phi = (0,180]$ allows us to write the well-known FBP algorithm as

$$\hat{c}(\mathbf{x}) = \left\langle \left\langle |k_{x,\phi}| \hat{P}_\phi(k_x)\mathrm{e}^{ik_x \cdot \mathbf{R}_\phi \mathbf{x}} \right\rangle_\phi \right\rangle_{k_{x,\phi}}, \tag{6.5}$$

where $\hat{c}(\mathbf{x})$ is an estimate of the true object, $|k_{x,\phi}|$ is a ramp filter calculated as the magnitude of the determinate also known as the Jacobian which arises from the matrix transformation from a cylindrical coordinate system to a Cartesian coordinate system, $\mathrm{e}^{ik_x \cdot \mathbf{R}_\phi \mathbf{x}}$ is the inverse Fourier transform kernel in rotated coordinates. The inner brackets sum the spatial frequency information of the object in Fourier space and the outer brackets along with the inverse Fourier kernel perform the inverse Fourier transform. The quality of the reconstruction is defined in eqn. 6.5 will be heavily dependent on the number of projections used to reconstruct the object. A typical number of projections is greater than 100 angular projections per 180 degrees of rotation. Note, that in CT, it is only necessary to acquire data over 180-degree range, if the full 360 degrees is acquired the second half yields no new information and is completely redundant to the first half of the data.

Up to this point, we have only talked about computed tomography with x-ray illumination, however, it is possible to use CT with longer wavelengths such as optical light. One of the primary methods that use the FBP algorithm with visible light is Optical Projection Tomography (OPT) [29, 91, 30]. OPT takes advantage of the fact that in an imaging system, there is a region about the focal plane that is well approximated by plane waves that can be considered diffraction free and everything in this region is in focus. This region is known as the Rayleigh range. In the Rayleigh range of the focus, the illumination light travels in a straight line in a similar manner to x-ray illumination. Provided that the object is contained within the Rayleigh range,

standard CT algorithms can be used to produce 3D reconstructions of small objects such as zebrafish and developing embryos. If the object lies outside the Rayleigh range blurring of the reconstructed object will occur. This lead to the primary limitation of OPT which is a coupling of the transverse resolution and the size of the object. That is, as the object gets larger, the Rayleigh range needs to increase. In order to increase the Rayleigh range a weaker focus must be used which leads to a decrease in spatial resolution. Algorithms have been developed to help mitigate this problem so that larger objects can be imaged, however, there still exists this fundamental coupling between the object size and spatial resolution.

6.2.2 Optical Diffraction Tomography

Optical Diffraction Tomography (ODT) [82, 127, 93], as the name suggests, takes into account the diffraction experienced by the illumination light used to image the sample. As discussed in section 1.2.3, diffraction is the scattering or spreading of light due to the wave nature of photons. One of the key results of solving Maxwell's equations is the wave equation, in particular, the dispersion relationship of the Helmholtz equation,

$$k_z = \sqrt{k^2 - k_x^2 - k_y^2}. \tag{6.6}$$

The dispersion relationship describes how the spatial frequencies in (x, y, z)-coordinates are related to each other and the wavelength of the illumination light, $k = 2\pi/\lambda$. Eqn. 6.6 describes a spherical shell where the spatial frequencies at a given wavenumber reside in k-space, as described in section 1.2.3. It is the job of ODT to measure the amplitude and phase of the spatial frequency support of the object and stitch together the measured support. Note, this is the same procedure that was taken in CT, however, the object spatial frequency information lay on a straight line whereas in ODT the object spatial frequency lies on a semicircle. This is the key difference between CT and ODT.

Optical diffraction tomography utilizes the first Born scattering approximation and the Fourier diffraction theorem (derived below) to reconstruct an object illuminated by visible light.

The light will experience diffraction as it travels through the specimen, the specimen is assumed to be a phase object, weakly scattering and weakly absorbing. The scattered field will be detected via holographic detection, interference of a plane wave at the detector plane, eqn. 4.9, so that the complex field information can be recovered. Holographic detection is necessary so that the back-propagation in the diffraction tomographic reconstruction can be carried out, as we will see below. There are many excellent resources that cover ODT with detailed derivations, I will refer the reader to these resources [78, 32, 56].

Following Goodman's derivation of the time-independent Helmholtz equation, we start with Maxwell's equations, [56]. The four Maxwell equations are

$$\nabla \times \mathbf{E} = -\mu \frac{\mathrm{d}\mathbf{H}}{\mathrm{d}t} \tag{6.7}$$

$$\nabla \times \mathbf{H} = \epsilon \frac{\mathrm{d}\mathbf{E}}{\mathrm{d}t} \tag{6.8}$$

$$\nabla \cdot \mathbf{E} = 0 \tag{6.9}$$

$$\nabla \cdot \mathbf{H} = 0 \tag{6.10}$$

We see that the electric field, **E**, is coupled with the magnetic field, **H**, in the first and second Maxwell's equations, eqn. 6.7 and 6.8, respectively. We will assume the medium of interest is a dielectric, nonmagnetic, linear, and isotropic in the region of propagation, the goal is to manipulate the above equations so that we can decouple the two fields. This is done by first taking the curl of 6.7 giving

$$\nabla \times \nabla \times \mathbf{E}(\mathbf{x}, t) = -\mu \frac{\mathrm{d}}{\mathrm{d}t} \nabla \times \mathbf{H}(\mathbf{x}, t). \tag{6.11}$$

Substituting the second equation, eqn. 6.8, into the above equation, we can get rid of the magnetic field giving

$$\nabla \times \nabla \times \mathbf{E}(\mathbf{x}, t) = -\mu \frac{\mathrm{d}}{\mathrm{d}t} \left(\epsilon \frac{\mathrm{d}\mathbf{E}(\mathbf{x}, t)}{\mathrm{d}t} \right) = -\mu\epsilon \frac{\mathrm{d}^2}{\mathrm{d}t^2} \mathbf{E}(\mathbf{x}, t). \tag{6.12}$$

Using the vector identity $\nabla \times \nabla \times \mathbf{A} = \nabla(\nabla \cdot \mathbf{A}) - \nabla^2 \mathbf{A}$, we can rewrite our above equation as

$$\nabla(\nabla \cdot \mathbf{E}(\mathbf{x}, t)) - \nabla^2 \mathbf{E}(\mathbf{x}, t) = -\mu\epsilon \frac{\mathrm{d}^2}{\mathrm{d}t^2} \mathbf{E}(\mathbf{x}, t). \tag{6.13}$$

From Maxwell's third equation, eqn. 6.9, we see that the first term on the left-hand side is equal to zero gives

$$\nabla^2 \mathbf{E}(\mathbf{x}, t) = \mu\epsilon \frac{\mathrm{d}^2}{\mathrm{d}t^2} \mathbf{E}(\mathbf{x}, t). \tag{6.14}$$

It is common to use the identity for the speed of light in a medium, $c_m = (\mu\epsilon)^{-1/2}$, to rewrite eqn. 6.14 giving,

$$\nabla^2 \mathbf{E}(\mathbf{x}, t) - \frac{1}{c_m^2} \frac{\mathrm{d}^2}{\mathrm{d}t^2} \mathbf{E}(\mathbf{x}, t) = 0. \tag{6.15}$$

Using the assumption of a nonmagnetic material we know, $\mu = \mu_0$, and the definition of the refractive index, $n = (\epsilon/\epsilon_0)^{1/2}$ we can write the well known vector wave equation

$$\nabla^2 \mathbf{E}(\mathbf{x}, t) - \frac{n^2}{c^2} \frac{\mathrm{d}^2}{\mathrm{d}t^2} \mathbf{E}(\mathbf{x}, t) = 0. \tag{6.16}$$

Not surprisingly if we repeat this derivation where we instead isolate the magnetic field we arrive at a similar result as the electric field,

$$\nabla^2 \mathbf{H}(\mathbf{x}, t) - \frac{n^2}{c^2} \frac{\mathrm{d}^2}{\mathrm{d}t^2} \mathbf{H}(\mathbf{x}, t) = 0. \tag{6.17}$$

So now we have wave equations for both the electric and magnetic fields no longer coupled with the other field, respectively. If we can consider one component of the electric field we can write a scalar wave equation

$$\nabla^2 E_x(\mathbf{x}, t) - \frac{n^2}{c^2} \frac{\mathrm{d}^2}{\mathrm{d}t^2} E_x(\mathbf{x}, t) = 0. \tag{6.18}$$

We note that we could write any component of the electric field or magnetic field and it acts independent of the other components so we can write the scalar wave equation without explicitly

writing which component is being considered giving

$$\boldsymbol{\nabla}^2 u(\mathbf{x}, t) - \frac{n^2}{c^2}\frac{\mathrm{d}^2}{\mathrm{d}t^2} u((\mathbf{x}, t) = 0. \tag{6.19}$$

Again this is valid for dielectric, nonmagnetic, linear, and isotropic media. Let's write the complex electric field as $u(x,t) = A(x)\exp\{i(2\pi\nu t + \phi(x)\}$, where $A(x)$ of the field amplitude, ν it the optical frequency, and $\phi(x)$ is the phase. Substituting the electric field into eqn. 6.19 gives,

$$\boldsymbol{\nabla}^2 A(x)\exp\{i(2\pi\nu t + \phi(x)\} - \frac{1}{c^2}\frac{\mathrm{d}^2}{\mathrm{d}t^2} A(x)\exp\{i(2\pi\nu t + \phi(x)\} = 0. \tag{6.20}$$

Taking the time derivative gives

$$\boldsymbol{\nabla}^2 A(x)\exp\{i(2\pi\nu t + \phi(x)\} + \frac{4\pi^2\nu^2 n^2}{c^2} A(x)\exp\{i(2\pi\nu t + \phi(x)\} = 0. \tag{6.21}$$

Using the definition of wavenumber, $k = 2\pi n\nu/c$, and since we are not interested in how the field, $u(\mathbf{x}, t)$, evolves in time we can separate the two variables allowing us to write the well-known time-independent homogeneous Helmholtz equation,

$$(\boldsymbol{\nabla}^2 + k^2)\, u(\mathbf{x}) = 0. \tag{6.22}$$

This equation is valid for homogeneous media, however, when light propagates through inhomogenous media (the refractive index varies in space), i.e.

$$\left[\boldsymbol{\nabla}^2 + k^2(\mathbf{x})\right] u(\mathbf{x}) = 0, \tag{6.23}$$

then our scalar Helmholtz equation becomes an approximation that experiences an error. This is the result of the coupling of the vector components of the wave at the boundaries of the refractive index change, [56]. However, it is known to be a good approximation when the size of the refractive index change is larger than the wavelength of the wave.

The scalar homogeneous Helmholtz equation, eqn. 6.22, can be rewritten in the form which is commonly referred to as the inhomeogeous Helmholtz equation. This is done by adding zero to the left-hand side and performing some simple algebra as shown below. Starting with the homogeneous equation, let $k(\mathbf{x})$ be the local wavenumber due to local changes of refractive index from the presence of a sample. Making these changes and adding zero to eqn. 6.22 we get

$$\left[\nabla^2 + k^2(\mathbf{x})\right] u(\mathbf{x}) + k_m^2 u(\mathbf{x}) - k_m^2 u(\mathbf{x}) = 0, \tag{6.24}$$

where $k_m = 2\pi n_m/\lambda$ be the wavenumber of the immersion media and n_m is the refractive index of the immersion media. Rewriting the above equation and moving several terms to the right-hand side gives,

$$(\nabla^2 + k_m^2) u(\mathbf{x}) = [k_m^2 - k^2(\mathbf{x})] u(\mathbf{x}) \tag{6.25}$$

$$(\nabla^2 + k_m^2) u(\mathbf{x}) = -k_m^2 [k^2(\mathbf{x})/k_m^2 - 1] u(\mathbf{x}) \tag{6.26}$$

where $k(\mathbf{x}) = 2\phi n(\mathbf{x})/\lambda$ is the local wavenumber and $n(\mathbf{x})$ is the local refractive index of the object. Plugging in the definitions of the wavenumbers, into the above equation, gives

$$(\nabla^2 + k_m^2) u(\mathbf{x}) = -k_m^2 [n^2(\mathbf{x})/n_m^2 - 1] u(\mathbf{x}). \tag{6.27}$$

It is common to define $c(\mathbf{x}) = k_m^2 [n^2(\mathbf{x})/n_m^2 - 1]$ as the scattering potential, yielding the scalar inhomogenous Helmholz equation

$$(\nabla^2 + k_m^2) u(\mathbf{x}) = -c(\mathbf{x}) u(\mathbf{x}). \tag{6.28}$$

ODT starts by solving the inhomogeneous Helmholtz equation,$(\nabla^2 + k_m^2) u(\mathbf{x}) = -c(\mathbf{x}) u(\mathbf{x})$, where $k_m = 2\pi n_m/\lambda$ is the wavenumber in the immersion medium, n_m is the refractive index of the immersion medium, $c(\mathbf{x})$ is the sample to be imaged or the scattering potential, and $u(\mathbf{x})$ is the complex electric field. Note, the homogeneous Helmholtz equation is $(\nabla^2 + k_m^2) u(\mathbf{x}) = 0$,

which we will utilize below. There is no known analytical solution to the inhomogeneous Helmholtz equation. The reason for this is that the electric field depends on both the input field and scattered field, $u(\mathbf{x}) = u_0(\mathbf{x}) + u_s(\mathbf{x})$, however, the scattered field also depends on the scattered field from secondary scattering which leads to a recursive solution to the wave equation. For this reason, it is common to utilize an approximation known as the first Born approximation.

In order to derive the Born approximation, we start by plugging in the decomposed electric field into the inhomogeneous wave equation gives,

$$(\boldsymbol{\nabla}^2 + k_m^2)\big(u_0(\mathbf{x}) + u_s(\mathbf{x})\big) = -c(\mathbf{x})\big(u_0(\mathbf{x}) + u_s(\mathbf{x})\big).$$

We recognize the first term on the left-hand side as the homogeneous Helmholtz equation which is equal to zero, therefore, it will disappear. Rewriting the above equation gives,

$$(\boldsymbol{\nabla}^2 + k_m^2)\, u_s(\mathbf{x}) = -c(\mathbf{x})\, u(\mathbf{x}). \tag{6.29}$$

Now we clearly see that the scattered wave will depend on the object and the total electric field. To find a solution to this equation we can plug in a Green's function with a delta source

$$(\boldsymbol{\nabla}^2 + k_m^2) G(\mathbf{x}) = \delta(\mathbf{x}).$$

This equation says that there is some function $G(\mathbf{x})$ that will give an impulse response to a point object. Once we have that solution we can use the principle of linear superposition for a general object. Solving this equation yields the well-known solution for a spherical wave, $G(\mathbf{x}) = -\mathrm{e}^{i2\pi k\mathbf{x}}/4\pi\mathbf{x}$. Using the Greens function we can write the scattered field as

$$u_s(\mathbf{x}) = -\left\langle G(\mathbf{x}-\mathbf{x}')\, c(\mathbf{x})\, u(\mathbf{x}')\right\rangle_{\mathbf{x}'}. \tag{6.30}$$

What this solution says is that the scattered field, $u_s(\mathbf{x})$, is a convolution of the Green's function (impulse response) with the object and the total field. Therefore, the scattered field can be calculated as an iterative equation. That is the first iteration the total field is simply the input illumination, and the second iteration is the sum of the initial field with the previously calculated scattered field, then repeated until the desired accuracy has been achieved. The first iteration can be written as,

$$u(\mathbf{x}) = u_0(\mathbf{x}) + \left\langle G(\mathbf{x}-\mathbf{x}')c(\mathbf{x})u(\mathbf{x}')\right\rangle_{\mathbf{x}'}.$$

To arrive at the Born approximation we truncate the series at the first order. This means that we replace the total field in the second term on the right-hand side with the initial field, yielding the desired result,

$$u(\mathbf{x}) = u_0(\mathbf{x}) + \left\langle G(\mathbf{x}-\mathbf{x}')c(\mathbf{x})u_0(\mathbf{x}')\right\rangle_{\mathbf{x}'}.$$

The first Born approximation simply states that only single scattering will be taken into account and scattering does not perturb the input illumination (weak scattering) as the input illumination propagates through the scattering potential. By inspection of the above equation, we can conclude the approximate scattered field is

$$u_B(\mathbf{x}) = \left\langle G(\mathbf{x}-\mathbf{x}')c(\mathbf{x})u_0(\mathbf{x}')\right\rangle_{\mathbf{x}'} \tag{6.31}$$

where $u_0(\mathbf{x}) = a_0\exp(i\mathbf{k}_0\mathbf{x})$ is the input plane wave and the Greens function is a spherical wave translated to position $\mathbf{x}'$. An alternative form of the Green's function can be written as

$$G(\mathbf{x}-\mathbf{x}') = \frac{i}{4\pi}\left\langle \frac{1}{k_z}\exp\left(i\mathbf{k}|\mathbf{x}-\mathbf{x}'|\right)\right\rangle_{k_x}. \tag{6.32}$$

Plugging in the input illumination field, the Green's function into eqn. 6.31, and utilizing the definition of the Fourier transform of the object as well as placing the object in a rotated frame yields measured field

$$u_B(\mathbf{R}_\phi x) = \frac{i a_0}{4\pi}\left\langle \frac{2\pi}{k_z}\hat{C}(\Delta\mathbf{k})\exp\left(i\mathbf{k}\cdot\mathbf{R}_\phi\mathbf{x}\right)\right\rangle_{k_x} \tag{6.33}$$

where $R_\phi \mathbf{x} = (x\cos\phi - z\sin\phi, x\sin\phi + z\cos\phi) \longrightarrow (x_\phi, z_\phi)$ is the rotated coordinate system and $\hat{C}(k) = 1/2\pi \int c(\mathbf{x}) \exp(-ik\mathbf{x}) d\mathbf{x}$ is the Fourier transform of the scattering potential. Taking the Fourier transform of eqn. 6.33 along $R_\phi \mathbf{x}$ along with some mathematical manipulations results in the Fourier diffraction theorem,

$$\hat{U}_{B,\phi_0}(k_x) = \frac{i a_0}{k_z} \sqrt{\frac{\pi}{2}} \hat{C}(\Delta\mathbf{k}) \exp\left(i k_z z_\phi\right). \tag{6.34}$$

The Fourier diffraction theorem is the x-ray analog to the Fourier slice theorem. The Fourier diffraction theorem is nearly identical to the Fourier slice theorem except for the complex scalar out front and the spatial frequency information lies on an arc, $\exp\left(i k_z z_\phi\right)$, defined by a semicircle from the Ewald sphere, where $k_z = \sqrt{k^2 - k_x^2}$, again coming from the dispersion relationship from the Helmholtz equation.

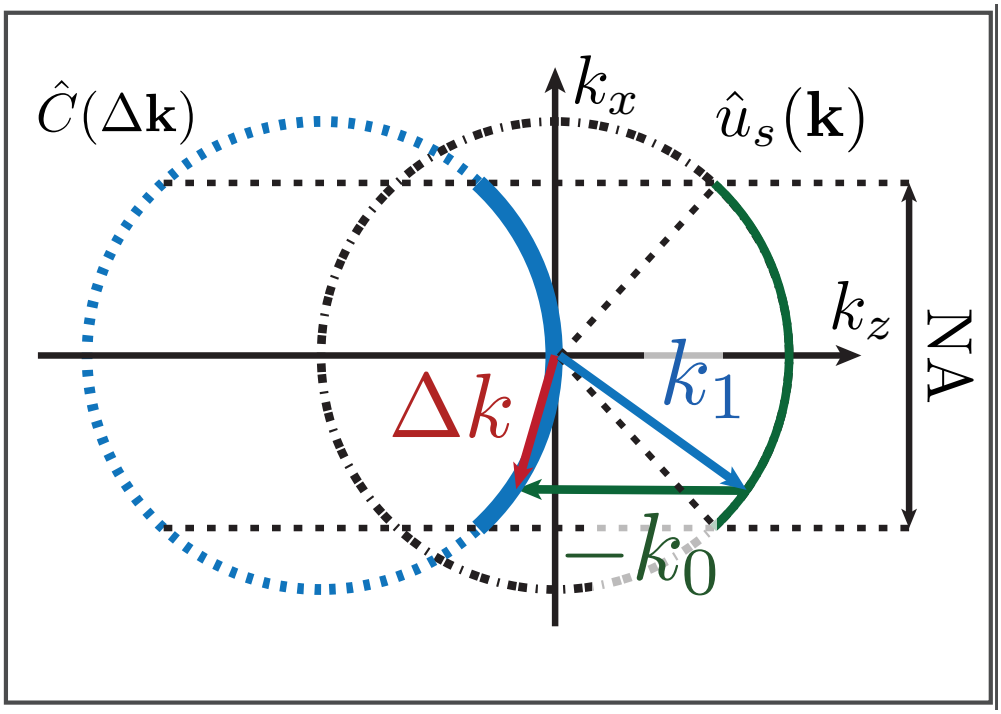

Figure 6.2: Frequency support of the scattered field and object information. The black dotted circle shows the scattered frequency information. The blue dotted circle shows the measured object's spatial frequency information. The solid arcs represent the collected or observable spatial frequency in the forward direction for a given optical system with some numerical aperture (NA). The blue arrow represents the scattered spatial frequency, the green arrow represents the illumination spatial frequency, and the red arrow represents the measured difference spatial frequency, figure adapted from [135]

Rearranging eqn. 6.34 to solve for the frequency representation of the scattering potential gives some insight into the measured object spatial frequency information, rearranging gives,

$$\hat{C}(\Delta\mathbf{k}) = \frac{k_z}{i a_0}\sqrt{\frac{2}{\pi}}\hat{U}_{B,\phi_0}(k_x)\exp\left(-i k_z z_\phi\right). \tag{6.35}$$

We see that the scattered field, $\hat{U}_{B,\phi_0}$, lies on a circular arc centered at the origin, fig. 6.2 illustrates this with the black dotted circle and the green arc represents the collected spatial frequency content. The second observation is that the object's spatial frequency lies on a circular arc as well, however, it is shifted to the left by, $-k_0$, illustrated in fig. 6.2 by the dotted blue circle and the solid blue arc represents the measured spatial frequency information.

Eqn. 6.34, [151], is used to develop a method for reconstructing the object from the ODT projections. It is done by summing the complex spatial frequency information, information on an arc, we will be able to recover the full object from the set of projections in an analogous way to what was done for CT. Fig. 6.3(a) shows how the sum of spatial frequency information in the frequency domain for CT, note that each colored line represents the spatial frequency information obtained from one projection at an angle, ϕ_0, which lies on a straight line through the origin. Fig. 6.3(b) shows the sum of spatial frequency information for ODT, note that each colored line represents the spatial frequency information from the same projection angle as in CT but this time the information lies on a semicircle. Additionally, it can be seen that there is a resolution enhancement from ODT compared to CT, in fig. 6.3 (a) and (b) both have the same numerical aperture, NA of 1, however, (b) covers a larger area thereby having a higher cutoff spatial frequency. In fact, the cutoff frequency of ODT is $\sqrt{2}$ times larger than that of CT at an NA = 1.

The object, from a set of angular projections eqn. 6.34, can be reconstructed using the filtered backpropagation (FBP) algorithm. In an analogous manner to the filtered back-projection algorithm used in CT, ODT reconstructs the object by summing together the frequency space with an appropriate filter. The key difference here is that diffraction must be accounted for which causes the measured frequency information to lie on an arc instead of a straight line.

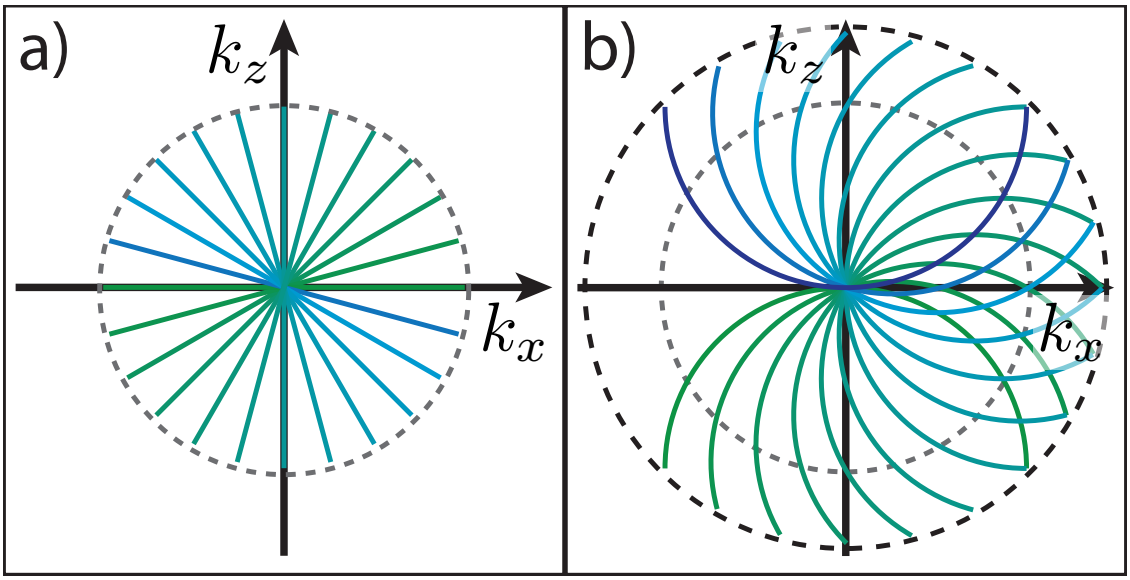

Figure 6.3: Computed Tomography and Optical Diffraction Tomography comparison of measured frequency space data for $\phi_0 = [0, 180]$ degrees. (a) illustrates the sampled spatial frequency information of computed tomography (CT), where the information lies on a straight line. (b) illustrates the sampled spatial frequency information of optical diffraction tomography (ODT), where the information lies on semicircles due to diffraction. The gray dotted circles represent the spatial frequency cutoff for an imaging system with some numerical aperture. Note that (b) has $\sqrt{2}$ larger frequency support when the NA approaches 1 indicated by the black dotted circle. Figure adapted from [101]

The FBP algorithm can be written as

$$\hat{c}(\mathbf{x}) = -\sqrt{\frac{2}{\pi}} \frac{i}{a_0 (2\pi)^{3/2}} \left\langle |k_x| \, \hat{U}_{B,\phi}(k_x) \exp\left(-i k_z z_\phi\right) \exp\left(i \Delta \mathbf{k} \mathbf{R}_\phi \mathbf{x}\right) \right\rangle_{k_x,\phi}. \tag{6.36}$$

Due to the use of Dirac integral notation, the limits to the integral are suppressed, however, it is critical to note that the integral over dϕ range from $(-\pi, \pi]$. These limits differ from that of CT since they are not symmetric about the origin (fig. 6.3(b)), therefore, to fill out the frequency space uniformly a full 360-degree rotation is necessary. The factor $|k_x|$ serves as the filter which due to the Jacobian for the transformation from cylindrical to Cartesian coordinate system, the exponent $\exp\left(-i k_z z_\phi\right)$ causes the frequency information to reside on an arc.

Optical diffraction tomography allows 3D reconstruction of phase objects. It requires coherent illumination so that a stable phase can be extracted from the intensity measurement from holographic imaging at each angle, ϕ_0. ODT does have some drawbacks, in the derivation the

first Born approximation was used which turns out to be fairly restrictive on the properties of the object, because of this the recovered object tends to have artifacts, [93, 58, 102]. This can be mitigated by using the Rytov approximation allowing for a larger range of objects to be imaged with few artifacts. Fortunately, the transformation from the Born approximation to the Rytov approximation is fairly simple allowing the above derivation for FBP to still be valid. In order to use the Rytov approximation, the complex field in the algorithm above need only substitute for $u_R(\mathbf{x}) = u_0(\mathbf{x})[exp(u_B(\mathbf{x})/u_0(\mathbf{x}) + 1]$ [102]. With the Rytov approximation much larger objects have been successfully reconstructed fewer aberrations compared to reconstruction done with the Born approximation.

ODT, while a very useful technique, has one primary limitation which is that it can only work with coherent illumination where the phase can be recovered. Because of this limitation, ODT has not been able to be utilized on incoherent emission. In chapter 8.2.5, I discuss a new technique that allows ODT to be extended to incoherent emission such as fluorescence, aptly named Fluorescent Diffraction Tomography (FDT). This technique is built off of CHIRPT, discussed in section 5.2.1. We will see that FDT does not rely on any assumptions of the object so the sample may be highly scattering and still reconstruct the object well.

Chapter 7

Fourier Computed Tomography

7.1 Summary

This chapter introduces a new form of tomographic imaging that is particularly advantageous for a new class of super-resolution optical imaging methods. This method of Fourier computed tomography (FCT) operates in a conjugate domain to conventional computed tomography techniques. FCT is the first optical tomography method that records complex projections of the object's spatial frequency distribution. From these spatial frequency projections, the Spatial Slice Theorem is derived which is used to build a tomographic imaging reconstruction algorithm. The ability to enhance the spatial frequency support along a single spatial direction to be isotropic in the entire transverse spatial frequency domain is demonstrated with FCT. This fluorescent optical tomography technique opens a path for three-dimensional super-resolution imaging with fluorescent light emission using spatial frequency projection methods.

7.2 Introduction

Optical microscopy is an indispensable tool in many fields of science. A major advantage is that visible light is gentle on biological specimens and, in combination with fluorescent labeling, gives high-contrast images with excellent specificity. The information recorded in an imaging system is limited by constraints of optical wavelength, propagation, and detection geometry. These constraints combine to limit the recorded information to a subset of the total information potentially available to fully describe the object. More-complete object information can be obtained from a sequence of measurements designed to add diversity and record information from a set of measurements that more closely represent the true object. Imaging systems that expand the recorded information through a sequence of measurements are known as tomographic imaging methods. These methods measure a set of projections in a low-spatial

dimension to recover objects in a higher-spatial dimension. The classic method of computed tomography (CT) uses x-ray illumination to measure the object's integrated absorption along the x-ray beam propagation direction. High-quality spatial maps of x-ray absorption or object density can be reconstructed from a set of projections measured at distinct angles [32, 78].

Tomography has been extended to visible light by taking into account photo-physics such as optical diffraction [32, 125]. Each tomographic image reconstruction strategy exploits an understanding of the underlying physics, from which an image projection model is constructed. A wide variety of tomographic imaging methods have emerged that provide detailed object information from a range of measurements, such as backscattered light gated by low-coherence interferometry for optical coherence tomography (OCT) [68, 127], diffraction tomographic microscopy [58], the diffuse propagation of light in tissues [118, 93], phase nanoscopy [156], fluorescent optical projection tomography [29, 30], white light diffraction tomography [81], limited angle quantitative phase tomography [24], and forward scattered light [122].

Many of these optical tomographic imaging systems, use a camera-based optical microscope to form images, while the object is rotated or translated along the optic axis or the illumination angle is swept. While modern cameras are well developed and provide exceptional imaging quality and speed, in applications where the sample exhibits optical scattering, the illumination light, and recorded images are significantly distorted [65]. Single-pixel imaging methods, such as confocal microscopy, multiphoton, and OCT are able to perform robust imaging in scattering media; however, all of these methods record one spatial point at a time, and sequential image acquisition significantly slows image acquisition rates. To address this limitation, we have developed several single-pixel optical tomographic imaging techniques based on mapping spatial position to distinct temporal modulation frequencies of illumination light [125, 45, 136, 49]. These techniques fall into a class of imaging methods called Spatial Frequency Projection (SFP) imaging, where images are formed by a series of spatial frequency projections enabled by periodically modulated illumination light. SFP gives a unique mapping of temporal modulation frequency to points in space by linearly sweeping through all spatial fre-

quencies supported by the imaging system. The idea of spatial frequency projections can be extended to super-resolution by driving nonlinear optical interactions in the sample, which we have demonstrated with Multi-Photon SPatIal Frequency Projection Imaging (MP-SPIFI) [46]. MP-SPIFI uses an intense ultrafast laser pulse brought to a line focus that drives a nonlinear optical response in the sample to generate spatial frequency harmonics. The spatial frequency harmonics driven by the nonlinear response produce signals that obtain information from spatial frequencies outside of the diffraction-limited spatial frequency imaging bandwidth, thus allowing super-resolution imaging. MP-SPIFI is the only general super-resolution technique that is able to provide super-resolution images for both coherent and incoherent imaging modalities. Although high-quality images are produced with this approach, to date, the improvements in imaging resolution are limited to the modulated spatial direction (e.g., x). In principle, the full spatial resolution of the SFP imaging process can be extended to the 2D lateral plane (x, y) by using a previously reported method of lateral tomographic (LT) imaging [125], this approach is not practical for MP-SPIFI because LT requires spatial expansion of the illumination beam, reducing the peak illumination intensity and thereby shutting down the nonlinear optical process.

In this work, we introduce a new 2-dimensional tomographic imaging technique that enables nearly isotropic lateral resolution. This new Fourier Computed Tomography (FCT) technique, is based on collecting *spatial frequency projections* of the object in the x-y plane when the illumination beam is brought to a tight line focus. The method is a conjugate domain analog to computed and lateral tomography techniques. In CT and LT, line integrals along a coordinate (z_ϕ or y_ϕ, respectively) are formed in the spatial domain. In the spatial frequency domain, these projections are localized to a point and the sequence of projections form a line at the same rotation angle, ϕ; see conceptual diagram Fig. 7.1(a). The formal mathematical description of these projections lead to the Fourier Slice Theorem [78]. However, in FCT, the projection operates in the conjugate domain to CT/LT by acquiring line images with SFP illumination in the spatial domain. The tightly focused line in space is equivalent to recording a line projection in

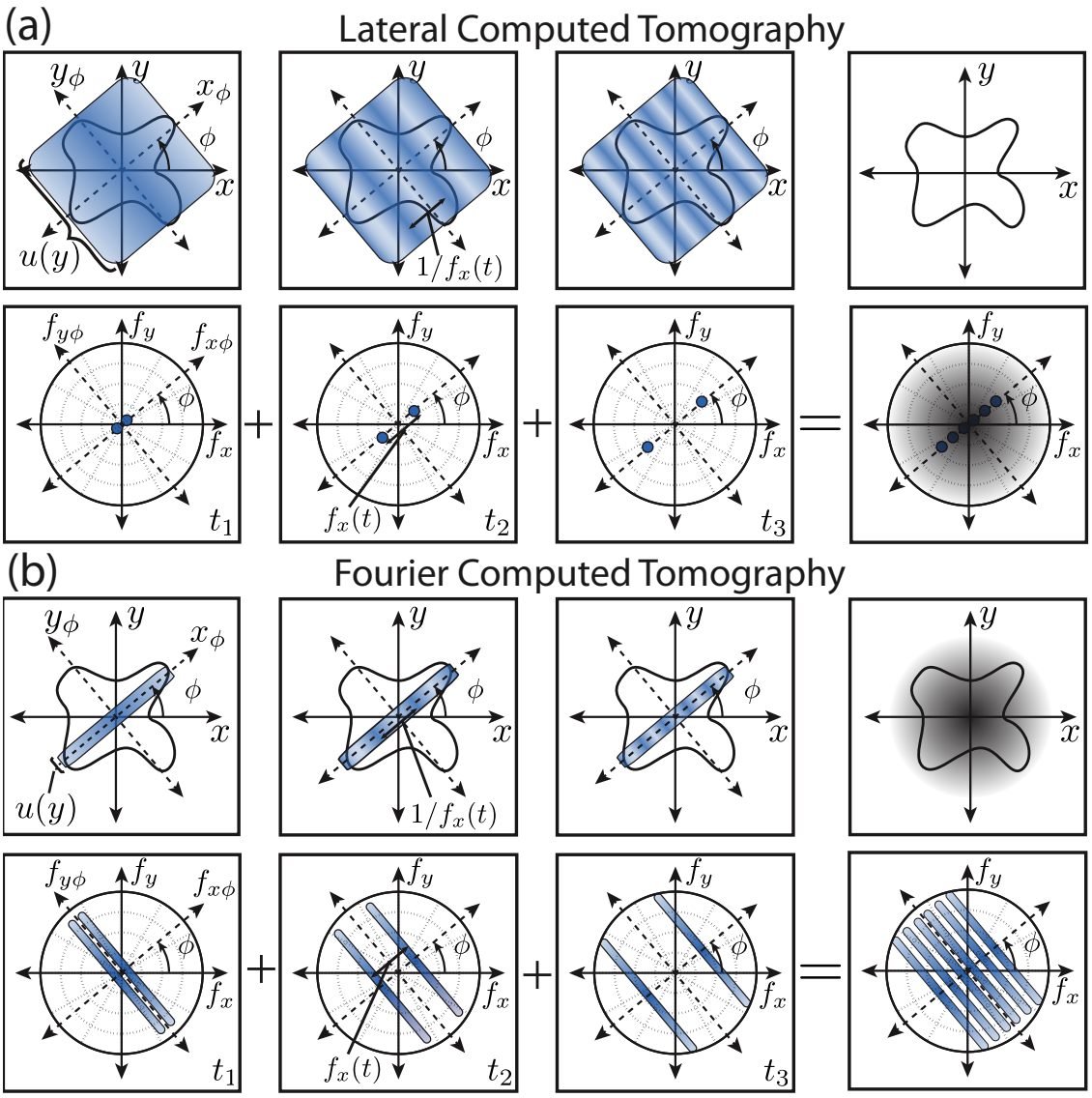

Figure 7.1: Panel (a) shows the data flow for lateral computed tomography (CT). The top three figures show a series of snapshots in time of the illumination beam and the object at an illumination angle ϕ. At each point in time a unique spatial frequency, $f_x(t) = \kappa t$, is projected onto the sample. The detection photodiode performs a 2D spatial integration and acts like a Fourier transform, sensing the object in the spatial frequency domain. The bottom figures show the spatial frequencies probed as a function of time. The projections are summed together and weighted with a radial filter. Rotating the illumination beam 180 degrees maps out the full frequency support of the microscope. An inverse Fourier transform yields a reconstruction of the 2D object. Panel (b) shows the conjugate analog of Lateral CT called Fourier CT. The top three figures show a series of snapshots in time of the illumination and object at an angle ϕ. The bottom three figures show the corresponding spatial frequency support probed as a function of time. The frequency support is summed together (bottom right). An inverse Fourier transform is taken and a radial spatial filter is applied to yield a reconstruction of the object. Figure from [137].

the spatial frequency domain for each instantaneous spatial frequency projection, $f_x(t)$, of the illumination pattern, Fig. 7.1(b). In FCT, we find an analogous Spatial Slice Theorem that motivates the development of a spatial frequency-filtered back-projection reconstruction algorithm to produce 2D images from measured FCT sinograms.

7.3 Theory

The single pixel tomographic imaging process uses an illumination light pattern that imparts a distinct temporal modulation frequency to each spatial position along a line of illumination, $I_i(x,y,t) = u(y)[1+\cos(\omega_c t + 2\pi\kappa x t)]^2$. Here, we have suppressed unimportant scaling coefficients and $u(y)$ is the intensity profile along the y coordinate. Spatio-temporal modulation parameters are set by the carrier frequency, ω_c, and the modulation chirp parameter, κ, that relates the modulation frequency of the illumination light to x position as $\omega_m(x) = \omega_c + 2\pi\kappa x$. Light collected from the sample is detected on a photodiode or photomultiplier tube (PMT) and the acquired temporal signal can be written as a spatial projection of the illumination intensity onto the object, $S_t = \left\langle I_i(x,y,t)c(x,y)\right\rangle_{x,y}$. Here the Dirac integral notation, $\langle\cdot\rangle_{\bar{v}} = \int d\bar{v}$ denotes the spatial integral performed by a single pixel detector that sums the local photocurrent from light intensity impinging across the detector surface. The object, $c(x,y)$, is assumed to be thin, however, the theory developed below can be extended to optically thick objects.

The object information is collected on the Fourier basis and can be easily isolated in a sideband centered at the carrier frequency, ω_c, with a simple discrete Fourier transform applied to the collected signal. In order to develop the theory below, it is convenient to work with the demodulated single sideband [46], $\tilde{S}_t^{(q)} = \left\langle u(y)c(x,y)e^{-i2\pi q\kappa t x}\right\rangle_{x,y}$, where $q = [1,2,...]$ describes the imaging order, $f_x(t) = \kappa t$ is the projected spatial frequency at a time, t, and $e^{-i2\pi q\kappa t x}$ is the complex modulation; see conceptual diagram Fig. 7.1. Note that q scales the effective coherent spatial frequency pass band of the imaging process allowing for lateral resolution enhancement [136, 46]. To observe information corresponding to $q > 2$, intense illumination light can be used to drive nonlinear processes, such that the illumination pattern with respect to the sam-

ple becomes distorted. The distorted illumination can be described as an effective illumination light pattern, $I_{\text{eff}} = F[I_i]$, where $F[\cdot]$ is some nonlinear function that models a physical process, such as 2-photon, coherent nonlinear scattering, or saturated absorption. The effective illumination contains modulation frequency harmonics of the temporal modulation, $\omega_m(t)$. The modulation harmonics encode higher spatial frequency projections allowing for resolution enhancement along the modulated dimension. We have applied this technique to simultaneously acquire super-resolution images of 2-photon absorption and second harmonic generation, i.e., $I_{\text{eff}} = I_i^2$, which can produce spatial frequency harmonics up to 4× the diffraction limit [46].

Since resolution enhancement is restricted to one spatial dimension - along the modulated spatial direction - we developed a new imaging tomography to homogenize the resolution enhancement across the lateral plane. By rotating the illumination, or equivalently the object, the acquired signal can be expressed in a rotated frame as $\tilde{S}^{(q)}_{t,\phi} = \left\langle u(y_\phi) c_\phi(x_\phi, y_\phi) e^{-i2\pi q\kappa t x_\phi} \right\rangle_{x_\phi, y_\phi}$, where $x_\phi = \cos\phi\ x + \sin\phi\ y$ and $y_\phi = -\sin\phi\ x + \cos\phi\ y$. The function $u(y_\phi)$ determines the behavior of the projection, i.e. LT or FCT.

Lateral tomography is represented by uniform illumination along y (the direction perpendicular to the modulation direction, x) where we consider the case $u(y_\phi) \to 1$. With this illumination pattern, we duplicate the formalism described in [125]. Inserting the spatial frequency Fourier expansion of the object, $c_\phi(x_\phi, y_\phi) = \left\langle \hat{C}_\phi(f_{x_\phi}, f_{y_\phi}) e^{-i2\pi(f_{x_\phi} x_\phi + f_{y_\phi} y_\phi)} \right\rangle_{f_{x_\phi}, f_{y_\phi}}$, and the rotated frame, $\hat{C}(x, y) \to \hat{C}_\phi(x_\phi, y_\phi)$, into the single sideband projection, we readily yield the Fourier Slice Theorem, Eq. (7.1),

$$\tilde{S}^{(q)}_{t,\phi}(f_{x_\phi}, f_{y_\phi}) = \left\langle \hat{C}_\phi(q f_{x_\phi}, f_{y_\phi}) \delta(f_{y_\phi}) \right\rangle_{f_{y_\phi}} = \hat{C}_\phi\left(q f_{x_\phi}, 0\right) \tag{7.1}$$

after a few algebraic manipulations. This equation describes a projection of the object's spatial frequency distribution along the rotated coordinate system, f_{x_ϕ}, where the spatial frequency points are sampled as a spatial frequency-angle pair, as represented in Fig. 7.1(a). Equation (7.1) can also be written in the temporal frequency domain, $\tilde{S}^{(q)}_{\nu,\phi} = \left\langle c_\phi(\frac{\nu}{q\kappa}, y_\phi) \right\rangle_{y_\phi}$, where it is clear that the LT is performing a spatial integral along y_ϕ as shown in the top row in Fig. 7.1(a).

Figure 7.1(a) illustrates the concept of LT data acquisition where a modulated light illumination pattern is used for the projection operator. The top row shows the spatial projection with an intensity modulation pattern at a particular time instance t and a spatial period given by $f_x^{-1}(t)$, while the bottom row shows the resulting spatial frequency support that is probed with time. In the back-projection algorithm, the spatial frequency support is summed together and a radial spatial frequency filter is applied, which is represented by the shaded gray radial ramp in the last column in the second row. The object is recovered with an inverse Fourier transform, the last column in the first row in Fig. 7.1(a). Note, the formalism for CT can be recovered by substituting $y \rightarrow z$ and allowing $q = 1$.

Fourier Computed Tomography (FCT), by contrast, uses a line focus so that nonlinear optical processes can be driven efficiently by the illumination light. The line focus spatial distribution in y_ϕ is modeled, in the limiting case, as a Dirac-δ function, i.e. $u(y_\phi) \rightarrow \delta(y_\phi)$. It is convenient to represent the time signal in the temporal frequency domain by taking the Fourier transform of the signal with respect to time, $\tilde{S}^{(q)}_{\nu,\phi} = \left\langle u(y_\phi) c_\phi(x_\phi, y_\phi) \delta(\nu - q\kappa x_\phi) \right\rangle_{x_\phi, y_\phi}$. Here ν is the reciprocal variable for time. The projections and spatial integral produce an analogous Spatial Slice Theorem, given by

$$\tilde{S}^{(q)}_{\nu,\phi}\left(\frac{x_\phi}{q}, y_\phi\right) = \left\langle c_\phi\left(\frac{x_\phi}{q}, y_\phi\right)\delta(y_\phi)\right\rangle_{y_\phi} = c_\phi\left(\frac{x_\phi}{q}, 0\right). \tag{7.2}$$

FCT is a limiting case of a thin spatial illumination where the Spatial Slice Theorem is relevant. In the Spatial Slice Theorem, $\tilde{S}^{(q)}_{\nu,\phi}$ is a projection in a rotated frame defined by $x_\phi = \frac{\nu}{\kappa}$. Finally, $c_\phi(\frac{x_\phi}{q}, 0)$ is a spatial slice of the object along y_ϕ. The spatial slice is equivalent to performing the projection operation along the spatial frequencies perpendicular to the modulation direction, $\tilde{S}^{(q)}_{t,\phi} = \left\langle \hat{C}_\phi(q\kappa t, f_{y_\phi}) \right\rangle_{f_{y_\phi}}$, this is illustrated in the bottom row of Fig.7.1(b).

Once all the line images have been acquired with respect to ϕ, an FCT sinogram can be formed in the spatial frequency domain. The spatial frequency sinogram leads to a filtered spatial frequency back-projection algorithm which is a conjugate domain analog of the filtered back-projection algorithm [32]. The *filtered spatial frequency back-projection algorithm* makes

use of a radial spatial coordinate filter, rather than the radial spatial frequency filter employed in CT and LT. The filtered spatial frequency back-projection algorithm reconstructs images according to the formula

$$\hat{C}(qf_x, f_y) = \iint \tilde{S}^{(q)}_{\nu,\phi} e^{-i2\pi q f_{x_\phi} x_\phi} |x_\phi| \mathrm{d}x_\phi \mathrm{d}\phi, \tag{7.3}$$

where $\hat{C}(qf_x, f_y)$ is the spatial frequency representation of the object, $e^{-i2\pi q f_{x_\phi} x_\phi}$ is the Fourier transform kernel in polar coordinates, and $|x_\phi|$ is the radial spatial filter due to the Jacobian in the transformation from polar coordinates to Cartesian coordinates. A simple inverse Fourier transform recovers the 2D object in the spatial domain.

The object information probed with FCT is illustrated in Fig. 7.1(b), where the top row shows the spatial projections of the illumination onto the object and the bottom row is the resulting spatial frequency support that is probed with time. The spatial frequency support is summed together and the inverse Fourier transform is taken, bottom row last column of Fig. 7.1(b). In this case, a spatial radial filter is applied in real space to recover the object, as shown by the shaded gray radial ramp, top row last column of Fig. 7.1(b).

7.4 Experimental Setup

A schematic of the experimental setup is shown in Fig. 8.4(a). The specimen was illuminated by a spatially modulated λ = 532-nm wavelength continuous-wave (cw) laser (Lighthouse, Sprout). The spatial modulation on the line illumination is produced by bringing the illumination beam to a line focus onto a spinning modulator disk with a cylindrical lens [45, 136]. The modulated line was image relayed to the object plane with a 4-f imaging system constructed from lenses with focal lengths of 250 mm and 35 mm, respectively. The sample was mounted on a rotation stage (Newport PR50CC) to allow full 360-degree rotation about the optic axis. Transmitted light was collected with a 0.25 NA aspheric lens and the image was relayed to a photodiode detector (Thorlabs DET100A). Fluorescent light emitted by the object was collected in the epi-direction and by relay imaging the object plane onto the surface of a PMT

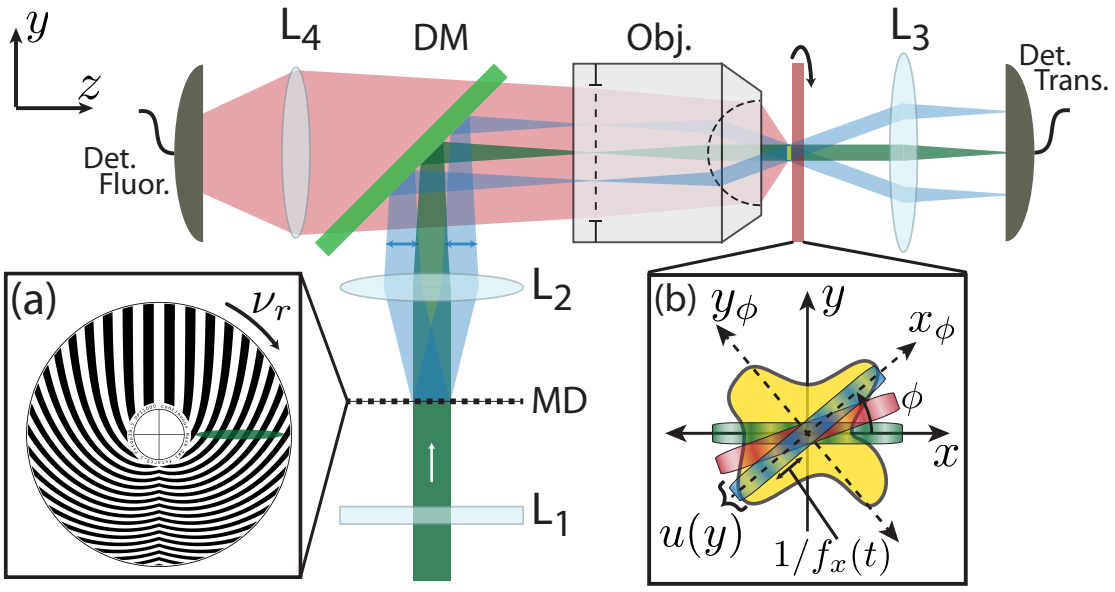

Figure 7.2: Panel (a) shows the FCT microscope schematic. The illumination beam is brought to a line focus on the modulator disk. The modulator disk is imaged onto the sample. Both fluorescence (red beam) and absorption are collected by single-pixel detectors. The sample is rotated on a rotation stage from $[0, 2\pi]$. Panel (b) shows the coordinate rotation of the beam with respect to the sample by an angle ϕ. x_ϕ and y_ϕ represent the rotated coordinate system. The various beam colors represent unique rotation angles with respect to the sample at a snapshot in time. $f_x(t)$ is the projected spatial frequency and $u(y)$ is the intensity profile of the illumination beam in the y direction. Figure from [137].

(Hamamatsu H9305). The fluorescent light was isolated using a dichroic beamsplitter (Semrock FF562-Di03) and an interference filter (Semrock FF01-593/40).

The 35 mm achromatic lens was chosen instead of an objective lens to minimize the effect of the axial and transverse wobble of the rotation stage, which needs to be corrected in order to obtain a properly aligned spatial frequency sinogram. The axial wobble was sufficiently small so that the object stayed within the Rayleigh range of the focused beam throughout the entire rotation. The transverse wobble was $25-30\mu m$ over the rotation range, therefore a correction protocol was adopted to mitigate this problem; the details are described in the following section.

Figure 8.4(b), illustrates the illumination pattern at a snapshot in time. The green, red, and blue colors represent distinct rotation angles, ϕ, with respect to the sample. The width of the illumination, $u(y)$, in our experimental setup we calculated to be ~$6.7\mu m$ using the Gaussian beam equations. The size of the beam in the back aperture was ~5 mm by ~3 mm in the x and

y directions, respectively. The illumination numerical aperture (NA) was calculated to be ~0.07 and ~0.04, in x and y, respectively.

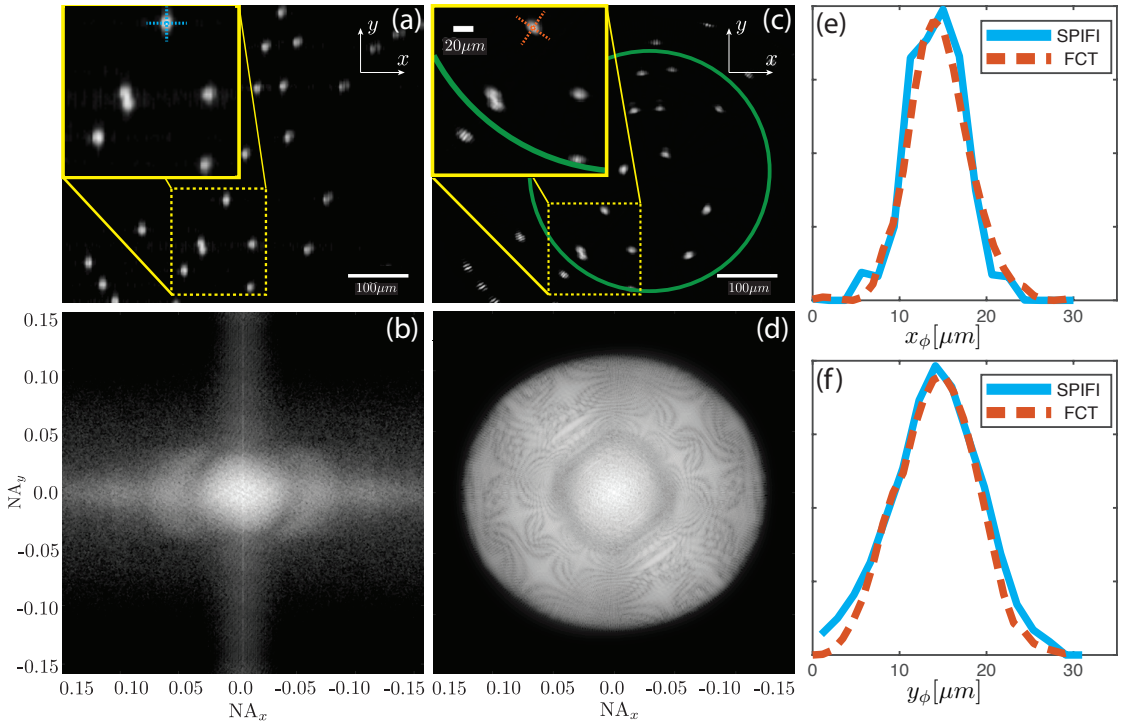

Figure 7.3: Panel (a) shows a second order SPIFI image of fluorescent stained $15\mu m$ polystyrene beads. The beads are elongated vertically because the resolution enhancement is only along the x coordinate. Panel (b) shows the Fourier transform of panel (a), the x coordinate contains 2x higher spatial frequency support than the y coordinate. Panel (c) shows the second-order FCT reconstruction of the fluorescent stained $15\mu m$ polystyrene beads. The yellow boxes indicate a zoomed-in region of the images to illustrate the resolution improvement between the two imaging types. Panel (d) shows the Fourier transform of panel (c); the spatial frequency support is isotropic. The sharp cutoff in the spatial frequency is due to the filtering used in the image reconstruction. Figure from [137].

7.5 Results and Discussion

Each FCT image was produced by using 360 uniformly spaced line images from angles ranging from $[0, 2\pi]$. In principle, only the line images are needed to perform an FCT reconstruction. However, the transverse wobble from the rotation stage caused the center of rotation to migrate resulting in an error in the image center. To correct this transverse wobble, and thus to enable demonstration of the FCT imaging method, 2D images at every angle, ϕ, were acquired

by scanning the line focus vertically [52]. Every 2D image was numerically derotated by $-\phi$. The derotated images were aligned in the $x-y$ coordinates by maximizing the cross-correlation between the images. The aligned images were then rotated back to their original rotation angle, ϕ. Finally, the center line image was extracted from the aligned 2D images, which formed the set of rotated line images required by the Spatial Slice Theorem. The image-centering protocol allowed us to correct the transverse wobble of the rotation stage. With the corrected line images, the FCT reconstruction using filtered spatial frequency back-projection in Eq. (7.3) was used to reconstruct 2D images of the object. This alignment procedure could be avoided by using a more precise rotation stage with a less severe wobble.

While FCT works with both absorption and fluorescence, we present the fluorescence results for brevity. Figure 7.3(a-d) shows a comparison between second-order fluorescent SPIFI and second-order FCT using $15\mu m$ fluorescent stained polystyrene beads (LifeTechnologies, FocalCheck Slide 1, Well A1). Figure 7.3(a) shows a second-order SPIFI image. The yellow box shows a zoomed-in region to better see the asymmetry in the resolution due to the enhanced resolution in the x direction. Figure 7.3 (b) shows the Fourier transform of Fig. 7.3 (a). The frequency support shows the NA in the x coordinate extends to 0.13 while the NA in the y coordinate extends to 0.04 which gives rise to the anisotropy in Fig. 7.3 (a). Figure 7.3 (c) shows the second-order FCT reconstruction of the fluorescent stained beads. The yellow box shows a zoomed-in region to better visualize the improvement in the resolution. Figure 7.3 (d) shows the Fourier transform for Fig. 7.3 (c). The frequency support extends to 0.13 NA isotropically. The dark ring is caused by the filtering applied in the FCT reconstruction.

We see that the resolution is radially enhanced in the second-order image in Fig. 7.3 (c). This enhancement causes the fluorescent beads to appear elongated azimuthally. We also note that on the edge of the reconstructed image, there is an azimuthal oscillation. This is a result of deficient angular coverage causing a void in the acquired information.

7.6 Conclusion

In this chapter, a new form of tomography, called Fourier Computed Tomography (FCT), was derived and demonstrated to operate in the conjugate spatial and spatial frequency domains as compared to conventional computed and lateral tomography. We showed mathematically that FCT is a conjugate analog to both Computed Tomography and Lateral Tomography. By controlling the shape of the illumination along y via $u(y)$, we can change the imaging modality and subsequent reconstruction algorithm, that is, for $u(y) \rightarrow 1$, Lateral Tomography applies, and for $u(y) \rightarrow \delta$, Fourier Computed Tomography applies. We derived the Spatial Slice theorem and saw how the equivalent sinogram in the spatial frequency domain led to a filtered spatial frequency back-projection algorithm. We have operated this new tomography in both absorbing and fluorescent modes for second-order enhancement of imaging resolution. Finally, we showed that FCT is capable of achieving nearly isotropic enhanced lateral resolution, mitigating the anisotropic spatial frequency support of spatial frequency-modulated imaging. While only three-beam spatial frequency illumination was reported, we also note that the FCT algorithm is general so that other line imaging techniques could be used, such as Coherent Holographic Image Reconstruction by Phase Transfer, to achieve holographic 3D volume information, [45], or Direct Optical Phase Extraction for quantitative phase-contrast [136].

This new tomography is applicable to any computational imaging technique that forms images with line illumination and can combine anisotropic spatial resolution images together to form a nearly isotropic high-resolution image. Additionally, this method opens a pathway to extending spatial frequency projection super-resolution imaging from one dimension to an isotropic-enhanced image of the object in the lateral plane.

In future work, we will be able to adapt FCT from a transverse 2D tomographic imaging process to three dimensions through a careful analysis of projections recorded during the single-pixel imaging process. We anticipate this method of single-pixel imaging will work well for imaging deep inside scattering media (e.g., biological tissues). Finally, we note that SFP imaging methods directly record and report aberrations in the imaging process in the form of phase

modulation of the recorded signal [76]. This property of SFP imaging will be used in combination with generalized FCT imaging to permit super-resolution imaging in complex specimens where phase distortions accumulated through refractive index variations in the tissue cause severe errors and degradation of super-resolution imaging methods [16]. With SFP-based FCT imaging, we will be able to record and correct these instruments and specimen-induced aberrations, because those aberrations are automatically encoded and can be removed in the reconstruction algorithm.

Chapter 8

Single-Pixel Fluorescent Diffraction Tomography

8.1 Summary

Optical diffraction tomography is an indispensable tool for studying objects in three-dimensions due to its ability to accurately reconstruct scattering objects. Until now this technique has been limited to coherent light because spatial phase information is required to solve the inverse scattering problem. We introduce a method that enables the concept of optical diffraction tomography to be applied to imaging incoherent contrast mechanisms such as fluorescent emission. Our strategy mimics the coherent scattering process with two spatially coherent illumination beams. The interferometric illumination pattern encodes spatial phase in temporal variations of the fluorescent emission, thereby allowing incoherent fluorescent emission to mimic the behavior of coherent illumination. The temporal variations permit recovery of the propagation phase, and thus the spatial distribution of incoherent fluorescent emission can be recovered with an inverse scattering model. A computational and experimental demonstration of this new imaging method is performed showing isotropic resolution in the 3D reconstruction of a fluorescent object.

8.2 Introduction

In fluorescence microscopy, light emitted from the specimen is spatially incoherent. Consequently, 3D imaging techniques require some form of spatial gating to map detected photons to the location from which they were emitted. This spatial gating is often achieved through some combination of confining the illumination volume and detection volumes. Examples of such strategies include selective plane illumination microscopy (SPIM) [70], where the illumination volume is restricted to a thin axial plane, or laser-scanning confocal microscopy, where both the illumination and detection volumes are restricted to a diffraction-limited spot in 3D [149].

These strategies allow each detected photon to be mapped to a 3D location in the specimen from which it was emitted and often involve high numerical aperture (NA) optics that tightly focus the illumination light and/or restrict the volume over which light is detected.

Other strategies for 3D imaging rely on inverting a quantitative model of the illumination, emitted, and collected light to estimate the concentration of fluorescent emitters from detected intensity images. These computational imaging methods, such as optical projection tomography (OPT) and deconvolution imaging (DI), require axially scanning or rotating the object to collect a set of data to be reconstructed [91]. 3D computational imaging of a scattering object with partially coherent illumination is possible within the Born approximation using the weak optical transfer function [138]. However, the use of partially coherent illumination for fluorescent imaging requires the use of incoherent OPT or DI methods.

Conventional fluorescent imaging methods suffer from limitations such as photobleaching and anisotropic spatial resolution between the axial and transverse directions [124]. While SPIM can partially mitigate the effects of photobleaching, anisotropic spatial resolution is a persistent problem [91]. In all of these methods, tissues must be optically cleared to reduce distortions from optical scattering to suitably low levels [91]. A more stringent restriction on SPIM and OPT microscopes is that the spatial resolution is coupled to the size of the object [91] – leading to decreased spatial resolution for in increased imaging region.

Coherent imaging strategies enable 3D imaging by making use of the direction of the scattered light. Emil Wolf recognized that the inverse scattering problem for coherent light propagating in an object can be solved by recording the complex, spatially coherent, scattered field [151]. Directional scattering allows the recording of spatial frequency components of an object by exploiting knowledge of the complex amplitude of light scattered in a particular direction when illuminated by a spatially coherent input wave. This concept is illustrated schematically in Fig. 8.1(a), where the illumination field, E_0, and scattered field, E_1, have corresponding wavevectors $\mathbf{k}_0$ and $\mathbf{k}_1$ respectively.

Interferometric techniques, e.g., holography, are able to record the complex scattered field that, within the Born approximation, can be mapped to an arc of spatial frequency information defined by the Ewald sphere by applying the Fourier diffraction theorem [151] shown in Fig. 8.1(b). The position in spatial frequency space is given by the wavevector difference, $\Delta\mathbf{k} = \mathbf{k}_1 - \mathbf{k}_0$. This sparse spatial frequency information is encoded by the complex scattered field obtained in a single scattered field measurement. More complete object information can be acquired by introducing a relative rotation between the illumination and the object to fully sample the object's spatial frequency distribution, yielding optical diffraction tomography (ODT).

Optical holography, and thus ODT, normally relies on spatially coherent light to interferometrically record the complex scattered field, allowing interior spatial frequency information to be acquired. Coherent scattering data can be inverted to solve the scattering problem for variations in the refractive index of the specimen. Using coherent illumination allows object position to be encoded in the complex scattered field. The phase is critical since it encodes the axial location of the scatterer, and it is this phase that is required to enable diffraction tomography to be extended to incoherent fluorescent light. ODT uses a rotation of the object or illumination wave to capture a sequence of scattered fields that fill out the object's spatial frequency information. Then computational imaging tools are applied to invert the information recorded in order to recover the object's spatial frequency distribution, and thus the object's spatial information. ODT has the advantage of not being constrained to imaging objects in the Rayleigh range of the illumination beam, as the light is allowed to diffract before encountering the optical detector.

ODT is conventionally thought to be impossible with fluorescent light because, in the case of incoherent emission, the phase is lost due to the random emission of the molecular emitters and this unstable phase obscures the relationship between the location of the emitter and the propagation direction and phase. If fluorescence is to be imaged in a similar manner as ODT, it is necessary to encode the coherent illumination propagation phase onto fluorescent light so

that the phase can be recovered. It is possible to exploit the fact that an incoherent emitter is coherent with itself to encode the spatial location of the emitter [132, 90], but a general adaptation of coherent-like imaging methods to incoherent light remains elusive.

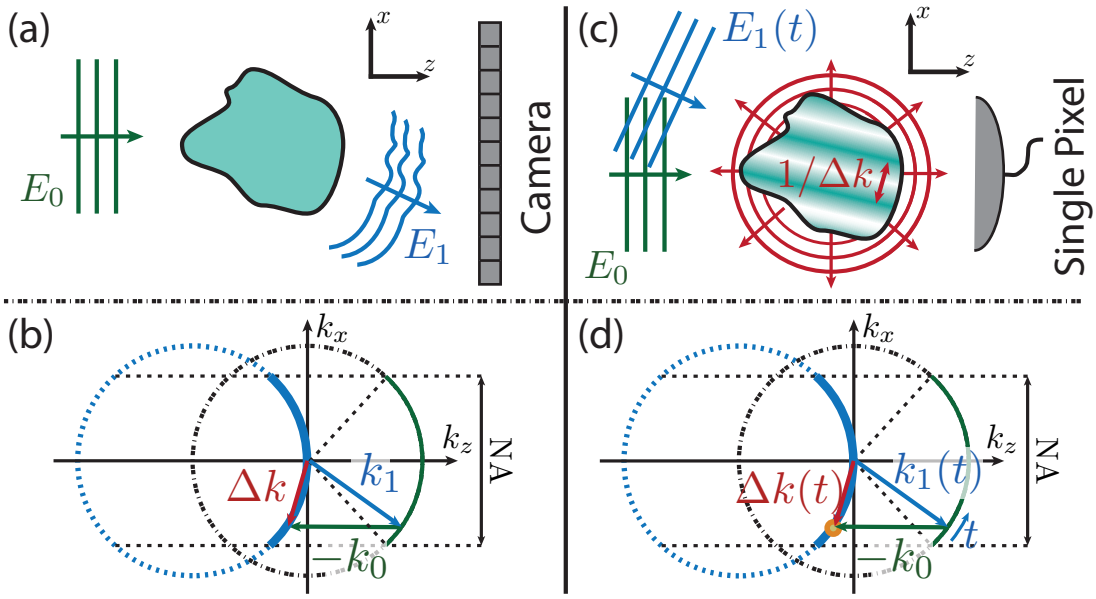

Figure 8.1: ODT compared to FDT. (a) The standard optical diffraction tomography scattering picture. (b) The spatial frequency support is probed by diffraction tomography. The thick blue arc is the measured spatial frequency information. (c) The FDT picture, with the signal light collected by a single-pixel detector. (d) The spatial frequency representation of FDT. Figure from [135].

In this chapter, we introduce the first method that uses fluorescent light emission for diffraction tomographic imaging. As fluorescent light is spatially incoherent, it is necessary to mimic the process of coherent scattering to enable optical diffraction tomography with fluorescence. We mimic spatially coherent scattering by transferring the phase difference from a pair of spatially coherent illumination beams [49] into a time-variation of fluorescent emission brightness, enabling ODT with fluorescent light recorded on a single-element optical detector. By mimicking the incident and scattered fields in the illumination of a fluorescent object, we are able to perform optical diffraction tomography using fluorescent light. We refer to this method as Fluorescence Diffraction Tomography (FDT).

The FDT concept is illustrated in Fig. 8.1(c) and (d). A pair of illumination beams substitute for the incident and scattered waves in coherent scattering. The reference wave, E_0, in Fig. 8.1(c), plays the role of the incident wave in coherent scattering and interferes with an illumination plane wave, E_1, that represents the scattered wave. To map out the equivalent information as in coherent scattering, the incident direction of $E_1(t)$ is scanned in time, producing a modulation of the illumination intensity that depends on the relative phase of the two illumination beams, $\Delta\mathbf{k}(t)\cdot\mathbf{x}$, where $\mathbf{x} = (x, z)$ is the spatial coordinate vector in the $x-z$ plane. The difference wavevector, $\Delta\mathbf{k}(t) = \mathbf{k}_1(t) - \mathbf{k}_0$, behaves as the scattering vector in coherent scattering that is defined as the difference between the k-vector of the scattered field, $\mathbf{k_1}(\mathbf{t}) = k\big(\sin[\theta(t)], \cos[\theta(t)]\big)$, and incident waves, $\mathbf{k}_0 = k(0, 1)$, where $k = 2\pi/\lambda$ is the wavenumber of the illumination.

The collected fluorescence recorded with a single-pixel detector serves as the FDT time signal. These measurements imprint the relative phase of the two spatially coherent illumination beams into an intensity modulation in space and time that allows the detected incoherent fluorescent light power to be treated as if it came from a coherent source. Because fluorescent light is incoherent, the detected fluorescent light power is equivalent to the overlap integral between the spatial distribution of the fluorophore concentration – our object – and the illumination intensity. Each measurement at time t samples the complex amplitude of the object spatial frequency distribution at the different spatial frequency wavevector, $\Delta\mathbf{k}(t)$. The result is that for each incident angle of $E_1(t)$, a spatial frequency projection is recorded that exactly mimics the complex spatial frequency information traditionally obtained through coherent scattering measurements; compare Figs. 8.1(b) and (d).

The key aspect of FDT is coherent transfer mediated by the modulated illumination intensity. The intensity arises from the interference of the reference and scanned fields, i.e., $I_{\text{ill}} \propto \left|E_0 + E_1[\theta(t)]\right|^2$ [49], where $\theta(t)$ denotes the incidence angle of E_1 with respect to k_z axis, or equivalently the angle between $\mathbf{k}_1$ and $\mathbf{k}_0$, at time t. The model for the interference is written as $I_{ill}(\mathbf{x}, t) = 1 + \mu(t)\cos[\Delta\Phi(\mathbf{x}, t)]$, where $\mu(t)$ is the fringe visibility and $\Delta\Phi$ is the phase difference between the reference and scanned fields in Fig. 8.1(c) [45, 48]. The phase difference between

the illumination fields, $\Delta\Phi(\mathbf{x}, t) = \omega_c\, t + \Delta\mathbf{k}(t)\cdot\mathbf{x}$, imparts a temporal modulation pattern at each spatial position in the $x-z$ plane. Here, ω_c is a carrier frequency in the modulation, which is critical for isolating the complex phase information in the time signal [45, 49], and $\Delta\mathbf{k}(t)\cdot\mathbf{x}$ is the spatial phase variation that encodes the location of the object in the $x-z$ plane. The stable relative phase difference between the pair of illumination beams is critical to producing the time-varying interference used to label fluorophores, disallowing the use of partially or fully incoherent illumination in FDT.

The elements of $\Delta\mathbf{k}(t) = (\Delta k_x(t), \Delta k_z(t))$ are difference frequencies. In our work, we set $\Delta k_x(t) = k_c\, t/T$, corresponding to $\sin\theta(t) = t\,\mathrm{NA}/T$, where $k_c = k\,\mathrm{NA}$ is the coherent imaging cutoff spatial frequency for the illumination optics and $t \in [-T, T]$ with $2T$ denoting the total collection time. For this choice, we have $\Delta k_z = k(\sqrt{1-(t\,\mathrm{NA}/T)^2} - 1)$. The spatio-temporal intensity modulation encodes the relative spatial phase of the illumination fields as a temporal modulation of the emitted fluorescent power from the object, thereby transferring coherent propagation behavior to fluorescent emission [45].

The time trace is generated by detecting the collected fluorescent emission as the scanning field sweeps through the range of incident angles supported by the NA of the illumination objective [45, 49, 48]. The temporal signal $S(t, \phi)$ is the projection of the spatial distribution $c(\mathbf{x})$ of the fluorophore concentration onto illumination intensity at incidence angle ϕ:

$$S(t, \phi) = \langle I_{ill}(\mathbf{R}_\phi \mathbf{x}, t)\, c(\mathbf{x}) \rangle_{\mathbf{x}} \tag{8.1}$$

where Dirac integral notation, $\langle\cdot\rangle_{\mathbf{x}} = \int \cdot\, \mathrm{d}\mathbf{x}$, denotes the spatial integration over x and z, performed by the single-pixel detector, and $\mathbf{R}_\phi$ is a rotation matrix by ϕ that yields the coordinate transform $\mathbf{x} = (x, z) \longrightarrow \mathbf{R}_\phi \mathbf{x} = (x\cos\phi - z\sin\phi, x\sin\phi + z\cos\phi)$. We have not included a measurement noise term $\varepsilon(t)$ in writing (8.1) to keep subsequent equations simple in form, but it is understood that an additive noise term is always present.

An equivalent representation of (8.1) is to write it in its complex-valued form, using Euler's identity, by including only a single sideband of the sinusoidal term in the illumination pattern.

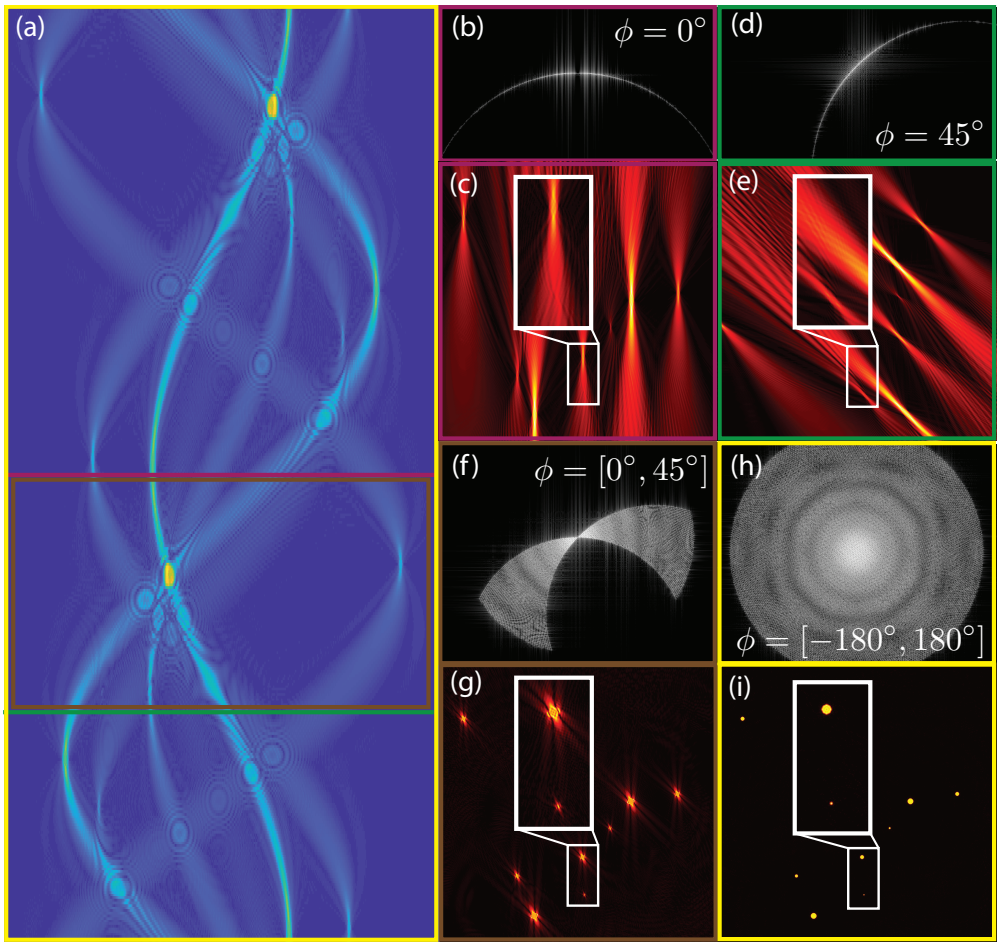

Figure 8.2: FDT sinogram and reconstruction. (a) Simulated FDT sinogram from a fluorescence distribution where the object has been rotated over $[-180°, 180°]$. (b), (d), (f), and (h) show the frequency support that is measured and mapped onto the Ewald sphere and ϕ indicates the illumination angle in degrees. (c), (e), (g), and (i) show the reconstructed object generated by applying the dual operator to the FDT time signal, (8.3). The colored boxes around panels (b-i) correspond to the colored lines and boxes in panel (a) and represent the measured information used in the reconstruction. Figure from [135].

This representation is given by

$$\tilde{S}^{(1)}(t,\phi) = \langle \Psi_\phi(\mathbf{x}, \Delta\mathbf{k}(t)) c(\mathbf{x}) \rangle_{\mathbf{x}} \tag{8.2}$$

where $\Psi_\phi(\mathbf{x}, \Delta\mathbf{k}(t)) = \exp\left[i(\Delta\mathbf{k}(t) \cdot \mathbf{R}_\phi \mathbf{x}) \right]$ is the complex Fourier kernel in rotated coordinates $\mathbf{R}_\phi\mathbf{x}$ and we have assumed $\mu(t) = 1$ for simplicity. The procedure for obtaining this representation from the data is illustrated in supplementary material Fig. S4(a,b), [45]. The value of this complex-valued representation in (8.4) is showing that each time sample corresponds to a

complex amplitude of the object spatial frequency distribution – equivalent to the data in an individual ODT line image, establishing (8.4) as the forward model for FDT, which is equivalent to the Fourier Diffraction theorem [151, 32]. We refer to (8.4) as the forward model for FDT with forward operator $\mathscr{D}\{c(\mathbf{x})\}(t,\phi) = \langle \Psi_\phi(\mathbf{x}, \Delta\mathbf{k}(t))\, c(\mathbf{x})\rangle_{\mathbf{x}}$.

The spatial distribution of the data collected for each angle is referred to as a sinogram which is computed from a Fourier transform of the single side band time signal, $s(\mathbf{R}_\phi \mathbf{x}) = \mathscr{F}\{\tilde{S}^{(1)}(t,\phi)\}$. The least-squares estimate (minimum $\mathscr{L}^2$ norm for error) of the fluorescent concentration, denoted by $\hat{c}(\mathbf{x})$, is then computed by applying the inverse operator $\mathscr{D}^{-1}$:

$$D^{-1}\{\tilde{S}^{(1)}(t,\phi)\}(\mathbf{x}) = \langle \tilde{\Psi}^{\dagger}_{\phi}(\mathbf{x}, \Delta\mathbf{k}(t))\, \tilde{S}^{(1)}(t,\phi)\rangle_{t,\phi} = \hat{c}(\mathbf{x}) \tag{8.3}$$

where † denotes adjoint (complex-conjugate for Fourier kernel). The kernel of the inverse operator, $\tilde{\Psi}_\phi$, forms a biorthogonal system with the kernel of the forward operator, Ψ_ϕ, at the limit of high NA, as shown in Supplementary Material. In a noiseless case, this biorthogonality leads to a perfect reconstruction of the object. The dual kernel is given by $\tilde{\Psi}_\phi = \gamma(t)\,\Psi_\phi$, where $\gamma(t) = |t|/T\sqrt{1-(\mathrm{NA}\, t/T)^2}$ is the determinant of the Jacobian of the coordinate transformation $t \longrightarrow \Delta\mathbf{k}(t)$. The estimate in Eq. (8.3) is formally equivalent to the ODT backpropagation reconstruction [32].

A full simulation of the forward model, Eq. (8.4), and the reconstruction, (8.3), is shown in Fig. 8.2. The FDT microscope was simulated using an illumination wavelength of 532 nm, NA = 0.90, and a field of view of 20 μm; the full time trace signal processing workflow to generate the FDT sinogram is illustrated in Supplementary material Fig. S4. Panel (a) shows an FDT sinogram in the spatial domain where the scan angles range from $[-180, 180]$ degrees. The colored lines and boxes represent the time trace(s) used to generate the corresponding figures on the right of the sinogram. The first and third rows in Fig. 8.2 show the mapping of measured spatial frequency support onto the Ewald sphere in the spatial frequency domain constrained by optical diffraction generated by taking the Fourier transform of the second and fourth rows, respectively. Panels (b) and (d) show the frequency support measured by a time trace when $\phi = 0$

and $\phi = 45$ degrees, respectively. Panels (f) and (h) show the spatial frequency support when multiple projections are used in the reconstruction, $\phi = [0, 45]$ and $\phi = [-180, 180)$ degrees, respectively. Panels (c,e,g,i) show the reconstructed object. Notice that the object localization improves as additional projection angles are used in the reconstruction.

The FDT microscope was experimentally implemented by using a spinning modulation mask that behaves as a time-varying grating spatial frequency [52]. The mask is illuminated by a line focus that is image relayed to the object region. At a snapshot in time, the mask appears as a static grating creating a zero-order beam, E_0, as well as positive, $E_1(t)$, and negative order diffracted beams. The negative diffracted order is blocked by a spatial filter, leaving the zero and positive diffracted order beams to be image relayed to the object plane [45]. Interference between the beams produces the desired spatio-temporally modulated illumination intensity pattern. The object is rotated a full 360 degrees. At each rotation angle, a time trace is acquired. Rotation in the spatial domain also causes the spatial frequency arc, Fig. 8.1(d), to rotate. Once data from all illumination angles has been acquired, the full $(k_x - k_z)$ frequency plane will have been sampled so that we may estimate the object with isotropic spatial resolution. See the supplementary information for details on the experimental apparatus and reconstruction algorithm.

FDT imaging was demonstrated experimentally using an object fabricated from cotton fibers stained with fluorescein. The stained fibers were mounted on an eight-axis stage, Fig. S1(c). The mounting stage allowed for full 360-degree rotation of the sample as well as the ability to position the sample precisely in the microscope focus. Fig. 8.3 shows a 3D reconstruction of fluorescein stained fibers using alpha blending from Volume Viewer in imageJ. The image was generated with 200 evenly spaced $x - z$ slices obtained by scanning along y. Due to the mechanical instability of the y-axis stage, each $x - z$ slice was shifted to align adjacent slices to avoid object discontinuity in the 3D reconstruction. The sub-images in Fig. 8.3 are slices from the 3D reconstruction and the colored frames correspond to the rectangular boxes in the

3D image. An absorption contrast image was simultaneously acquired with the fluorescence, however, for brevity, this image is not shown in the main text; see Fig. S5.

The FDT image of fluorescent stained fibers in air shown in Fig. 8.3 is an image obtained with a highly scattering sample as the refractive index for cotton is 1.54. This strong scattering violates the Born approximation, yet we still recover a nearly exact image with FDT for the fluorophore concentration. We do note that the scattering by the fibers does distort the illumination patterns, and thus introduces image distortions that likely produce the artifacts seen in the upper left panel of Fig. 8.3. The quantitative impact of illumination distortion on FDT image reconstruction will be explored in future work.

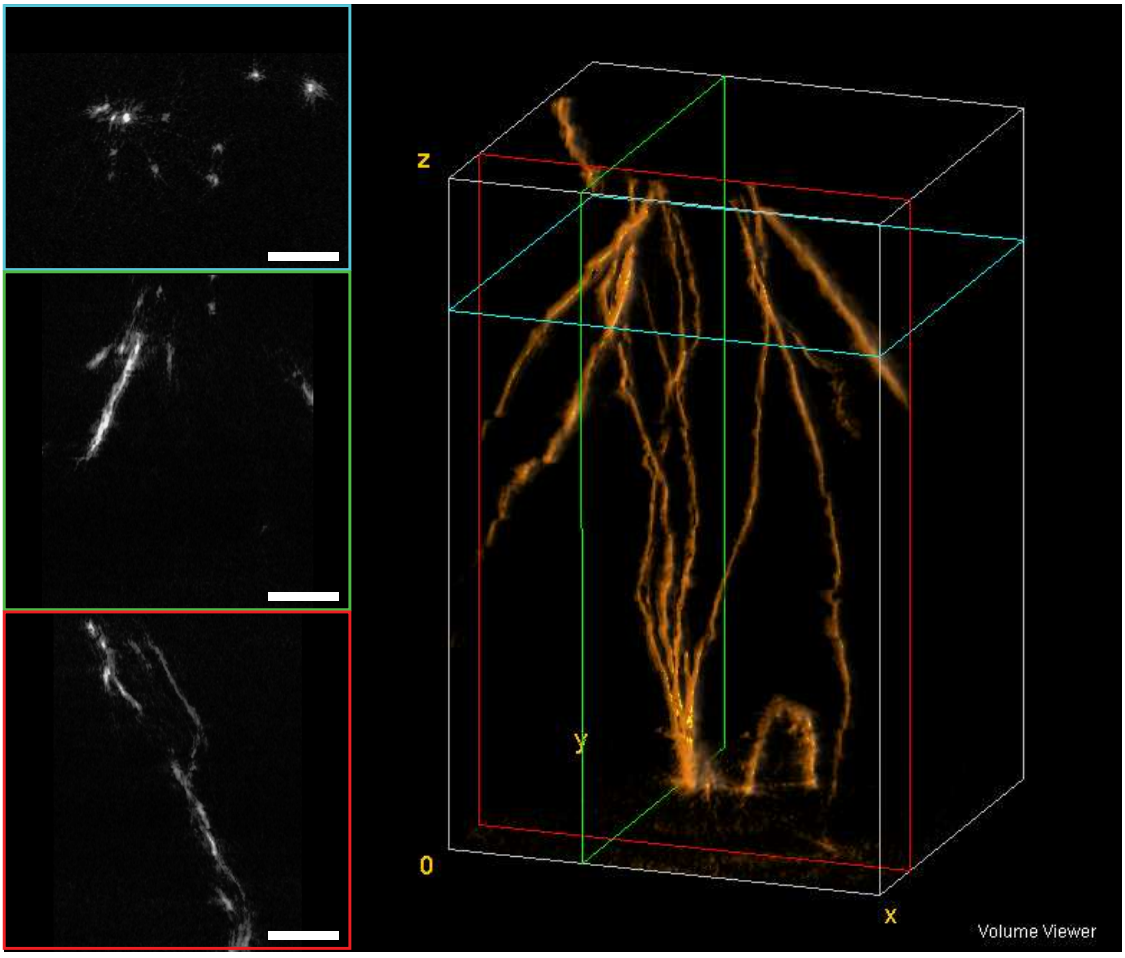

Figure 8.3: 3D reconstruction of fluorescent stained cotton fibers. The blue, green, and red panels are slices of the object from $x-y$, $y-z$, and $x-z$ slices, indicated by the colored rectangle in the main figure on the right. Scale bar equals 60μm. Figure from [135].

There are several differences between standard optical diffraction tomography (ODT) and FDT that should be noted. While ODT and FDT obtain the complex spatial frequency values that follow the arc of spatial frequency information governed by diffraction as shown in Figs. 8.1(b) and (d), the physical origin of these data are remarkably different. ODT relies on the spatial coherence of the light scattered by the spatial variation in the refractive index of the object. As a result, ODT projection operation deviates from FDT by a complex scaling constant of $-2i\Delta k_z$. In contrast, FDT records information from the spatial variation of fluorophore concentration from the interference of two spatially coherent illumination beams. Each method samples complex amplitudes that lie on the Ewald sphere, which naturally leads to recording data in the $k_x - k_z$ spatial frequency plane by relative rotation of the object and illumination beams to spatially resolve the object in the $x-z$ plane. However, in the derivation of the Fourier diffraction theorem for FDT the only assumption made is illumination by plane waves, and there is no need to invoke the Born approximation or Rytov approximation. Therefore, FDT does not have the same object size or object variation limitations that standard ODT experiences [82].

FDT mitigates the coupling between object size and spatial resolution typically seen in fluorescence imaging. Comparatively, in optical projection tomography, where the fluorescent light is detected with a camera, the object is restricted to the region of good focus (the Rayleigh range) to avoid background blur from out-of-focus light [91, 29]. This causes the coupling of spatial resolution and object size conventionally seen with incoherent imaging modalities. In FDT, incoherent light emission may be treated as a coherent source allowing the object to extend over a much larger region not constrained by the Rayleigh range. Therefore, FDT decouples the need to reduce the numerical aperture of the illumination as the object size increases.

In summary, we introduced a new tomographic imaging technique, Fluorescence Diffraction Tomography (FDT), that extends optical diffraction tomography to incoherent contrast mechanisms, such as fluorescence and Raman scattering. We developed theory for both forward and inverse models. The forward model uses CHIRPT illumination and detection as a projection of spatial frequencies onto the sample [45, 49, 136, 48]. The projection uses mod-

ulation transfer to encode the spatial phase of the illumination to allow phase transfer to incoherent sources. We demonstrate FDT reconstruction with dual functions that are biorthogonal to the intensity and illumination of the rotated Fourier elements in the forward model. Additionally, we showed experimentally that FDT works for both coherent and incoherent contrast mechanisms. In principle, it can be used for any contrast mechanism including nonlinear mechanisms. We expect this technique will expand the range of samples that can be imaged and provide an easy method to co-register multiple contrast distributions simultaneously.

8.2.1 Experimental Setup

The experimental setup for Fluorescent Diffraction Tomography (FDT) is shown in Fig. 8.4. A continuous-wave (CW) laser (Lighthouse, Sprout) wavelength, $\lambda = 532$-nm, is collimated and brought to a line focus with a cylindrical lens on a spinning modulator disk, Fig. 8.4(a). The modulator is a transmission mask designed to impart a unique modulation frequency as a function of disk radius [52, 45, 49, 47]. As the disk spins at a constant angular velocity, the transmission pattern presents a time-varying grating producing diffracted orders. A slit spatial filter is placed in the back focal plane of a 2f optical system, see Fig. 8.4(b), and selects only the zero and first diffracted orders [45] to produce a stationary reference beam and an angle scanning beam, which act as the incident field and scattered field in a coherent scattering experiment, respectively [151]. The filtered beams are image relayed to the sample region with a 4-f imaging configuration with a tube lens, $f_{tube} = 250$ mm, and objective lens, $f_{obj} = 35$ mm. The sample was mounted on a rotation stage (Newport, URB100CC) to allow full 360-degree rotation in the $x-z$ plane, Fig. 8.4(c). The transmitted light was collected by a 0.25 NA aspheric lens (New Focus, 5725-A) and image relayed to a photodiode detector (Thorlabs, DET100A). The fluorescence was collected in the epi-direction and image relayed to a PMT (Hamamatsu H9305). The fluorescence was separated from the illumination light with a dichroic beamsplitter (Semrock, FF562-Di03) and an interference filter (Semrock, FF01-593/40).

The objective lens, a 35 mm focal length achromatic lens (Thorlabs, AC254-035-A), was chosen, instead of a typical high NA objective, to alleviate the transverse wobble seen by the mounting stage, ~30μm, which can lead to significant reconstruction distortions. In order to correct the transverse wobble, a large field of view (FOV), ~260μm, was used to ensure that the sample stayed in the central region of the FOV so the sample image could be shifted laterally in post-processing to remove the effect of transverse wobble.

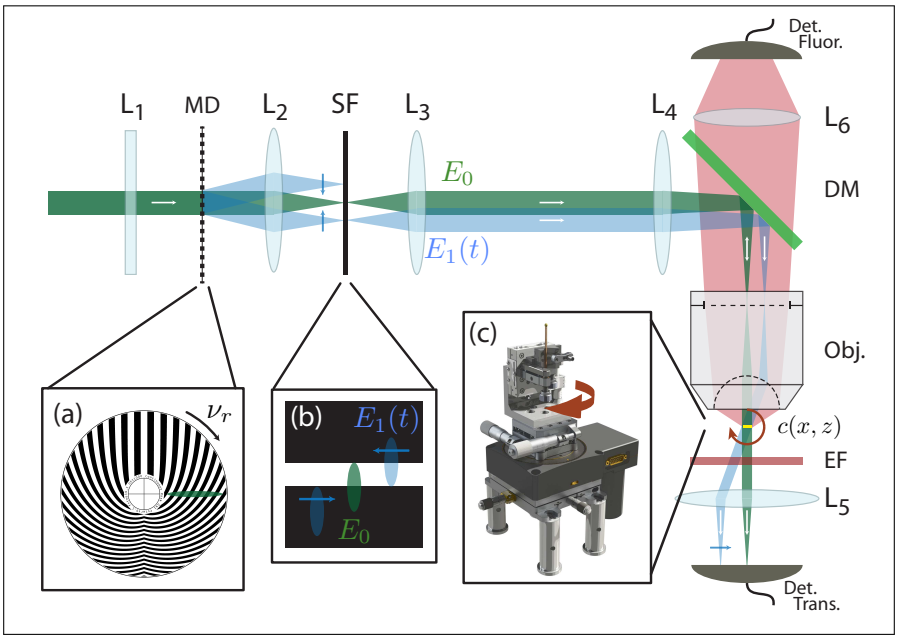

Figure 8.4: Schematic of Fluorescence Diffraction Tomography microscope. Panel (a) modulator mask. Panel (b) isolating spatial filter. Panel (c) sample mounting rotation stage. L_1 - Cylindrical lens, L_{2-5} - Spherical lens, MD - modulator disk, SF - Spatial filter, DM - Dichroic Mirror, Obj. - Objective lens, $c(x,z)$ - Sample, EF - Emission filter, Det. - single-pixel detector, ν_r - Rotation frequency, E_0 - Zeroth order illumination field, $E_1(t)$ - Positive first order scan field. Figure from [135].

8.2.2 Mathematical description of FDT image formation

The forward operator $\mathscr{D}$ can be viewed as a map from $\mathscr{L}^2(\mathbb{R}^2)$, where the concentration function $c(\mathbf{x})$ lives, to $\mathscr{L}^2(\mathbb{R}\times(-\pi,\pi])$, where $\tilde{S}^{(1)}(t,\phi)$ lives:

$$\mathscr{D}\{c(\mathbf{x})\} = \langle \Psi_\phi(\mathbf{x}, \Delta\mathbf{k}(t))c(\mathbf{x})\rangle_{\mathbf{x}} = \tilde{S}^{(1)}(t,\phi). \tag{8.4}$$

The kernel of this operator is the Fourier kernel in rotated spatial coordinates $\mathbf{R}_\phi \mathbf{x}$:

$$\Psi_\phi(\mathbf{x}, \Delta\mathbf{k}(t)) = \exp\left(i\,\Delta\mathbf{k}(t)\cdot\mathbf{R}_\phi\mathbf{x}\right),$$

where

$$\mathbf{R}_\phi = \begin{pmatrix} \cos\phi & \sin\phi \\ -\sin\phi & \cos\phi \end{pmatrix}$$

is a rotation matrix by $\phi \in [0, 2\pi)$, and $\Delta\mathbf{k}(t) = (\Delta k_x(t), \Delta k_z(t))$ is the difference wavevector parameterized by time, with $\Delta k_x(t) = k_c\, t/T$ and $\Delta k_z = k\,(\sqrt{1-(\mathrm{NA}\, t/T)^2} - 1)$ for $t \in [-T, T]$. Because of this parameterization, sampling in time is equivalent to sampling in spatial frequency or wavenumber on a linear grid in Δk_x and a parabolic grid in Δk_z.

The forward operator in (8.4) is an inner product in $\mathscr{L}^2(\mathbb{R}^2)$. The adjoint operator is given by

$$\mathscr{D}^\dagger\left\{\tilde{S}^{(1)}(t,\phi)\right\}(\mathbf{x}) = \int_0^{2\pi}\int_{-T}^{T} \Psi_\phi^\dagger(\mathbf{x}, \Delta\mathbf{k}(t))\,\tilde{S}^{(1)}(t,\phi)\,dt\,d\phi \tag{8.5}$$

with the kernel

$$\Psi_\phi^\dagger(\mathbf{x}, \Delta\mathbf{k}(t)) = \exp\left(-i\,\Delta\mathbf{k}(t)\cdot\mathbf{R}_\phi\mathbf{x}\right).$$

Applying the adjoint operator to $\tilde{S}^{(1)}(t)$ is equivalent to doing correlation processing (matched filtering) on the data and furnishes an estimate of $c(\mathbf{x})$. However, this estimate in general does not enjoy any sense of optimality.

The least-squares (minimum $\mathscr{L}^2$-norm error) estimate is obtained by building the inverse operator $\mathscr{D}^{-1}$:

$$\mathscr{D}^{-1}\left\{\tilde{S}^{(1)}(t,\phi)\right\}(\mathbf{x}) = \int_0^{2\pi}\int_{-T}^{T} \tilde{\Psi}_\phi^\dagger(\mathbf{x}, \Delta\mathbf{k}(t))\,\tilde{S}^{(1)}(t,\phi)\,dt\,d\phi. \tag{8.6}$$

The kernel for $\mathscr{D}^{-1}$, called the dual kernel, is given by

$$\tilde{\Psi}_\phi(\mathbf{x}, \Delta\mathbf{k}(t)) = \gamma(t)\,\Psi_\phi(\mathbf{x}, \Delta\mathbf{k}(t)) = \gamma(t)\exp\left(i\Delta\mathbf{k}(t)\cdot\mathbf{R}_\phi\mathbf{x}\right),$$

where

$$\gamma(t) = \frac{|t|/T}{\sqrt{1-(\mathrm{NA}\, t/T)^2}}$$

is the determinant of the Jacobian of the coordinate transformation $t \longrightarrow \Delta\mathbf{k}(t)$.

As the numerical aperture NA goes to 1, this dual kernel forms a biorthogonal system with the forward kernel, and at the limit we have

$$Q := \int_0^{2\pi} \int_{-T}^{T} \Psi_\phi^\dagger(\mathbf{x}, \Delta\mathbf{k}(t))\, \tilde{\Psi}_\phi(\mathbf{x}', \Delta\mathbf{k}(t))\, dt\, d\phi = \delta^2(\mathbf{x}-\mathbf{x}'), \tag{8.7}$$

where $\delta^2(\cdot)$ denotes a bivariate Dirac delta. To see this, let us define $\Delta\mathbf{x} = \mathbf{x}-\mathbf{x}'$. Then, Q can be written as

$$\begin{aligned} Q &= \int_0^{2\pi} \int_{-T}^{T} \gamma(t) \exp\left(-i\, \Delta\mathbf{k}(t)\cdot \mathbf{R}_\phi \mathbf{x}\right) \exp\left(i\, \Delta\mathbf{k}(t)\cdot \mathbf{R}_\phi \mathbf{x}'\right)\, dt\, d\phi \\ &= \int_0^{2\pi} \int_{-T}^{T} \gamma(t) \exp\left(-i\, \Delta\mathbf{k}(t)\cdot \mathbf{R}_\phi \Delta\mathbf{x}\right)\, dt\, d\phi \\ &= 2\pi \int_{-T}^{T} \gamma(t) J_0(\|\Delta\mathbf{k}(t)\|_2 \|\Delta\mathbf{x}\|_2)\, dt. \end{aligned}$$

where $J_0(\cdot)$ is the Bessel function of the first kind in two dimensions and $\|\cdot\|_2$ denotes 2-norm. Substituting for $\Delta\mathbf{k}(t)$, this can be simplified to

$$Q = \frac{4\pi \mathrm{NA}}{T} \int_0^1 \frac{\tau}{\sqrt{1-(\mathrm{NA}\,\tau)^2}} J_0\left(\sqrt{2}\, k \|\Delta\mathbf{x}\|_2 \sqrt{1-\sqrt{1-(\mathrm{NA}\tau)^2}}\right) d\tau$$

where $\tau = t/T$. Let $\Delta\kappa(\tau) := \sqrt{2(1-\sqrt{1-(\mathrm{NA}\,\tau)^2})}$. Then, the integral Q can be expressed in the simplified form

$$Q = \frac{4\pi}{\mathrm{NA}\, T} \int_0^{\Delta\kappa_c} J_0\left(k \|\Delta\mathbf{x}\|_2\, \Delta\kappa\right) \Delta\kappa\, d\Delta\kappa,$$

where $\Delta\kappa_c = \Delta\kappa(1) = \sqrt{2\left(1-\sqrt{1-\mathrm{NA}^2}\right)}$. The value of the above integral is

$$Q = \frac{4\pi\, k\, \Delta\kappa_c}{\mathrm{NA}\, T\, \|\Delta\mathbf{x}\|_2} J_1\left(k\, \|\Delta\mathbf{x}\|_2\, \Delta\kappa_c\right).$$

The biorthogonality property in (8.7) is satisfied when NA $\to 1$ or equivalently when $\Delta\kappa_c \to \sqrt{2}$, whereupon $Q \to \delta^2(\mathbf{x}-\mathbf{x}')$. However, physical constraints imposed by the experimental system limit the maximum value of $\Delta\kappa_c$. In the experiment, the illumination light is propagating within the region of the object and can be described by the Helmholtz equation. The dispersion relationship of the Helmholtz equation requires that a plane wave propagating with the transverse spatial frequency k_x carries an axial spatial frequency of $k_z = \sqrt{k^2 - k_x^2}$. This condition sets the difference axial spatial frequency to $\Delta k_z = \sqrt{k^2 - k_x^2} - k$. These restrictions enforce a maximum value of the difference wavevector norm of $\Delta\kappa_c = \sqrt{2}$ for NA = 1. This solution to the integral (8.7) is plotted in Fig. 8.5. The horizontal axis is $k\,\|\Delta\mathbf{x}\|_2$. In the limiting case, and if there is no noise, this biorthogonality property results in the exact reconstruction of the object through the inverse operator. For smaller numerical apertures, the width of Q limits the reconstruction resolution.

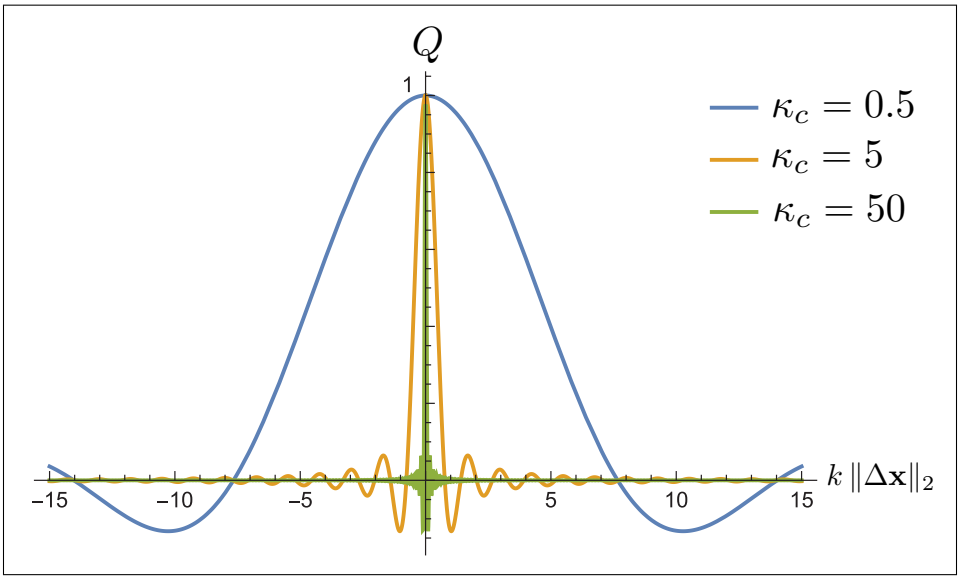

Figure 8.5: Plots of the biorthogonal relationship of the relationship given in (8.7). In the limit as $\kappa_c \to$ inf, the dual and forward model kernels become biorthogonal. Figure from [135].

8.2.3 Data Processing

Equations (2) and (3) in the Letter describe the forward and inverse models for Fluorescence Diffraction Tomography (FDT). Here we describe the detailed signal processing steps required for processing experimental data and using that data for image reconstruction.

As a single scan is taken over one rotation of the modulator mask, the time trace, modeled by Eq. (1), is generated by collecting the signal light on a single-pixel photodetector (Fig. 8.6(a)). The complex demodulated sideband given in Eq. (2) is isolated by first taking a simple Fourier transform of the time trace. The carrier frequency, ω_c, causes the spatial distribution of the projection, $s_\phi(x_\phi)$, to be centered at $+\omega_c$ and a conjugate image is centered at $-\omega_c$, as shown in Fig. 8.6(b) [45, 46]. The carrier frequency plays a role that is analogous to the off-axis reference beam for holography, avoiding the twin image problem [87].

In order to recover the complex object information, the positive single side band is isolated by applying a bandpass filter in the frequency domain, shown as a red dotted line in 8.6(c). Once the bandpass filter has been applied, the signal is converted back into the time domain by taking the inverse Fourier transform. This operation results in a complex time signal that contains the carrier frequency, i.e., the rapid oscillation of the real part of the time signal shown in Fig. 8.6(d). This complex temporal data is then demodulated by the carrier frequency to bring the line image information to the baseband (Fig. 8.6(e)). In total, these operations provide the complex single sideband given by Eq. (2). At this point in the reconstruction workflow, known optical aberrations can be corrected, such as spherical aberration and so-called wobble phase imparted by an imperfectly mounted disc [45, 76, 49, 46].

The demodulated time signal is downsampled to reduce the data size and speed up the reconstruction algorithm, thereby reducing data pressure. Since the time signal is already bandlimited, it is not necessary to apply a lowpass filter in the downsampling operation. The figure in Fig. 8.6(e) shows the real part of the demodulated single sideband signal, $\tilde{S}^{(1)}(t)$, which is used in the FDT reconstruction algorithm (main text, Eq. (3)). Scanning the object over $\theta \in (-180, 180]$ degrees, processing the time traces as described above, and Fourier transform-

ing the downsampled, demodulated, single side band, time trace results in the sinogram shown in the main text, Fig. 2(a).

Each time point in $\tilde{S}^{(1)}(t)$ is a measurement of the magnitude and phase of object spatial frequency representation at the instantaneous projected spatial frequency pair $(\Delta k_x(t), \Delta k_z(t))$ [45, 49, 46]. The inlaid figures in Fig. 8.6(e), above the time trace, show the illumination intensity at a snapshot in time, which is the interference between the reference beam, E_0, and the scanning beam, $E_1(t)$, at a crossing angle, $\theta(t)$, which produces a spatial frequency $\Delta\mathbf{k}(t)$. The illumination intensity excites the fluorescent concentration distribution at the given spatial frequency. The emitted fluorescent light is collected by a single-pixel detector, performing a spatial integration along the spatial coordinates x and z, modeled by Eq. (1). Note that in this work, we assume the detector is infinite in extent for simplicity in our forward model. This large detector size is a good approximation to the experimental system that we have described here; although it should be noted that there are cases in which the finite size of the detector and point-spread-function of detection must be accounted for [48].

The measured spatial frequency information is mapped into the object's spatial domain by the inverse operator (8.6). The action of the inverse operator is illustrated by the inlaid figures below the time trace in Fig. 8.6(e). These inlays illustrate how the measured spatial frequency information is mapped into the object spatial distribution with (8.6). As the disc rotates, each measured spatial frequency component is obtained from an arc that traverses the Ewald sphere over the range of transverse spatial frequencies supported by the NA of the illumination objective. In this way all spatial frequencies supported by the illumination objective are sequentially scanned as the field, E_1, passes through the full spatial frequency support of the imaging system [45, 47]. The green and orange points illustrate high and low spatial frequencies, respectively.

Due to the fact that we sample discrete time points, it is appropriate to express the inverse operator, (8.6), as a Riemann sum. The time points, at time t_i, sampled on a regularly spaced grid with a time step Δt. A fixed set of rotation angles, ϕ_j, are acquired over an angular span of

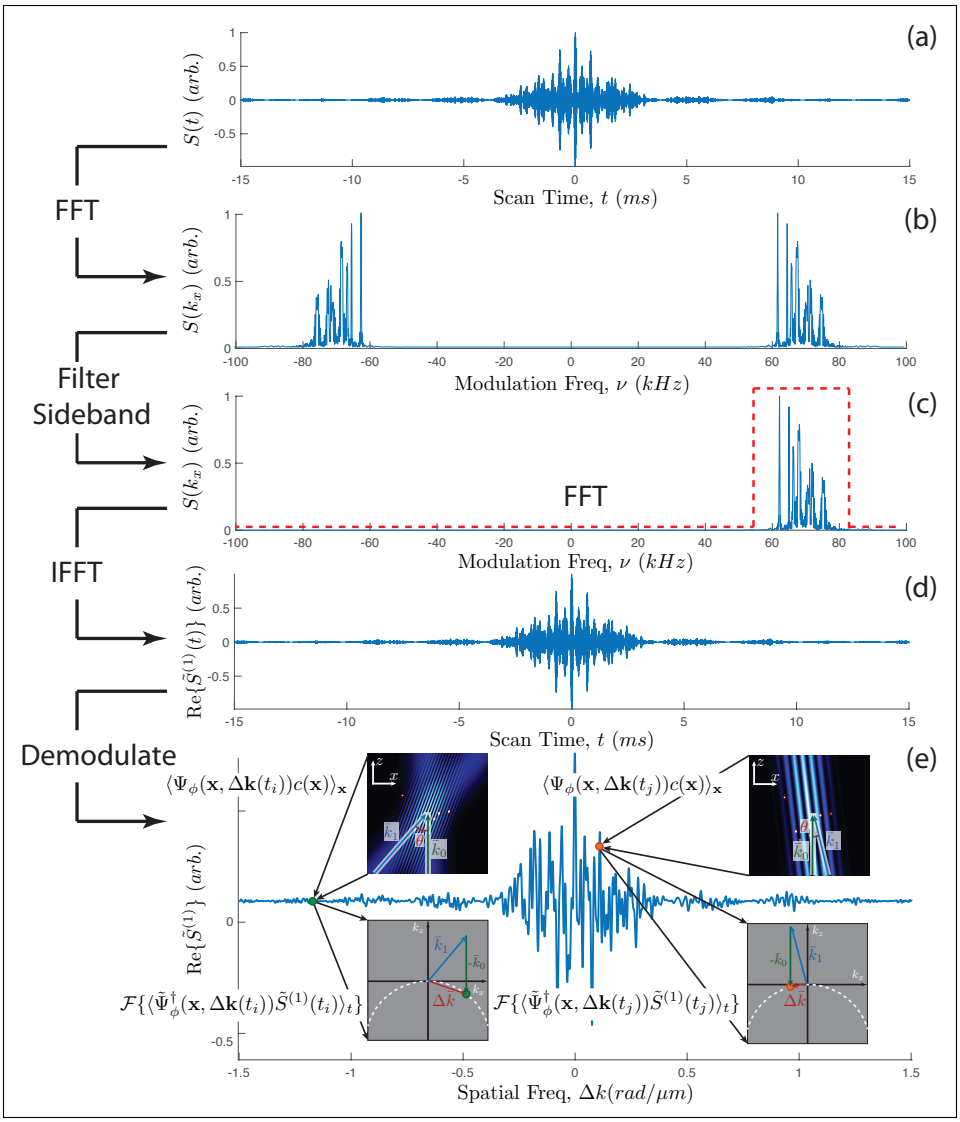

Figure 8.6: The signal processing procedure to generate the FDT sinogram using simulated data. (a) A single time trace, $S(t)$, at an arbitrary angle collected by a photodiode. (b) The spectral density, $\mathscr{F}\{S(t)\}$, displays conjugate symmetry about DC modulation frequency. (c) The spectral density is filtered to isolate the positive sideband, dotted red line. (d) The inverse Fourier transform (iFFT) of the filtered spectral density encodes the spatial phase difference between the illumination beams. (e) The complex time trace is demodulated by the carrier frequency to remove the linear phase ramp. The figures above the time trace illustrate how each time point is generated by two-beam interference and spatial integration by the single-pixel detector, $x-z$ space. The figures below the time trace illustrate how each measured time point represents the complex object spatial frequency, which is mapped to the Ewald sphere in the FDT reconstruction, k_x-k_z space. Figure from [135].

2π with uniform angular spacing $\Delta\phi$, using the index j. This discrete representation leads us to rewrite Eq. (3) in the main text as

$$\hat{c}(x,z) = \sum_{i=0}^{T} \sum_{j=1}^{2\pi} \tilde{\Psi}_{i,j} \tilde{S}^{(1)}_{i,j} \tag{8.8}$$

which can be written explicitly as

$$\hat{c}(x,z) = \sum_{i=0}^{T} \sum_{j=1}^{360} \gamma_i \exp\left[i(\Delta k_{x_i} x_{\phi_j} + \Delta k_{z_i} z_{\phi_j}) \right] \tilde{S}^{(1)}_{i,j} \tag{8.9}$$

where $\gamma_i = k|\Delta k_{x_i}|/(\sqrt{k^2 - [\Delta k_{x_i}]^2})$ is the magnitude of the determinant of the Jacobian, and Δk_{x_i} and Δk_{z_i} are difference wavenumbers in x and z, respectively, x_{ϕ_j} is the rotated x-coordinate vector, and z_{ϕ_j} is the z-coordinate vector. From (8.9), we see that the reconstruction algorithm applied to discrete data is performed in the spatial domain by weighting the dual operator kernel functions, that are sampled on the discrete reconstruction spatial grid, by the complex, demodulated, single sideband time signal samples.

8.2.4 Absorption Contrast

FDT can be used for many contrast mechanisms (we demonstrate fluorescence and absorption), regardless of whether the light emerging from the specimen is coherent or incoherent. While in the main text, we have primarily focused on FDT for fluorescent light, we also demonstrate the ability to extend fluorescent diffraction tomography to simultaneously image light lost to absorption or scattering in transmission. Here, we demonstrate the absorption contrast mechanism, which was simultaneously acquired along with fluorescence on a separate single-pixel detector. The absorption signal was acquired by collecting the transmitted excitation light, 532 nm, on a photodiode (Thorlabs, DET100A). Fig. 8.7 shows the 3D reconstruction of the absorption contrast. The left-hand columns show slices along the $x-y$, $y-z$, and $x-z$ planes in descending order, respectively.

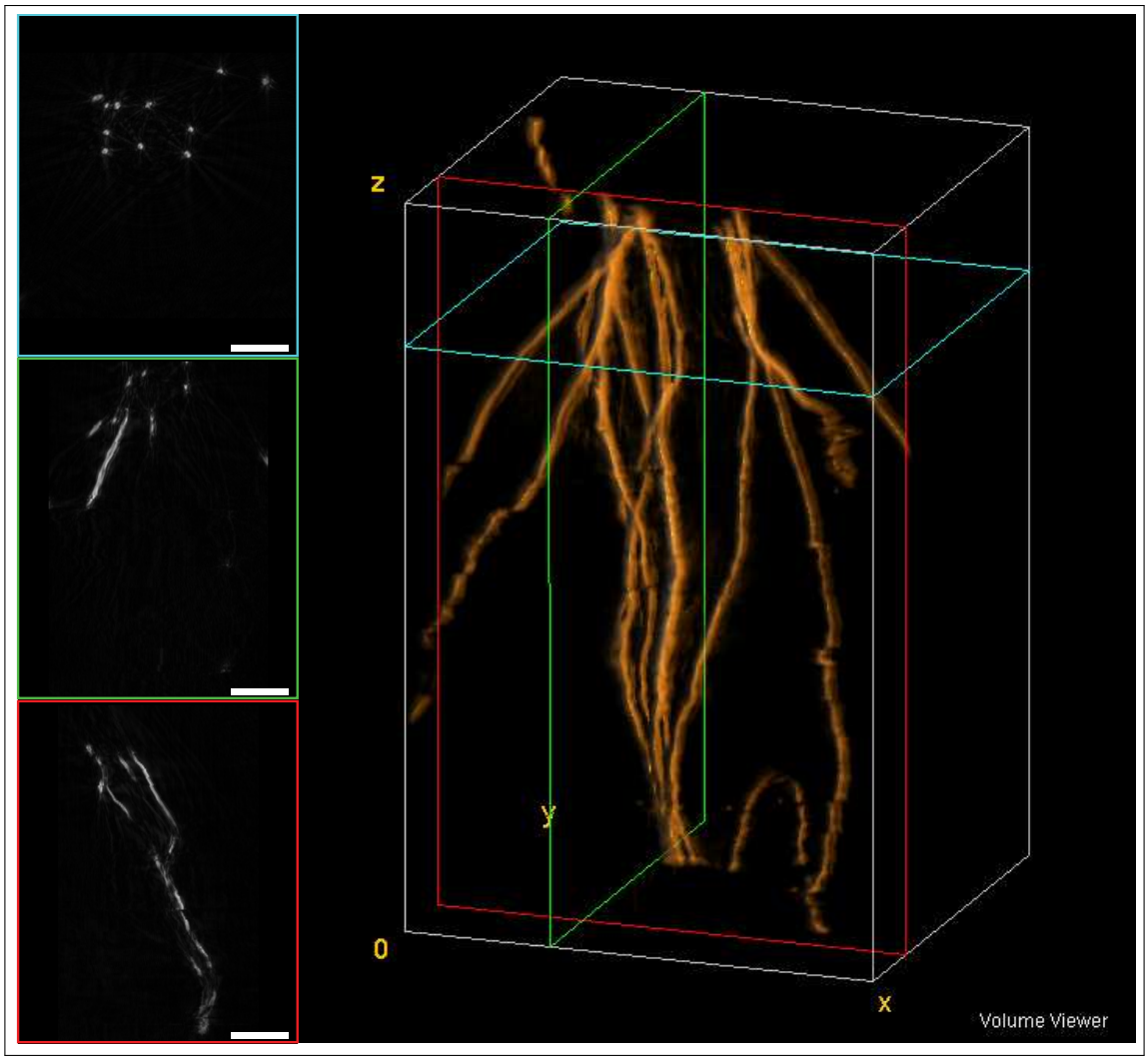

Figure 8.7: 3D reconstruction of absorption contrast of fluorescent stained cotton fibers. The blue panel is an $x-y$ slice of the object indicated by the blue rectangle in the main figure on the right. The green panel is an $y-z$ slice indicated by the green rectangle. The red panel is an $x-z$ slice indicated by the red rectangle. Scale bar equals 60μm. Figure from [135].

8.2.5 FDT Comparison with Backprojection

In the introduction of the main text, we mention one of the major limitations of Optical Projection Tomography (OPT) and Selective Plane Illumination Microscopy (SPIM) is the fact that both techniques exhibit coupling between the object size and spatial resolution [58, 29, 70, 91]. That is, the object being imaged may not be larger than roughly twice the Rayleigh range of the line focus [91]. The reason for this limitation is that both OPT and SPIM assume that the illumination light is approximately planar in the object region so that diffraction is negligible. These

assumptions are only valid inside the Rayleigh range of a beam focus (or the focal region of the point spread function). Therefore, larger objects require a thicker line focus of illumination for SPIM to extend the Rayleigh range over the object, and in the case of OPT, a lower NA objective is used so that the PSF is approximately collimated throughout the object thickness [91]. If this assumption is violated, an out-of-focus blur will result in the final reconstructed image. It is worth noting that several SPIM approaches have appeared that use virtual light sheets with PSF engineering approaches to create diffraction-free light sheets to circumvent this coupling [114].

With FDT, we do not make an assumption of planar illumination since the propagation phase is directly encoded in the measured temporal data. This allows FDT to numerically refocus the entire volume measured by the illumination beams in a similar manner to holography. In previous work, we have demonstrated that the technique underlying FDT, CHIRPT microscopy, not only enables this holographic refocusing of fluorescent images but also exhibits a depth-of-field up to 83× that of conventional imaging at the same NA without sacrificing spatial resolution (~440 μm) [49]. This DOF was measured to extend beyond 1 cm with the same optical components but at the cost of a loss of spatial frequency support. In the reconstruction presented here, it is not necessary to explicitly backpropagate or numerically refocus the line image [49]. Instead, the reconstruction algorithm uses a dual operator to directly synthesize the object in $x-z$. The sum over the kernel function of the inverse dual operator weighted by the complex demodulated values of the time trace recorded for each rotation angle ϕ directly gives the backpropagated object distribution for that measurement angle. The encoded propagation phase allows objects to reside well outside the Rayleigh range of the focus of the illumination light sheet. This allows FDT to effectively decouple the spatial resolution from the maximum object size.

In order to illustrate the importance of encoding the propagation phase has on the reconstruction and the effect it has on the maximum aberration-free field-of-view, we perform two simulations. We start by simulating a sinogram using fluorescence as the contrast mechanism. The sinogram was generated using an illumination wavelength, $\lambda = 532$ nm , a numerical aper-

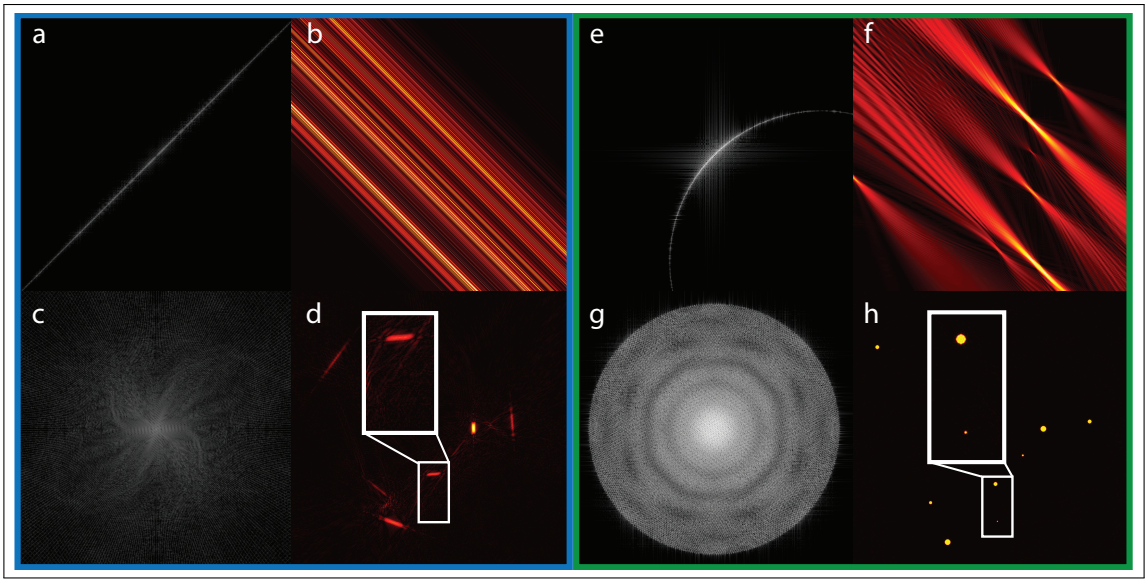

Figure 8.8: Comparison between computed tomography using fluorescence intensity and Fluorescence Diffraction Tomography with phase encoding. Panel (a) shows the 2D spatial frequency support of computed tomography measured at a 45-degree angle. Panel (b) is the 2D FFT of (a) resulting in a 2D image of the object. Panel (c) shows the frequency support when the full sinogram is used in the computed tomography reconstruction. Panel (d) shows the 2D reconstructed object when diffraction is not accounted for in the reconstruction. Panel (e) illustrates how FDT, using modulation transfer, can extract the complex phase information, even from fluorescence, to map the measured spatial frequencies onto the Ewald sphere. Panel (f) shows the 2D object reconstruction using only one line image at a 45-degree angle. Panel (e) shows the full spatial frequency support when the full sinogram is used in the FDT reconstruction. Panel (h) shows the 2D reconstructed object generated by taking the 2D FFT of panel (g). Figure from [135].

ture, NA = 0.90, field of view, FOV = 20 μm, and 360 evenly spaced illumination angles ranging from $\theta = [-180, 180)$ deg, sinogram shown in the main text, Fig. 2(a).

Using the sinogram, two reconstruction strategies were tested. First, we reconstructed the object without the phase information that we obtained from the complex spatial frequency values by using the magnitude of the sinogram, which is equivalent to the information that would be obtained in OPT if the object size was much larger than the Rayleigh range. We reconstructed this data with the filtered back-projection algorithm using an inverse Radon transform (iradon() function in Matlab). The inverse Radon transform is relevant for line-projection tomographies [126, 134]. The results of this reconstruction strategy are shown in Figs. 8.8(a-d). Fig. 8.8 (a) is the 2D frequency support measured at $\theta = 45$ deg. Notice, the frequency support lies on a straight line in the $(k_x - k_z)$ plane at a 45-degree angle, corresponding to the illumination angle,

in agreement with the Fourier slice theorem [78]. Fig. 8.8(b) is the resulting 2D object reconstruction in the $x-z$ plane, generated by taking the 2D inverse Fourier transform of Fig. 8.8(a). The reconstructed object does not exhibit diffraction, i.e., the objects appear as uniform lines of constant magnitude rotated by 45°, which is in accordance with the assumptions made by OPT. Figure 8.8(c) is the frequency support using the full sinogram. The resulting 2D $x-z$ object reconstruction, Fig. 8.8(d), was generated by taking the 2D inverse Fourier transform of Fig. 8.8(c). A radially dependent azimuthal blurring is evident in the reconstructed object. This result is expected since the Rayleigh range of the simulated illumination beam was $\sim 0.365\ \mu$m, while the reconstructed field of view was 20 μm.

By contrast, we compare these same conditions to the inverse operator using Eq. (3) from the Letter. Figures 8.8(e-h) show those results. The reconstructed object using one angle of the discrete algorithm in (8.9), here at $\theta = 45$ deg, is shown in Fig. 8.8(f). Taking a two dimensional FFT of this reconstructed object gives the measured spatial frequency support for the single illumination angle of $\theta = 45$ deg that is shown in Fig. 8.8(e). Notice that the frequency support lines on a curve that is predicted by Fourier diffraction theory. The full object reconstruction using a full 2π angles is shown in Fig. 8.8(h). The spatial frequency support obtained from the 2D FFT of the object estimate is shown in Fig. 8.8(g). We see that the reconstructed object does not contain an azimuthal blur and the points localize the object position, only limited by the diffraction limit set by the NA of the objective.

We note that this simulation considered planar illumination in the $x-z$-plane only, neglecting effects caused by the DOF of the light sheets used for illumination in the orthogonal (y) dimension. We have previously described that CHIRPT has two distinct DOF metrics – one based on intensity modulations in the $x-z$ plane, and the other dictated by the properties of the focused illuminating light sheet [48]. While this DOF in the vertical dimension would ultimately place a practical limit on the spatial resolution in y, the fidelity of the reconstructed image in the $x-z$-plane should not suffer. Further, we note that a variety of PSF engineering

strategies could be employed to maintain spatial resolution in the vertical dimension over the full FOV [48].

Chapter 9

Introduction to Super Resolution

9.1 Introduction

Optical imaging has played a key role in many biological discoveries due to its ability to spatially resolve the dynamics and internal components of live cells and organisms. Until recently, microscopes have only been able to resolve spatial features slightly smaller than half the wavelength of light, ~250 nm. This spatial diffraction limit has been shattered by the introduction of super-resolution (SR) imaging [**1**, **2**]. SR microscopy has transformed our ability to probe intracellular dynamics on an extremely fine spatial scale. The list of discoveries from SR microscopy studies are growing rapidly, which includes observations of the architecture of the nuclear pore complex [**3**], the discovery of periodic actin-spectrin-adducin cytoskeletal rings in neuronal axons [**4**], observation of the process of *in situ* aggregation and the aggregate morphology of intracellular β-Amyloid Fibrils [**5**], observation of the structure of DNA at the end of the linear chromosome [**6**], the discovery that shelterin complex protects chromosome ends from unwanted DNA repair processes [**7**], and the measurement of nanostructures involved in DNA replication [**8**].

The potential of SR imaging to uncover new mechanisms of signaling pathways and biochemical interactions in healthy and sick organisms is vast. Such discoveries could lead to new paradigms for treatments and new drug targets. Yet current SR microscope technology offers only limited potential for the application of translating a new understanding of fundamental biological mechanisms to new targets for disease detection and treatment. A major impediment is that the clear majority of studies using SR microscopy are with cultured cells grown outside of their natural environment, *i.e.,* in vitro 2D cultures [**2**]. In many cases 2D cell culture results fail to translate into successful treatments [**9**]. Increasing attention has been directed to the use of three-dimensional (3D) cell cultures and in vivo experiments due to the limitations of 2D cul-

tures [**10**, **11**]. SR microscopy methods rapidly fail when imaging in tissues and 3D cultures due to strong optical scattering.

SR imaging techniques are routinely used for biomedical experiments in cells. The microscopes are based on either localization microscopy (LM), such as photoactivated localization microscopy (PALM) [**12**] and stochastic optical reconstruction microscopy (STORM) [**13**], or spatially structured illumination, such as structured illumination microscopy (SIM) [**14**] and stimulated emission depletion (STED) [**15**]. While each of these methods has achieved spatial resolution down to tens of nanometers, these methods are not able to operate in optically scattering specimens, such as uncleared biological tissues. This has largely prevented SR imaging in live animals or in vitro organotypic tissue slices.

Imaging in tissues is challenged by light scattering, absorption, and specimen-induced optical aberrations, limiting the penetration depth of optical SR imaging in tissue. Specimen-induced aberrations degrade SR images even at depths of a few micrometers [**16**]. Both LM and SIM rely on widefield microscopy. LM forms images by activating sparse groups of individual fluorophores in a specimen. The centroid of the point-spread function (PSF) from each fluorescent spot is estimated, and the centroids are used to build a final image from a sequence of images, each with a random distribution of excited fluorophores. Similarly, nonlinear structured illumination microscopy (NSIM) [**14**] achieves super-resolution through the measurement of multiple widefield images with a sequence of periodic illumination intensity patterns. Unfortunately, widefield imaging rapidly fails in tissues because scattering blurs the fluorescent light as it exits the specimen. Optical aberrations further degrade these techniques [**17**].

Conversely, STED and related ground state depletion (GSD) [**18**] and REversible Saturable Optical Linear Fluorescence Transitions (RESOLFT) [**19**] methods utilize single-pixel detection, such as a photomuliplier tube (PMT), to collect super-resolved image data. STED uses two laser beams. The excitation beam excites fluorophores in a diffraction-limited spot. A second depletion beam that is shaped like a doughnut drives excited molecules back to the ground state, producing a sub-diffraction-limited fluorescent emission spot. These beams are then simul-

taneously scanned to form an image. STED image resolution is highly sensitive to the spatial shape of the depletion beam, which degrades rapidly with optical aberrations and undergoes significant distortion due to scattering in biological media, limiting imaging depth. Despite these challenges, STED has been used for imaging dendritic processes in acute mouse brain slices revealing previously unobserved dendritic spine morphologies up to 50 μm deep [**19**, **20**], and actin in dendritic spines at a penetration depth of up to 120 μm [**21**].

In this chapter, a unified theory is discussed to compare all major super-resolution techniques on the basis of their optical transfer function (OTF) given the photo-physics utilized to obtain super-resolution. Additionally, we develop theory for CHIRPT and SPIFI unrestricted super-resolution (URSR) imaging which allows easy comparison to the other major super-resolution techniques, namely STED, RESOLFT, and SAX.

One challenge for computing the PSF and OTF for CHIRPT, SPIFI, and SAX URSR imaging is that the spatial frequency amplitudes must be determined for a set of harmonic orders generated by the nonlinear functions (either Saturated Absorption (SA) or RESOLFT). In this chapter, I present expressions for the PSF and OTF of URSR spatial frequency imaging techniques. We apply the same theory to both RESOLFT and SAX URSR imaging methods to facilitate a direct comparison so that the relative advantages and disadvantages can be readily compared. For periodic modulation of illumination intensity, the imaging properties can be readily computed by making use of a cosine series expansion of the modulated illumination intensity.

9.1.1 Single pixel imaging of fluorescent probes

While conventional optical imaging generally produces a real optical image that is recorded with a segmented optical detector, such as a camera chip, single-pixel imaging utilizes a sequence of measurements with a single optical detector surface so that the total incident optical power is recorded for each measurement. The most common single-pixel imaging methods are confocal and nonlinear laser scanning microscopies [100]. These methods have been widely adopted for their ability to form three-dimensional images in addition to providing some im-

munity to image contamination from optical scattering [66]. A full spatial image is produced by sequentially scanning the object position, tailoring a sequence of illumination light intensity spatial distributions, or a combination of the two.

In 2.1, a general framework for single-pixel imaging was described, here that framework will be used to describe imaging with self-luminescent objects such as fluorophores. The key to single-pixel imaging is that the object information is encoded in time rather than in space as is the case when an image is formed on a camera. The single-pixel detector generates a photocurrent directly proportional to the light collected from the object. Considering a molecular probe such as a fluorescent emitter, the emitted fluorescence is proportional to the population of the electronically excited bright state $|e\rangle$. The emitted power for each excited molecule is $W_f = \hbar\omega_f k_r |e(\mathbf{r},t)\rangle$, so that the emitted fluorescent intensity for a fluorophore concentration distribution $c(\mathbf{r})$ reads as:

$$I_f(\mathbf{r},t) = \hbar\omega_f k_r |e(\mathbf{r},t)\rangle\, c(\mathbf{r}) \tag{9.1}$$

Here, ω_f is the fluorescent emission optical frequency, $\hbar$ is Planck's constant divided by 2π, and k_r is the fluorescent (radiative) emission rate. Note that the excited state of the molecule is denoted as a function of position and time. The positional dependence will be important when structured illumination is introduced and the temporal dependence allows for temporal saturation. It has also been assumed no interaction between the molecules.

In a weak excitation regime, the excited state population is directly proportional to illumination light intensity that drives the molecules into the excited state:

$$|e(\mathbf{r},t)\rangle \approx \frac{I_{\text{ill}}(\mathbf{r},t)}{I_{sat}} \equiv \alpha(\mathbf{r},t) \tag{9.2}$$

where I_{ill} is the illumination intensity of the excitation beam, and the saturation intensity of the transition reads $I_{\text{sat}} = \hbar\omega_a/\sigma_{\text{abs}}\tau_e$. The absorption transition frequency is ω_a and the transition displays an absorption coefficient of σ_{abs} with an excited state lifetime τ_e. In the linear regime, $\alpha \ll 1$.

The signal collected by the single-pixel detector,

$$S_t = \frac{\eta}{\hbar\omega_f}\left(\frac{\Omega_c}{4\pi}\right)\langle I_f(\mathbf{r},t)\rangle_{\mathbf{r}} = A\langle I_{\text{ill}}(\mathbf{r},t)\,c(\mathbf{r})\rangle_{\mathbf{r}}, \tag{9.3}$$

is a projection of the illumination intensity onto the object's spatial distribution. The fluorescent intensity $I_f(\mathbf{r},\mathbf{t})$ depends on position and time. The positional dependence is due to the object molecular concentration, $c(\mathbf{r})$, and the molecular excited state population which is controlled by the spatial variation of the illumination intensity. Here also, time, t, denotes a slowly varying illumination intensity, which varies slowly compared to the timescale of the molecular excitation kinetics. The proportionality constant, A, is determined by both the fluorophore excitation coefficients in (9.1), and the fraction of collected light emitted by the object, $(\Omega_c/4\pi)$, where Ω_c is the solid angle of the light collected on the detector, the detector efficiency, η, and the fluorescent light photon energy, $\hbar\omega_f$. For convenience, we will set $A = 1$ in the expressions that follow to simplify the presentation of the theoretical results. This scaling factor can be easily restored in the expressions when absolute signal levels and signal-to-noise ratio (SNR) values need to be computed.

An object reconstruction estimate can be readily built from the measured projections and the imaging point spread function can be derived from the object response and illumination intensity, leading to the expression for the estimate of the object [45, 46, 47, 136]:

$$\hat{c}(\mathbf{r}) = \text{PSF}(\mathbf{r}) * c(\mathbf{r}). \tag{9.4}$$

Here, the reconstructed object is equal to the point spread function convolved with the object concentration.

9.2 Population kinetics of electronic states

Superresolution imaging is benchmarked relative to the performance of conventional diffraction-limited imaging techniques. In both cases, metrics are assigned to the spatial reso-

lution of the imaging system or the spatial frequency support (passband) of the system. These metrics are convenient, but fail to fully characterize spatially resolved structure in an image. Imaging quality depends critically on the signal-to-noise ratio (SNR) of the image information at each recorded spatial frequency, and the method that we present here enables higher-quality image formation, even within the same spatial frequency band. Moreover, utilizing saturated absorption theoretically allows unrestricted spatial resolution to be achieved.

Unrestricted super-resolution (URSR) imaging is based on nonlinear switching of the population of energy states in a probe molecule. The light emitted by a fluorescent molecular probe is proportional to the population of an excited energy level, $|e\rangle$, in a molecule with a high quantum yield. In conventional fluorescent imaging, the spatial variation in the linearly excited state population, $|e(\mathbf{r}, t)\rangle$, is directly proportional to the spatial distribution of the illumination light that excites the molecule, $I_{\text{ill}}(\mathbf{r})$, producing a diffraction-limited region of fluorescent emission. In this linear limit, the spatial distribution of the emitted fluorescent light reads $I_f(\mathbf{r}) = \sigma_f I_{\text{ill}}(\mathbf{r})$, where σ_f is the fluorescence emission cross-section. URSR imaging uses spatially modulated control light to drive nonlinear switching of molecules to reshape the spatial distribution of the excited molecules that are emitting fluorescent light – either by restricting the spatial region where spatial information is captured or by expanding the recorded spatial frequency information about the specimen. Optically controlled nonlinear switching is induced by driving stimulated transitions between electronic states in molecules to manipulate electronic population levels through laser control of the energy level population kinetics.

A number of photophysical and photochemical mechanisms have been developed for nonlinear switching of fluorescent emission to achieve sub-diffraction limited imaging with each URSR strategy. It is the spatial-temporal excited state population of the molecules which dictates the imaging properties of the fluorescent microscope. Here, we show that the disparate strategies can be described in a unified manner by considering the process of saturation of stimulated absorption. In Unrestricted Super Resolution (URSR) imaging, the excited state population of molecules are controlled using an excited bright state with a spatial dependence that

allows microscope resolution to go beyond the diffraction limit. There are many methods of achieving this with varying numbers of laser beams, however, all of these techniques can be described by the excited state population. Using stimulated optical interactions, the spatial and temporal variation of the population of fluorescing molecules is given by a nonlinear function that depends on the illumination intensity, $I_{\rm ill}(\mathbf{r})$, through a nonlinear mapping of the population of the excited state in the molecule, $|e(\mathbf{r})\rangle = F[\alpha(\mathbf{r})]$. Here, we have defined the saturation parameter for the resonant interaction as $\alpha(\mathbf{r}) = I_{\rm ill}(\mathbf{r}) I_{sat}^{-1}$, which depends on the saturation intensity $I_{sat} = \hbar\omega/(\sigma_{\rm abs}\tau_e)$, the excited state lifetime, $\tau_e = (k_r + k_{\rm nr})^{-1}$, the absorption cross-section $\sigma_{\rm abs}$ at the absorption frequency ω, and the radiative k_r and nonradiative $k_{\rm nr}$ relaxation rates.

The behavior of URSR laser control kinetics can be understood by observing the saturation of the excited state population behavior that follows from solving the population rate equations for a three-level model of an atom or molecule,

$$\frac{\mathrm{d}\,|e\rangle}{\mathrm{d}\,t} = -\frac{\mathrm{d}\,|g\rangle}{\mathrm{d}\,t} = -k_i\,|g\rangle + (k_r + k_{\rm nr})\,|e\rangle\,, \tag{9.5}$$

where the stimulated absorption rate driven by a resonant illumination light beam is $k_i = \alpha(\mathbf{r})/\tau_i$, Here, we have assumed a molecular system so that we can neglect stimulated emission of the illumination beam due to rapid relaxation on the excited state vibrational manifold.

URSR microscopies can be uniformly understood by considering the nature of the nonlinear saturation function for the simple molecular system kinetics given above. The excited state population for a molecular absorber driven into saturation can be written as $|e(\mathbf{r}_\perp)\rangle = F[I_\ell(\mathbf{r}_\perp) I_{\rm sat}^{-1}]$. The nonlinear saturation function, $F[\cdot]$, can be readily described in the limiting cases for both the case of steady-state (continuous wave – cw) excitation and pulsed excitation:

$$F[\alpha(\mathbf{r},t)] = \begin{cases} \alpha(\mathbf{r},t)\;(1+\alpha(\mathbf{r},t))^{-1} & \text{cw case} \\ 1-\exp(-\alpha(\mathbf{r},t)\,T/\tau_e) & \text{pulse case} \end{cases} \tag{9.6}$$

where we define $\alpha = I_\ell(\mathbf{r}, t)/I_{\text{sat}}$ as the saturation parameter that is a function of space and time driven by the illumination beam.

The CW approximation is valid for a pulse duration that is long compared to the excited state lifetime. Alternately, for the pulsed case, we consider pulses with a temporal duration that is short compared to the excited state lifetime. In general, the nonlinear population function depends on the specific temporal shape of the pulse. For simplicity, in (9.6), we present the result for a square pulse of duration T given by $I_{\text{ill}}(\mathbf{r}, t) = I_{\text{ill}}(\mathbf{r})\text{rect}(t/T)$.

When the illumination beam is well below saturation, then linear excitation is recovered, where $F \approx \alpha(\mathbf{r})$ for CW illumination and $F \approx (T/\tau_e)\alpha(\mathbf{r})$ for pulsed excitation. At intensity levels that exceed the saturation intensity, the single illumination beam switches molecules to the excited on state more readily than in the linear excitation regime producing a larger spatial area of fluorescent light emission. The saturated absorption mechanism has been used in various imaging modalities [162, 57].

9.3 Super resolution through excited state population control

Controlling the spatial distribution of the excited state population is the mechanism that admits the feasibility of unrestricted super-resolution imaging. URSR imaging may be described in terms of a linear translation invariant (LTI) model in the same matter as linear, diffraction-limited imaging, however, we now define an effective PSF.

$$\hat{c}(\mathbf{r}) = \text{PSF}_{\text{eff}}(\mathbf{r}) * c(\mathbf{r}) \tag{9.7}$$

where the effective PSF is defined as $PSF_{\text{eff}} = PSF_c(\mathbf{r})\eta(\mathbf{r})$. The conventional point spread function, $PSF_c(\mathbf{r})$, is the diffraction-limited PSF defined by the Abbe limit and $\eta(\mathbf{r})$ is the spatial sharpening efficiency which depends on the specific super-resolution technique. The general prescription for determining $\eta(\mathbf{r})$ changes form depending on the nonlinear photon interac-

tion, i.e. excitation or de-excitation.

$$\eta(\mathbf{r},t) = \begin{cases} \beta F[\alpha(\mathbf{r},t)] & \text{Switching ON} \\ 1-\beta F[\alpha(\mathbf{r},t)] & \text{Switching OFF} \end{cases} \tag{9.8}$$

The spatial sharpening efficiency is also going to depend on the photo-physics of the URSR technique. β is a lifetime ratio, a type of efficiency, that is equal to 1 when there is only one excited state, however, when there are multiple excited state β will be less than 1 and defined as $(1+k_t/k_{isc})^{-1}$, where k_t is the triplet decay rate and k_{isc} is the intersystem crossing rate. Finally, the OTF can be determined by taking the Fourier transform of the effective PSF, $OTF = \mathscr{F}\{PSF_{eff}\}$. With these parameters defined the PSF of any URSR technique can be analyzed.

URSR imaging is accomplished through controlled population switching with the illumination light field, the spatial resolution is determined by the excited state population that remains after the interaction with the excitation and depletion beams. The effective point spread function, $\mathrm{PSF}_{\mathrm{eff}}(\mathbf{r})$ can be physically understood by considering the final excited state population, $|e(\mathbf{r})\rangle \propto \mathrm{PSF}_{\mathrm{eff}}(\mathbf{r})$.

9.4 REversible Saturable Optical Linear Fluorescence Transitions (RESOLFT)

The majority of URSR methods make use of self-luminous light emission by an object, and we focus our discussion on those techniques here that make use of single-pixel detection. The techniques of REversible Saturable Optical Linear Fluorescence Transitions (RESOLFT) and Saturated Absorption Excitation (SAX) are firmly established, and we will briefly review the theoretical description of these techniques as a point of comparison of our theory that we present for URSR using CHIRPT and SPIFI imaging.

The general idea of RESOLFT imaging is point spread function engineering by controlling the excited state population of fluorescent molecular probes. This is typically accom-

plished by an initial excitation set to operate well below the saturation intensity so that the excitation is linear, and the initial excited state population is proportional to the diffraction-limited point spread function, $|e_0(\mathbf{r})\rangle \propto \mathrm{PSF_c}(\mathbf{r})$. The efficiency of the depleted population, $\eta_D(\mathbf{r}) = (1 - \beta\ F[I_D(\mathbf{r},t)])$, describes the fraction of the initially excited population, $|e_0(\mathbf{r})\rangle$, that has been switched back to the dark state. It follows that the effective point spread function for RESOLFT imaging is then defined by $\mathrm{PSF_{eff}}(\mathbf{r}) = \mathrm{PSF_c}(\mathbf{r})\,\eta_D(\mathbf{r})$ and is a factorable product of $\mathrm{PSF}_c(\mathbf{r})$, the image response function for conventional diffraction-limited imaging and the efficiency of depletion, $\eta_D(\mathbf{r})$. The effect of switching off the excited state molecules reduces the spatial width of the excited fluorescent molecules – leading to a narrower spatial width of the $\mathrm{PSF_{eff}}$, and a correspondingly broadened spatial frequency support. The calculation of the $\mathrm{PSF_{eff}}$ and the corresponding OTF are straightforward since we have a direct functional dependence from the solution of the rate equations.

Using the above general theory of super-resolution, we will analyze several popular techniques, namely STED, GSD, and SAX. In this way of demonstrating by example, we will be well prepared to apply the theory to SPIFI and CHIRPT imaging allowing us to readily see how all these URSR techniques are related.

9.4.1 STimulated Emission Depletion (STED)

Stimulated emission depletion (STED) was one of the first URSR techniques to be developed and remains a dominant technique. Because of its dominance, there have been many improvements or modifications to the technique, however, they all follow the same unifying principle so we will focus on the vanilla technique, knowing that the general theory can be readily applied to any of the variants. The initial excitation beam operates in a linear regime, and we will describe that excited population by the parameter $|e_0(\mathbf{r})\rangle$. For a CW laser beam, $|e_0(\mathbf{r})\rangle = \alpha_e(\mathbf{r})$ where we define the saturation parameter for excitation as $\alpha_e(\mathbf{r}) = I_e(\mathbf{r})I_{\mathrm{sat},e}^{-1}$ where $I_e(\mathbf{r})$ is the excitation beam intensity and the saturation intensity for the excitation beam as $I_{\mathrm{sat},e} = \hbar\omega_e/(\sigma_e\tau_e)$, where σ_e is the absorption cross section at the excitation beam frequency ω_e. For a pulsed ex-

citation intensity, $I_e(\mathbf{r}, t) = I_e(\mathbf{r})u_e(t)$ for a square pulse with a duration T_e and $u_e(t)$ is the pulse temporal profile, the excited state population in the linear regime reads $|e_0(\mathbf{r})\rangle = (T_e/\tau_e)\alpha_e(\mathbf{r})$.

In this regime of linear excitation, the spatial region of the excitation beam is determined by the size of the excitation beam intensity, $I_e(\mathbf{r})$, and is thus diffraction-limited. To attain URSR, a depletion beam intensity is co-focused with the excitation beam so that the edges of the excited molecules are switched off. While this depletion beam is also diffraction limited, the fact that the switching is driven nonlinearly by saturating the depletion intensity allows the excited molecules to be confined to a small region near the center of the excited molecules – enabling a region of probe molecules much smaller than the diffraction-limited spatial spot to be imaged.

In STED, two lasers are used: an excitation laser and a depletion laser. The excitation laser promotes electrons in the ground singlet state to the first excited singlet state. The depletion beam is shifted to a longer wavelength and a stimulated emission interaction depletes the population in the excited state and sends it back to the ground singlet state. The excitation beam is typically a diffraction-limited spot, we can assume that it is Gaussian, whereas the depletion beam is shaped to spatially restrict the distribution of the fluorophores in the bright state to a region much smaller than the excitation light distribution by virtue of the nonlinear switching mechanism. With the application of these two laser fields, the population of the bright state in the excited singlet state is given by

$$|e(\mathbf{r})\rangle = |e_0(\mathbf{r})\rangle\,(1 - \beta\, F[I_D(\mathbf{r}, t)]). \tag{9.9}$$

Here, the nonlinear functions for de-excitation are given by the same nonlinear functional forms as saturated absorption, (9.6) the saturation intensity used for the depletion interaction is determined by the spectroscopic parameters at the depletion transition frequency ω_D for an absorption coefficient σ_D, leading to $I_{\mathrm{s,D}} = \hbar\omega_D/\sigma_D\tau_e$. When the depletion beam is pulsed with a form given by $I_D(\mathbf{r}, t) = I_D(\mathbf{r})u_D(t)$.

The parameter β depends on the particular RESOLFT process employed for superresolution imaging. In the case of STED and photoswitching, $\beta = 1$. These same functional forms are valid

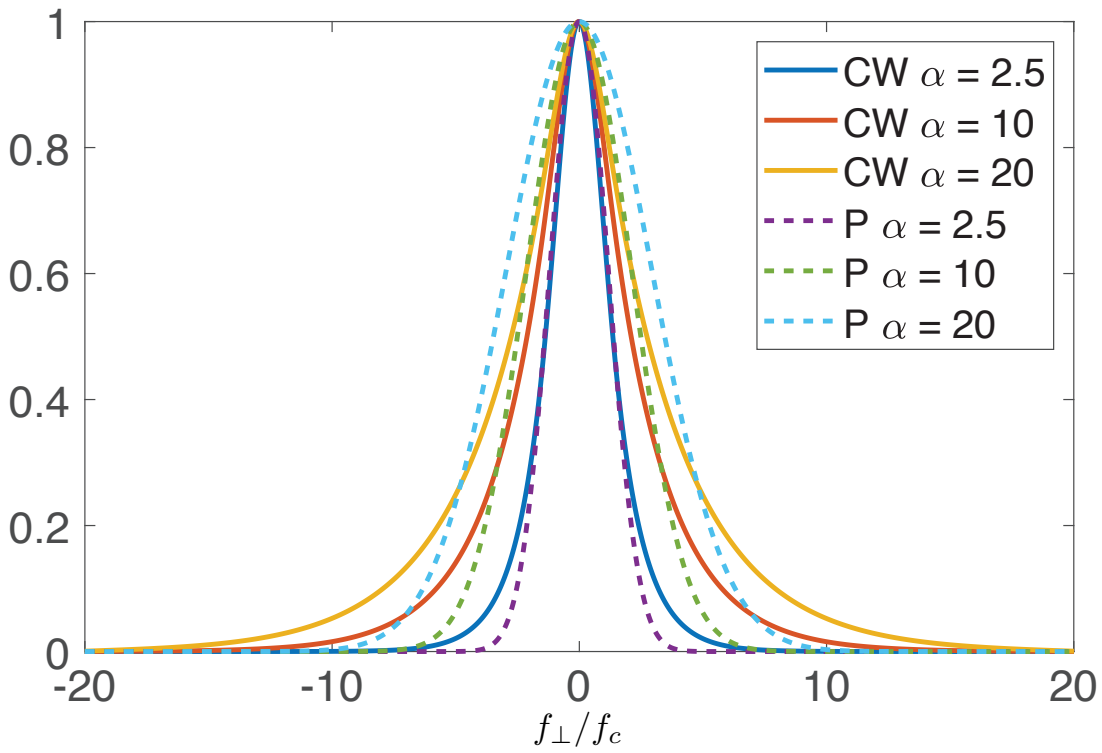

Figure 9.1: This figure shows the MTF of continuous-wave (CW) and pulsed (P) STED imaging at various saturation levels (α). The dotted lines show the MTFs for pulsed illumination and the solid lines show the MTFs for CW illumination. The code used for generating data for the plot can be found in appendix D.

for photoswitching molecules, where the primary distinction is that the molecules are switched between metastable states with long excited bright state lifetimes which allows for significantly reduced illumination intensities of the excitation and depletion/switching beams.

The depletion beam is a doughnut beam produced in the focal plane with a peak intensity of the sidelobes that are driven deep into saturation. The zero of the doughnut beam is centered on the peak of the excitation beam, $\mathrm{PSF_c}$. The functional form of the depletion efficiency can be approximated by a second-order Taylor expansion about the zero [60] so that $I_D(\mathbf{r}_\perp) \approx a\,\mathbf{r}_\perp^2$. For the case of the imaging of a beam that has passed through a spiral phase plate, the parameter a is given by [60]

$$a \approx 0.429[I_D(\mathbf{r}_\perp)]_{max}\left(\frac{2\pi\ \mathrm{NA}}{\lambda}\right)^2. \tag{9.10}$$

Here, $[I_D(\mathbf{r}_\perp)]_{\max}$ is the maximum value of the doughnut beam lobes. The spatially varying depletion efficiency is then computed by making use of the nonlinear saturation function given in (9.6). For the case of pulsed excitation with a square pulse of duration T, the depletion is given by $\eta_D(\mathbf{r}_\perp) = \exp\left(-(T/\tau_e)\, a\mathbf{r}_\perp^2\right)$, and the effective point spread function reads

$$\begin{aligned} \mathrm{PSF}_{\mathrm{eff}}(\mathbf{r}_\perp) &= \mathrm{PSF}_c(\mathbf{r}_\perp)\eta_D(\mathbf{r}_\perp) \\ &= \mathrm{PSF}_c(\mathbf{r}_\perp)\, \exp\left(-(T/\tau_e)\, a\mathbf{r}_\perp^2\right). \end{aligned} \tag{9.11}$$

The optical transfer function is found by a Fourier transform of $\mathrm{PSF}_{\mathrm{eff}}(\mathbf{r}_\perp)$.

The expressions above show that the nonlinear switching of URSR process can be fully characterized by the nonlinear saturated absorption function given in (9.6). The shape of the modulation transfer function (MTF), the magnitude of the Fourier transform of the PSF, is shown in fig. 9.1 for both continuous-wave (CW) and pulsed illumination for various levels of saturation. It is seen in the figure that CW illumination outperforms pulsed illumination for the same saturation level. In theory, the resolution enhancement is unlimited assuming the molecules can be driven deep into saturation, however, in practice, there are restrictions on the level of saturation that can be achieved which depends on how much power the molecules can take before ionizing and getting destroyed by the illumination intensity.

9.4.2 Ground State Depletion (GSD)

Ground state depletion (GSD) imaging gets its inspiration from STED, however, it uses a very different mechanism to control the electronic population. In GSD, the depletion beam aims to promote ground-state electrons to a long-lived triplet state. The kinetics parameters for involving the triplet state are the rate of spontaneous relaxation from the triplet state to the ground state, k_t, and the rate of inter-system crossing from the bright excited singlet state to the triplet state, k_{isc}. With these parameters, we may defined a GSD parameter $\beta = (1 + k_t/k_{\mathrm{isc}})^{-1}$. This leads to the excited state lifetime $\tau_{\mathrm{GSD}} = \tau_e/(1-\beta)$, that is used to define the GSD saturation intensity, $I_{\mathrm{sat,e}} = \hbar\omega_e/(\sigma_{\mathrm{abs}}\tau_{\mathrm{GSD}})$. This saturation intensity is reduced by a factor of $(1-\beta)$)

compared to the saturation intensity for saturated absorption (SA), STED, or photoswitching processes. The cost for this reduced intensity is slower population recovery dynamics microseconds as compared to nanoseconds for saturated absorption and STED processes, slowing down image formation.

The illumination intensity of the depletion beam, $I_{D,GSD}$, has a donut profile that is identical to STED depletion beam profile, so the same quadratic beam approximation can be used here. However, in the case of ground state depletion (GSD), a resonant excitation beam is used to place the molecule in the excited singlet state for some time. If the inter-system crossing rate is higher than the triplet decay rate, then a significant population can be shuttled to the triplet state and stored there (for μs - ms times). This is the "depletion beam" and is applied for some initial time duration. Then, the remaining molecules are "read out" by exciting the molecules (not in the triplet state) with a diffraction-limited illuminated field of the same frequency. This is what we will compute, and we will distinguish the two fields as depletion (D) and illumination (e). After turning off the depletion beam, the illumination beam can be turned on to excite the remaining molecules not in the triplet state in the excited singlet state which relaxes back down in a few nanoseconds.

The effective PSF can be computed as

$$\begin{aligned} PSF_{eff}(\mathbf{r}_\perp) &= PSF_c(\mathbf{r}_\perp)\eta_D(\mathbf{r}_\perp) \\ &= PSF_c(\mathbf{r}_\perp)\big[1-\beta F[I_{GSD}]\big] \end{aligned} \tag{9.12}$$

Here, again we make use the general theory to describe the specific case of GSD. The MTF can be readily calculated by taking the magnitude of the Fourier transform of the effective PSF. Note that the shape of the MTF for GSD is the same as that of STED; the only difference is that the efficiency of the excitation is determined by the factor β.

9.5 Saturated Absorption Excitation (SAX)

Saturated absorption methods are techniques that utilize harmonic distortion, either temporally or spatially, to access spatial frequency information beyond the diffraction limit. Saturated absorption also benefits from only needing a single illumination beam, however, the saturation process switches more molecules on as the saturation parameter, α, increases. The increased switching of molecules leads to a number of problems, in particular, increased photobleaching rates.

Saturated Absorption Excitation (SAX) imaging uses an illumination beam that is modulated in time and focused to a point. This leads to a spatio-temporally modulated illumination intensity of $I_\ell(\mathbf{r},t) = (I_{\max}/2)[1+\cos(\Phi_t)]$ where the temporal modulation is described by $\Phi_t = \omega_m t$. For low modulation frequencies, $\omega_m < 2\pi/\tau_e$, the excited state population depends on the illumination intensity and the fluorophore concentration. When higher modulation frequencies are used, super-resolved lifetime imaging is possible []. When the maximum intensity is on the order of or larger than the saturation intensity, i.e., $\alpha = I_{\max}/I_{\text{sat}} \gtrsim 1$, the excited state population of the fluorophore excited state population is given by $|e(\mathbf{r})\rangle = F[\alpha\{1+\cos(\omega_m t)\}\text{PSF}_c(\mathbf{r})]$. In a SAX imaging experiment, the q^{th} harmonic of the modulation frequency is detected – resulting in increased spatial resolution due to a narrower PSF at the harmonic.

9.5.1 SAX cosine series expansion

SAX makes use of a temporally periodic illumination pattern to produce a signal that is proportional to the nonlinear functional response to the periodic illumination pattern, i.e., $S \propto F[I_\ell(\mathbf{r},t)]$. The super-resolution image signal is extracted from the harmonics of the periodic signal and can thus be represented by a cosine series expansion of the signal fluctuations from the mean, $\Delta S = \sum_q b_q \cos\big(q\,\Phi\big)$. The cosine expansion coefficients are defined by

$$b_q \equiv \frac{1}{2\pi}\int_{-\pi}^{\pi} F[I_\ell(\Phi)]\cos\big(q\Phi\big)\mathrm{d}\Phi \tag{9.13}$$

The nonlinear saturation and depletion functions can be expressed as a cosine series using the same set of expansion coefficients for both processes that switch ON (+: saturated absorption and discrete nonlinear excitation) and switch OFF (-: RESOLFT, STED, GSD, photoswitching) the final population of the bright excited state

$$\left|e^{\pm}(\mathbf{r})\right\rangle = |e_0(\mathbf{r})\rangle \left[b_0^{\pm} \pm 2\, b_q \sum_{q=1}^{\infty} \cos\left(q\, \Phi\right) \right] \tag{9.14}$$

and there the DC level, $b_0^{\pm}$, shifts according to whether the URSR process switches molecules ON or OFF, $b_0^{+} = b_0$ and $b_0^{-} = 1 - b_0$. The positive term (+) is for saturated absorption and nonlinear absorption of order m, where the molecules are switched ON, and (-) is reserved for depletion where molecules are switched to an OFF state. In addition, RESOLFT mechanisms switch OFF (-) the initial excited state population $|e_0(\mathbf{r})\rangle$, whereas for processes that switch ON (+), $|e_0(\mathbf{r})\rangle = 1$. We note that while some work has made use of a Taylor expansion using (9.6), we find that the expansion diverges when $\alpha \geq 0.5$, making the cosine series expansion more robust. Note that the expansion coefficients do not depend on whether we are exploiting a URSR process that switches ON or switches OFF excited state population. The consequence of this property is that the magnitude of the super-resolution imaging is the same for both processes. SA offers an easier experimental implementation as only one beam is required, but this experimental simplicity comes at the expense of a greater background signal (b^0) and more rapid photobleaching than in the case of RESOLFT-like processes that switch OFF the excited state population to restrict the spatial extent of fluorescent emission.

SAX imaging cosine series PSF and OTF

SAX imaging uses the harmonics of a pure sinusoidal modulation of the beam intensity focused to a diffraction-limited focal spot. As the sample is driven into saturation, the sinusoidal modulation experiences harmonic distortion. Each harmonic in the detected signal can be extracted from the measurement. The extracted harmonics can be thought of as a projection of the effective illumination onto the object spatial distribution, $I_{\text{eff}}(\mathbf{r}, t) =$

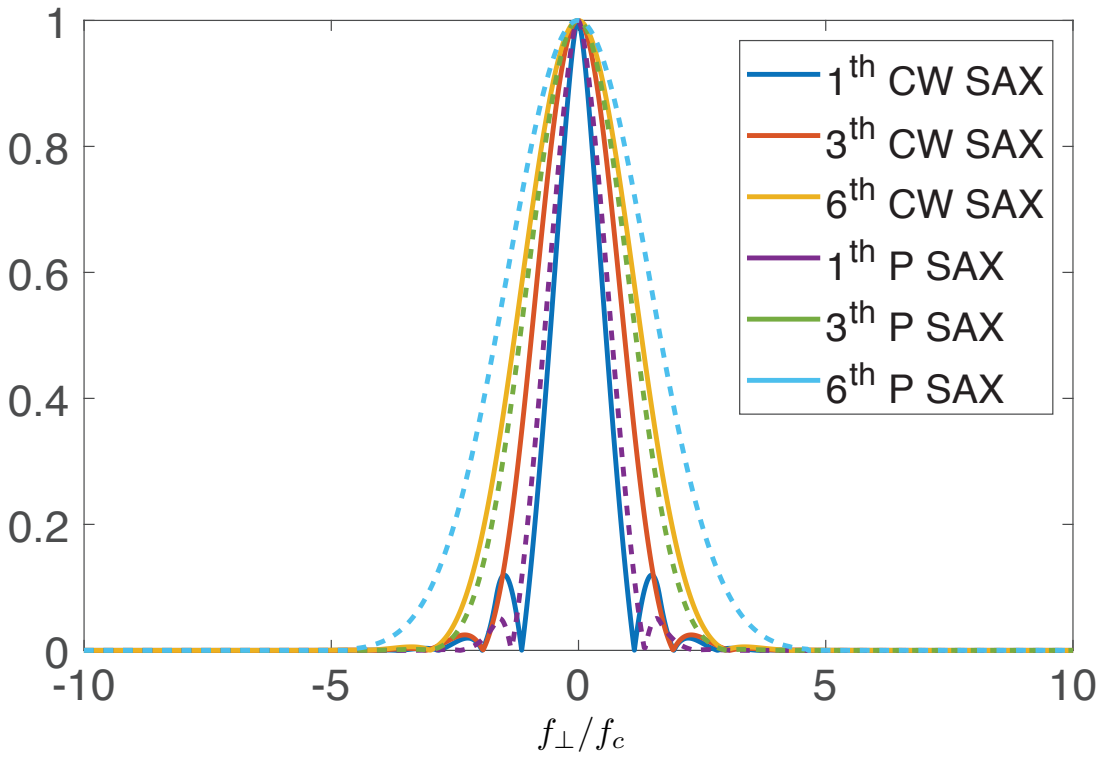

Figure 9.2: This figure shows the MTF of continuous-wave (CW) SAX imaging at various harmonic orders. This figure shows the MTF of pulsed (P) illumination SAX imaging at various harmonic orders. The code used for generating data for the plot can be found in appendix D.

$F[(\alpha/2)(1+\cos\Phi_t)\mathrm{PSF}_c(\mathbf{r})]$. The resulting signal for a sequence where either the relative position of the object or illumination beam is scanned by a displacement vector $\mathbf{r}_s$, the sequence of measurements reads $S_{\mathrm{SAX}}(\mathbf{r}_s) = \langle I_{\mathrm{eff}}(\mathbf{r},t)c(\mathbf{r}-\mathbf{r}_s)\rangle_{\mathbf{r}}$. Separate images at the q^{th} harmonics of the fundamental modulation frequency are then decomposed with the cosine series, leading to the q^{th} image as

$$I^{(q)}_{\mathrm{SAX}}(\mathbf{r}) = \left[b^{\mathrm{SAX}}_q\{\alpha,\mathbf{r}\} * c(\mathbf{r}) \right]_{\mathbf{r}} \tag{9.15}$$

The q^{th}-order PSF for the SAX imaging process is readily identified as $\mathrm{PSF}^{(q)}_{SAX}(\mathbf{r}) = b^{\mathrm{SAX}}_q\{\alpha,\mathbf{r}\}$ in the cosine series expansion, in which we explicitly write the SAX cosine expansion as

$$b^{\mathrm{SAX}}_q = \frac{1}{2\pi}\int_{-\pi}^{\pi} F\left[\frac{1}{2}\alpha\,(1+\cos\Phi_t)\,\mathrm{PSF}_c(\mathbf{r})\right]\cos\big(q\Phi\big)\mathrm{d}\Phi \tag{9.16}$$

The PSF is easily computed by numerically evaluating the integral (9.16). The OTF can then be computed with the Fourier transform of the PSF. Figure 9.2 shows the MTF of SAX for 1^{st}, 3^{rd}, and 6^{th} order harmonics for both CW and pulsed illumination. We see that pulsed illumination has a greater frequency support that that of CW illumination for the same saturation level, $\alpha = 2.5$.

9.5.2 CHIRPT and SPIFI

In the case of CHIRPT and SPIFI, when the illumination intensity drives a nonlinear response in the medium, the signal strength, or excited state population in the case of real transitions, is proportional to $S_t \propto |e(\mathbf{r}_\perp)\rangle = F[I_\ell(\mathbf{r}_\perp, t)]$, where the illumination intensity for CHIRPT and SPIFI are given by (3.4) and (3.11), respectively. We have previously demonstrated super-resolution imaging with SPIFI by driving a nonlinear response in the medium with a SPIFI illumination pattern []. In that work, the nonlinear response was second order, or $F[I_\ell(\mathbf{r}, t)] = I_\ell^2(\mathbf{r}, t)$, and we demonstrated the application of super-resolution imaging to coherent nonlinear scattering as well as two-photon absorption. In general, we can use multiple photons (MP) to drive a discrete nonlinear response with $F[I_\ell(\mathbf{r}, t)] = I_\ell^m(\mathbf{r}, t)$, where $m > 1$ is an integer describing the nonlinearity of the interaction. While MP-SPIFI and MP-CHIRPT are capable of super-resolution imaging, the enhancement of the spatial frequency support is limited to twice the order of nonlinearity, $2m$, for MP-SPIFI and m for MP-CHIRPT. However, SPIFI and CHIRPT imagining can also be used with the SA or RESOLFT URSR mechanisms. In the case of saturated absorption (SA), the population driven by a CHIRPT or SPIFI line illumination intensity pattern will produce an excited state population $|e(\mathbf{r})\rangle = F[I_\ell(\mathbf{r}, t)]$. For a RESOLFT interaction, a line focus excitation beam would be used to produce the initial population, where $|e_0(\mathbf{r})\rangle = I_e(\mathbf{r}) I_{\text{sat},e}^{-1}$, followed by a CHIRPT or SPIFI modulated depletion beam, which will produce a final excited state population of $|e(\mathbf{r})\rangle = |e_0(\mathbf{r})\rangle \{1 - F[I_\ell(\mathbf{r}_\perp, t)]\}$.

CHIRPT and SPIFI imaging cosine series PSF and OTF

Both CHIRPT and SPIFI imaging make use of the cosine expansion given in (9.14) to build the PSF and OTF for the USRS imaging process. However, in the case of spatial frequency projection methods, the object's spatial frequency information is directly obtained by the measurement. This can be readily seen by considering (3.9) for $y = 0$, whereupon we obtain $\tilde{S}_q(t) = \langle \exp\big(-i\ q\ k_t\ x\big) c(x) \rangle_x = C(k_t)$, where $C(k_x) = \langle c(x) \exp(-i k_x\ x) \rangle_x$ defines the one-dimensional spatial frequency transform of the object, $c(x)$. In the two-dimensional plane spanned by $\mathbf{r}_\perp$, each CHIRPT/SPIFI measurement produces a projection of the object $c(\mathbf{r}_\perp)$ onto the effective illumination intensity $I_{\text{eff}}(\mathbf{r}_\perp, t) F\left[I_\ell(\mathbf{r}_\perp, t)\right]$ — producing a mixed representation projection onto an object (or illumination pattern line focus) that is scanned along y_s to build a two-dimensional image. This becomes clear when we insert (9.14) into the expression for the SPIFI/CHIRPT signal given by (3.12), and we find that the SSB signal reads

$$\tilde{S}_q^{\text{FP}}(k_t, y_s) = \langle b_q^{\text{FP}}(k_t, y) e^{-i\ q\ k_t\ x} c(x, y - y_s) \rangle_{\mathbf{r}_\perp}. \tag{9.17}$$

Here, we have defined a spatial frequency difference that is swept linearly in time, so that $\Delta\mathbf{k}(t) = 2\pi\ \kappa\ t\ \hat{e}_x \equiv k_t\ \hat{e}_x$, and κ is the rate at which the transverse spatial frequency is swept [] and assumed that the illumination beam is centered at point x_c, which makes $\varphi_t = \omega_c t$ and $\Phi_{\text{FP}}(x, t) = \omega_c t + k_t x$. We may define a mixed representation of the object where a Fourier transform is taken along the modulation direction, x, so that we write $\hat{C}(k_x, y) = \langle c(x, y) \exp(-i\ k_x\ x) \rangle_{\mathbf{r}_\perp}$. With this form, (9.17) is compactly expressed as

$$\tilde{S}_q^{\text{FP}}(k_t, y) = \left[b_q^{\text{FP}}(k_t, y) * \hat{C}(k_t, y) \right]_y. \tag{9.18}$$

We immediately identify the optical transfer function, $\hat{\text{OTF}}_q(k_x, y) = b_q^{\text{FP}}(k_t, y)$. The expansion integral is given explicitly by inserting either (3.4) or (3.11) into the cosine expansion in (9.13) to the case of SA and discrete harmonic CHIRPT and SPIFI imaging.

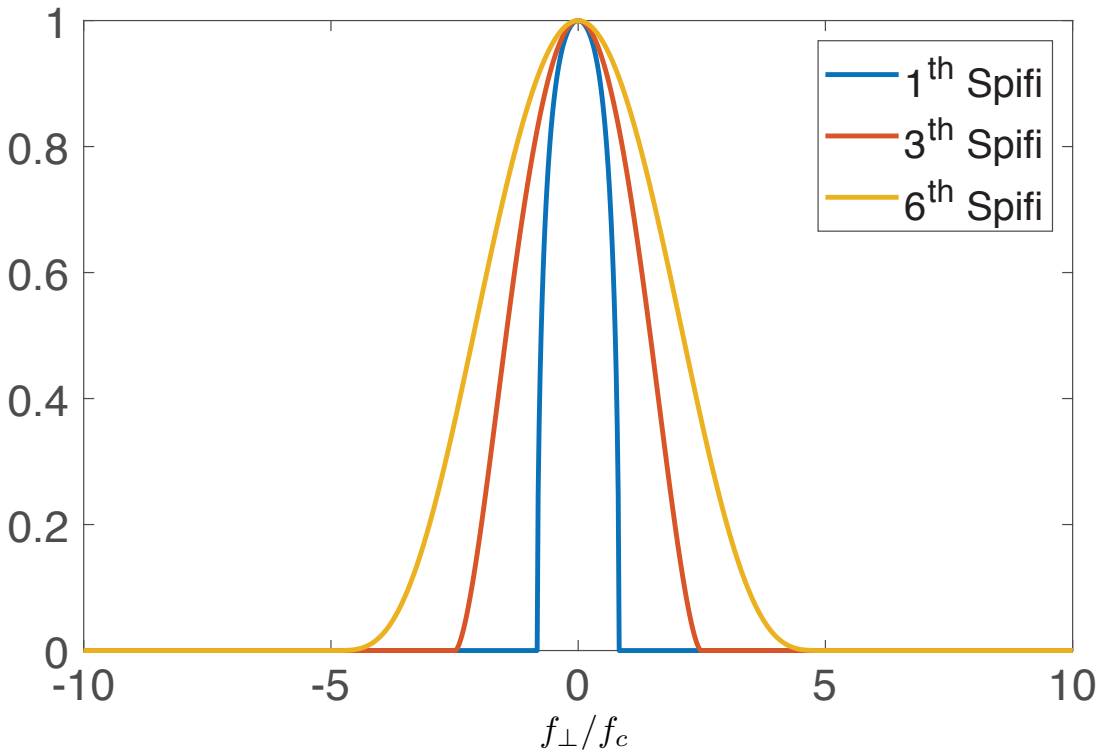

Figure 9.3: This figure shows the MTF of SPIFI/CHIRPT imaging at various harmonic orders. The code used for generating data for the plot can be found in appendix D.

In the case of RESOLFT CHIRPT/SPIFI imaging, the expansion coefficient gives a mixed representation of the depletion efficiency, $\eta_D(k_x, y) = b_q^{\mathrm{FP}}(k_t, y)$, with the full mixed representation OTF that reads $\hat{\mathrm{OTF}}_q(k_x, y) = u_0^2(y) b_q^{\mathrm{FP}}(k_t, y)$. The full OTF is obtained with a Fourier transform of the mixed OTF along the y-direction, $\mathrm{OTF}_q(k_x, k_y) = \langle \hat{\mathrm{OTF}}_q(k_x, y) \exp(-i\ k_y\ y) \rangle_y$. Similarly, the full PSF is obtained with an inverse Fourier transform along the x-direction, $\mathrm{PSF}_q(x, y) = \langle \hat{\mathrm{OTF}}_q(k_x, y) \exp(i\ k_x\ x) \rangle_{k_x}$. Figure 9.3 shows the MTF of saturated SPIFI for the 1^{st}, 3^{rd}, and 6^{th} order harmonics for a saturation level, $\alpha = 2.5$. Interestingly, the MTF is the same for both pulsed and CW illumination, however, in practice, it is much easier to reach saturation with a pulsed source.

9.6 Comparison of URSR imaging method

Perhaps the best way to compare imaging systems is through the PSF or equivalently the MTF. The reason for this is that the PSF directly informs how the imaging system will perform

and how much blurring will occur. Therefore, the narrower the PSF the better resolved the final image will be. Alternatively, the MTFs can be compared which is simply the magnitude of the Fourier transform of the PSF. By comparing the MTFs, one can immediately compare the cutoff spatial frequency and the magnitude of all the spatial frequencies of the entire image. It turns out that the magnitude is just as important, if not more important, than the cutoff spatial frequency. The reason for this is that the magnitude or the shape of the MTF describes how much of a particular spatial frequency will be represented in the image compared to the other spatial frequencies. Additionally, the magnitude of each spatial frequency tells how robust to noise that spatial frequency will be. That is, if the magnitude of a high spatial frequency is very small, it is likely that it will be buried in the noise and will not be well represented well in the final image, however, if that same frequency has a large amplitude then it is very likely going to be well represented in the final image even in the presence of noise leading to better imaging performance.

9.6.1 URSR OTF comparisons

Figure 9.4 compares the MTFs for STED, SAX, and Saturated SPIFI at a saturation parameter of $\alpha = 2.5$. With the exception of CW STED all the other techniques have a cut-off spatial frequency of approximately 4.5x that of the diffraction-limited cut-off. We can clearly see that CW STED, purple line, has the highest spatial frequency cut-off of around 7.5x that of the diffraction-limited cut-off. The MTF has a concave shape which causes the highest spatial frequencies to be lost in noise fairly easily. However, it is regularly reported that STED can achieve 50 nm resolutions with the record being 10 nm. Notice, that all RESOLFT techniques (STED, GSD, Photoswitching) have the same MTFs at a give saturation parameter, the primary difference is the photo-physics that drive the electronic populations will determine the efficiency of the resolution enhancement. While CW STED has the highest cut-off frequency, the mid-band frequency is lower than that of 6^{th} order pulsed SAX, dashed blue line, and 6^{th} order SPIFI, green line. While pulsed SAX is only slightly better in the mid-band frequencies, one would not

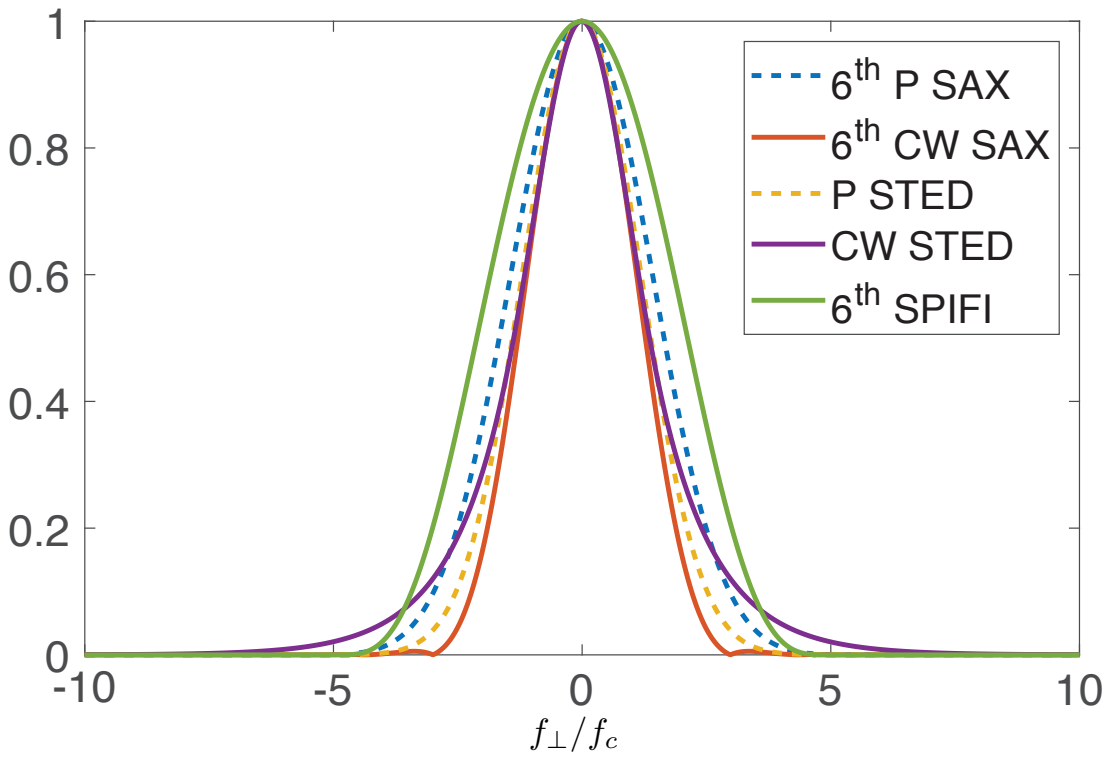

Figure 9.4: This figure compares the MTFs of STED, SPIFI, and SAX all with a saturation parameter of $\alpha = 2.5$. The code used for generating data for the plot can be found in appendix D.

expect the imaging performance to be better than that of CW STED. In practice, the 3^{rd} harmonic can be readily recovered, however, it is fairly typical for the 4^{th} and higher harmonics to be buried in the noise limiting the imaging performance. The 6^{th} order SPIFI is significantly higher amplitude for the mid-band frequencies and makes a big difference in the imaging performance, see fig. 9.5. In practice, achieving high SNR for the 4^{th} and higher orders has proven to be quite an arduous task. In the next chapter, I discuss a computation approach that allows a more consistent extraction of high-frequency information by solving the inverse problem with regularization and joint estimation of the measurement matrix.

9.6.2 URSR imaging comparisons

Figure 9.5 shows noise-free simulations of the imaging performance of STED, SAX, and SPIFI. This simulation used a numerical aperture (NA) of 1.1 with water immersion, $n_b = 1.33$, an illumination wavelength of $\lambda_{ill} = 500$nm, and a saturation parameter of $\alpha = 2.5$. Panel (a)

shows the true object, (b) is CW STED, (c) is pulsed STED, (d-f) is 1^{st}, 3^{rd}, and 6^{th} order harmonics of SAX, and (g-i) is 1^{st}, 3^{rd}, and 6^{th} order harmonics of SPIFI. We see that the imaging quality for CW STED, panel (b), is well resolved and is expected to have significantly better imaging performance compared to all the other image modalities presented here. Surprisingly, the 6^{th} order SPIFI looks to have better contrast than that of CW STED. The reason for this is the shape of the MTF of each respective imaging modality. Since SPIFI has superior mid-band support the overall image quality is comparable to a technique that has 66% higher cut-off spatial frequency. This illustrates the importance of the shape of the MTF and not just the cut-off frequency. SPIFI has the unique property of having a more convex MTF compare to that of most imaging systems.

Using the above theory, it is very easy to directly compare the various super-resolution techniques described above. It is worth noting here that the above theory is capable of holding many of the variables constant to allow for direct comparison, however, in practice this is never the case. That is, when it comes to implementing a given system there will be differences in the absorption cross-sections, emission and collection efficiencies, signal-to-noise, ease of alignment, illumination wavelength, photobleaching, and imaging speed to name a few variables. All of these details should be considered when implementing a real system, however, for the sake of comparison the theory described above allows one to compare the imaging performance for a given system where an illumination wavelength, saturation level, and numerical aperture are all equal, this allows for straight forward comparison of expected imaging performance between the various systems.

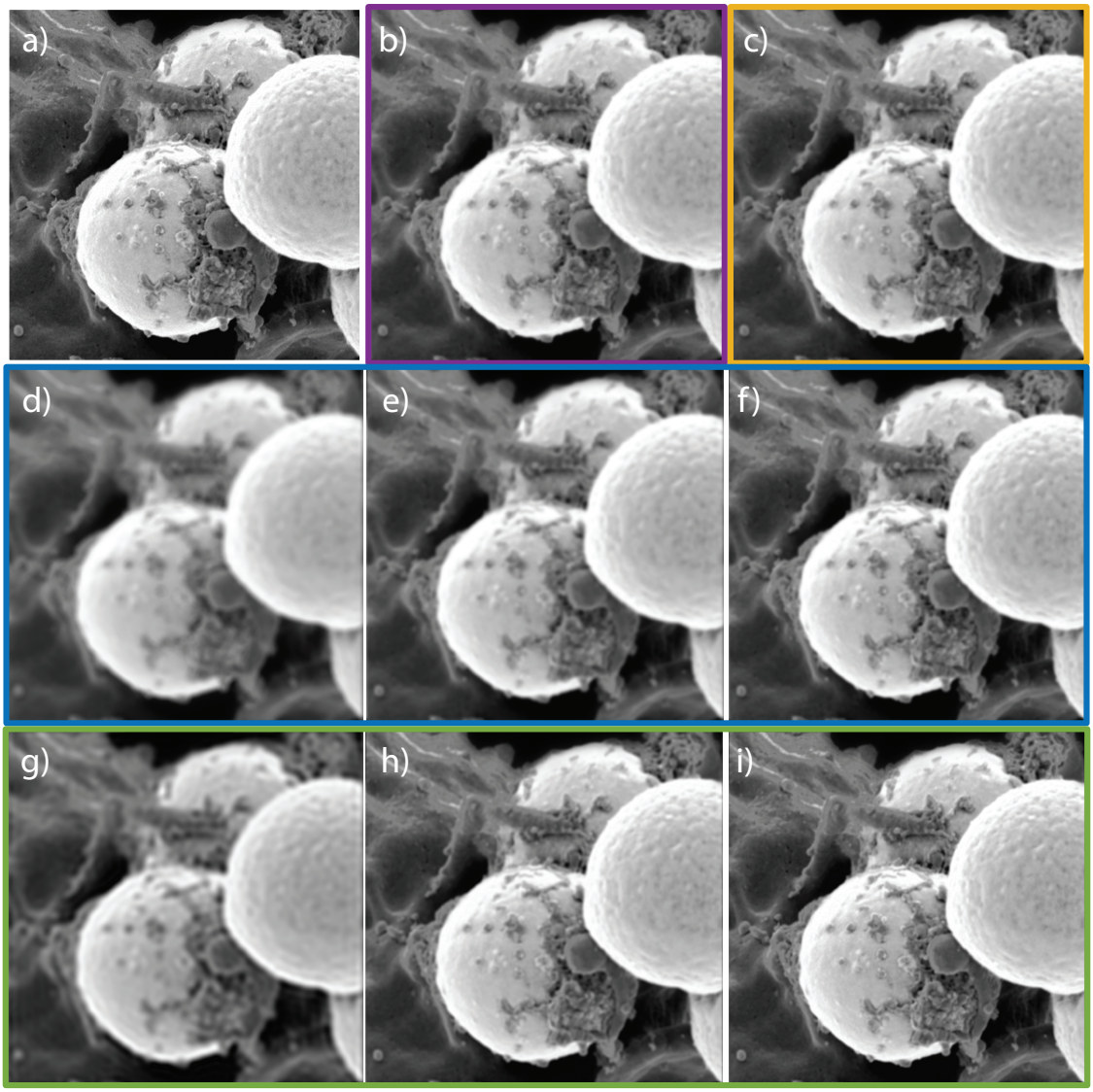

Figure 9.5: This figure compares the simulated noise-free imaging performance of STED, SAX, and SPIFI. Panel (aa is the true object, panels (b) and (c) are STED images with a saturation parameter of $\alpha = 2.5$ illuminated with CW and pulsed light, respectively, panels (d-f) are images of SAX at harmonics 1, 3, and 6, panel (g-i) are images of SPIFI at harmonics 1, 3, and 6. The code used for generating data for the plot can be found in appendix D.

Chapter 10

Computational Super Resolution SPIFI with Joint Estimation

10.1 Introduction

Optical microscopy is an indispensable tool for determining the spatial structure of microscopic samples. In recent years, there have been many major innovations for improving the spatial resolution of microscopes well beyond the diffraction limit defined by the numerical aperture (NA) of the imaging system. These resolution improvements have primarily been achieved by controlling the excited state population using nonlinear optical interactions, such as photoswitching, stimulated emission, and saturated excitation to name a few.

In recent years, SPatIal Frequency modulated Imaging (SPIFI) and more broadly Spatial Frequency Projection (SFP) imaging was developed as a way to access super-resolution information of coherent and incoherent multi-photon (MP) contrast mechanisms such as second harmonic generation or 2-photon fluorescence using single-pixel detection [125, 46]. SPIFI, in contrast to laser scanning microscope, multiplexes spatial information together using line-focus illumination. The object information is measured by illumination of the sample with a narrow band of spatial frequencies where the measured spatial frequencies are varied linearly from $[-NA/\lambda, NA/\lambda]$. Using nonlinear excitation super-resolution information can be accessed along the modulation direction. This leads to an anisotropic resolution in the 2D reconstructed image. There have been several techniques developed to homogenize the resolution, SPIFI lateral tomography [52, 150] and Fourier computed tomography [137].

The primary advantage of SFP imaging is the improved modulation transfer function (MTF), fig. 10.1(g), compared to other state-of-the-art techniques. The improved MTF allows the high

spatial frequencies to be better represented in the reconstructed image leading to better contrast and imaging performance [130].

In this chapter, we demonstrate that solving the inverse problem (IP) with regularization produces superior image quality compared to processing the data with a simple fast Fourier transform (FFT). While processing of SFP data with an FFT is fairly robust to the model mismatch between expected and experimental illumination patterns which may be introduced by aberrations such as optical misalignment, modulator accelerations, and the specimen itself, several disadvantages arise. Firstly, noise is distributed across the entire image in a multiplexing imaging modality, [105, 64]. Secondly, SFP imaging contains multiple images with an increasing range of spatial frequency support, but decreasing amplitude, which appears centered on harmonics of the fundamental carrier frequency. Solving the IP allows integration of the information contained in each of the imaging orders which results in a high signal-to-noise (SNR) and a well-resolved image. Finally, through refinement of the model of the SFP illumination pattern obtained through joint estimation of the model and the object, improved imaging quality is demonstrated, even in the case of linear illumination, where super-resolution performance is not anticipated.

10.2 Background

Imaging performance is usually evaluated with a single metric such as the spatial resolution δr or the cutoff spatial frequency, f_c [56, 127]. A single metric is not adequate for capturing the imaging capabilities of a given microscopy modality, an assertion best illustrated by comparing images. The differences in performance of a number of imaging modalities is shown in Fig. 10.1. The modulation transfer function (MTF), defined as the magnitude of the optical transfer function, for a number of imaging methods are shown in Fig. 10.1(e), along with the true object and simulated images for a number of modalities under noise-free conditions.

Fig. 10.1(b,c, and d) compares confocal imaging, pixel reassignment confocal microscopy (PRCM), and second-order SPIFI which display a coherent cutoff spatial frequency of 4x, 4x, and

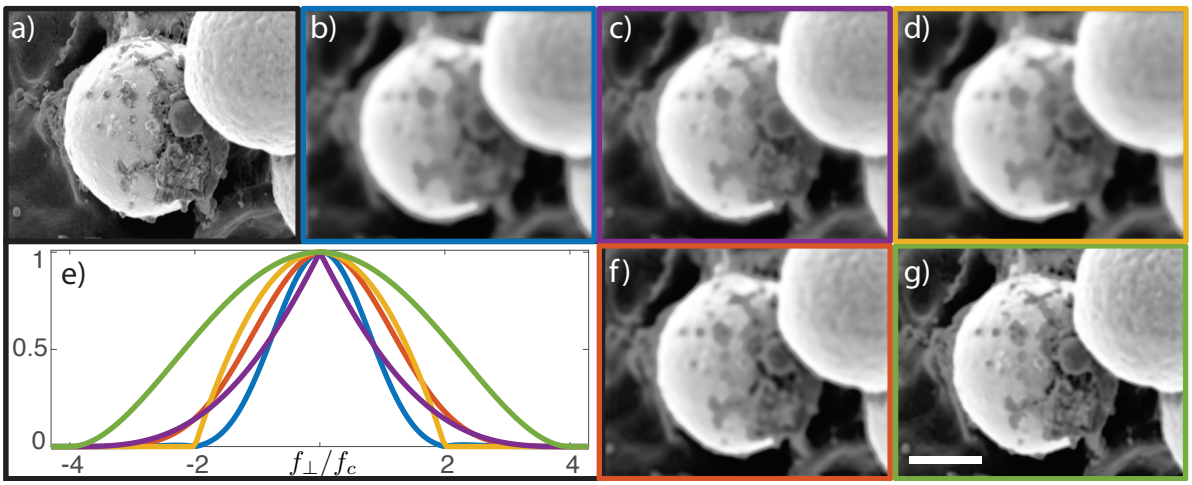

Figure 10.1: a) True Object, b) 1 Airy diameter Confocal, c) Pixel Reassignment Confocal, d) 2nd order SPIFI, f) 2-photon LSM, g) 4th order SPIFI, e) MTF. Code used for generating figures can be found in appendix D.

2x set by the numerical aperture of the imaging system, $f_c = \mathrm{NA}/\lambda$, respectively. PRCM imaging shows superior imaging performance compared to standard confocal because the amplitude of the MTF is higher at the mid to high spatial frequencies at the cost of the low spatial frequency amplitude [74]. Even the slight increases in the spatial frequency support of the MTF has generated great excitement for PRCM due to the increased imaging performance [129, 131]. We see that the MTF for second order SPIFI, yellow in fig. 10.1(g), has a lower cutoff spatial frequency, however, the amplitude of the overlapping spatial frequencies is higher than standard confocal resulting in a sharper image compared to confocal. PRCM has superior frequency support at high frequencies resulting in the best image of the three modalities.

Improvements in imaging quality for SFP for second order and higher are more striking with SFP imaging due to the convex shape of the MTF support that significantly boosts information obtained at the highest spatial frequencies. The MTF in SFP imaging is determined by the fringe visibility of the projected spatial frequencies. Since the illumination pattern samples a sub-aperture of the illumination objective lens pupil [135, 46], the fringe visibility is significantly higher than what is present in laser scanning microscopes (LSM), where the full spatial frequency support of the objective is focused simultaneously. The advantage of SFP is shown in Figs. 10.1(e and f) that compare LSM for two photon excitation fluorescence (2PEF) imaging

with 4th order SPIFI [46, 158] and LSM [31]. The improvements in MTF amplitude are evident in figs. 10.1(e and f).

The key conjecture that motivates this work is that estimation of SFP images through solving the inverse problem (IP) with regularization is able to exploit high SNR measurement regions (at high photon flux levels) and extract high spatial frequency information content (at low photon flux regions). In addition, the use of the inversion problem automatically fuses information from all SPIFI orders to combine the information across the full range of spatial frequency support contained in the SFP illumination patterns. The challenge posed by early image reconstruction using the FFT-based image processing is illustrated for two-photon excitation fluorescent SPIFI imaging in simulations shown in Fig. 10.3(a-d and f-i) with two different shot noise levels. The multiplexed shot noise is evident in the reduced SNR for the dim objects but also in the noise that bleeds across to the higher SPIFI orders, Fig. 10.3(d) and (i). The multiplexed noise presents a serious restriction on the extraction of high spatial frequency information content from super-resolution SPIFI imaging systems. The problem with traditional processing is that the higher image orders have significantly less power compared to the fundamental order, this, coupled with the multiplexed shot noise, causes the highest orders to have a low SNR making it challenging to recover high-quality super-resolution images.

10.3 Theory

The SPIFI implementation of an SFP microscope uses a modulated illumination intensity pattern imaged from a spinning modulator disk [125, 49, 46] onto the object region which can be modeled as $I_{\text{ill}}(x,t) = I_0\,\rho(x)\,[1+\mu(t)\cos(\omega_c\,t + f_t\,x)]^2/4$. This modulation is a sequence of spatial frequency projections with the instantaneous spatial frequency $f_t = 2f_m\,M\,t/T$, f_m is the highest spatial frequency on the modulator, and M is the magnification from the object region to the modulator. The fringe visibility, $\mu(t) = 2\sqrt{1-(f_t/f_c)^2}$, determines the amplitude of the MTF at time t where the scan time is limited by the coherent cutoff spatial frequency of the illumination imaging system, $f_c = NA/\lambda$, NA is the numerical aperture of the imaging

system, and λ is the illumination wavelength. The modulation pattern spans time ranging from $[-T/2, T/2]$, where T is the modulator rotation period. The modulated intensity possesses a carrier frequency ω_c that plays a key role in image estimation [49, 47, 48]. The illumination intensity beam profile is denoted by $\rho(x)$ which is normalized to a maximum value of unity so that $|\rho(x)| \leq 1$.

The forward model is determined from the effective illumination intensity $I_{\text{eff}}(x,t) = F[I_{\text{ill}}(x,t)]$ that can be modified by the photophysics of the excitation that is modeled as a non-linear function $F[\cdot]$. In the case of a η-photon excitation in fluorescent imaging, $F[I] = I^{\eta}$, where η is the number of photons that participate in the excitation. The presence of the carrier frequency enables the cosine series expansion of the effective illumination intensity,

$$I_{\text{eff}}(x,t) = \sum_{q=0}^{N} I_0^{(q)} \rho^{(q)}(x)\, b_q(t) \cos[q f_t\, x + \omega^{(q)}\, t], \tag{10.1}$$

where the sum contains N terms and we have defined the carrier frequency at order q as $\omega^{(q)} = q\,\omega_c$. In the case of η-photon excitation, $N = 2\eta$. The cosine expansion coefficients, $b_q(t)$, determine $\text{MTF}_q(f_x)$ for the q^{th} SPIFI order [46, 158]. Given the illumination intensity, the signal model for fluorescent light emission is $S(t) = \langle I_{\text{eff}}(\mathbf{x}, t)\, c(\mathbf{x})\rangle_{\mathbf{x}}$, for a spatial variation in fluorophore concentration, $c(\mathbf{x})$, that represents the desired object. Here we are using Dirac integral notation, $\langle\cdot\rangle_x = \int \cdot\, \mathrm{d}^n x$, and n is the dimension of the image.

Data are acquired by sampling a fraction of the emitted fluorescent power measured on a single element detector such as a photomultiplier tube (PMT) at sampling interval Δt at a set of discrete times, t_j, that span $[-T/2, T/2]$, with a total number of samples $N_t = T/\Delta t$. The data signal vector $\mathbf{y} = \mathbf{S} + \mathbf{n}$ contains the elements sampled from the expected signal $[\mathbf{S}]_j = \Delta t\, S(t_j)$ and noise introduced in the measurement $[\mathbf{n}]_j$. An estimate of the object, $\hat{\mathbf{c}}$, may then be directly obtained from the signal data vector $\mathbf{y}$. We focus on shot noise, which is given by $\mathbf{n} = \text{Poisson}\{\mathbf{S}\} - \mathbf{S}$.

By solving the inverse problem (IP), superior images can be obtained from the measured data vector using joint estimation of the measurement matrix, [157, 17]. To do so, we form a lin-

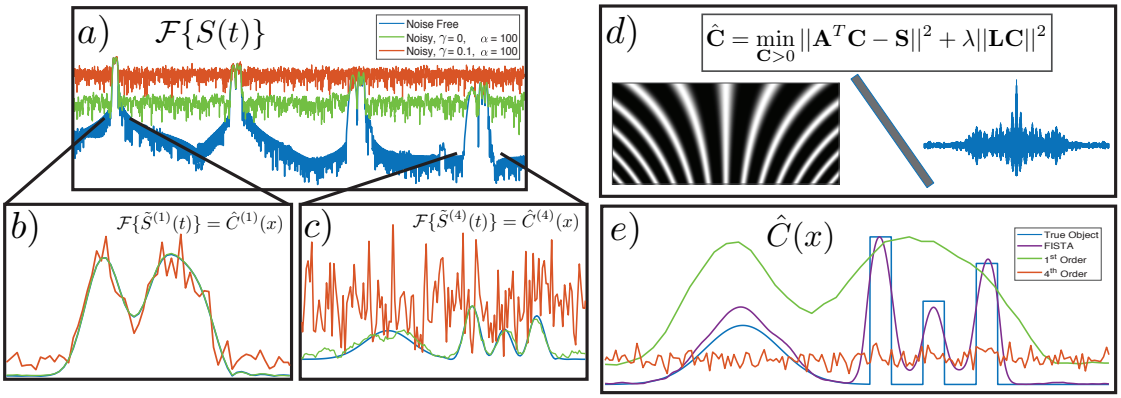

Figure 10.2: This figure shows the workflow for processing MP-SPIFI data with both the FFT-based method and the iterative inverse problem. Panel (a) shows the FFT of the time trace with three different noise levels, blue-noise free, green-shot noise with 100 counts, and orange-shot noise with 100 counts plus 10% 1/f noise. Panel (b) shows the first-order FFT reconstruction, and (c) shows the fourth-order FFT reconstruction. Panel (d) shows the measurement matrix on the left and the noise time trace on the right. Panel (e) is the reconstruction using the iterative inverse solver, purple. The blue trace is the true object, green is the first order, and orange is the fourth order.

ear model of the form $\mathbf{y} = \mathbf{A}\mathbf{c} + \mathbf{n}$. Solving the IP estimates the object for each line acquired from the data vector at a given y position in the object. Implementation of this model requires that we produce a discrete object vector $\mathbf{c}$ that is sampled on a spatial grid $\mathbf{x}$ with N_x samples spaced by Δx with spatial samples $[\mathbf{x}]_i = i\,\Delta x$. The measurement matrix, $\mathbf{A}$, is then constructed from the sampled points of the effective illumination model given in Eq. (10.1) as $[\mathbf{A}]_{i,j} = I_{\text{eff}}(x_i, t_j)$.

Estimation of the object is obtained by solving the minimization problem

$$\hat{\mathbf{c}} := \underset{\hat{\mathbf{c}},\,\text{s.t.}\,\hat{\mathbf{c}}>0}{\arg\min} \left\|\mathbf{A}\mathbf{c} - \mathbf{y}\right\|_2 + \tau\, R\{\mathbf{c}\}. \tag{10.2}$$

Here a regularization operator, $R\{\cdot\}$, scaled by τ employs prior information to mitigate the impact of noise in the estimated object. Figure 10.2 shows a brief data processing workflow for both traditional MP-SPIFI and MP-SPIFI utilizing iterative solvers. Panel (a) show the FFT of a simulated time trace with three different noise levels, the blue trace has no noise added and serves as a reference for ideal performance, and the green trace has photon shot noise (poison noise) added to it with a simulated average 100 photon counts, and the orange trace has the same level of shot noise (100 counts) plus 1/f electronic noise was added with an amplitude of

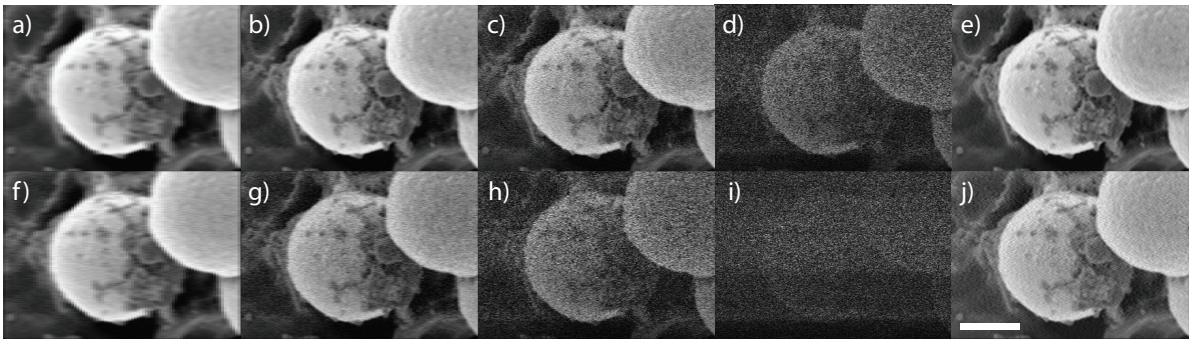

Figure 10.3: Top row has Poisson noise with a maximum photon count of 1000. (a - d) $1^{st} - 4^{th}$ FFT based SPIFI orders, respectively. (e) IP-based reconstruction. The bottom row has Poisson noise with a maximum photon count of 100. (f - i) $1^{st} - 4^{th}$ FFT based SPIFI orders. (j) IP-based reconstruction. Scale bar: $64\mu m$. The code used for generating figures can be found in appendix E.

10% of the maximum signal level. Panels (b) and (c) show the recovered first and fourth image order, respectively, of all three traces. Panel (b) illustrates the inverse problem where the left-hand side shows an example of the measurement matrix and the right-hand side shows the simulated time trace. Panel (e) shows a comparison of the performance of solving the iterative inverse problem compared to the FFT-based method, where the blue trace is the true object, the purple trace is the recovered object using the iterative solver, the green trace is the FFT first order, and the orange trace is the FFT fourth order. We can see that the iterative solver has significantly better performance than that of the FFT-based processing giving high SNR as well as maintaining good spatial resolution.

Figure 10.3(e) and (j) show the results of solving the eqn. 10.2 with Tikhonov regularization. We see that the SNR is improved compared to the FFT-based processing.

10.4 Experimental Setup

To demonstrate the advantage of the computational approach described above, a multi-photon (MP)-SPIFI microscope was constructed. The microscope used an amplified ANDi laser that was built in-house with a center wavelength of λ_0 = 1035nm and a bandwidth of ≈ 50nm FWHM producing a transform-limited pulse duration of 31.5 fs. The SPIFI modulator disc had a $\Delta k = 35$ [lines/mm]. The objective lens was a water immersion 1.10 NA 20x Nikon which was

overfilled in the back aperture. The signal light (SHG or 2PF) was collected in the epi direction and the fundamental light was filtered by a dichroic mirror (Semrock) and an interference filter (Semrock). The signal light was detected by a PMT (Hamamatsu), and the signal was amplified by a trans-impedance amplifier (Fempto) and digitized with a NI DAQ (NI PCIe).

The measurement matrix, A, must accurately represent the signal formation of the imaging system otherwise the IP reconstruction is very likely to produce poor reconstructions. Several calibration protocols were developed in order to obtain a quality measurement matrix that would serve as the starting point for solving the inverse problem. In order to calibrate the MP-SPIFI microscope so that quality reconstructions could be obtained it was necessary to a scan small probe emitter across the line focus in the modulation direction. The emitter was translated along the line focus and a 2-photon fluorescent signal was collected along 200 x-positions. From this calibration data, the measurement matrix was constructed. Additionally, with this calibration protocol disc wobble and optical aberrations are automatically encoded in the measurement matrix eliminating the need for aberration correction previously implemented, [46, 65].

Even with the calibration protocol described above, the IP reconstruction can be quite sensitive to model mismatch of the measurement matrix and the true illumination patterns [23]. To further improve the IP performance, the measurement matrix was jointly estimated to adapt to modulator acceleration instability, optical aberrations, and modulator aberrations. Provided that the measurements contain sufficient redundancy, it is possible to jointly estimate the desired object and the measurement matrix [141].

Joint estimation was done by first generating an initial estimate of the object using the measured A matrix from the calibration data and solving eqn. 10.2 with Tikhonov regularization. Using the estimated object and measurement matrix, a time trace was estimated and compared to the measured time trace to generate an error measure against the recorded data to enforce data consistency. This quantifies the combined error of our model and object estimate. The measurement matrix was parameterized with a set of variables $\vec{\alpha}$. These can represent natural

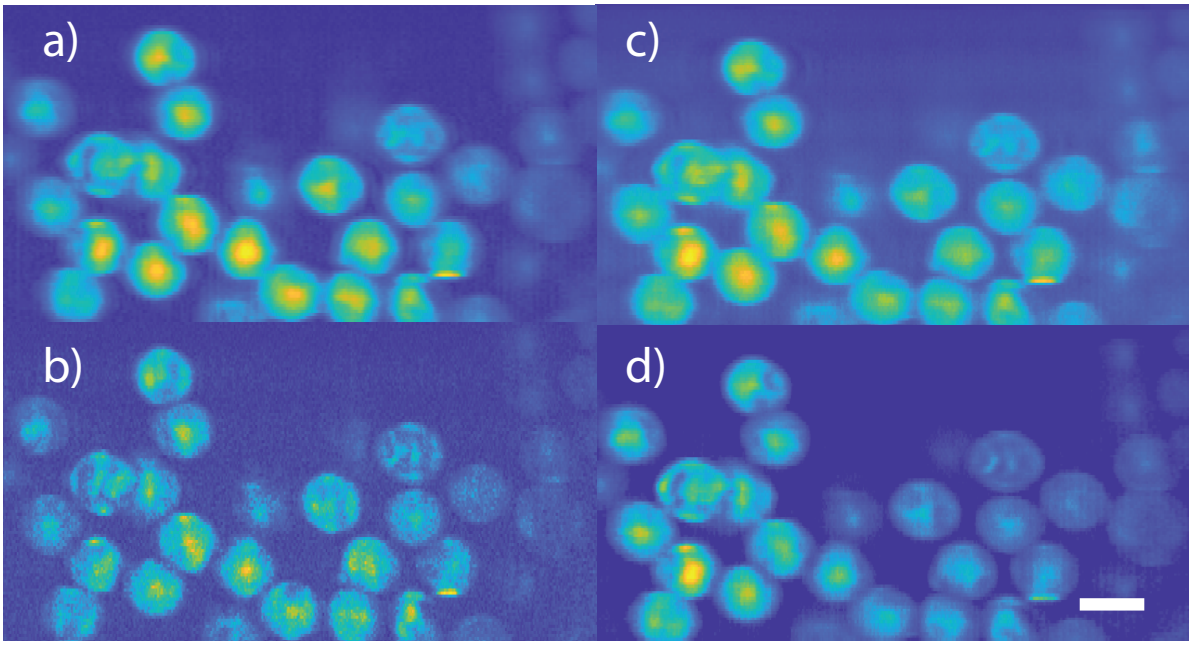

Figure 10.4: Panels a) and b) are 2-photon MP-SPIFI images of fluorescent stained polystyrene beads corresponding to the 1^{st} and 2^{nd} order images, respectively. Panel c) is the result of solving the inverse problem before joint estimation. Panel d) is the resulting image solving the inverse problem with joint estimation of the measurement matrix. Scale bar represents $10\mu m$. The processing code used to process the data using the inverse reconstruction algorithm can be found in appendix F

variables of the system i.e. $(\omega_c,\gamma...)$ or they can be used to describe the weighting coefficients of an appropriate basis to build an arbitrary function that describes aberrations of the system. For example, the chirp rate, γ, may vary in time in a stochastic way due to motor instability, $\gamma(t) \approx \sum_{n=0}^{N} H_n(t)\alpha_n$. By using a basis, these aberrations can be captured with a sparse set of parameters $\vec{\boldsymbol{\alpha}}$. The Zernike polynomials were used as the basis to estimate optical aberrations to improve the measurement matrix. After parametrizing the matrix, the error is minimized between the simulated data and the recorded data given the object estimate and initial guess of the $\vec{\boldsymbol{\alpha}}$ parameters. A new image is then generated with the updated $\vec{\boldsymbol{\alpha}}$ and the process is repeated until convergence. This process is shown as pseudo-code in algorithm 1. Joint estimation is carried out successively for each aspect of the system we wish to better estimate.

Ultimately, the goal is that this procedure will lead to a more accurate model of the system and therefore improve imaging performance.

Algorithm 1: Joint Estimation

Input: Function that generates $\mathbf{A}$ given parameters $\vec{\boldsymbol{\alpha}}$, regularization parameter τ

Output: Updated estimate of image $\vec{\mathbf{c}}_{out}$ and model parameters $\vec{\alpha}_{out}$

Data: Measured time trace y

$\hat{\boldsymbol{\alpha}}_0$ = intial guess or from fit to measured $\mathbf{A}$

$\hat{\mathbf{c}}_0 := \underset{\mathbf{c},\,\text{s.t.}\,\mathbf{c}>0}{\arg\min}\ \frac{1}{2}\left\|\mathbf{A}(\hat{\boldsymbol{\alpha}}_0)\,\mathbf{c}-\mathbf{y}\right\|_2 + \tau\, R\{\mathbf{c}\}$ `// Using FISTA`

$i = 1$

while $\|\vec{\boldsymbol{\alpha}}_{i-1} - \vec{\boldsymbol{\alpha}}_i\|_2 > tolerance$ **do**

  $\hat{\boldsymbol{\alpha}}_i := \underset{\vec{\boldsymbol{\alpha}}}{\arg\min}\ \frac{1}{2}\left\|\mathbf{A}(\vec{\boldsymbol{\alpha}})\,\hat{\mathbf{c}}_{i-1}-\mathbf{y}\right\|_2$ `// Using Levenburg-Marquardt`

  $\hat{\mathbf{c}}_i := \underset{\mathbf{c},\,\text{s.t.}\,\mathbf{c}>0}{\arg\min}\ \frac{1}{2}\left\|\mathbf{A}(\hat{\boldsymbol{\alpha}}_i)\,\mathbf{c}-\mathbf{y}\right\|_2 + \tau\, R\{\mathbf{c}\}$ `// Using FISTA`

  $i = i + 1$

$\vec{\mathbf{c}}_{out} = \hat{\mathbf{c}}_i\ \vec{\alpha}_{out} = \hat{\boldsymbol{\alpha}}_i$

10.5 Experimental Results

Figure 10.4 shows object reconstructions of 2-photon fluorescence from $10\mu m$ fluorescent stained polystyrene beads (Bang Labs, Envy Green). Figure 10.4 (a) and (b) show FFT reconstruction of the 1^{st} and 2^{nd} order images, respectively, and fig 10.4(c) shows the IP before joint estimation. Finally, 10.4(d) shows the resulting image for solving the IP with joint estimation. From the figure, we see that the IP with joint estimation has better SNR and resolution compared to the second-order FFT-based reconstructions and the IP before joint estimation. Additionally, we see that we are able to take advantage of the high SNR data from the first order and fuse the high spatial frequency information from the higher orders to generate an overall improved image compared to any singular FFT order.

10.6 Discussion

In order to obtain a high-quality reconstruction, it was necessary to jointly estimate the measurement matrix by first estimating the line object. Using the recovered object and the initial measurement matrix, obtained from the system calibration, the forward problem was solved to generate a simulated time trace. The simulated time trace was compared to the measured time trace to give an error. The measurement matrix was then adjusted using gradient descent to minimize the error between the measured time trace and the simulated one. Once the measurement matrix had been updated the inverse problem was solved once more. This gives a new object estimation. This process was done until the process converged. While the reconstruction procedure takes significantly longer than the FFT-based reconstruction, the improved imaging performance is worth the added computation time.

One limitation of the reconstructing resolution is the fact that the resolution enhancement only occurs along the modulation direction. This results in anisotropic resolution. Due to the resolution anisotropy, the low-resolution experience in the direction perpendicular to the modulation causes blurring and a lose of overall resolution performance in the enhanced direction. There have been techniques developed to solve this problem [52, 137]. If these methods are utilized full isotropic resolution can be achieved.

10.7 Conclusion

In this chapter, it was shown that solving the joint estimation inverse problem with regularization for multi-photon SPIFI allows for superior imaging performance compared to traditional FFT-based processing. Joint estimation was necessary so that the estimated measurement matrix was able to more accurately represent the actual illumination pattern used to illuminate the sample. In addition, we showed through simulation that the convex-shaped MTF of the SPIFI imaging system outperforms other comparable imaging techniques which all have a concave-shaped MTF. Additionally, SPIFI is capable of imaging both coherent and incoherent contrast mechanisms such as second harmonic generation (shg) and 2-photon fluorescence.

Chapter 11

Future Research Possibilities

11.1 Broadband Direct Optical Phase Extraction (B-DOPE)

Direct optical phase extraction (DOPE) imaging has the potential to be extended to broadband illumination. Standard DOPE imaging systems operated using continuous wave (CW) illumination to measure the quantitative phase of the object of interest. CW illumination is an excellent choice for measuring phase in the forward direction to obtain the optical path length through the object which can ultimately to converted into a refractive index using the knowledge of the illumination wavelength. However, there are some drawbacks to CW illumination, such as speckle contaminating the overall quality of the image. Interestingly, speckle was not observed in any DOPE images. Single wavelength illumination often will result in points singularities where the phase is not defined resulting in an improperly defined phase. These points of singularity will cause the unwrapped phase image to be significantly distorted at and around the point of singularity. Finally, the collection of backscattered illumination light does not have a clear interpretation of the meaning of the recovered phase, that is the recovered image could be interpreted as a topography of the object's first interface or it could be interpreted as a confocal-like image that depends on the location of object's z-position.

It is possible to minimize the effect or limitation of CW illumination by utilizing broadband illumination. There are at least two primary advantages of broadband illumination. First, both speckle and phase singularities are significantly reduced or eliminated with the use of broadband illumination. The second advantage and perhaps the most important advantage is the information obtained in the backward (epi) direction. When broadband illumination is used for DOPE imaging a large amount of spatial frequency information is obtained. The obtained spatial frequency information is similar to that of optical coherent tomography (OCT) with the exception that broadband epi-DOPE obtains transverse spatial frequencies, not just the on-

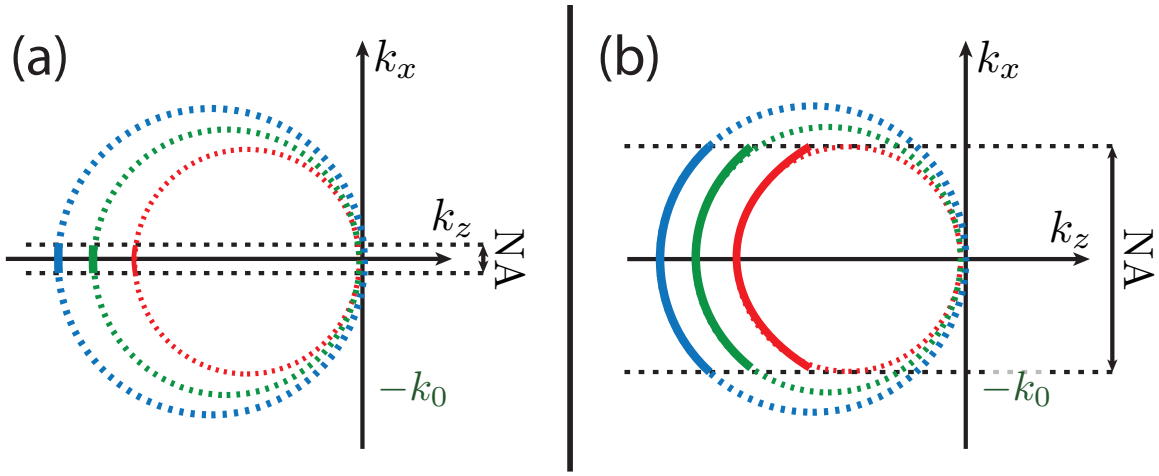

Figure 11.1: Panel a) shows the spatial frequency support of optical coherence tomography from a broadband source. Panel b) shows the spatial frequency support of epi-DOPE.

axis frequencies. This information should allow for optical sectioning with a z-resolution of $1/\Delta\lambda$ where $\Delta\lambda$ is the optical bandwidth of the illumination. The transverse resolution should be equal to the optical resolution of the illumination objective lens. Figure 11.1(a) shows the collected spatial frequency of OCT and fig. 11.1(b) shows the collected spatial frequencies of broadband epi-DOPE. We see that the epi-DOPE collects significantly more information than that of OCT. This increased information should allow for faster scan speeds compared to that of OCT since only one transverse direction needs to be scanned.

11.2 Super Resolution

One potential research direction of SPIFI and/or Multi-photon SPIFI is to perform imaging deep in scattering media. MP-SPIFI has several potential advantages that would lend itself to performing well in scattering media. The first advantage is that SPIFI is a single-pixel detection technique. This advantage allows an image to be formed from the signal light regardless of where the signal light falls on the detector's surface. In other words, the signal light does not need to be in an imaging condition that allows the signal light to experience multiple scattering without degrading the quality of the reconstructed image. Another advantage of SPIFI is how the signal light is encoded with the illumination beam interference. The encoded signal should

allow for some rejection of signal light outside the interference region to be rejected allowing for a background-free signal after signal processing, however, this light will still produce shot noise which will be a problem that needs to be addressed. Additional background rejection should be achieved when illumination light is scattered before it excites the sample. This effect is due again to the fact that encoding of the signal light depends on the interference of two or more beams, since it is unlikely that scattered light will have a coherent phase relationship with surrounding illumination light, interference is not likely to occur. Finally, since there is a well-defined phase relationship between the interfering illumination beams it should be possible to correct phase distortions such as optical distortions, cover slip mismatch, and even phase distortion induced by the sample. Correcting such distortions should allow for even better imaging performance deep in scattering media.

It may also be possible to use a beam propagator to recover the object and correct for object-induced distortion. This idea is similar to that of the multi-slice ptychography, [89]. In this case, CHIRPT absorption and fluorescence microscopy would likely be utilized. The idea would be to numerically refocus the object to a plane near the surface where scattering is going to be less prevalent. The object, both fluorescence and absorption, could be estimated at that plane, $z_{surface}$, then the beam could be propagated a small distance, δz, and the object refocused to that corresponding plane. The refocused object would serve as an initial object estimate at that plane, then the beam-propagated absorption could be used to estimate the scattering distortion. This process of joint estimation could be carried out several times. The result should be that the phase distortion deep in the scattering medium should be systematically corrected which should improve the image quality throughout the medium.

Bibliography

[1] George B. Arfken and Hans J. Weber. *Mathematical methods for physicists 6th ed.* 2005.

[2] C. Ba et al. "Dual-modality endomicroscopy with co-registered fluorescence and phase contrast". In: *Biomed. Opt. Express* 7.9 (Sept. 2016), pp. 3403–3411.

[3] R. Barer. "Determination of Dry Mass, Thickness, Solid and Water Concentration in Living Cells". In: *Nature* 172.4389 (Dec. 1953), pp. 1097–1098.

[4] Stephen Barnett and Rodney Loudon. "The enigma of optical momentum in a medium". In: *Philosophical transactions. Series A, Mathematical, physical, and engineering sciences* 368 (Mar. 2010), pp. 927–39. DOI: 10.1098/rsta.2009.0207.

[5] ED Barone-Nugent, ANTON Barty, and KA Nugent. "Quantitative phase-amplitude microscopy I: optical microscopy". In: *Journal of microscopy* 206.3 (2002), pp. 194–203.

[6] H.H. Barrett and K.J. Myers. *Foundations of Image Science*. Wiley Series in Pure and Applied Optics. Wiley, 2004. ISBN: 9780471153009. URL: https://books.google.com/books?id=pHBTAAAAMAAJ.

[7] A. Barty et al. "Quantitative optical phase microscopy". In: *Optics Letters* 23.11 (1998), pp. 817–819. DOI: 10.1364/OL.23.000817.

[8] Wolfgang Becker. *Advanced time-correlated single photon counting applications*. Vol. 111. Springer, 2015.

[9] B.J. Berne and R. Pecora. *Dynamic Light Scattering: With Applications to Chemistry, Biology, and Physics*. Dover Books on Physics. Dover Publications, 2013. ISBN: 9780486320243. URL: https://books.google.com/books?id=xg3CAgAAQBAJ.

[10] Stefan Bernet et al. "Quantitative imaging of complex samples by spiral phase contrast microscopy". In: *Optics Express* 14.9 (2006), pp. 3792–3805.

[11] Basanta Bhaduri et al. "Diffraction phase microscopy with white light". In: *Optics Letters* 37.6 (2012), pp. 1094–1096.

[12] Basanta Bhaduri et al. “Diffraction phase microscopy: principles and applications in materials and life sciences”. In: *Advances in Optics and Photonics* 6.1 (2014), pp. 57–119.

[13] Konstantin Y. Bliokh, Aleksandr Y. Bekshaev, and Franco Nori. “Optical Momentum, Spin, and Angular Momentum in Dispersive Media”. In: *Phys. Rev. Lett.* 119 (7 Aug. 2017), p. 073901. DOI: 10.1103/PhysRevLett.119.073901. URL: https://link.aps.org/doi/10.1103/PhysRevLett.119.073901.

[14] Erica Block et al. “Simultaneous spatial frequency modulation imaging and micromachining with a femtosecond laser”. In: *Optics Lettets* 41.2 (2016), pp. 265–268.

[15] Pierre Bon et al. “Quadriwave lateral shearing interferometry for quantitative phase microscopy of living cells”. In: *Optics express* 17.15 (2009), pp. 13080–13094.

[16] Martin Booth et al. “Aberrations and adaptive optics in super-resolution microscopy”. In: *Microscopy* 64.4 (July 2015), pp. 251–261.

[17] Stephen Boyd and Lieven Vandenberghe. *Convex Optimization*. Cambridge University Press, 2004. DOI: 10.1017/CBO9780511804441.

[18] R. N. Bracewell. “Numerical Transforms”. In: *Science* 248.4956 (May 1990), pp. 697–704. DOI: 10.1126/science.248.4956.697.

[19] RN Bracewell et al. “Affine theorem for two-dimensional Fourier transform”. In: *Electronics Letters* 29.3 (1993), pp. 304–304.

[20] Steven L. Brunton and J. Nathan Kutz. *Data-Driven Science and Engineering: Machine Learning, Dynamical Systems, and Control*. Cambridge University Press, 2019. DOI: 10.1017/9781108380690.

[21] Rémi Carminati and John C. Schotland. *Principles of Scattering and Transport of Light*. Cambridge University Press, 2021. DOI: 10.1017/9781316544693.

[22] Wai Lam Chan et al. “A single-pixel terahertz imaging system based on compressed sensing”. In: *Applied Physics Letters* 93.12 (2008), p. 121105.

[23] Yuejie Chi et al. “The Sensitivity to Basis Mismatch of Compressed Sensing for Spectrum Analysis and Beamforming”. In: (Jan. 2009).

[24] Wonshik Choi et al. “Tomographic phase microscopy”. In: *Nature Methods* 4 (Aug. 2007).

[25] Pere Clemente et al. “Single-pixel digital ghost holography”. In: *Physical Review A* 86.4 (2012).

[26] Katherine Creath. “V phase-measurement interferometry techniques”. In: *Progress in optics* 26 (1988), pp. 349–393.

[27] Etienne Cuche, Frédéric Bevilacqua, and Christian Depeursinge. “Digital holography for quantitative phase-contrast imaging”. In: *Optics Letters* 24.5 (1999), pp. 291–293. DOI: 10.1364/OL.24.000291.

[28] Claire L Curl et al. “Quantitative phase microscopy: a new tool for investigating the structure and function of unstained live cells”. In: *Clinical and experimental pharmacology and physiology* 31.12 (2004), pp. 896–901.

[29] Alex Darrell et al. “Improved fluorescence optical projection tomography reconstruction”. In: *Spie Newsroom* (2008).

[30] Alex Darrell et al. “Weighted filtered backprojection for quantitative fluorescence optical projection tomography.” In: *Physics in medicine and biology* 53 14 (2008), pp. 3863–81.

[31] W Denk, J H Strickler, and W W Webb. “Two-photon laser scanning fluorescence microscopy”. In: *Science* 248.4951 (1990), pp. 73–76.

[32] A.J. Devaney. “A filtered backpropagation algorithm for diffraction tomography”. In: *Ultrasonic Imaging* 4.4 (1982), pp. 336–350.

[33] Alberto Diaspro et al. “Multi-photon excitation microscopy”. In: *BioMedical Engineering OnLine* 5 (2006), pp. 36–36.

[34] Eric D. Diebold et al. “Digitally synthesized beat frequency multiplexing for sub-millisecond fluorescence microscopy”. In: *Nature Photon* 7.10 (Oct. 2013), pp. 806–810.

[35] Scott R. Domingue and Randy A. Bartels. “General theoretical treatment of spectral modulation light-labeling spectroscopy”. In: *J. Opt. Soc. Am. B* 33.6 (2016), p. 1216.

[36] Scott R. Domingue, David G. Winters, and Randy a. Bartels. “Hyperspectral imaging via labeled excitation light and background-free absorption spectroscopy”. In: *Optica* 2.11 (2015), p. 929.

[37] Scott R Domingue et al. “Transient absorption imaging of hemes with 2-color, independently tunable visible-wavelength ultrafast source”. In: *Biomedical Optics Express* 8.6 (2017), pp. 2807–2821.

[38] V. Durán et al. “Compressive imaging in scattering media”. In: *Optics Express* 23.11 (2015), pp. 14424–14433.

[39] Rahul Dutta et al. “Single-pixel imaging of the retina through scattering media”. In: *Biomed. Opt. Express* 10.8 (Aug. 2019), pp. 4159–4167. DOI: 10.1364/BOE.10.004159. URL: http://opg.optica.org/boe/abstract.cfm?URI=boe-10-8-4159.

[40] E. Evans. “Comparison of the diffraction theory of image formation with the three-dimensional, first Born scattering approximation in lens systems”. In: *Optics Communications* 2.7 (1970), pp. 317–320.

[41] Daniel Feldkhun and Kelvin H Wagner. “Doppler encoded excitation pattern tomographic optical microscopy.” In: *Applied optics* 49.34 (2010), pp. 47–63.

[42] A F Fercher et al. “Optical coherence tomography - principles and applications”. In: *Reports on Progress in Physics* 66.2 (2003), p. 239.

[43] J J Field et al. “Differential Multiphoton Laser Scanning Microscopy”. In: *Selected Topics in Quantum Electronics, IEEE Journal of* 18.1 (2012), pp. 14–28.

[44] Jeffrey J. Field, David G. Winters, and Randy A. Bartels. “Single-pixel fluorescent imaging with temporally labeled illumination patterns”. In: *Optica* 3.9 (Sept. 2016), pp. 971–974.

[45] Jeffrey J. Field, David Winters, and Randy Bartels. “Plane wave analysis of coherent holographic image reconstruction by phase transfer (CHIRPT)”. In: *J. Opt. Soc. Am. A* 32.11 (2015), pp. 2156–2168.

[46] Jeffrey J. Field et al. “Super-resolved multimodal multiphoton microscopy with spatial frequency-modulated imaging”. In: *Proc. Nat. Acad. Sci. USA* 113.24 (2016), pp. 6605–6610.

[47] Jeffrey J. Field et al. “Three-dimensional single-pixel imaging of incoherent light with spatiotemporally modulated illumination”. In: *J. Opt. Soc. Am. A* 35.8 (Aug. 2018), pp. 1438–1449.

[48] Jeffrey J Field, Jeff A Squier, and Randy A Bartels. “Fluorescent coherent diffractive imaging with accelerating light sheets”. In: *Optics Express* 27.9 (2019), pp. 13015–13030.

[49] Jeffrey Field, David Winters, and Randy Bartels. “Single-pixel fluorescent imaging with temporally labeled illumination patterns”. In: *Optica* 3.9 (Sept. 2016), pp. 971–974.

[50] Martin C. Fischer et al. “Invited Review Article: Pump-probe microscopy”. In: *Review of Scientific Instruments* 87.3 (2016).

[51] Greg Futia et al. “Spatially-chirped modulation imaging of absorbtion and fluorescent objects on single-element optical detector”. In: *Optics Express* 19.2 (2011), pp. 1626–1640.

[52] Greg Futia et al. “Spatially-chirped modulation imaging of absorbtion and fluorescent objects on single-element optical detector”. In: *Opt. Express* 19.2 (Jan. 2011), pp. 1626–1640.

[53] D Gabor. “A new microscopic principle.” In: *Nature* 161.4098 (1948), p. 777.

[54] Goldie Goldstein and Katherine Creath. “Quantitative Phase Microscopy: how to make phase data meaningful”. In: *Proceedings of SPIE–the International Society for Optical Engineering* 8949 (Mar. 2014).

[55] J. W. Goodman and R. W. Lawrence. “DIGITAL IMAGE FORMATION FROM ELECTRONICALLY DETECTED HOLOGRAMS”. In: *Applied Physics Letters* 11.3 (1967), pp. 77–79. DOI: 10.1063/1.1755043. eprint: https://doi.org/10.1063/1.1755043. URL: https://doi.org/10.1063/1.1755043.

[56] Joseph W Goodman. *Introduction to Fourier optics*. Roberts and Company Publishers, 2005.

[57] Mats G. L. Gustafsson. “Nonlinear structured-illumination microscopy: Wide-field fluorescence imaging with theoretically unlimited resolution”. In: *Proceedings of the National Academy of Sciences* 102.37 (2005), pp. 13081–13086. DOI: 10.1073/pnas.0406877102. eprint: https://www.pnas.org/doi/pdf/10.1073/pnas.0406877102. URL: https://www.pnas.org/doi/abs/10.1073/pnas.0406877102.

[58] Olivier Haeberlé et al. “Tomographic Diffractive Microscopy: Basics, techniques and perspectives”. In: *Journal of Modern Optics* 57.9 (2010), pp. 686–699.

[59] S. Hahamovich E.and Monin, Hazan Y., and et al. “Single pixel imaging at megahertz switching rates via cyclic Hadamard masks”. In: *Nature Communications* (2021).

[60] Stefan W. Hell. “Far-Field Optical Nanoscopy”. In: *Science* 316.5828 (May 2007), p. 1153.

[61] Fritjof Helmchen and Winfried Denk. “Deep tissue two-photon microscopy”. In: *Nature Methods* 2.12 (2005), pp. 932–940.

[62] Daniel J Higley, David G Winters, and Randy A Bartels. “Two-dimensional spatial frequency-modulated imaging through parallel acquisition of line images”. In: *Optics Letters* 38.11 (2013), pp. 1763–1765.

[63] Daniel J Higley et al. “Theory of diffraction effects in spatial frequency-modulated imaging”. In: *J. Opt. Soc. Am. A* 29 (2012), p. 2579.

[64] T. Hirschfeld. “Fellgett’s Advantage in uv-VIS Multiplex Spectroscopy”. In: *Appl. Spectrosc.* 30.1 (Jan. 1976), pp. 68–69.

[65] Erich E. Hoover et al. “Eliminating the scattering ambiguity in multifocal, multimodal, multiphoton imaging systems”. In: *Journal of Biophotonics* 5.5-6 (2012), pp. 425–436.

[66] Erich E Hoover et al. “Eliminating the scattering ambiguity in multifocal, multimodal, multiphoton imaging systems”. In: *Journal of biophotonics* 5.5-6 (2012), pp. 425–436.

[67] Scott S Howard et al. “Frequency-multiplexedin vivomultiphoton phosphorescence lifetime microscopy”. In: *Nature Photonics* (2012), pp. 1–5.

[68] D Huang et al. “Optical coherence tomography”. In: *Science* 254.5035 (1991), pp. 1178–1181.

[69] Pengwei Huang et al. “Depth imaging denoising of photon-counting lidar”. In: *Appl. Opt.* 58.16 (June 2019), pp. 4390–4394. DOI: 10.1364/AO.58.004390. URL: http://opg.optica.org/ao/abstract.cfm?URI=ao-58-16-4390.

[70] Jan Huisken et al. “Optical Sectioning Deep Inside Live Embryos by Selective Plane Illumination Microscopy”. In: *Science* 305.5686 (2004), pp. 1007–1009.

[71] H. C. van de (Hendrik Christoffel) Hulst. *Light scattering by small particles*. eng. New York: Dover Publications, 1981 - 1957. ISBN: 0486642283.

[72] Takahiro Ikeda et al. “Hilbert phase microscopy for investigating fast dynamics in transparent systems”. In: *Optics Letters* 30.10 (2005), pp. 1165–7.

[73] Hidenao Iwai et al. “Quantitative phase imaging using actively stabilized phase-shifting low-coherence interferometry”. In: *Optics letters* 29.20 (2004), pp. 2399–2401.

[74] Pawley James. “Handbook of Biological Confocal Microscopy”. In: *Scanning* 29.3 (2006), pp. 91–91. DOI: https://doi.org/10.1002/sca.20059. URL: https://onlinelibrary.wiley.com/doi/abs/10.1002/sca.20059.

[75] Y. Jauregui-Sánchez et al. “Single-pixel imaging with Fourier filtering: application to vision through scattering media”. In: (Oct. 2018).

[76] Randy A. Bartels Jeffrey J. Field. “Digital aberration correction of fluorescent images with coherent holographic image reconstruction by phase transfer (CHIRPT)”. In: 9713 (2016).

[77] Chulmin Joo et al. “Spectral-domain optical coherence phase microscopy for quantitative phase-contrast imaging”. In: *Optics Letters* 30.16 (2005), pp. 2131–2133.

[78] AninashC. Kak and Malcom Slaney. *Principles of Computerized Tomographic Imaging*. SIAM, 2001. ISBN: 089871494X.

[79] Tuhin Khan. “Chemical and Physical Strategies for Modulation of Excited State Dynamics and Consequent Emission Enhancement of Schiff Bases”. PhD thesis. Oct. 2017. DOI: 10.13140/RG.2.2.29866.11201.

[80] Taewoo Kim et al. “White-light diffraction tomography of unlabelled live cells”. In: *Nature Photonics* 8.3 (2014), pp. 256–263.

[81] Taewoo Kim et al. “White-light diffraction tomography of unlabelled live cells”. In: *Nature Photonics* 8 (Jan. 2014).

[82] Tomasz Kozacki, Małgorzata Kujawińska, and P. Kniażewski. “Investigation of limitations of optical diffraction tomography”. In: *Opto-Electronics Review* 15 (June 2007), pp. 102–109.

[83] Peter D Lax and Ralph S Phillips. *Scattering Theory, Revised Edition*. eng. Burlington: Elsevier Science Technology, 1990. ISBN: 9780124400511.

[84] KyeoReh Lee et al. “Quantitative phase imaging techniques for the study of cell pathophysiology: from principles to applications”. In: *Sensors (Basel)* (2013), pp. 4170–4191.

[85] KyeoReh Lee et al. “Quantitative phase imaging techniques for the study of cell pathophysiology: from principles to applications”. In: *Sensors* 13.4 (2013), pp. 4170–4191.

[86] Emmett N. Leith and Juris Upatnieks. “Reconstructed Wavefronts and Communication Theory*”. In: *Journal of the Optical Society of America* 52.10 (1962), pp. 1123–1130.

[87] Emmett N. Leith and Juris Upatnieks. “Reconstructed Wavefronts and Communication Theory∗”. In: *J. Opt. Soc. Am.* 52.10 (Oct. 1962), pp. 1123–1130. DOI: 10.1364/JOSA.52.001123. URL: http://www.osapublishing.org/abstract.cfm?URI=josa-52-10-1123.

[88] Emmett N Leith and Juris Upatnieks. “Wavefront reconstruction with continuous-tone objects”. In: *JOSA* 53.12 (1963), pp. 1377–1381.

[89] Peng Li and Andrew Maiden. “Multi-slice ptychographic tomography”. eng. In: *Scientific reports* 8.1 (2018), pp. 2049–10. ISSN: 2045-2322.

[90] Jeanne Linarès-Loyez, Pierre Bon, and et al. “Self-Interference (SELFI) Microscopy for Live Super-Resolution Imaging and Single Particle Tracking in 3D”. In: *Frontiers in Physics* 7 (2019), p. 68.

[91] A. Liu et al. “Comparison of optical projection tomography and light-sheet fluorescence microscopy”. In: *Journal of Microscopy* 275.1 (2019), pp. 3–10.

[92] Yang Liu and J.K. Aggarwal. “3.12 - Local and Global Stereo Methods”. In: *Handbook of Image and Video Processing (Second Edition)*. Ed. by AL BOVIK. Second Edition. Communications, Networking and Multimedia. Burlington: Academic Press, 2005, pp. 297–308. ISBN: 978-0-12-119792-6. DOI: https://doi.org/10.1016/B978-012119792-6/50081-4. URL: https://www.sciencedirect.com/science/article/pii/B9780121197926500814.

[93] Guillaume Maire et al. “Experimental inversion of optical diffraction tomography data with a nonlinear algorithm in the multiple scattering regime”. In: *Journal of Modern Optics* 57.9 (2010), pp. 746–755.

[94] Jerome Mertz. *Introduction to Optical Microscopy*. Roberts and Company Publishers, 2010.

[95] Jerome Mertz. *Introduction to Optical Microscopy*. 2nd ed. Cambridge University Press, 2019. DOI: 10.1017/9781108552660.

[96] Mustafa Mir et al. “Quantitative Phase Imaging”. In: *Progress in Optics* 57 (2012), pp. 133–217.

[97] Mustafa Mir et al. “Quantitative Phase Imaging”. In: *Progress in Optics* 57 (July 2012), pp. 133–217.

[98] Mustafa Mir et al. “Quantitative phase imaging”. In: *Progress in optics* 57 (2012), pp. 133–217.

[99] Jennifer (Jennifer L.) Mueller and Samuli Siltanen. *Linear and nonlinear inverse problems with practical applications Jennifer Mueller, Samuli Siltanen*. eng. Computational science and engineering series. Philadelphia, Pa.: Society for Industrial and Applied Mathematics SIAM, 3600 Market Street, Floor 6, Philadelphia, PA 19104, 2012. ISBN: 1-61197-233-7.

[100] Michiel Muller. *Introduction to Confocal Fluorescence Microscopy*. 2nd ed. SPIE Publications, 2005.

[101] Paul Müller, Mirjam Schürmann, and Jochen Guck. *The Theory of Diffraction Tomography*. 2015. DOI: 10.48550/ARXIV.1507.00466. URL: https://arxiv.org/abs/1507.00466.

[102] Paul Müller, Mirjam Schürmann, and Jochen Guck. *The Theory of Diffraction Tomography*. 2016. arXiv: 1507.00466 [q-bio.QM].

[103] Ren Ng. “Fourier Slice Photography”. In: *ACM Trans. Graph.* 24.3 (July 2005), pp. 735–744. ISSN: 0730-0301. DOI: 10.1145/1073204.1073256. URL: https://doi.org/10.1145/1073204.1073256.

[104] Lukas Novotny and Bert Hecht. *Principles of Nano-Optics*. 2nd ed. Cambridge University Press, 2012. DOI: 10.1017/CBO9780511794193.

[105] C. J. Oliver and E. R. Pike. “Multiplex Advantage in the Detection of Optical Images in the Photon Noise Limit”. In: *Appl. Opt.* 13.1 (Jan. 1974), pp. 158–161. DOI: 10.1364/AO.13.000158. URL: http://opg.optica.org/ao/abstract.cfm?URI=ao-13-1-158.

[106] Xiaoze Ou et al. “Quantitative phase imaging via Fourier ptychographic microscopy”. In: *Optics Letters* 38.22 (2013), pp. 4845–4848. DOI: 10.1364/OL.38.004845.

[107] D. Paganin and K. A. Nugent. “Noninterferometric Phase Imaging with Partially Coherent Light”. In: *Physical Review Letters* 80.12 (Mar. 1998), pp. 2586–2589.

[108] YongKeun Park et al. “Diffraction phase and fluorescence microscopy”. In: *Optics Express* 14.18 (Sept. 2006), pp. 8263–8268. DOI: 10.1364/OE.14.008263.

[109] Ashwin B. Parthasarathy et al. “Quantitative phase imaging using a partitioned detection aperture”. In: *Optics Letters* 37.19 (2012), pp. 4062–4064. DOI: 10.1364/OL.37.004062.

[110] Sri Rama Prasanna Pavani et al. “Three-dimensional, single-molecule fluorescence imaging beyond the diffraction limit by using a double-helix point spread function”. In: *Proceedings of the National Academy of Sciences* 106.9 (2009), pp. 2995–2999. DOI: 10.1073/pnas.0900245106. URL: https://www.pnas.org/doi/abs/10.1073/pnas.0900245106.

[111] Justin Peatross and Michael Ware. *Physics of Light and Optics*. 2015. URL: https://optics.byu.edu/home.

[112] Frank L. Pedrotti, Leno M. Pedrotti, and Leno S. Pedrotti. *Introduction to Optics*. 3rd ed. Cambridge University Press, 2017. DOI: 10.1017/9781108552493.

[113] Zachary F. Phillips, Michael Chen, and Laura Waller. “Single-shot quantitative phase microscopy with color-multiplexed differential phase contrast (cDPC)”. In: *PLOS ONE* 12.2 (Feb. 2017).

[114] Thomas A Planchon et al. “Rapid three-dimensional isotropic imaging of living cells using Bessel beam plane illumination”. In: *Nature Methods* 8.5 (2011), pp. 417–423. DOI: 10.1038/nmeth.1586. URL: https://doi.org/10.1038/nmeth.1586.

[115] Gabriel Popescu. *Quantitative phase imaging of cells and tissues*. McGraw Hill Professional, 2011.

[116] Gabriel Popescu et al. “Diffraction phase microscopy for quantifying cell structure and dynamics”. In: *Optics letters* 31.6 (2006), pp. 775–777.

[117] Gabriel Popescu et al. “Fourier phase microscopy for investigation of biological structures and dynamics”. In: *Optics letters* 29.21 (2004), pp. 2503–2505.

[118] Vitaliy N. Pustovit and Vadim A. Markel. “Propagation of Diffuse Light in a Turbid Medium with Multiple Spherical Inhomogeneities”. In: *Appl. Opt.* 43.1 (Jan. 2004), pp. 104–112.

[119] Johann Radon. “Uber die Bestimmung von Funktionen durch ihre Integralwerte l¨angs gewisser Mannigfaltigkeiten”. In: *Tech. rep. Leipzig: Berichte ¨uber die Verhandlungen der K¨oniglich-S¨achsischen Gesellschaft der Wissenschaften zu Leipzig* (1917).

[120] Matthew Rinehart, Yizheng Zhu, and Adam Wax. “Quantitative phase spectroscopy”. In: *Biomedical Optics Express* 3.5 (2012), pp. 958–965.

[121] Justin Romberg. “Imaging via compressive sampling”. In: *IEEE Signal Processing Magazine* 25.2 (2008), pp. 14–20.

[122] Gregory Samelsohn. “Transmission tomography of forward-scattering structures”. In: *J. Opt. Soc. Am. A* 33.6 (June 2016), pp. 1181–1192.

[123] Jeffery S Sanders et al. “Imaging with frequency-modulated reticles”. In: *Opt. Eng.* 30.11 (1991), pp. 1720–1724.

[124] P. Sarder and A. Nehorai. “Deconvolution methods for 3-D fluorescence microscopy images”. In: *IEEE Sig. Proc. Magazine* 23.3 (2006), pp. 32–45.

[125] Philip Schlup, Greg Futia, and Randy A Bartels. “Lateral tomographic spatial frequency modulated imaging”. In: *Applied Physics Letters* 98.21 (2011), p. 211115.

[126] Philip Schlup, Greg Futia, and Randy A. Bartels. “Lateral tomographic spatial frequency modulated imaging”. In: *Applied Physics Letters* 98.21 (2011), p. 211115. DOI: 10.1063/1.3595305. eprint: https://doi.org/10.1063/1.3595305. URL: https://doi.org/10.1063/1.3595305.

[127] Anne Sentenac and Jerome Mertz. “Unified description of three-dimensional optical diffraction microscopy: from transmission microscopy to optical coherence tomography: tutorial”. In: *J. Opt. Soc. Am. A* 35.5 (May 2018), pp. 748–754.

[128] Jeffrey H. Shapiro and Robert W. Boyd. “The physics of ghost imaging”. In: *Quantum Information Processing* 11.4 (2012), pp. 949–993.

[129] Colin J. R. Sheppard, Shalin B. Mehta, and Rainer Heintzmann. “Superresolution by image scanning microscopy using pixel reassignment”. In: *Opt. Lett.* 38.15 (Aug. 2013), pp. 2889–2892. DOI: 10.1364/OL.38.002889. URL: http://opg.optica.org/ol/abstract.cfm?URI=ol-38-15-2889.

[130] Colin J. R. Sheppard et al. “Interpretation of the optical transfer function: Significance for image scanning microscopy”. In: *Opt. Express* 24.24 (Nov. 2016), pp. 27280–27287. DOI: 10.1364/OE.24.027280. URL: http://opg.optica.org/oe/abstract.cfm?URI=oe-24-24-27280.

[131] Colin J. R. Sheppard et al. “Pixel reassignment in image scanning microscopy: a re-evaluation”. In: *J. Opt. Soc. Am. A* 37.1 (Jan. 2020), pp. 154–162. DOI: 10.1364/JOSAA.37.000154. URL: http://opg.optica.org/josaa/abstract.cfm?URI=josaa-37-1-154.

[132] Nisan Siegel et al. “High-magnification super-resolution FINCH microscopy using birefringent crystal lens interferometers”. In: *Nature Photonics* 10 (2016).

[133] J. Stephens David and J. Allan Victoria. “Light microscopy techniques for live cell imaging”. In: *Science* 300.5616 (2003), pp. 82–86.

[134] Patrick A. Stockton et al. “Fourier computed tomographic imaging of two dimensional fluorescent objects”. In: *APL Photonics* 4.10 (2019), p. 106102. DOI: 10.1063/1.5100525. eprint: https://doi.org/10.1063/1.5100525. URL: https://doi.org/10.1063/1.5100525.

[135] Patrick A. Stockton et al. “Tomographic single pixel spatial frequency projection imaging”. In: *Optics Communications* (2021).

[136] Patrick Stockton, Jeffrey Field, and Randy Bartels. “Single pixel quantitative phase imaging with spatial frequency projections”. In: *Methods* 136 (2018). Methods in Quantitative Phase Imaging in Life Science, pp. 24–34.

[137] Patrick Stockton et al. “Fourier computed tomographic imaging of two dimensional fluorescent objects”. In: *APL Photonics* 4 (Oct. 2019), p. 106102. DOI: 10.1063/1.5100525.

[138] N Streibl. “Three-dimensional imaging by a microscope”. In: *Journal of the Optical Society of America A* 2.2 (1985), pp. 121–127. DOI: 10.1364/JOSAA.2.000121.

[139] Enrique Tajahuerce et al. “Image transmission through dynamic scattering media by single-pixel photodetection”. In: *Opt. Express* 22.14 (July 2014), pp. 16945–16955. DOI: 10.1364/OE.22.016945. URL: http://opg.optica.org/oe/abstract.cfm?URI=oe-22-14-16945.

[140] Michael Reed Teague. “Deterministic phase retrieval: a Green’s function solution”. In: *JOSA* 73.11 (1983), pp. 1434–1441.

[141] Lei Tian et al. “Computational illumination for high-speed in vitro Fourier ptychographic microscopy”. In: *Optica* 2.10 (Oct. 2015), pp. 904–911. DOI: 10.1364/OPTICA.2.000904. URL: http://opg.optica.org/optica/abstract.cfm?URI=optica-2-10-904.

[142] Mohammad Torabzadeh et al. “Compressed single pixel imaging in the spatial frequency domain”. In: *Journal of Biomedical Optics* 22.3 (2017).

[143] J.A. Tropp. “Just relax: convex programming methods for identifying sparse signals in noise”. In: *IEEE Transactions on Information Theory* 52.3 (2006), pp. 1030–1051. DOI: 10.1109/TIT.2005.864420.

[144] Lihong V. Wang. *Biomedical optics : principles and imaging / Lihong V. Wang, Hsin-i Wu.* eng. Hoboken, N.J: Wiley-Interscience, 2007. ISBN: 9780471743040.

[145] Zhuo Wang et al. “Spatial light interference microscopy (SLIM)”. In: *Optics Express* 19.2 (2011), pp. 1016–1026.

[146] Adam Wax et al. “Optical Spectroscopy of Biological Cells”. In: *Adv. Opt. Photon.* 4.3 (Sept. 2012), pp. 322–378.

[147] J. W. Wilson and R. A. Bartels. “Rapid Birefringent Delay Scanning for Coherent Multiphoton Impulsive Raman Pump–Probe Spectroscopy”. In: *IEEE Journal of Selected Topics in Quantum Electronics* 18.1 (Jan. 2012), pp. 130–139.

[148] Robert H Wilson et al. “Review of short-wave infrared spectroscopy and imaging methods for biological tissue characterization.” In: *Journal of biomedical optics* 20 (Mar. 2015), p. 30901.

[149] Tony Wilson and Colin Sheppard. “Theory And Practice Of Scanning Optical Microscopy”. In: *London: Academic Press* -1 (Oct. 1984).

[150] David G. Winters and Randy A. Bartels. “Two-dimensional single-pixel imaging by cascaded orthogonal line spatial modulation”. In: *Optics Letters* 40.12 (2015), pp. 2774–2777.

[151] Emil Wolf. “Three-dimensional structure determination of semi-transparent objects from holographic data”. In: *Optics Communications* 1.4 (1969), pp. 153–156.

[152] Nathan Worts et al. “Fabrication and characterization of modulation masks for multimodal spatial frequency modulated microscopy”. In: *Appl. Opt.* 57.16 (June 2018), pp. 4683–4691. DOI: 10.1364/AO.57.004683. URL: http://opg.optica.org/ao/abstract.cfm?URI=ao-57-16-4683.

[153] Nathan Worts et al. “Simultaneous multi-dimensional spatial frequency modulation imaging”. In: *International Journal of Optomechatronics* 14.1 (2020), pp. 1–17. DOI: 10.1080/15599612.2019.1694610. URL: https://doi.org/10.1080/15599612.2019.1694610.

[154] Wenbo Xu et al. “Digital in-line holography for biological applications”. In: *Proceedings of the National Academy of Sciences* 98.20 (2001), pp. 11301–11305.

[155] Ichirou Yamaguchi and Tong Zhang. “Phase-shifting digital holography”. In: *Optics Letters* 22.16 (1997), pp. 1268–1270.

[156] Cotte Yann et al. “Marker-free phase nanoscopy”. In: *Nature Photonics* 7 (Jan. 2013).

[157] Li-Hao Yeh, Lei Tian, and Laura Waller. “Structured illumination microscopy with unknown patterns and a statistical prior”. In: *Biomed. Opt. Express* 8.2 (Feb. 2017), pp. 695–711. DOI: 10.1364/BOE.8.000695. URL: http://opg.optica.org/boe/abstract.cfm?URI=boe-8-2-695.

[158] Michael D. Young et al. “A pragmatic guide to multiphoton microscope design”. In: *Adv. Opt. Photon.* (2015). DOI: 10.1364/AOP.7.000276.

[159] F. Zernike. “How I discovered phase contrast”. In: *Science* 121.3141 (1955), pp. 345–349.

[160] F. Zernike. “Phase contrast, a new method for the microscopic observation of transparent objects part II”. In: *Physica* 9.10 (1942), pp. 974–986. ISSN: 0031-8914. DOI: https://doi.org/10.1016/S0031-8914(42)80079-8. URL: https://www.sciencedirect.com/science/article/pii/S0031891442800798.

[161] Taiping Zhang et al. “A solar azimuth formula that renders circumstantial treatment unnecessary without compromising mathematical rigor: Mathematical setup, application and extension of a formula based on the subsolar point and atan2 function”. In: *Renewable Energy* 172 (2021), pp. 1333–1340. ISSN: 0960-1481. DOI: https://doi.org/10.1016/j.renene.2021.03.047. URL: https://www.sciencedirect.com/science/article/pii/S0960148121004031.

[162] Guangyuan Zhao et al. “Saturated absorption competition microscopy”. In: *Optica* 4.6 (June 2017), pp. 633–636. DOI: 10.1364/OPTICA.4.000633. URL: http://opg.optica.org/optica/abstract.cfm?URI=optica-4-6-633.

Appendix A

Comparison of Coherent Verse Incoherent Imaging Systems

```
%% Simulation of the Incoherant and Coherent Imaging comparison

clear all
close all
clc
%%
set(0,'DefaultFigureWindowStyle','docked')
set(0,'fontsize',14)

%% Set Up Variables
mm = 10-3;

Nx = 2^12;                          % Number of spatial points
xmax = 1*mm;                        % Max size of spatial grid
x = linspace(-xmax,xmax,Nx);        % Spatial vector
dx = mean(diff(x));                 % Sampling size

fx = 1/(Nx*dx)*[-Nx/2:Nx/2-1];      % Frequency vector
fmax = 1/dx;
fc = fmax*0.01;                     % Cuttoff Frequency

MTF = abs(fx)<=fc;                  % Modulation transfer function, coh
```

```
CSF = (fftshift(fft(fftshift(MTF)))); % Coherent spread function, coh

PSF = CSF.*conj(CSF);              % Point spread function, incoh
OTF = fftshift(ifft(fftshift(PSF)));  % Optical transfer function, incoh
OTF = OTF/max(OTF);

figure(1)
plot(fx/fc, MTF, fx/fc, OTF/max(OTF),'linewidth',2)
title('CTF and OTF')
xlabel('Normalized Frequency [fx/fc]')
ylabel('Amplitude')
legend('Coherent CTF (Field)','Incoherent OTF (Intensity)','location','
    southeast')
xlim([-2.5,2.5])

figure(2)
plot(x/mm,real(CSF)/max(real(CSF)),x/mm,PSF/max(PSF),'linewidth',2)
title('CSF and PSF')
xlabel('Space [mm]')
ylabel('Amplitude')
legend('Coherent CSF (Field)','Incoherent PSF (Intensity)','location','
    southeast')
xlim([-max(x)/mm*0.1,max(x)/mm*0.1])

%%
fobj = fc*0.85;                    % Frequency of the object
% obj = exp(-1i*0.5*pi*cos(2*pi*fobj*x));          % Object vector
```

```
% obj = abs(cos(2*pi*fobj*x));          % Object vector
obj = cos(2*pi*fobj*x);    % Object vector


ftObj = 1/Nx*fftshift(fft(fftshift(obj)));
ftObjCor = autoCorr(ftObj);

fxx = linspace(2*fx(1),2*fx(end),2*Nx);
xx  = linspace(x(1),x(end),2*Nx);

figure(3)
plot(fx/fc,abs(ftObj)/max(abs(ftObj)),fxx/fc, abs(ftObjCor)/max(abs(
    ftObjCor)),'--','linewidth',2)
title('C(fx) and C(fx) * C(fx)')
xlabel('Spatial Frequency [fx/fc]')
ylabel('Amplitude')
legend('Obj Spectrum','Autocorr of Obj Spectrum')
xlim([-2.5,2.5])

% Coherent
HGg = MTF.*ftObj;
ftIcoh = autoCorr(HGg);
Icoh = abs(fftshift(fft(ifftshift(ftIcoh))));

% Incoherent
Gg_Gg = autoCorr(ftObj);
OTF_new = autoCorr(MTF);
```

```
OTF_new = OTF_new/max(OTF_new);
ftIincoh = Gg_Gg.*OTF_new;
Iincoh = abs(ifftshift(ifft(fftshift(ftIincoh))));

figure(4)
plot(fx/fc,MTF,fx/fc,HGg/max(HGg),fxx/fc,ftIcoh/max(ftIcoh),'linewidth',2)
title('Coherent Imaging')
xlabel('Spatial Frequency [fx/fc]')
ylabel('Amplitude')
legend('MTF','Coherent Filtered Spectrum','Coherent Intensity Spectrum')
xlim([-2.5,2.5])

figure(5)
plot(fx/fc,OTF,fxx/fc,Gg_Gg/max(Gg_Gg),fxx/fc,ftIincoh/max(ftIincoh),'--',
    'linewidth',2)
title('Incoherent Imaging')
xlabel('Spatial Frequency [fx/fc]')
ylabel('Amplitude')
legend('OTF','Autocorr of Obj Spectrum','Incoherent Intensity Spectrum')
xlim([-2.5,2.5])

figure(6)
plot(fxx/fc,ftIcoh/max(ftIcoh),fxx/fc,ftIincoh/max(ftIincoh),'linewidth'
    ,2)
title('Intesity Spectrum: Coherent Vs. Incoherent')
xlabel('Spatial Frequency [fx/fc]')
ylabel('Amplitude')
```

```
legend('Coherent Intensity Spectrum','Incoherent Intensity Spectrum')
xlim([-2.5,2.5])

figure(7)
plot(x/mm,real(obj),xx/mm,Icoh/max(Icoh),xx/mm,Iincoh/max(Iincoh),'
    linewidth',2)
title('Intesity: Coherent Vs. Incoherent')
xlabel('Space [mm]')
ylabel('Amplitude')
legend('True Object','Coherent Iintensity Image','Incoherent Intensity
    Image','location','southeast')
xlim([-0.1,0.1])

%%
function autocorr = autoCorr(x)
    Nx = numel(x);
    xPad = zeros(1,Nx*3);
    xPad(Nx:2*Nx-1) = x;

    autocorr = zeros(1,2*Nx);
    jj = 1;
    for ii = 1:1:2*Nx
        autocorr(jj) = sum(x.*conj(xPad(ii:Nx+ii-1)));
        jj = jj+1;
    end
end
```

Appendix B

Plane Wave Focal Spot Generation

```
%% Sum Electric Field at Many Different Angle
noiseON = 0;                                    % Switch for noise
lambda  = 500e-9;                               % Illumination wavelength
k       = 2*pi/lambda;                          % Radial spatial frequency

res     = 0.01e-6;                              % Spatial resolution
fov_x   = 10*500e-9;                            % Field of View in x
fov_y   = 20*lambda;                             % Field of View in y
nPnts_x = ceil(fov_x/res);                      % Number of x points
nPnts_y = ceil(fov_y/res);                      % Number of y points
y       = linspace(-fov_y/2,fov_y/2,nPnts_y);   % y vector
x       = linspace(-fov_x/2,fov_x/2,nPnts_x);   % x vector
[yy,xx] = meshgrid(x,y);                        % 2D x y grids

theta_max = 20;                                 % Max angle of
   illumination

theta = [0:theta_max];                          % Angles of illumination

if noiseON == 1
    phase_ab = linspace(-1.5,1.5,2*numel(theta)).^3;
    phase_ab = rand(1,2*numel(theta))*0+phase_ab;
else
    phase_ab = zeros(1,2*numel(theta));
```

```
end

E_tot = zeros(size(xx));                    % Intial Electic Field

for i = 1:numel(theta)

    % Add the on axis plane wave
    if i == 1
        Ep = exp(-1i*(2*pi*t - k*sind(theta(i))*yy + k*cosd(theta(i))*xx))
            ;
        E_tot = Ep;
    % Add the positive and negative angle plane waves
    else
        Ep = exp(-1i*(2*pi*t - k*sind(theta(i))*yy + k*cosd(theta(i))*xx +
             phase_ab(round(end/2)+i)));
        En = exp(-1i*(2*pi*t - k*sind(-theta(i))*yy + k*cosd(-theta(i))*xx
             + phase_ab(round(end/2)-i+1)));
        E_tot = E_tot + Ep + En;
    end

    figure(2)
    imagesc(x/1e-6,y/1e-6,abs(E_tot).^2)
    title(['Intensity: \theta = ', num2str(theta(i)), ' NA = ', num2str(
       sind(theta(i)))])
    xlabel(['x [\mum]'])
    ylabel(['z [\mum]'])
    daspect([1,1,1])
```

```
    pause(0.1)
    set(gca,'xtick',[-5:1:5])
    set(gca,'ytick',[-5:2:5])
end
```

Appendix C

Plane Wave Interference for CHIRPT and SPIFI

```
% Plane Wave Interference
% This code defines 2 or more plane waves at some angle theta1 and theta 2
% then allows them to interfer to demonstrate spatial frequencies

clear all
clc
close all

%% Setup Parameters
SPIFIIll = 0;                                   % Switch between SPIFI and
    CHIRPT Illumination
lambda   = 600e-9;                              % Illumination wavelength
k        = 2*pi/lambda;                         % Radial spatial frequency
t        = 0;                                   % Time for temporal
    propagation

res      = 0.01e-6;                             % Spatial resolution
fov_x    = 100*500e-9;                          % Field of View in x
fov_y    = 100*lambda;                          % Field of View in y
nPnts_x = ceil(fov_x/res);                      % Number of x points
nPnts_y = ceil(fov_y/res);                      % Number of y points
y        = linspace(-fov_y/2,fov_y/2,nPnts_y); % y vector
x        = linspace(-fov_x/2,fov_x/2,nPnts_x); % x vector
[yy,xx] = meshgrid(x,y);                        % 2D x y grids
```

```
theta_0 = 0;
theta_1 = 30;
theta_N1= -theta_1;

widthX = fov_x/5;
beamProfile0  = exp(-(sind(theta_0)*xx + cosd(theta_0)*yy).^2/(widthX)^2);
beamProfile1  = exp(-(sind(theta_1)*xx + cosd(theta_1)*yy).^2/(widthX)^2);
beamProfileN1 = exp(-(sind(theta_N1)*xx + cosd(theta_N1)*yy).^2/(widthX)
    ^2);

if SPIFIIll == 1    % SPIFI Illumination
    E0 = beamProfile0.*exp(-1i*(2*pi*t - k*sind(theta_0)*yy + k*cosd(
        theta_0)*xx)); % 1st e field
    E1 = beamProfile1.*exp(-1i*(2*pi*t - k*sind(theta_1)*yy + k*cosd(
        theta_1)*xx)); % 2st e field
    EN1 = beamProfileN1.*exp(-1i*(2*pi*t - k*sind(theta_N1)*yy + k*cosd(
        theta_N1)*xx)); % neg 2st e field
else                % CHIRPT Illumination
    E0 = beamProfile0.*exp(-1i*(2*pi*t - k*sind(theta_0)*yy + k*cosd(
        theta_0)*xx)); % 1st e field
    E1 = beamProfile1.*exp(-1i*(2*pi*t - k*sind(theta_1)*yy + k*cosd(
        theta_1)*xx)); % 2st e field
    EN1= 0;
end

figure(1)
```

```
imagesc(x/500e-9,y/lambda,abs(E0+E1+EN1).^2)
if SPIFIIll == 1
    title(['SPIFI Intensity)])
else
    title(['CHIRPT Intensity])
end
xlabel(['x [\lambda = ',num2str(lambda*10^9),' nm]'])
ylabel(['z [\lambda = ',num2str(500),' nm]'])
daspect([1,1,1])
```

Appendix D

Unrestricted Super-Resolution Calculators

```
%% Unrestricted Super Resolution Calculator
% This code takes in imaging input parameters and calculates the PSF and
% Resolution

% --- Set default properties for axes fonts ---
font='Helvetica';
set(0,'defaultaxesfontsize',18);
set(0,'defaultaxesfontname',font);

set(0,'DefaultFigureWindowStyle','docked')

un = Units();
%% Imaging Pararmeters

% I_max = 1e6;                  % Max illumination intensity

lambda = 532*un.nm;           % Illumination wavelength
NA     = 0.15;                % Numerical aperture
n      = 1;                   % Immersion media refractive index

%% Sample Parameters

tau       = 0.2*un.ps;        % Excited state lifetime
sigma_abs = 10e-16;           % Absorption cross-section [cm^2]
```

```
h_bar      = 1.0545718*10^-38;   % Planks constant [J s] = [kg*cm^2/s^2]
v          = 2.99e8;             % Speed of Light [m/s]
omega      = 2*pi*n*v/lambda;    % Anglular frequency

I_sat      = h_bar*omega/(sigma_abs*tau);        % Saturation Intensity
I_max      = I_sat*10;                           % Max Intensity
%% Calculate Effective PSF

x = linspace(-250*un.um/4,250*un.um/4,2^10);
u = 2*pi*x*NA/lambda;
PSF_c = (sin(u)./u).^2;
delta_r = lambda/(2*NA);
% [PSF_c, width] =

figure(1)
clf
hold on
plot(x/un.um, PSF_c)
title('Convential PSF')
xlabel('x-axis [\mum]')
ylabel('Intensity [Arb.]')
xlim([-5*delta_r,5*delta_r]/un.um)
%%
URSR   = 'sted';             % Type of Microscope 'sted','gsd','
    photoswithing','sax','spifi','chirpt'
Illum  = 'cw';               % Type of illumination 'pulsed','cw'
Imaging_setup
```

```
PSF_sted =  PSF_c .* (1-beta*F(alpha(I_max,I_sat,NA,lambda,x)));

figure(1)
plot(x/un.um, PSF_sted/max(PSF_sted))
title('Effective PSF')
xlabel('x-axis [\mum]')
ylabel('Intensity [Arb.]')

%% Generate OTFs
Nx = numel(x);
dx = mean(diff(x));

fx = (-Nx/2:Nx/2-1)*1/(dx*Nx);

figure(3)
clf
plot(fx/(NA/lambda),abs(FFT(PSF_c))/max(abs(FFT(PSF_c))))
hold on
plot(fx/(NA/lambda),abs(FFT(PSF_sted))/max(abs(FFT(PSF_sted))))
xlim([-10,10]);

%%
URSR   = 'gsd';            % Type of Microscope 'sted','gsd','
    photoswithing','sax','spifi','chirpt'
Illum  = 'cw';             % Type of illumination 'pulsed','cw'
Imaging_setup
```

```
PSF_gsd =  PSF_c .* (1-beta*F(alpha(I_max,I_sat,NA,lambda,x)));

figure(1)
plot(x/un.um, PSF_gsd/max(PSF_gsd))
title('Effective PSF')
xlabel('x-axis [\mum]')
ylabel('Intensity [Arb.]')

%% Generate OTFs
Nx = numel(x);
dx = mean(diff(x));

fx = (-Nx/2:Nx/2-1)*1/(dx*Nx);

figure(3)
hold on
plot(fx/(NA/lambda),abs(FFT(PSF_gsd))/max(abs(FFT(PSF_gsd))))
xlim([-10,10]);

%%
URSR   = 'photoswitching';            % Type of Microscope 'sted','gsd','
    photoswithing','sax','spifi','chirpt'
Illum  = 'cw';               % Type of illumination 'pulsed','cw'
Imaging_setup

PSF_photo =  PSF_c .* (1-beta*F(alpha(I_max,I_sat,NA,lambda,x)));
```

```
figure(1)
plot(x/un.um, PSF_photo/max(PSF_photo))
title('Effective PSF')
xlabel('x-axis [\mum]')
ylabel('Intensity [Arb.]')

%% Generate OTFs
Nx = numel(x);
dx = mean(diff(x));

fx = (-Nx/2:Nx/2-1)*1/(dx*Nx);

figure(3)
hold on
plot(fx/(NA/lambda),abs(FFT(PSF_photo))/max(abs(FFT(PSF_photo))))
xlim([-10,10]);

%% SAX
clc
URSR    = 'sax';              % Type of Microscope 'sted','gsd','
    photoswithing','sax','spifi','chirpt'
Illum   = 'cw';               % Type of illumination 'pulsed','cw'
Imaging_setup

omega_m = 2*pi*50*un.kHz;
t = linspace(0,10/omega_m,1024);
```

```
q = 2;

for ii = 1:numel(t)
    bq = @(phi) F(1/2*alpha*(1+cos(2*pi*omega_m.*t(ii))))*cos(q*phi);
    PSF_sax(ii) = 1*(2*pi) * integral(bq,-pi,pi);
end

%% Convert 1D PSV vector into 2D PSF Matrix

PSF_c_2D = PSF_1Dto2D(PSF_c,x);
PSF_sted_2D = PSF_1Dto2D(PSF_sted,x);
PSF_gsd_2D = PSF_1Dto2D(PSF_gsd,x);
PSF_photo_2D = PSF_1Dto2D(PSF_photo,x);
% PSF_sax_2D = PSF_1Dto2D(PSF_sax,x);
% PSF_spifi_2D = PSF_1Dto2D(PSF_6th,x);

figure; imagesc(iFFT2(FFT2(P.CI.OBJ).*FFT2(PSF_sted_2D)))
axis equal; axis off

figure;
histeq(IDLSP6)
%% Set up the spatial grid parameters

P.sw_plotassignment = 1;

%% Run the setup file
```

```
% pull the set up parameters structure
P = SPIFIImageCompareSetup;

% set the imaging NA
P.ImagingParameters.NA = 0.15;
% cutoff spatial frequency
P.fcut = P.ImagingParameters.NA/P.lambda0;

% Airy units
P.rAiry = 0.61/P.fcut;

%% Set up imaging parameters: diffraction-limited coherent imaging
P.BeamParameters.beamchoice = 'point'; %
P.ImagingParameters.filterchoice = 'circular';
P.FilterParameters.aberchoice ='diffractionlimit';
P.BeamParameters.z0 = 0; % image in focus

% diffraction-limited spatialy coherent image
Pc = PupilFilter(P);
CohMTF = Pc(floor(end/2),:);
Eim = P.CI.OBJspatfreq.*Pc;
eim = ifftshift(ifft2(ifftshift(Eim)));
OBJDL = eim;
IDL = eim.*conj(eim);
IDL = IDL/max(abs(IDL(:)));
```

```
% plot counter
P.plt_ctr = P.plt_ctr + 1;

% axis scaling and labels
P.PlotVariables.xvar = P.x/P.um;
P.PlotVariables.yvar = P.y/P.um;
P.PlotVariables.xlab = 'x (\mum)';
P.PlotVariables.ylab = 'y (\mum)';
P.PlotVariables.fxvar = P.fx/P.fcut;
P.PlotVariables.fyvar = P.fy*P.um;
P.PlotVariables.fxlab = 'f_\perp/f_c';
P.PlotVariables.fylab = '\kappa_y (\mum^{-1})';

% feed in the spatial freuqency support
P.PlotVariables.Support.Coh = CohMTF;
%P.PlotVariables.title2 = 'Imaged Object';
P.PlotVariables.Panel1xlim = 4*[-1,1];
P.PlotVariables.Panel1ylim = [0,1.01];

% feed in the original object
P.PlotVariables.Object = P.CI.OBJ;
P.PlotVariables.title1 = 'Object';
P.PlotVariables.Panel2xlim = 40*[-1,1];
P.PlotVariables.Panel2ylim = 20*[-1,1];

%% Set up imaging parameters: diffraction-limited incoherent imaging
```

```
% incoherent input real object image
I0    = abs(P.CI.OBJ).^2;
I0FT = fftshift(fft2(ifftshift(I0)));

% diffraction-limited spatialy incoherent image
h        = ifftshift(ifft2(fftshift(Pc))); %j coherent spread function
OTF      = fftshift(fft2(ifftshift(abs(h).^2))); % OFT FFT of |CSF|^2
OTF      = OTF/max(max(abs(OTF)));
IFTim    = I0FT.*OTF;
Iim      = ifftshift(ifft2(ifftshift(IFTim)));
IincDL   = Iim;
IincDL = IincDL/max(abs(IincDL(:)));

% feed in the diffraction limited incoherent image
P.PlotVariables.InCohImg = IincDL;
P.PlotVariables.Support.InCoh = OTF(floor(end/2),:);
P.PlotVariables.Support.InCoh = P.PlotVariables.Support.InCoh/ ...
    max(abs(P.PlotVariables.Support.InCoh));

%% linear SPIFI: first and second order

% transfer function
mu = @(ft, fc, ord)  (real(sqrt(1 - (ft.^2)/(ord*fc)^2 ))).^ord;

% transfer functions
% first order
SPOTF1 = mu(P.FRt, P.fcut, 1);
```

```
SP1MTF = SPOTF1(floor(end/2),:);
% second order
SPOTF2 = mu(P.FRt, P.fcut, 2);
SP2MTF = SPOTF2(floor(end/2),:);

% simulate the images: first order
EimSP1 = P.CI.OBJspatfreq.*SPOTF1;
eimSP1 = ifftshift(ifft2(ifftshift(EimSP1)));
IDLSP1 = eimSP1.*conj(eimSP1);
IDLSP1 = IDLSP1/max(abs(IDLSP1(:)));

% simulate the images: second order
EimSP2 = P.CI.OBJspatfreq.*SPOTF2;
eimSP2 = ifftshift(ifft2(ifftshift(EimSP2)));
IDLSP2 = eimSP2.*conj(eimSP2);
IDLSP2 = IDLSP2/max(abs(IDLSP2(:)));

% feed in the diffraction limited linear SPIFI images
P.PlotVariables.ISP1 = IDLSP1;
P.PlotVariables.Support.SP1 = SP1MTF;
P.PlotVariables.ISP2 = IDLSP2;
P.PlotVariables.Support.SP2 = SP2MTF;

%% SHG SPIFI: third and fourth orders

% transfer functions
% third order
```

```
SPOTF3 = mu(P.FRt, P.fcut, 3);
SP3MTF = SPOTF3(floor(end/2),:);
% fourth order
SPOTF4 = mu(P.FRt, P.fcut, 4);
SP4MTF = SPOTF4(floor(end/2),:);

% simulate the images: first order
EimSP3 = P.CI.OBJspatfreq.*SPOTF3;
eimSP3 = ifftshift(ifft2(ifftshift(EimSP3)));
IDLSP3 = eimSP3.*conj(eimSP3);
IDLSP3 = IDLSP3/max(abs(IDLSP3(:)));

% simulate the images: second order
EimSP4 = P.CI.OBJspatfreq.*SPOTF4;
eimSP4 = ifftshift(ifft2(ifftshift(EimSP4)));
IDLSP4 = eimSP4.*conj(eimSP4);
IDLSP4 = IDLSP4/max(abs(IDLSP4(:)));

% feed in the diffraction limited SHG SPIFI images
P.PlotVariables.ISP3 = IDLSP3;
P.PlotVariables.Support.SP3 = SP3MTF;
P.PlotVariables.ISP4 = IDLSP4;
P.PlotVariables.Support.SP4 = SP4MTF;

%% SPIFI: sixth order

% transfer functions
```

```
% fifth order
SPOTF5 = mu(P.FRt, P.fcut, 5);
SP5MTF = SPOTF5(floor(end/2),:);
% sixth order
SPOTF6 = mu(P.FRt, P.fcut, 6);
SP6MTF = SPOTF6(floor(end/2),:);

% simulate the images: fifth order
EimSP5 = P.CI.OBJspatfreq.*SPOTF5;
eimSP5 = ifftshift(ifft2(ifftshift(EimSP5)));
IDLSP5 = eimSP5.*conj(eimSP5);
IDLSP5 = IDLSP5/max(abs(IDLSP5(:)));

% simulate the images: sixth order
EimSP6 = P.CI.OBJspatfreq.*SPOTF6;
eimSP6 = ifftshift(ifft2(ifftshift(EimSP6)));
IDLSP6 = eimSP6.*conj(eimSP6);
IDLSP6 = IDLSP6/max(abs(IDLSP6(:)));

% feed in the diffraction limited higher order SPIFI images
P.PlotVariables.ISP5 = IDLSP5;
P.PlotVariables.Support.SP5 = SP5MTF;
P.PlotVariables.ISP6 = IDLSP6;
P.PlotVariables.Support.SP6 = SP6MTF;

%% make the plots!
SPIFIComparePlot(P)
```

```
%% ************ Functions ************

% ------------------------------------------------------------------------

function f = jinc(x)
    f = 2*besselj(1,x)./x;
    J = find(x==0);
    f(J) = 1;
end

% ------------------------------------------------------------------------

function PSF_2d = PSF_1Dto2D(PSF_1d,x)

     r = x(end/2+1:end);              % starts at zero, faster to just interp
        first quadrant then concatenate
     input = PSF_1d(end/2+1:end);

     M = sqrt(r.^2+r'.^2);          % dummy matrix of different radii from
        origin
     M = M(:);
     PSF_2d = interp1(r, input, M,'spline',0);          % interpolate onto 1D
         list
     PSF_2d = reshape(PSF_2d, [length(r),length(r)]); % make back into
        array
```

```
    % put into all four quadrants
    PSF_2d = [rot90(PSF_2d); PSF_2d];
    PSF_2d = [rot90(rot90(PSF_2d)) PSF_2d];

end

% ------------------------------------------------------------------------

% ImageSetup.m
% Note code below should be saved as a separate '.m' file to be called by
    above code

% Setup Specific Imaging Parameter for the Technique being used
switch Illum
    case 'pulsed'
        T = 2*un.ps;                                % Pulse duration
        F = @(alpha) 1 - exp(-alpha.*T/tau);    % alpha = I_max/I_sat
    case 'cw'
        F = @(alpha) alpha ./ (1+alpha);
    otherwise

end

switch URSR
    case 'sted'
        beta = 1;
```

```
        alpha  = @(I_max,I_sat,NA,l,r) 0.429*I_max*(2*pi*NA/l)^2*r.^2/
            I_sat;
        switchingType = 'OFF';
    case 'gsd'
        k_fl  = 1/(4.5*un.ns);    % Decay rate from the radiative and
            nonradiative 4.5 ns
        k_isc = 1/(100*un.ns);      % Intersystem crossing rate 100 ns
        k_t   = 1/(20*un.us);    % Decay rate from the triplet state 1/(1
            us to 1 ms)
        beta  = 1/(1+k_t/k_isc);
%         beta  = k_isc/(k_isc+k_fl)
        alpha   = @(I_max,I_sat,NA,l,r) 0.429*I_max*(2*pi*NA/l)^2*r.^2/
            I_sat;
        switchingType = 'ON';
    case 'photoswitching'
        beta = 1;
        alpha  = @(I_max,I_sat,NA,l,r) 0.429*I_max*(2*pi*NA/l)^2*r.^2/
            I_sat;
        switchingType = 'OFF';
    case 'sax'
        beta = 1;
        alpha = I_max/I_sat;
        switchingType = 'ON';
    case 'spifi'
        beta = 1;
        switchingType = 'ON';
    case 'chirpt'
```

```
        beta = 1;
        switchingType = 'ON';
    otherwise
end

switch switchingType
    case 'ON'
%         eta = beta*F(alpha(I_max,I_sat,NA,lambda,x));
    case 'OFF'
        eta = 1-beta*F(alpha(I_max,I_sat,NA,lambda,x));
    otherwise
end

% ------------------------------------------------------------------------

function SPIFIComparePlot(P)

% coherent vs first order SPIFI

figure(P.plt_ctr); clf

Nrows = 2;
indx = 0;

% plot the MTFs
subplot(Nrows, 2, 1)
plot(P.PlotVariables.fxvar,abs(P.PlotVariables.Support.Coh),'r');
```

```
hold on
plot(P.PlotVariables.fxvar,abs(P.PlotVariables.Support.SP1),'b');
xlabel(P.PlotVariables.fxlab);
hold off
ylabel('MTF');
title('Coherent Widefield/1^s^t Order');
xlim([-1.2,1.2])
ylim(P.PlotVariables.Panel1ylim)
V = get(gcf,'position');

%plot the original object
subplot(Nrows, 2, 2)
imagesc(P.PlotVariables.xvar,P.PlotVariables.yvar,abs(P.PlotVariables.
    Object));
title('Original Object');
xlabel(P.PlotVariables.xlab);
ylabel(P.PlotVariables.ylab);
colormap gray
axis equal
axis tight

% conventional linear coherent and incoherent images
% increment the index
indx = indx + 1;

% now plot the coherent image version
subplot(Nrows,2,2*indx + 1)
```

```
imagesc(P.PlotVariables.xvar,P.PlotVariables.yvar,histeq(abs(P.
    PlotVariables.CohImg),256));
title('Coherent Image');
xlabel(P.PlotVariables.xlab);
ylabel(P.PlotVariables.ylab);
colormap gray
axis equal
axis tight

% first order
subplot(Nrows,2,2*indx + 2)
imagesc(P.PlotVariables.xvar,P.PlotVariables.yvar,histeq(abs(P.
    PlotVariables.ISP1),256));
title('1^s^t Order Linear SPIFI');
xlabel(P.PlotVariables.xlab);
ylabel(P.PlotVariables.ylab);
colormap gray
axis equal
axis tight

%%
% incoherent vs second order SPIFI

% start an second order figure
P.plt_ctr = P.plt_ctr +1;
figure(P.plt_ctr); clf
indx = 0;
```

```
Nrows = 2;
indx = 0;

% plot the MTFs
subplot(Nrows, 2, 1)
plot(P.PlotVariables.fxvar,abs(P.PlotVariables.Support.InCoh),'r');
hold on
plot(P.PlotVariables.fxvar,abs(P.PlotVariables.Support.SP2),'b');
xlabel(P.PlotVariables.fxlab);
hold off
ylabel('MTF');
title('Incoherent Widefield/2^n^d Order');
xlim([-2.3,2.3])
ylim(P.PlotVariables.Panel1ylim)
V = get(gcf,'position');

%plot the original object
subplot(Nrows, 2, 2)
imagesc(P.PlotVariables.xvar,P.PlotVariables.yvar,abs(P.PlotVariables.
    Object));
title('Original Object');
xlabel(P.PlotVariables.xlab);
ylabel(P.PlotVariables.ylab);
colormap gray
axis equal
axis tight
```

```
% conventional linear coherent and incoherent images
% increment the index
indx = indx + 1;

% now plot the incoherent image version
subplot(Nrows,2,2*indx + 1)
imagesc(P.PlotVariables.xvar,P.PlotVariables.yvar,histeq(abs(P.
    PlotVariables.InCohImg),256));
title('Incoherent Image');
xlabel(P.PlotVariables.xlab);
ylabel(P.PlotVariables.ylab);
colormap gray
axis equal
axis tight


% plot the second order SPIFI image
subplot(Nrows,2,2*indx + 2)
imagesc(P.PlotVariables.xvar,P.PlotVariables.yvar,histeq(abs(P.
    PlotVariables.ISP2),256));
title('2^n^d Order Linear SPIFI');
xlabel(P.PlotVariables.xlab);
ylabel(P.PlotVariables.ylab);
colormap gray
axis equal
axis tight
```

```
%%

% start an SHG figure
P.plt_ctr = P.plt_ctr +1;
figure(P.plt_ctr); clf

% LSM SHG
Nrows = 2;
indx = 0;

% plot the SHG MTFs
subplot(Nrows, 2, 1)
plot(P.PlotVariables.fxvar,abs(P.PlotVariables.Support.LSMSHG),'r');
hold on
plot(P.PlotVariables.fxvar,abs(P.PlotVariables.Support.SP4),'b');
xlabel(P.PlotVariables.fxlab);
hold off
ylabel('MTF');
title('SHG, TPEF/4^t^h Order');
xlim([-4.3,4.3])
ylim(P.PlotVariables.Panel1ylim)
V = get(gcf,'position');

%plot the original object
subplot(Nrows, 2, 2)
```

```
imagesc(P.PlotVariables.xvar,P.PlotVariables.yvar,(abs(P.PlotVariables.
    Object)));
title('Original Object');
xlabel(P.PlotVariables.xlab);
ylabel(P.PlotVariables.ylab);
colormap gray
axis equal
axis tight

% SHG LSM & 4th order SPIFI images
% increment the index
indx = indx + 1;

% SHG LSM
subplot(Nrows,2,2*indx + 1)
imagesc(P.PlotVariables.xvar,P.PlotVariables.yvar,histeq(abs(P.
    PlotVariables.LSMSHGImg),256));
title('LSM SHG/TPEF');
xlabel(P.PlotVariables.xlab);
ylabel(P.PlotVariables.ylab);
colormap gray
axis equal
axis tight

% plot the 4th order SPIFI image
subplot(Nrows,2,2*indx + 2)
```

```
imagesc(P.PlotVariables.xvar,P.PlotVariables.yvar,histeq(abs(P.
    PlotVariables.ISP4),256));
title('4^t^h Order SPIFI');
xlabel(P.PlotVariables.xlab);
ylabel(P.PlotVariables.ylab);
colormap gray
axis equal
axis tight

%%

% start an THG figure
P.plt_ctr = P.plt_ctr +1;
figure(P.plt_ctr); clf

% LSM THG
Nrows = 2;
indx = 0;

% plot the THG MTFs
subplot(Nrows, 2, 1)
plot(P.PlotVariables.fxvar,abs(P.PlotVariables.Support.LSMTHG),'r');
hold on
plot(P.PlotVariables.fxvar,abs(P.PlotVariables.Support.SP6),'b');
xlabel(P.PlotVariables.fxlab);
hold off
ylabel('MTF');
```

```
title('THG, 3PEF/6^t^h Order');
xlim([-6.3,6.3])
ylim(P.PlotVariables.Panel1ylim)
V = get(gcf,'position');

%plot the original object
subplot(Nrows, 2, 2)
imagesc(P.PlotVariables.xvar,P.PlotVariables.yvar,(abs(P.PlotVariables.
    Object)));
title('Original Object');
xlabel(P.PlotVariables.xlab);
ylabel(P.PlotVariables.ylab);
colormap gray
axis equal
axis tight

% THG LSM & 6th order SPIFI images
% increment the index
indx = indx + 1;

% SHG LSM
subplot(Nrows,2,2*indx + 1)
imagesc(P.PlotVariables.xvar,P.PlotVariables.yvar,histeq(abs(P.
    PlotVariables.LSMTHGImg),256));
title('LSM THG/3PEF');
xlabel(P.PlotVariables.xlab);
ylabel(P.PlotVariables.ylab);
```

```
colormap gray
axis equal
axis tight

% plot the 6th order SPIFI image
subplot(Nrows,2,2*indx + 2)
imagesc(P.PlotVariables.xvar,P.PlotVariables.yvar,histeq(abs(P.
    PlotVariables.ISP6),256));
title('6^t^h Order SPIFI');
xlabel(P.PlotVariables.xlab);
ylabel(P.PlotVariables.ylab);
colormap gray
axis equal
axis tight

%%

% start an confocal figure
P.plt_ctr = P.plt_ctr +1;
figure(P.plt_ctr); clf

% confocal
Nrows = 2;
indx = 0;

% plot the confocal MTFs
subplot(Nrows, 2, 1)
```

```
plot(P.PlotVariables.fxvar,abs(P.PlotVariables.Support.CONF0),'r');
hold on
plot(P.PlotVariables.fxvar,abs(P.PlotVariables.Support.CONF1),'b');
plot(P.PlotVariables.fxvar,abs(P.PlotVariables.Support.CONFPR),'m');
xlabel(P.PlotVariables.fxlab);
hold off
ylabel('MTF');
title('CONF_0, CONF_1, CONF_P_R');

xlim([-4.3,4.3])
ylim(P.PlotVariables.Panel1ylim)
V = get(gcf,'position');

%plot the original object
subplot(Nrows, 2, 2)
imagesc(P.PlotVariables.xvar,P.PlotVariables.yvar,histeq(abs(P.
    PlotVariables.CONF0Img),256));
title('CONF_{delta pinhole}');
xlabel(P.PlotVariables.xlab);
ylabel(P.PlotVariables.ylab);
colormap gray
axis equal
axis tight

% THG LSM & 6th order SPIFI images
% increment the index
indx = indx + 1;
```

```
% Cofocal image with 1 AU radius pinhole
subplot(Nrows,2,2*indx + 1)
imagesc(P.PlotVariables.xvar,P.PlotVariables.yvar,histeq(abs(P.
    PlotVariables.CONF1Img),256));
title('CONF_{airy pinhole}');
xlabel(P.PlotVariables.xlab);
ylabel(P.PlotVariables.ylab);
colormap gray
axis equal
axis tight

% Pixel reassignment confocal
subplot(Nrows,2,2*indx + 2)
imagesc(P.PlotVariables.xvar,P.PlotVariables.yvar,histeq(abs(P.
    PlotVariables.CONFPRImg),256));
title('Pixel Reassignment Confocal');
xlabel(P.PlotVariables.xlab);
ylabel(P.PlotVariables.ylab);
colormap gray
axis equal
axis tight

pause(0.0001)

%%
```

```
% start an SHG figure

figure(10); clf

% LSM SHG
Nrows = 2;
Ncols = 2;
indx = 0;

%plot the original object
subplot(Nrows, Ncols, 1)
imagesc(P.PlotVariables.xvar,P.PlotVariables.yvar,(abs(P.PlotVariables.
    Object)));
title('Original Object');
xlabel(P.PlotVariables.xlab);
ylabel(P.PlotVariables.ylab);
colormap gray
axis equal
axis tight
axis off



% plot the SHG MTFs
subplot(Nrows, Ncols,[3,4])
% plot(P.PlotVariables.fxvar,abs(P.PlotVariables.Support.InCoh));
plot(P.PlotVariables.fxvar,abs(P.PlotVariables.Support.CONF1));
```

```
hold on
plot(P.PlotVariables.fxvar,abs(P.PlotVariables.Support.LSMSHG));
plot(P.PlotVariables.fxvar,abs(P.PlotVariables.Support.SP2));
plot(P.PlotVariables.fxvar,abs(P.PlotVariables.Support.CONFPR));
plot(P.PlotVariables.fxvar,abs(P.PlotVariables.Support.SP4));
xlabel(P.PlotVariables.fxlab);
hold off
ylabel('MTF');
title('SHG, TPEF/4^t^h Order');
xlim([-4.3,4.3])
ylim(P.PlotVariables.Panel1ylim)
V = get(gcf,'position');

subplot(Nrows,Ncols,2)
% Cofocal image with 1 airy AU
imagesc(P.PlotVariables.xvar,P.PlotVariables.yvar,histeq(abs(P.
    PlotVariables.CONF1Img),256));
title('CONF_{airy pinhole}');
xlabel(P.PlotVariables.xlab);
ylabel(P.PlotVariables.ylab);
colormap gray
axis equal
axis tight
axis off

figure(11)
% plot the second order SPIFI image
```

```
subplot(Nrows,Ncols,3)
imagesc(P.PlotVariables.xvar,P.PlotVariables.yvar,histeq(abs(P.
    PlotVariables.ISP2),256));
title('2^n^d Order Linear SPIFI');
xlabel(P.PlotVariables.xlab);
ylabel(P.PlotVariables.ylab);
colormap gray
axis equal
axis tight
axis off

% SHG LSM
subplot(Nrows,Ncols,1)
imagesc(P.PlotVariables.xvar,P.PlotVariables.yvar,histeq(abs(P.
    PlotVariables.LSMSHGImg),256));
title('LSM SHG/TPEF');
xlabel(P.PlotVariables.xlab);
ylabel(P.PlotVariables.ylab);
colormap gray
axis equal
axis tight
axis off

% plot the 4th order SPIFI image
subplot(Nrows,Ncols,4)
imagesc(P.PlotVariables.xvar,P.PlotVariables.yvar,histeq(abs(P.
    PlotVariables.ISP4),256));
```

```
title('4^t^h Order SPIFI');
xlabel(P.PlotVariables.xlab);
ylabel(P.PlotVariables.ylab);
colormap gray
axis equal
axis tight
axis off

% Pixel reassignment confocal
subplot(Nrows,Ncols,2)
imagesc(P.PlotVariables.xvar,P.PlotVariables.yvar,histeq(abs(P.
    PlotVariables.CONFPRImg),256));
title('Pixel Reassignment Confocal');
xlabel(P.PlotVariables.xlab);
ylabel(P.PlotVariables.ylab);
colormap gray
axis equal
axis tight
axis off

end
```

Appendix E

Simulated Computational SPIFI Reconstruction

```
%% MP-SPIFI Simulation
% This code simulates the signal, noise, and data processing for Mult-
    photon
% SPIFI. This code will be used to develop the full processing
% algorithm for the real data.  The goal is to improve SNR and stitch the
% harmonic orders together.
% Goals: Simulate the time trace with a continuous model
%        Generate PSFs and OTFs for Starndard SPIFI, Comp SPIFI, and
    thoery



%% --- Set default properties for axes fonts ---
font = 'Helvetica';
set(0,'defaultaxesfontsize',14);
set(0,'defaultaxesfontname',font);
set(0,'DefaultFigureWindowStyle','docked')
% --- units ---
un = Units();


%% Setup Parameters
% Optical parameters
lambda   = 1035*un.nm;             % Optical illumination wavelength
k0       = 2*pi/lambda;            % Wavenumber
NA       = 0.1;                    % Numerical Aperture
```

```
kc      = k0*NA;                % Cutoff Radial Spatial Frequency
fxc     = NA/lambda;            % Cutoff Spatial Frequency

% SPIFI Parameters
dk    = 35/un.mm;               % Highest spatial frequency
nu_r  = 33*un.Hz;               % Rotation Frequency
xc    = 20*un.mm;               % Beam center on modulator
wb    = 2.5*un.mm;              % Beam width

wc    = nu_r*xc*dk;             % Carrier frequency
fmin  = nu_r*(xc-wb/2)*dk;      % Minimum modulation frequency
fmax  = nu_r*(xc+wb/2)*dk;      % Maximum modulation frequency


T     = 1/nu_r;                 % Acquisition period
% Nt    = round(2^13*(1+5/17));    % Number of sampled points
Nt = round(1.717*T*(2*(fmax*4)));
% Nt = 2^14
tt    = linspace(-T/2,T/2,Nt);  % Time vector
dt    = mean(diff(tt));         % Sampling period

dft   = 1/dt;                   % Sampling frequency
ftt   = 1/(Nt*dt)*(-Nt/2:Nt/2-1);% Frequency vector

Nx    = 512;
Dx    = 256*un.um;               % Field of View
x     = linspace(-Dx/2,Dx/2,Nx); % Spatial vector
```

```
xObj = x;
dx   = mean(diff(x));              % Spatial resolution
fx   = 1/(Nx*dx)*[-Nx/2:Nx/2-1];

Ny   = 363;
Dy   = 180*un.um;                  % Field of View
y    = linspace(-Dy/2,Dy/2,Ny); % Spatial vector
yObj = y;
dy   = mean(diff(y));              % Spatial resolution
fy   = 1/(Ny*dy)*[-Ny/2:Ny/2-1];

kappa = (fmax-fmin)/Dx; % Mapping from modulation frequency to space
% kappa = 5e7;                     % Mapping from modulation frequency to
    space, value comes from experiment
fxObj= 1/(Nx*dx)*(-Nx/2:Nx/2-1);% Spatial frequency vector
dfx  = mean(diff(fxObj));          % Sampling spatial frequency
dxc  = lambda/(2*NA);              % Diffraction Limited Resolution

M = wb/Dx/2;
%% Create the Object

% Simulate Object
load('cell.mat');

% obj = data;
% clear data;
```

```
figure(1)
imagesc(x/un.um,y/un.um,obj)
colormap gray
axis equal
% xlabel('x (\mum)')
% ylabel('Ampiltude')
% title('Object')
% xlim([-13.75,3])
set(gca,'ytick',[])
set(gca,'xtick',[])
axis off

%% SPIFI modulation anonymous function

fxt = @(t) dk*M*t./(T/2);
tc  = fxc*T/(2*dk*M);                    % Cut-off time

mu = @(t) 2*sqrt(1-(t/tc).^2).*(t>-tc).*(t<tc);  % Pupil function
mu_x = @(fx,fc) 2*sqrt(1-(fx/fc).^2).*(fx>-fc).*(fx<fc);  % Pupil function

I2 = @(t,x) (1/16 + 3/pi^2*mu(t).^2 + 6/pi^4*mu(t).^4)...
    + (1/pi*mu(t)+12/pi^3*mu(t).^3).* cos(2*pi*fxt(t).*x + 2*pi*wc*t)...
    + (3/pi^2*mu(t).^2 + 8/pi^4*mu(t).^4).*cos(4*pi*fxt(t).*x + 4*pi*wc*t)
        ...
    + (4/pi^3*mu(t).^3).*cos(6*pi*fxt(t).*x + 6*pi*wc*t)...
    + (2/pi^4*mu(t).^4).*cos(8*pi*fxt(t).*x + 8*pi*wc*t);
```

```
%%
% A - measurement matrix -- A is going to contain all the temporal
% frequencies on the medium, i.e. rep. rate freq. and harmonics

Nphoton = 2;                    % Number of photons in the nonlinear process
A = zeros(Nx,Nt);               % Initialize measurement matrix

tic
% Generate Measurement matrix
for ii = 1:Nx
    A(ii,:) = I2(tt,x(ii));
end
A = A/max(max(A));
toc

%%
wy = lambda/(2*NA)/4;

uy = @(y,wy) exp(-y.^2/(2*wy.^2));

Ny_ill = round_odd(4*wy/dy);
y_ill  = linspace(-2*wy,2*wy,Ny_ill);

% Zero pad object for the y scanning
objPad = zeros(Ny+round(3/2*Ny_ill)-1,Nx);
objPad(round(Ny_ill/2):end-Ny_ill,:) = obj;
%%
```

```
Axy = repmat(A,1,1,Ny_ill);

for ii = 1:Ny_ill
    Axy(:,:,ii) = Axy(:,:,ii)*uy(y_ill(ii),wy).^2;
end

%%
figure(2)
imagesc(tt,x/un.um,A)
title('Ideal Illumination')
xlabel('Time')
ylabel('Space')
ylim([-5,5])


%% Create Time trace from A matrix
tic
for jj = 1:Ny
    for ii = 1:Nt
        sigA(ii,jj) = sum(sum(squeeze(Axy(:,ii,:)).*objPad(jj:jj+Ny_ill
            -1,:)'));
    end
end
toc

%% Trim Harmonics
Sp_t_demod = zeros(Nt,Ny,4);
```

```
for jj = 1:Ny
    for ii = 1:4
        Sp_t(:,jj,ii) = SpifiTrimHarmonic(tt,sigA(:,jj)',ii*wc,ii*2.5*un.
            kHz);
        demodVec = exp(-1i*2*pi*wc*tt*ii);
        Sp_t_demod(:,jj,ii) = squeeze(Sp_t(:,jj,ii)).*demodVec.';
    end
end

%%
figure(3);
clf; hold on;
for ii = 1:4
    subplot(2,2,ii)
    imagesc(ftt/un.kHz,y/un.um,fliplr(abs(iFFT(squeeze(Sp_t_demod(:,:,ii))
        ,1))'))
    title(['SPIFI Order ', num2str(ii)])
    xlim([-1.45,1.425]*ii)
    axis off
    colormap gray
end

%% Second order SPIFI image
indxMin = nearest(-1.45*4,ftt/un.kHz);
indxMax = nearest(1.425*4,ftt/un.kHz);
tmp = fliplr(abs(iFFT(squeeze(Sp_t_demod(:,:,4)),1))');
obj4 = tmp(:,indxMin:indxMax);
```

```
figure(4)
clf
imagesc(obj4)
colormap gray
axis off
%% Down Sample Signal
% T     = 1/nu_r;                    % Acquisition period
% Nt    = 2^14;                      % Number of sampled points
Nt    = round(1.015*T/(1/(2*(fmax*4))));
t     = linspace(-T/2,T/2,Nt);     % Time vector
dt    = mean(diff(t));             % Sampling period

dft   = 1/dt;                      % Sampling frequency
ft    = 1/(Nt*dt)*(-Nt/2:Nt/2-1);  % Frequency vector

Nx    = 2^9;
x     = linspace(-Dx/2,Dx/2,Nx);   % Spatial vector
dx    = mean(diff(x));             % Spatial resolution

dxLim  = lambda/(2*NA);
dfxLim = 1/dxLim;

% kappa = dt/dx;                   % Mapping from modulation frequency to
    space
% kappa = 5e7;                     % Mapping from modulation frequency to
    space, value comes from experiment
```

```
fx    = 1/(Nx*dx)*(-Nx/2:Nx/2-1);                    % Spatial frequency
    vector
dfx   = mean(diff(fx));                 % Sampling spatial frequency

clear sigDS
for ii = 1:Ny
    sigDS(:,ii) = interp1(tt,sigA(:,ii),t,'spline');
end

%% New A matrix on large grid

Ads = zeros(Nx,Nt);           % Initialize measurement matrix
% Generate Measurement matrix

for ii = 1:Nx
    Ads(ii,:) = I2(t,x(ii));
end

%% Add Noise

% sigN = addNoise(sigDS',0.00,10000,'')';
clear sigN
for ii = 1:Ny
    sigN(:,ii) = addNoise(abs(sigDS(:,ii))+0.02,0.0,100,'')';
end

figure(5)
```

```
clf
plot(ft/un.kHz,log(abs(FFT(sigDS(:,200)))),'linewidth',1.5)
hold on
plot(ft/un.kHz,log(abs(FFT(sigN(:,200)))),'linewidth',1.5)
title('')

title('FFT of Time Trace')
xlabel('Frequency [kHz]')

% xlim(1*[21.75,23.75])
%% xlim([39,43.5])
%% ylim([0,0.035])
% set(gca,'ytick',[])
% set(gca,'xtick',[])


%% Trim Harmonics
Sp_N = zeros(Nt,Ny,4);
for jj = 1:Ny
    for ii = 1:4
        Sp_tN(:,jj,ii) = SpifiTrimHarmonic(t,sigN(:,jj)',ii*wc,ii*2.5*un.
            kHz);
        demodVec = exp(-1i*2*pi*wc*t*ii);
        Sp_N(:,jj,ii) = squeeze(Sp_tN(:,jj,ii)).*demodVec.';
    end
end
```

```
%%
figure(6);
clf; hold on;
for ii = 1:4
    subplot(2,2,ii)
    imagesc(ft/un.kHz,y/un.um,fliplr(abs(iFFT(squeeze(Sp_N(:,:,ii)),1))'))
    title(['SPIFI Order ', num2str(ii)])
    xlim([-1.45,1.425]*ii)
    axis off
    colormap gray
end

%% Second order SPIFI image
indxMin = nearest(-1.45*2,ft/un.kHz);
indxMax = nearest(1.425*2,ft/un.kHz);
tmp = fliplr(abs(iFFT(squeeze(Sp_N(:,:,2)),1))');
obj2N = tmp(:,indxMin:indxMax);

figure(7)
imagesc(obj2N)
colormap gray
axis off

%% Fista Reconstruction with noise

% A is the measurment matrix
% Trace is the recorded data from photodiode
```

```
    [ob1, info] = IRfista(Ads',sigN,struct('x0','none', 'MaxIter',20, '
        x_true','none', ...
         'NoiseLevel','none', 'eta',1.01, 'NE_Rtol',1e-12, 'IterBar','off',
             ...
         'NoStop','off', 'RegParam',10, 'xMin',0, 'xMax',Inf, 'xEnergy','
            none')); % initial object estimate

%%
figure(8)
imagesc(x/un.um,y/un.um,ob1'/max(max(ob1)))
colormap gray


%% Plot the MTF

figure(9)
clf
plot(linspace(-1,1,size(obj,2)),mean(abs(FFT(obj-mean(mean(obj)),2)),1)/
    max(mean(abs(FFT(obj-mean(mean(obj)),2)),1)))
hold on;
plot(linspace(-1,1,size(obj2N,2)),mean(abs(FFT(obj2N-mean(mean(obj2N)),2))
    ,1)/max(mean(abs(FFT(obj2N-mean(mean(obj2N)),2)),1)))
plot(linspace(-1,1,size(obj4,2)),mean(abs(FFT(obj4-mean(mean(obj4)),2)),1)
    /max(mean(abs(FFT(obj4-mean(mean(obj4)),2)),1)))
plot(linspace(-1,1,size(obN,2)),mean(abs(FFT(obN-mean(mean(obN)),2)),1)/
    max(mean(abs(FFT(obN-mean(mean(obN)),2)),1)))
```

```
plot(linspace(-1,1,size(objInv2D',2)),mean(abs(FFT(objMed-mean(mean(
    objInv2D'))',2))',1)/max(mean(abs(FFT(objInv2D'-mean(mean(objInv2D'))',2)
    )',1)))

%% Useful Functions

function [obj] = objGen(x)
    %% Make object
    Nx      = numel(x);                          % Number of sample point
        on orginal grid

    obj = zeros(1,Nx);

    % Gaussian
    obj = 0.4*exp(-(x-x(round(Nx*0.28))).^2/(x(end)*0.1).^2);
%                 + 0.5*exp(-(xx-xx(round(Nxx*0.35))).^2/(xx(end)*0.04)
    .^2);
%     % Three bars
%     obj(round(Nx*0.400):round(Nx*0.402)) = 1;
%     obj(round(Nx*0.404):round(Nx*0.406)) = 1;
%     obj(round(Nx*0.408):round(Nx*0.41)) = 1;
%
%     % Three bars different heights
    obj(round(Nx*0.4):round(Nx*0.42)) = 1;
    obj(round(Nx*0.45):round(Nx*0.47)) = 0.564;
    obj(round(Nx*0.5):round(Nx*0.52)) = 0.82;
```

```
    % Delta function
%       obj(round(Nx*0.499):round(Nx*0.501)) = 1;
%       obj(round(Nx*0.539):round(Nx*0.54)) = 0.5;
%       obj(round(Nx*0.39):round(Nx*0.392)) = 0.31;
%       obj(round(Nx*0.19):round(Nx*0.192)) = 0.1;
%       obj = obj+0.02;

end

%%

function [dataOut,tOut] = PreProcessing(dataIn, t, ft, f0, fw, ds, order)

    % Filter time traces, trimming out the frequence of interest/ image
        band
    filter = exp(-(2*pi*(ft-f0*order)./(fw*order)).^6);
    % Sum all the time sequences
%       figure; plot(ft,filter)
%       hold on; plot(ft,abs(FFT(dataIn))/max(abs(FFT(dataIn))))
    ftData = FFT(dataIn) .* filter;

    % Demodulate
    dataDS = iFFT(ftData).*exp(-2i.*pi.*(f0*order).*t);
%
%       % Time domain and downsample
    dataOut = downsample((dataDS),ds);
    tOut = downsample(t,ds);
```

```
end


%%
function [y] = round_odd(x)
y = 2*floor(x/2)+1;
end
```

Appendix F

Computational SPIFI Reconstruction

```
%% MP_SPIFI_Data_Processing_Inverse_Reconstruction
% This code used an estimated A matrix to reconstruct the object
% I use Randy's maximum likelyhood code and IRFista to estimate the object

% Author: Patrick Stockton
% Date:   03/25/2021

ccc



%% --- Set default properties for axes fonts ---
font = 'Helvetica';
set(0,'defaultaxesfontsize',14);
set(0,'defaultaxesfontname',font);
set(0,'DefaultFigureWindowStyle','docked')
% --- units ---
un = Units();

%% ------ [ load data ] ------

display('loading data...');

% file.Path = 'D:\ets01173\HD-WHU3\Patrick\Dissertation\Data Processing\MP
    -SPIFI\data';
```

```
file.Path = 'D:\ets01173\My Book\Patrick\MP_SPIFI\data'
file.Date = '20210819';
file.Name = 'beads';
file.Number = '02';
file.Full = strcat([file.Path,'\',file.Date,'/',file.Name,'_',file.Number,
    '.mat']);
data = load(file.Full);

% Load A Matrix Data
% A = load(strcat([file.Path,'\',file.Date,'/measurementMatrix.mat']));
% A = load(strcat([file.Path,'\',file.Date,'/Amaxtrix_slitScan.mat']));

%% load kappa calibration
% kData = load(strcat([file.Path,'\',file.Date,'/calibration_file.mat']));

%% load kappaY calibration
% gData = load(strcat([file.Path,'\',file.Date,'/calibration_galvo.mat']))
    ;

% load disk aberration phase
% wcData = load(strcat([file.Path,'\',file.Date,'/disk_aberration.mat']));

% load time trace to align to
% align = load([file.Path,'\',file.Date,'/alignmentTrace.mat']);


%%
```

```
Algorithm = 'FistaEnet';        % 'Fista', 'EM', or 'FFT' 'Tik'
A.alignmentTrace = sum(A.A,1);
% figure out what kind of data set this is
% data.Y_t0 = data.Y_t0(30:80,:,:);
[i,j,k] = size(data.Y_t0(:,:,:));

% TODO: Will have to modify this to handle raster scans at some point...

if i == 1
    % data set consists of j traces at a single position
    imageType = 'nTraceAverage';
elseif j == 1
    % data set consists of a single time trace for numerous positions,
    % i.e., a single image with no averaging
    imageType = 'normalImage';
elseif i ~= 1 && j ~= 1
    % data set is an image with averaging
    imageType = 'averagedImage';
end

switch imageType;
    case 'nTraceAverage'
        % want to average the temporal traces by making them all conform
            to
        % the average rotational frequency
        display(['averaging ',num2str(j),' images...']);
        display(' ');
```

```
% the data is a simple matrix, so remove the superfluous index
Y_t0 = squeeze(Y_t0);

% shift temproal fringes
Y_t0 = chirpedTimeShiftingNew(data.t0,Y_t0,...
    A.alignmentTrace);

Yt = mean(Y_t0);

switch Algorithm
    case 'Fista'
        [obj info] = IRfista(A.A1',Yt',struct('x0','none', '
           MaxIter',50, 'x_true','none', ...
            'NoiseLevel','none', 'eta',1.01, 'NE_Rtol',1e-12, '
              IterBar','off', ...
            'NoStop','off', 'RegParam',1, 'xMin',0, 'xMax',Inf, '
              xEnergy','none')); % initial object estimate
    case 'EM'
        fseed = ones(1,size(A.A,1));
        iter = 50;          % number of interations for MLE

        [obj, delta, gk] = EM_Bartels(A.A', Yt', fseed, iter);
    case 'FFT'
        error('Not in script yet')
end
```

```
        figure;
        plot(A.x,obj)
        title([Algorithm,' MP-Spifi'])

        print('-dpng',[file.Path,'\',file.Date,'\',file.Name,'_',file.
            Number,...
                '_',Algorithm,'.png']);

    case 'normalImage'
        display('processing a single image...');
        display(' ');



        % the data is a simple matrix, so remove the superfluous index
        Y_t0 = squeeze(Y_t0);
        [Nz,Nt] = size(Y_t0);

        % shift temproal fringes
        Yt = chirpedTimeShiftingNew(data.t0,Y_t0,...
            A.alignmentTrace);

        obj = zeros(size(A.A,1),Nz);

        for ii = 1:Nz
            switch Algorithm
                case 'Fista'
```

```
                [obl info] = IRfista(A.A',Yt(ii,:)',struct('x0','none'
                    , 'MaxIter',100, 'x_true','none', ...
                     'NoiseLevel','none', 'eta',1.01, 'NE_Rtol',1e-12,
                        'IterBar','off', ...
                     'NoStop','off', 'RegParam',1, 'xMin',0, 'xMax',Inf
                        , 'xEnergy','none')); % initial object
                        estimate
            case 'EM'
                fseed = ones(1,size(A.A,1));
                iter = 5;           % number of interations for MLE

                [obl, delta2, gk2] = EM_Bartels(A.A', Yt(ii,:)', fseed
                    , iter);
            case 'FFT'
                error('Not in script yet')
        end
        obj(ii,:) = obl;
    end
    figure;
    imagesc(data.Z,A.x,obj)
    title([Algorithm,' MP-Spifi'])

    print('-dpng',[file.Path,'\',file.Date,'\',file.Name,'_',file.
        Number,...
            '_',Algorithm,'.png']);

case 'averagedImage'
```

```
% average each image in the spatial domain
display(['averaging ',num2str(j),' images']);
display(' ');

A.A2 = A.A(:,end/2-8192:end/2+8193);
obj = zeros(size(A.A2,1),i);

for ii = 1:i

    % shift temproal fringes
    Y_t0 = squeeze(data.Y_t0(ii,:,:));
    Yt = chirpedTimeShiftingNew(data.t0,Y_t0,...
        A.alignmentTrace);

    % remove disk phase
%       wcPhase = exp(-1i.*wcData.phi_wc);
%       wcMat = repmat(wcPhase,[Nz,1]);
%       Yt = Yt.*wcMat;

    Yt = mean(Yt);
%       Yt = circshift(Yt,100);
    Yt = Yt(end/2-8192:end/2+8193);

    % the data is a simple matrix, so remove the superfluous index
    [Nz,Nt] = size(Yt);

    switch Algorithm
```

```
                case 'Fista'
                    [ob1 info] = IRfista(A.A2',Yt',struct('x0','none', '
                       MaxIter',50, 'x_true','none', ...
                        'NoiseLevel','none', 'eta',1.1, 'NE_Rtol',1e-12, '
                           IterBar','off', ...
                        'NoStop','off', 'RegParam',.1, 'xMin',0, 'xMax',
                           Inf, 'xEnergy','none')); % initial object
                           estimate
                case 'EM'
                    fseed = ones(1,size(A.A,1));
                    iter = 5;           % number of interations for MLE

                    [ob1, delta, gk] = EM_Bartels(A.A', Yt', fseed, iter);
                case 'FFT'
                    error('Not in script yet')
                case 'Tik'
                    if ii == 1
%                           [U , S, V] =  svd(A.A2');
%                           s          =  diag(S);
                        lambda      = 10;
                    end
                    ob1 = V*(S'*(U'*Yt')./(s.^2+lambda));
                case 'Truncated'
                    if ii == 1
                        %% --- truncate the singular values of A ---
    %                       [U, S, V] = svd(A.A2);
                        %%
```

```
                Strim = zeros(size(S));

                % ... or set the number of modes directl
                nModes = 75;

                for ii=1:nModes
                    Strim(ii,ii) = S(ii,ii);
                end
                Atruncated = U * Strim * V';
            end
            ob1 = Yt * pinv(Atruncated)';
        case 'FistaEnet'

            initObj = sum(A.A2.*Yt,2);
            opts.lambda  = 0.001;
            opts.lambda2 = 0.25;
            ob1 = fista_enet(Yt',A.A2',initObj,opts);
    end

    obj(:,ii) = ob1;

    figure(10)
    imagesc(abs(obj))
    drawnow;
end

figure;
```

```
        imagesc(data.Z,linspace(A.x(1),A.x(end),800),obj')
        title([Algorithm,' MP-Spifi'])
%           daspect([1,A.x(end)/data.Z(end),1])

        print('-dpng',[file.Path,'\',file.Date,'\',file.Name,'_',file.
            Number,...
                '_',Algorithm,'A.png']);

end

%%

function [rec, delta, gk] = EM_Bartels(A, s, objInit, Niter)
% Expectation Maximization
% min ||g-Af||^2
% Assuming Poisson noise is dominant
%
% iterative Expectation Maximization algorithm
% (called Richardson-Lucy in image processing)
% finds this fixed-point by iteration:
% f_(k+1) = f_k/(A^T 1) *. A^T(g/(A^T f_k))


% Starting guess for the object
%    f = 3e-2*ones(size(A(1,:)));
f = objInit;
```

```
for kk = 1:Niter
    % compute the kth signal estimate
    % in the blurring case, the convolution of the object
    gk = A*f(:);

    % residual
    r = s - A*f(:);

    % correction factor
    CF = (A')*(s./gk);

    %       figure(101)
    %       clf
    %       plot(CF)
    %       title(num2str(kk))
    %       pause(0.001)

    % updated object estimate
    fnew = abs(f(:).*CF);

    df = (fnew(:) - f(:));
    delta(kk) = max(abs(df).^2);

    % update the result
    f = fnew;

end
```

```
rec = f;

% rescale the object
rec(find(isnan(rec)))=0;

end
```

Appendix G

License

Colorado State University LaTeX Thesis Template

by Elliott Forney – 2017

This is free and unencumbered software released into the public domain.

Anyone is free to copy, modify, publish, use, compile, sell, or distribute this software, either in source code form or as a compiled binary, for any purpose, commercial or non-commercial, and by any means.

In jurisdictions that recognize copyright laws, the author or authors of this software dedicate any and all copyright interest in the software to the public domain. We make this dedication for the benefit of the public at large and to the detriment of our heirs and successors. We intend this dedication to be an overt act of relinquishment in perpetuity of all present and future rights to this software under copyright law.

THE SOFTWARE IS PROVIDED "AS IS", WITHOUT WARRANTY OF ANY KIND, EXPRESS OR IMPLIED, INCLUDING BUT NOT LIMITED TO THE WARRANTIES OF MERCHANTABILITY, FITNESS FOR A PARTICULAR PURPOSE AND NONINFRINGEMENT. IN NO EVENT SHALL THE AUTHORS BE LIABLE FOR ANY CLAIM, DAMAGES OR OTHER LIABILITY, WHETHER IN AN ACTION OF CONTRACT, TORT OR OTHERWISE, ARISING FROM, OUT OF OR IN CONNECTION WITH THE SOFTWARE OR THE USE OR OTHER DEALINGS IN THE SOFTWARE.